



**HAL**  
open science

# Development of an Active-Fault Tolerant Control Applied to PV systems

Luis Antonio Garcia-Gutierrez

► **To cite this version:**

Luis Antonio Garcia-Gutierrez. Development of an Active-Fault Tolerant Control Applied to PV systems. Micro and nanotechnologies/Microelectronics. Université Toulouse 3 Paul Sabatier (UT3 Paul Sabatier), 2019. English. NNT: . tel-02147149v1

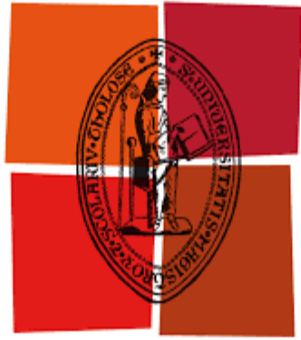
**HAL Id: tel-02147149**

**<https://laas.hal.science/tel-02147149v1>**

Submitted on 4 Jun 2019 (v1), last revised 8 Jul 2020 (v2)

**HAL** is a multi-disciplinary open access archive for the deposit and dissemination of scientific research documents, whether they are published or not. The documents may come from teaching and research institutions in France or abroad, or from public or private research centers.

L'archive ouverte pluridisciplinaire **HAL**, est destinée au dépôt et à la diffusion de documents scientifiques de niveau recherche, publiés ou non, émanant des établissements d'enseignement et de recherche français ou étrangers, des laboratoires publics ou privés.



Université  
de Toulouse

# THÈSE



En vue de l'obtention du

## DOCTORAT DE L'UNIVERSITÉ DE TOULOUSE ET L'UNIVERSIDAD DE LOS ANDES

Délivré par : *l'Université Toulouse 3 Paul Sabatier (UT3 Paul Sabatier)*  
Cotutelle internationale *UNIVERSIDAD DE LOS ANDES*

---

---

Présentée et soutenue le *29/03/2019* par :

**LUIS ANTONIO GARCÍA-GUTIÉRREZ**

Développement d'un Contrôle Actif Tolérant aux Défaillances Appliqué  
aux Systèmes PV

Development of an Active-Fault Tolerant Control Applied to PV systems

---

---

### JURY

MME. ANNE MIGAN	Professeur d'Université	Rapporteur
M. BRUNO ROBERT	Professeur d'Université	Rapporteur
M. OSWALDO LÓPEZ	Professeur d'Université	Rapporteur
MME. ANGELA CADENA	Professeur d'Université	Examineur
M. DANIEL HISSEL	Professeur d'Université	Examineur
MME. CORINNE ALONSO	Professeur d'Université	Directeur de thèse
M. FERNANDO JIMÉNEZ	Professeur d'Université	Co-directeur de thèse
M. MICHAEL BRESSAN	Professeur d'Université	Co-encadrant
M. BRUNO ESTIBALS	Professeur d'Université	Co-encadrant

---

### École doctorale et spécialité :

*GEET : Génie Electrique*

### Unité de Recherche :

*Laboratoire d'analyse et d'architecture des systemes (LAAS)*

### Directeur(s) de Thèse :

*Prof. Corinne ALONSO (UT3), Ph.D. Fernando JIMÉNEZ (UniAndes),*

*Co-encadrant Ph.D. Michael BRESSAN (UniAndes) et Prof. Bruno ESTIBALS (UT3)*

### Rapporteurs :

*Mme. Anne MIGAN, M. Bruno ROBERT et M. Oswaldo LÓPEZ*





# Development of an Active Fault Tolerant Control Applied to PV Systems

---

Luis Antonio GARCÍA GUTIÉRREZ

*A dissertation submitted in partial fulfilment of the requirements  
for the degree of Ph.D in Engineering  
at Universidad de los Andes (Uniandes)  
and  
for the degree of Ph.D in Electrical Engineering  
at Universidad Toulouse III Paul Sabatier (UT3)*

March 29, 2019

Thesis director: Prof. Corinne ALONSO (**UT3**)  
Ph.D. Fernando JIMÉNEZ (**Uniandes**)  
Co-advisor: Prof. Bruno ESTIBALS (**UT3**)  
Ph.D. Michael BRESSAN (**Uniandes**)



# Abstract

This work contributes by developing an active fault tolerant control (AFTC) for Photovoltaic (PV) systems. The fault detection and diagnosis (FDD) methodology is based on the analysis of a model that compares real-time measurement. We use a high granularity PV array model in the FDD tool to allow faults to be detected in complex conditions. Firstly, the research focuses on fault detection in complex shadow conditions. A real-time approach is presented to emulate the electrical characteristics of PV modules under complex shadow conditions. Using a precise emulators approach is a real challenge to study the high non-linearity and the complexity of PV systems in partial shading. The real-time emulation was validated with simple experimental results under failure conditions to design specific fault-detection algorithms in a first sample. The second part of the research addresses the FDD method for DC/DC and DC/AC power converters that are connected to the grid. Primary results allowed us to validate the system's recovery for normal operating points after a fault with this complete AFTC approach. Emulations based on the simulation of distributed power converters, fault detection methodologies based on a model, and a hybrid diagnostician were then presented.



# Résumé

Cette thèse de doctorat aborde la problématique de la réalisation d'un système de contrôle actif de détection de défaut et diagnostic (FDD) pour un système de conversion photovoltaïque. Ce type de système de production d'énergie électrique est composé de panneaux solaires, d'un dispositif MPPT, d'un convertisseur de courant DC-DC, d'un onduleur DC-AC et d'une charge. Le système de contrôle actif à tolérance de pannes qui a été développé dans cette thèse est composé de deux étages:

- Un étage assurant la fonction de diagnostic et comprenant les fonctions de détection de défauts, la fonction d'isolement de défauts, l'identification de défauts et l'estimation de l'ampleur du/des défaut(s)
- Une fonction de reconfiguration du système photovoltaïque.

Ce manuscrit est divisé en quatre chapitres:

- Introduction au problème et révision de l'état de la technique
- Modélisation mathématique du système photovoltaïque avec une validation expérimental de ce dernier effectué sur la plateforme PV de caractérisation du bâtiment réel ADREAM (Laboratoire LAAS-CNRS)
- Conception et mise en œuvre du système de diagnostic de pannes du système photovoltaïque comprenant un Système actif à tolérance de pannes
- Un système de diagnostic expérimental en cours de développement à l'aide d'un dispositif FPGA.

## 0.1 Introduction

Au cours des dernières années, l'énergie photovoltaïque a fait l'objet de beaucoup d'attentions, en particulier en raison de sa grande polyvalence et de sa mise en œuvre facile. Toutefois comme ce type de système de conversion d'énergie est composé de plusieurs fonctions et composants différents comme les panneaux solaires, les étages d'adaptation (convertisseurs DC-DC et/ou DC-AC) et leur commande associées dont la commande spécifique MPPT, la durée de vie de l'ensemble dépend du taux de panne possible provenant de chaque partie.

Les principaux facteurs qui influencent le processus de conversion de l'énergie photovoltaïque en électricité sont les suivants:

- Les facteurs liés au climat (températures élevées et peu de vent),

- Les facteurs associés à l'environnement géographique (obstacles, rayonnement solaire, nuages, etc.),
- Les facteurs associés au faible rendement des matériaux semi-conducteurs utilisés dans les panneaux solaires et des équipements de conversion tels que les convertisseurs DC-DC et les onduleurs DC-AC.

Pour chacun de ces facteurs, on associe un rendement pour tenir compte de leur impact plus ou moins défavorables sur la production. Toutefois ces derniers peuvent parfois être également associés à des comportements anormaux qui doivent alors être diagnostiqués pour les séparer et, si possible, arriver à minimiser les effets négatifs des premiers (augmenter les rendements) et trouver des solutions spécifiques aux seconds en terme de maintenance par exemple.

Ces travaux de thèse effectués dans le cadre d'une cotutelle académique a pour objectif de diagnostiquer les défaillances principales des systèmes photovoltaïques, puis à partir de ces informations, développer des stratégies de contrôles actifs tolérants aux défaillances.

- La stratégie de diagnostic des défaillances mise au point repose sur la comparaison en temps réel de comportement du système réel avec un modèle physico-mathématique du même système. S'il existe une différence entre les signaux comparés, cela peut signifier l'existence de comportements indésirables (généralement associés à la survenue de défaillances). Ces défaillances doivent être détectées, isolées et diagnostiquées pour éviter des défaillances plus importantes et des risques plus importants.
- Une fois que le diagnosticien indique qu'il y a un élément en défaut, le système doit prendre une décision pour par exemple corriger ou reconfigurer le système photovoltaïque afin de minimiser l'impact du défaut dans le temps.

## Diagnostic de défaut

Le terme "défaillance" dans les systèmes de contrôle signifie qu'il existe une déviation inadmissible dans le système. Deux stratégies principales peuvent être distinguées pour diagnostiquer les défauts:

1. Une technique basée sur des modèles qui repose sur le développement d'un modèle dynamique précis du système. Cela permet de comparer le modèle au système réel et de trouver les différences. A partir du traitement du type, de la forme et de la quantité de ces dernières un diagnostic peut être effectué. Cette stratégie est capable de détecter les défaillances imprévues, sans la nécessité de systèmes d'apprentissage complexes de détection de pannes.
2. Une technique basée sur les données: qui analyse les tendances, les comportements numériques, etc. pour extraire les caractéristiques anormales du système. Cette stratigraphie ne détecte que les défauts que le concepteur a pu anticiper.

Dans cette thèse, la stratégie de diagnostic basée sur le modèle est privilégiée.

## Modélisation d'un système photovoltaïque en condition de défaut

L'ensemble du système photovoltaïque (cellule, panneau, générateur photovoltaïque, MPPT, convertisseurs) est modélisé à l'aide d'une description de bilan énergétique appelée graphe de liaison (connue dans la communauté scientifique comme BondGraph description).

C'est une stratégie qui permet de modéliser de manière unifiée des systèmes de domaines multiples (électrique, mécanique, thermique, chimique, hydraulique, etc.), avec une dynamique pouvant être décrite par des équations analytiques ou par le biais d'événements discrets. Par exemple, cette stratégie nous permet de modéliser différentes sources de production d'énergie (solaire, éolienne, thermique, électrochimique) utilisées dans les réseaux intelligents.

Les méthodes de diagnostic des systèmes basés sur le modèle peuvent être dites qualitatives ou quantitatives. L'analyse des relations analytiques et des modèles de systèmes d'équations permet de générer des candidats possibles aux diagnostics de pannes.

1. Méthode Qualitative: méthode dérivée de l'analyse analytique ou d'équations fournissant un niveau d'abstraction.
2. Méthode Quantitative: méthode dérivée de l'analyse numérique des fonctions et des équations fournissant un niveau d'analyse numérique.

Les caractéristiques de la modélisation des graphes de liaison permettent de les utiliser pour l'analyse, la détection et le diagnostic de défauts dans les cas suivants par exemple : a) analyse de la causalité, b) analyse des flux, des efforts, de la puissance et de l'énergie.

## Système de reconfiguration

Un contrôle tolérant aux pannes regroupe un ensemble de techniques récentes développées pour augmenter la disponibilité des installations et réduire les risques de danger pour la sécurité. L'objectif de ces méthodes de surveillance et de contrôle est d'empêcher que de simples fautes ne dégénèrent en un défaut majeur définitif. Le contrôle tolérant aux pannes associe pour cela plusieurs disciplines pour atteindre cet objectif, notamment le diagnostic des pannes en temps réel, l'évaluation automatique des conditions et le calcul des actions à prendre en cas de détection d'une panne.

La structure réelle chargée de diagnostiquer les défauts sera partiellement implémentée dans un dispositif FPGA.

## 0.2 Création d'un modèle d'un système photovoltaïque orienté vers le diagnostic de défauts

### Modèle bond-graph de champ PV utilisant la photographie

Dans cette partie, le modèle du champ photovoltaïque devant être décrit avec de grandes granularité et précision pour être apte à être utilisé par les outils de détection de défaut, nous avons choisi d'effectuer l'identification des paramètres par le biais d'un système photographique. Dans la figure 1 sont représentés les différents éléments qui composent un système de conversion d'énergie photographique. Il est ainsi composé d'un générateur photovoltaïque pouvant aller d'une simple cellule jusqu'à un champ complet de panneaux en série/parallèle et d'au moins un convertisseur (dans cet exemple nous avons choisi d'associer un convertisseur continu-continu assurant la fonction MPPT et un convertisseur continu-alternatif pour assurer la connection à une charge AC) ainsi qu'une charge DC ou AC. Comme décrit précédemment, la production d'électricité dépend fortement des variables environnementales, de l'irradiation solaire, de la température et de l'environnement d'installation du système pouvant générer des ombres. Les convertisseurs disposent de systèmes de contrôle leur permettant d'obtenir une bonne conversion de la centrale photovoltaïque jusqu'à la connexion à la charge. Dans l'exemple traité, ce sera le réseau alternatif monophasé 220V/50hz.

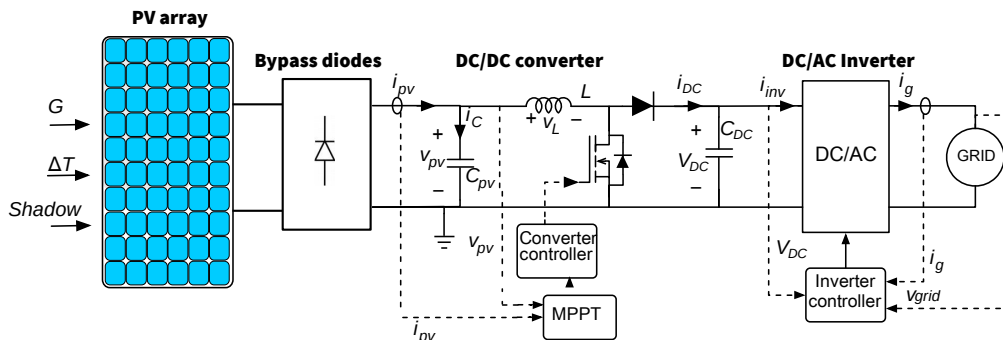


**Figure 1** Exemple de structure d'un système PV connecté réseau [1]

La figure 2 montre le système photovoltaïque complet étudié plus spécifiquement dans ce travail de thèse. Quatre blocs peuvent être identifiés à partir du système. Le premier bloc concerne la fonction conversion photovoltaïque. Le deuxième bloc concerne la fonction de commande MPPT. Le troisième bloc se concentre sur le premier convertisseur continu-continu associé au bloc précédent. Le quatrième bloc concerne la fonction onduleur connecté au réseau (convertisseur plus commande).

### Modélisation de panneaux photovoltaïques

La construction du modèle d'un panneau photovoltaïque dans cette thèse repose sur la modélisation détaillée à l'échelle d'une cellule photovoltaïque dans la

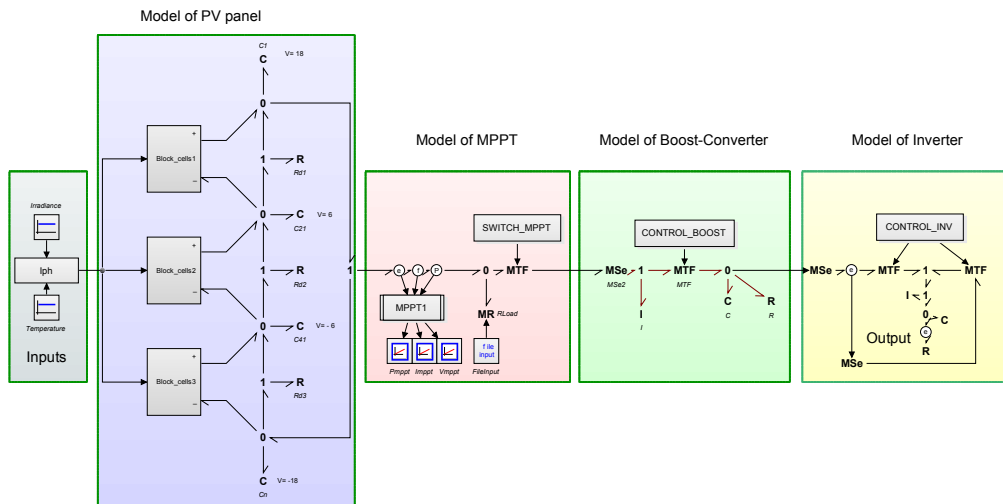


Figure 2 Modélisation d'un système photovoltaïque utilisant les bondgraphs

continuité des travaux de l'équipe encadrante [2]. L'équation 1 décrit le comportement de chaque cellule photovoltaïque sous un comportement normal ou un comportement anormal (cas d'ombrage avec ou sans diode by-pass).

$$I = I_{phT_i} - I_o \left[ e^{\frac{V_c + I \cdot R_s}{V_t}} - 1 \right] - \frac{V_c + I \cdot R_s}{R_{sh}} \left[ 1 + k \left( 1 - \frac{V_c + I \cdot R_s}{V_{br}} \right)^{-n} \right] \quad (1)$$

où  $I_{ph_{STC}}$  représente le photo-courant lorsque la cellule fonctionne en court-circuit en condition de test standard (STC),  $G(t)$  est l'irradiance globale que reçoit le générateur photovoltaïque,  $G_{STC}$  est l'irradiance en STC ( $1000W/m^2$ ),  $\alpha_I$  est le coefficient d'atténuation du courant dû à la température donnée par le fabricant du module PV (%/°C),  $T_c$  température de la cellule PV (°C),  $T_{c,STC}$  est la température en STC (25°C). La figure 3 montre le modèle d'une cellule photovoltaïque en représentation normée de type Bond-Graph.

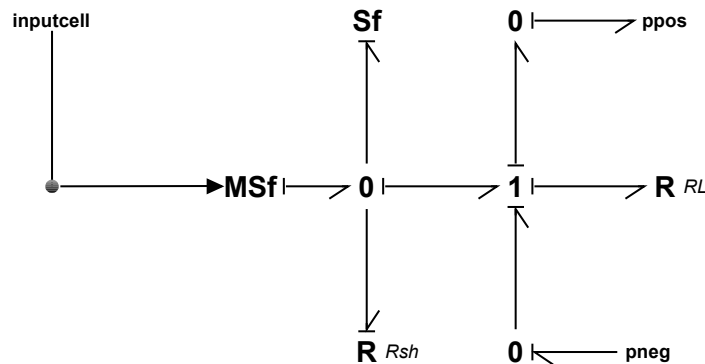


Figure 3 Modélisation d'une cellule photovoltaïque en Bond-Graph

La source  $M_{Sf}$  représente le photocourant,  $I_{ph}$  est le photocourant tenant compte du facteur d'atténuation  $\delta$ ,  $R_{sh}$  et  $R_s$  sont des résistances équivalentes parallèle et série.  $S_f$  représente l'état de connection de la jonction PN de la diode avec sa

valeur égale à 0 si la jonction est mise en parallèle et 1 si elle est mise en série. La figure 4 montre le modèle du panneau solaire développé.

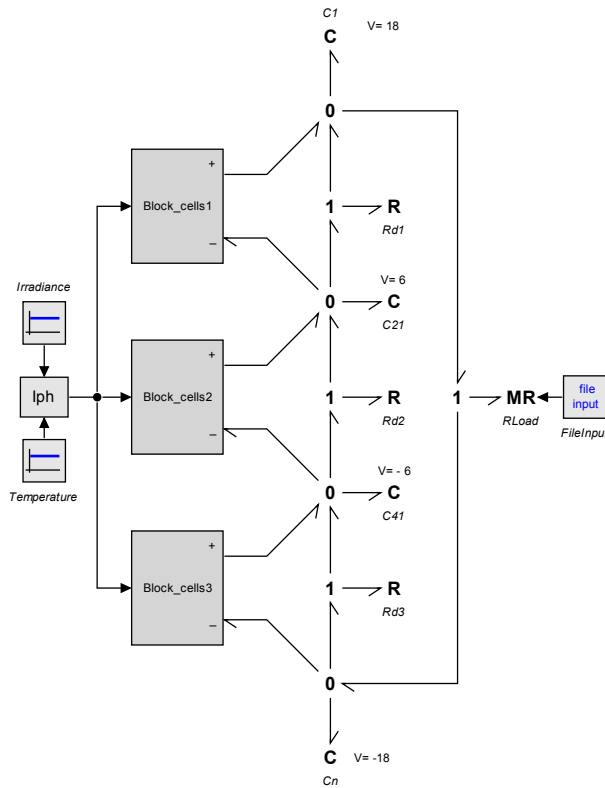


Figure 4 Modèle du panneau solaire représenté en Bond-Graph

$R$  correspond à la diode de dérivation,  $C$  est la capacité parasite,  $MR$  est la résistance variable ( $R_L$ ) qui permet d'obtenir les caractéristiques I(V) modifiant la valeur de la résistance  $R_L$  entre  $[0, \infty)$  comme dans la figure 5. Cette figure est la description du modèle que nous utilisons pour prendre en compte l'activation d'une diode de dérivation dite diode-bypass. Ce modèle a été validé en effectuant un test direct en faisant varier la résistance de la charge.

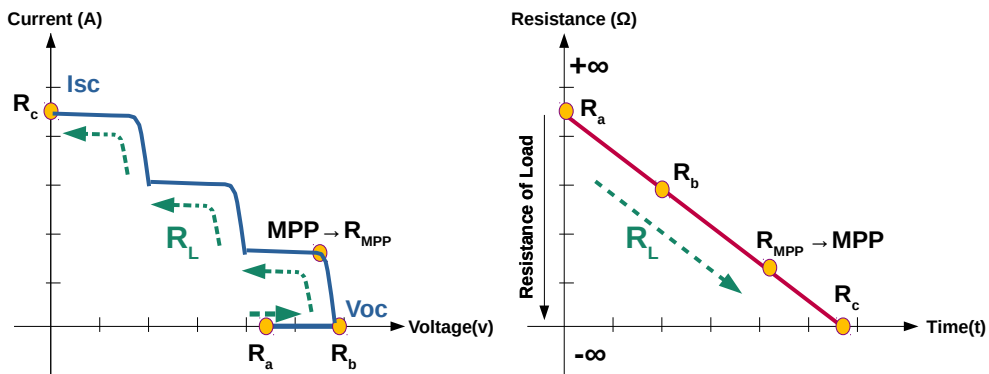


Figure 5 (a) Courbes I(V) avec activation des diodes de dérivation (condition d'ombrage) et (b) variation de la résistance de charge  $RL$

La variation de  $R_L$  est représentée par une flèche verte permettant d'obtenir les points de tension et de courant de la courbe.

### Modèle de module PV avec d'ombre

L'irradiation directe et l'irradiation indirecte sur toutes les cellules d'un panneau sont à chaque instant différentes en raison des ombres dues aux bâtiments ou des arbres, des fluctuations de l'atmosphère, de l'existence de nuages et des changements quotidiens de l'angle du soleil. L'impact de l'irradiation non uniforme dans la production d'énergie dépend de plusieurs aspects tels que le matériau de la cellule, la magnitude de la zone d'ombrage, l'emplacement de la diode de dérivation, la configuration de la chaîne photovoltaïque, etc. Pour cette raison, le module PV peut avoir en son intérieur différentes valeurs de  $I_{ph}$  inhérentes à chaque cellule. L'éclairement énergétique global reçue sur Terre (au niveau du sol) peut se décomposer en trois parties : l'irradiance directe, l'irradiance diffuse et l'irradiance réfléchie (2).

$$G_T = G_D + G_d + G_r \quad (2)$$

où  $G_T$  est l'irradiance globale,  $G_D$  le rayonnement direct,  $G_d$  le rayonnement diffus et  $G_r$  le rayonnement réfléchi comme décrit dans la figure(6).

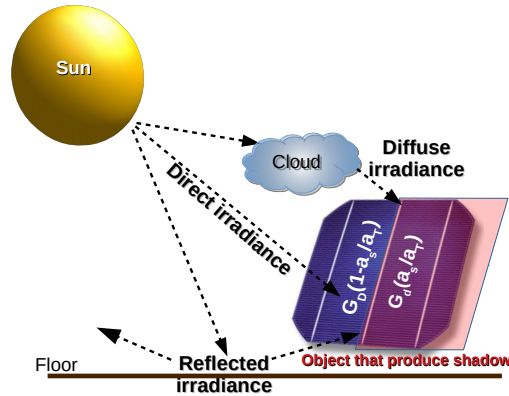


**Figure 6** Production d'un Photo-courant d'une cellule PV recevant plusieurs types d'irradiations et effectuant une combinaison d'irradiations directe et indirecte

Une expression mathématique pour modéliser l'ombrage partiel au niveau de la cellule PV peut être décrite par l'équation (3):

$$I_{ph} = \delta_T \cdot I_{phTi} \quad (3)$$

Où  $\delta_T$  est un facteur d'atténuation (par exemple un facteur sans ombre) ( $0 \leq \delta_T \leq 1$ ),  $I_{phTi}$  est le courant nominal en entrée de chaque cellule et  $I_{ph}$  est le courant d'entrée effectif. Les cellules PV peuvent avoir une valeur différente de  $\delta_T$ .

**Traitement d'image: Ombres:** Une méthodologie pour la détection des ombres et l'estimation de la surface des ombres a été proposée dans cette thèse. La configuration expérimentale du traitement des images a été réalisée dans le cadre de la plateforme ADREAM. Deux modules PV (TE2200) ont été utilisés, l'un servant de référence en mode de fonctionnement normal et l'autre permettant d'effectuer des tests d'ombrage, comme illustré à la figure 7.

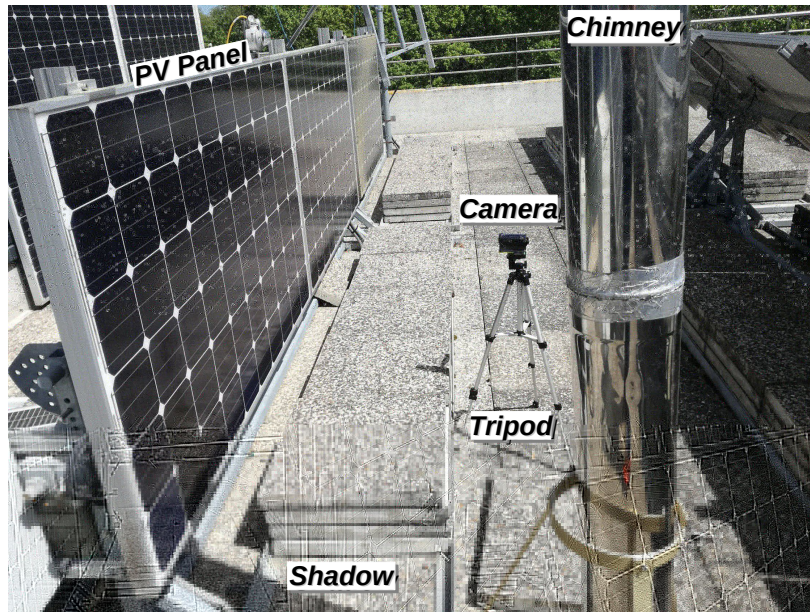


**Figure 7** Processus d'expérimentation pour obtenir la zone d'ombre sur le module PV

Plusieurs expériences sont proposées pour effectuer l'ensemble des validations expérimentales des paramètres du modèle selon la méthodologie proposée. Par exemple, sur la figure 8, le déplacement de l'ombre sur toute une journée est illustré. Ceci a fait l'objet d'une séquence de photos avec des ombres sur toute une journée. Dans le manuscrit plusieurs expériences sont consignées avec les courbes de production de courant en fonction de la tension  $I(V)$  en fonctionnement normal puis la comparaison des courbes  $I(V)$  entre le test expérimental sous ombrage complexe et le modèle  $I(V)$ .

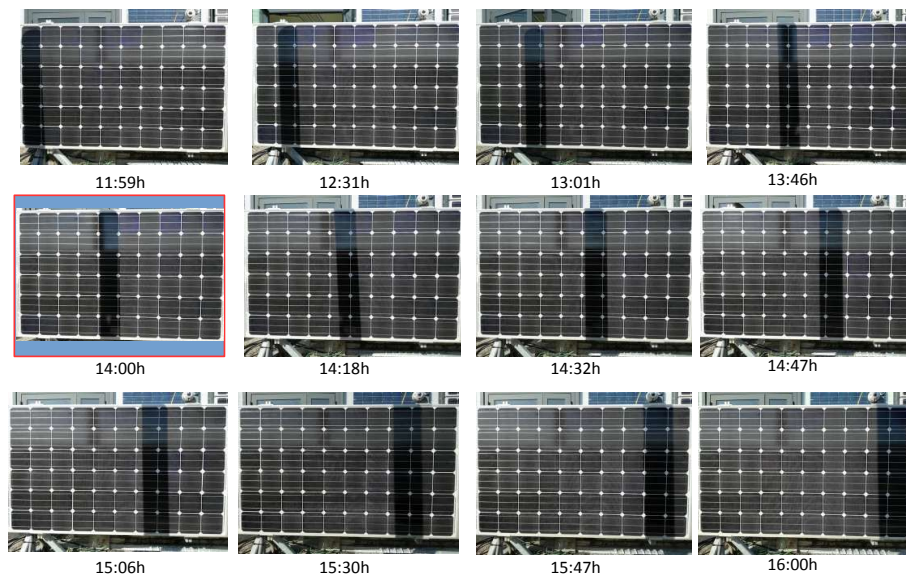


**Figure 8** Module PV affecté par une ombre mobile au cours de la journée du 27 février 2018

**Développement d'un algorithme GMPPT basé sur un modèle:** Dans cette section, la comparaison de l'algorithme GMPPT avec les mesures réalisées par le traceur de courbes I(V) est présentée (Figure 9). Cette comparaison a permis de construire une méthode de détection d'erreur y compris sur les algorithmes de type MPPT appliqués aux systèmes ombrés (nommés GMPPT).

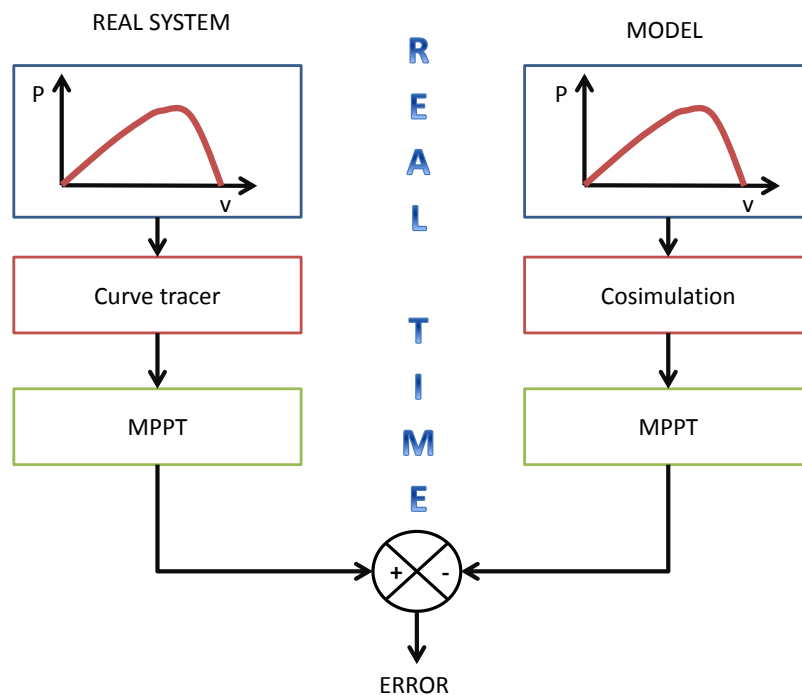


**Figure 9** Comparaison du modèle de GMPPT avec les mesures

### Modélisation d'un convertisseur boost DC-DC

Dans cette section, un convertisseur élévateur de tension est modélisé puis décrit à l'aide de Bondgraphs.  $S_e$  représente la source de tension,  $L$  l'inductance,  $R_L$  la résistance du charbon,  $C_i$  la capacité d'entrée,  $MR$  la cellule de commutation du transistor avec la diode,  $C$  la capacité de sortie,  $R_c$  est le condensateur résistance,  $R$  la résistance à la charge.  $D_e$  est un capteur de tension et  $D_f$  un capteur de courant.

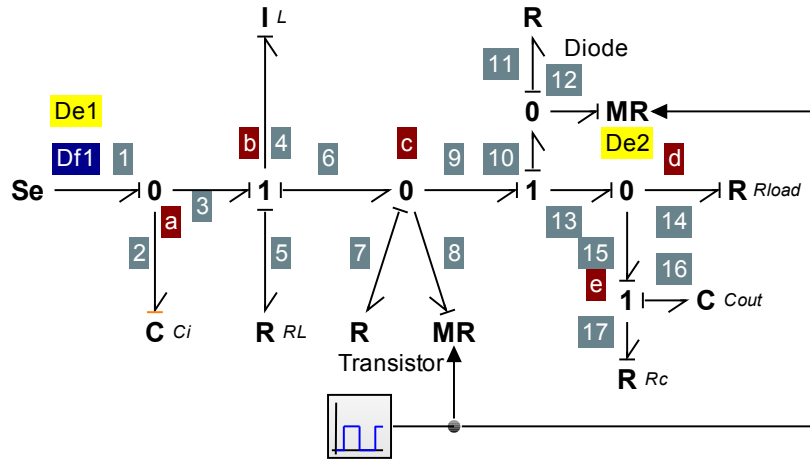


Figure 10 Modélisation d'un convertisseur boost DC-DCr

### Modélisation d'un onduleur

Dans cette section, un onduleur monophasé (pont en H) associé avec une commande permettant une connection au réseau électrique comme présenté en Figure (11). L'onduleur est en mode suiveur connecté à un réseau alternatif avec lequel il fonctionne en se synchronisant en amplitude de tension et fréquence.

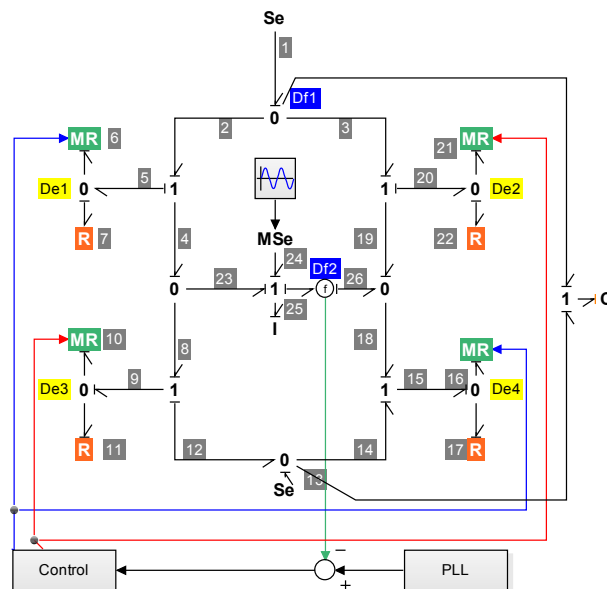
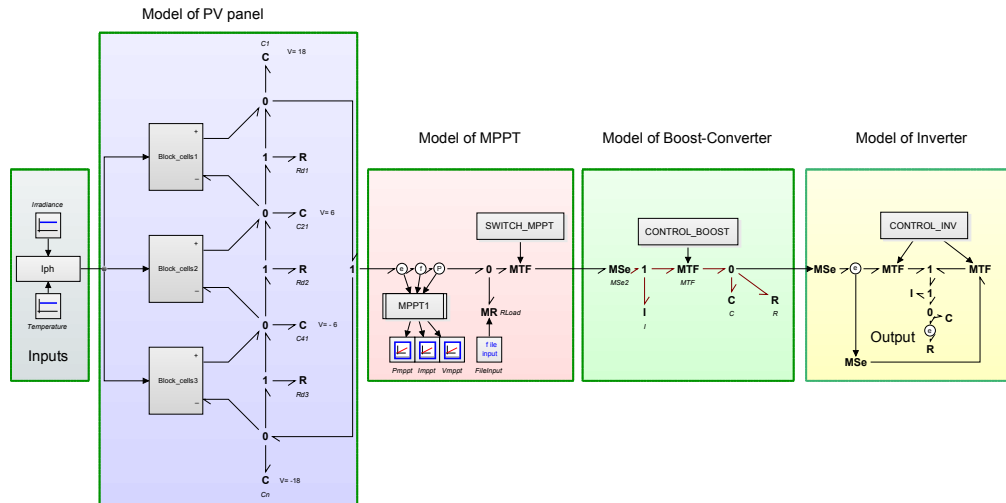


Figure 11 Modèle onduleur DC-AC avec BG

### Synthèse de tous les modèles pour former un système PV

L'ensemble du modèle du système PV présenté en figure 12 a été conçu de telle sorte que dans chacune des fonctions, les défaillances puissent être détectées.



**Figure 12** Modélisation BG de systèmes photovoltaïques

Des exemples de résultats obtenus une fois tous les blocs couplés sont présentés ci-dessous en Figure(13). Ce type de résultat peut être considéré comme une validation suffisante nous permettant l'utilisation de ce modèle pour effectuer des FDD.

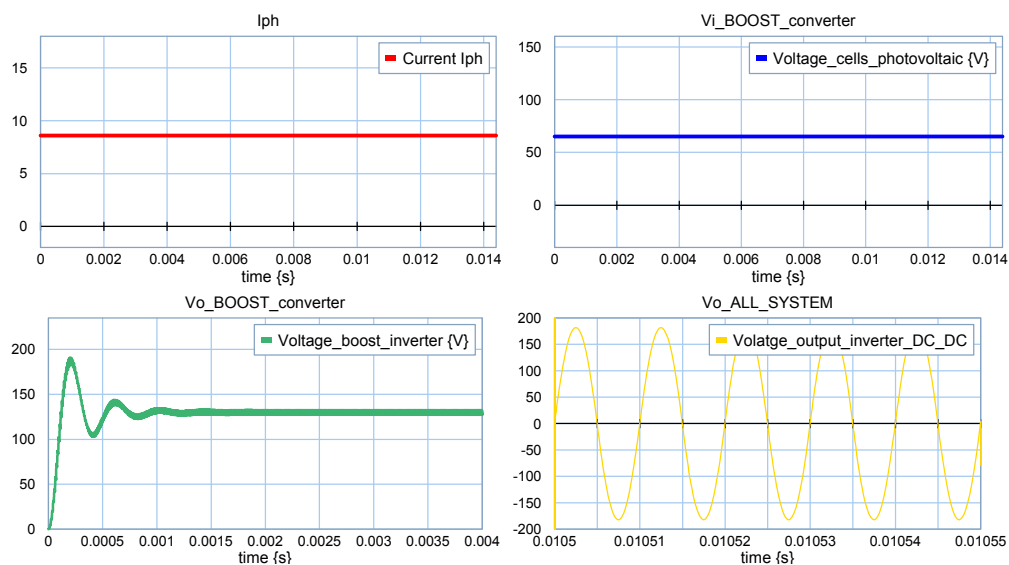


**Figure 13** a) Conversion de l'irradiation solaire en courant électrique b) Tension d'entrée du convertisseur élévateur c) Tension de sortie du convertisseur élévateur d) Tension de sortie convertisseur DC-AC

### 0.3 Diagnostic de défauts et contrôle actif de tolérance de pannes appliqué au PV

La détection et le diagnostic des pannes consistent à identifier la cause possible des pannes à l'aide d'un ensemble de fonctions associé à une chronologie spécifique basée sur l'analyse d'informations telles que le modèle de référence et/ou l'analyse de données et de signaux. La figure (14) montre le processus qu'il est nécessaire de suivre pour diagnostiquer les défauts.

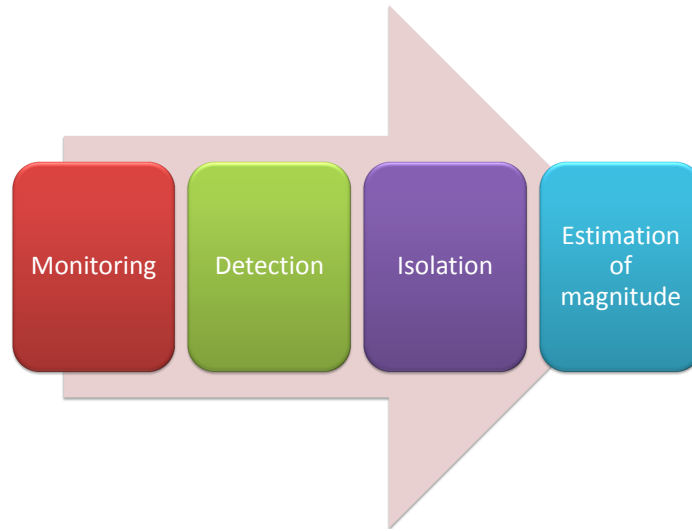


Figure 14 Processus de diagnostic de défaut (surveillance, détection, isolement, estimation de l'importance du défaut)

Dans cette partie, la stratégie de détection basée sur un modèle est montrée est décrite par la figure 15.

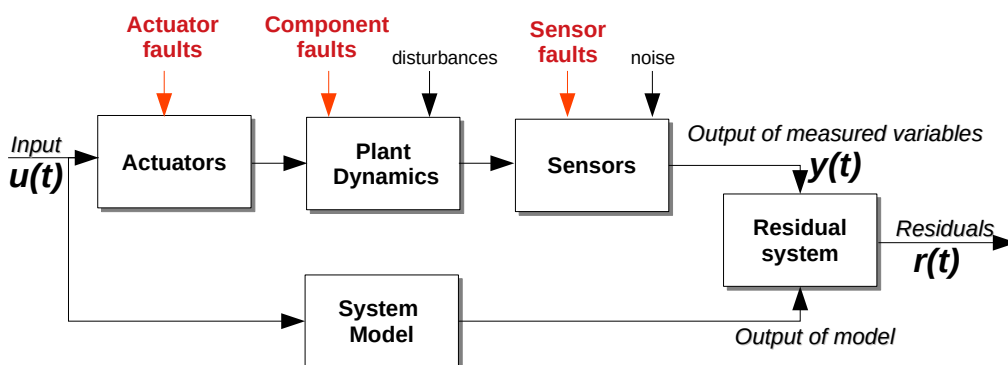
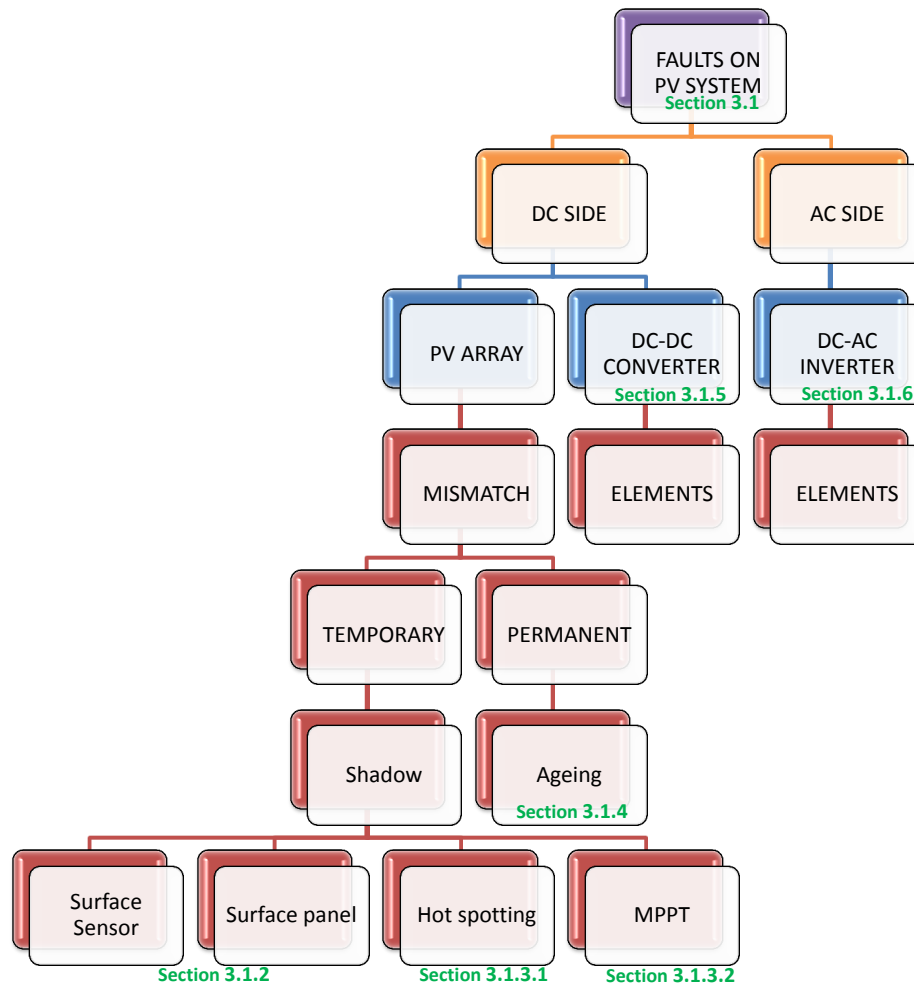


Figure 15 Diagnostic de défaut basé sur le modèle

## Classification des défauts du système PV

La figure (16) présente une proposition d'organisation des principaux défauts susceptibles de se produire dans un système PV. Seule une partie des défauts est prise en compte dans cette thèse. Les sections traitées dans ces travaux et décrites dans ce manuscrit sont notées en vert. Les défauts sont classés en fonction de leur emplacement dans le système PV. Ensuite, les défauts peuvent être localisés du côté DC [3,4] ou du côté AC [5].



**Figure 16** Schéma des défauts pour le diagnostic sur système PV

### Système de surveillance de système PV

Le système de surveillance mis en œuvre pour le système photovoltaïque est représenté sur la figure 17.

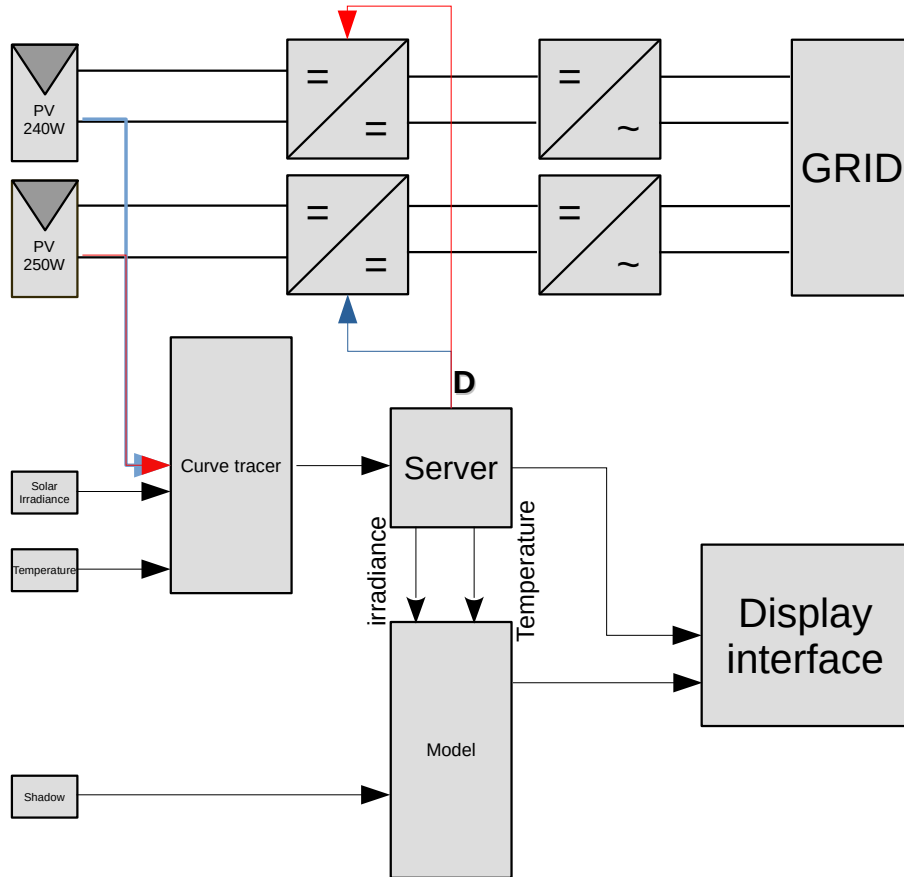


**Figure 17** Structure générale de l'interface de test et d'acquisition de données

### Détection de défaut basée sur le modèle

La granularité élevée (précision) du modèle proposé au chapitre 2 de cette thèse permet de mettre en évidence de nombreux phénomènes physiques. Avoir un modèle bien adapté est la première condition pour obtenir une FDD efficace. Concernant les cellules PV, les modules, les chaînes ou les matrices PV, tout réside dans la précision du modèle élémentaire de la cellule. Dans notre cas, les courbes  $I(V)$  et  $P(V)$  données par notre modèle de cellule contiennent suffisamment d'informations pour prendre en compte la plupart des problèmes électriques susceptibles de se produire sur les faces interne ou externe des modules PV composés d'un grand nombre de cellules. Ce qui nous a le plus préoccupé a été la description correcte des impacts d'ombrages inhomogènes notamment dans la modification des formes des courbes  $I(V)$  et  $P(V)$ . Le modèle PV mis au point dans ces travaux est aujourd'hui capable de décrire les réponses électriques du système pouvant se produire pendant toute la journée dans des conditions classiques de points de fonctionnement et dans différents cas d'ombres. Malgré sa complexité, la comparaison entre les simulations et les résultats expérimentaux

des modules PV permet aujourd'hui d'évaluer facilement l'état du système en temps réel.

La figure (18) montre un exemple de courbes I(V) et P(V) en fonctionnement normal et en condition de défaut, en particulier dans des conditions d'ombrage.

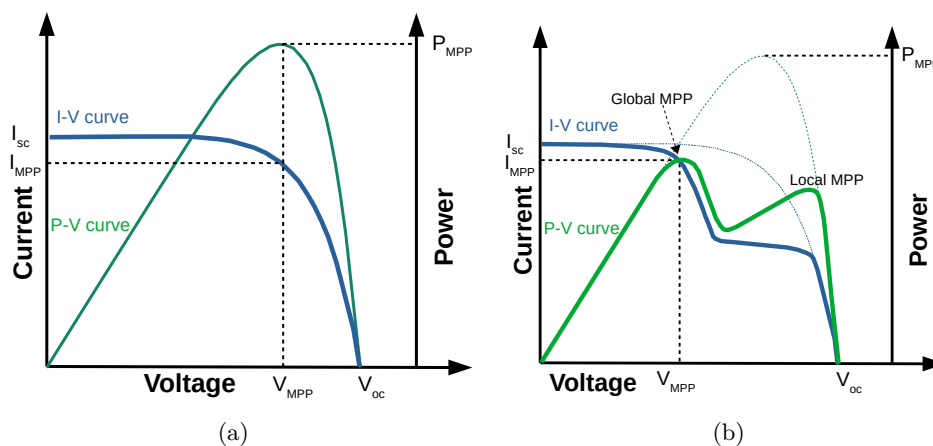


**Figure 18** (a) Courbes I-V et P-V sans ombre (b) Courbes I-V et P-V avec ombre

La figure 19 présente l'un des schémas décrivant le fonctionnement du diagnostic des défauts basé sur des modèles BG.

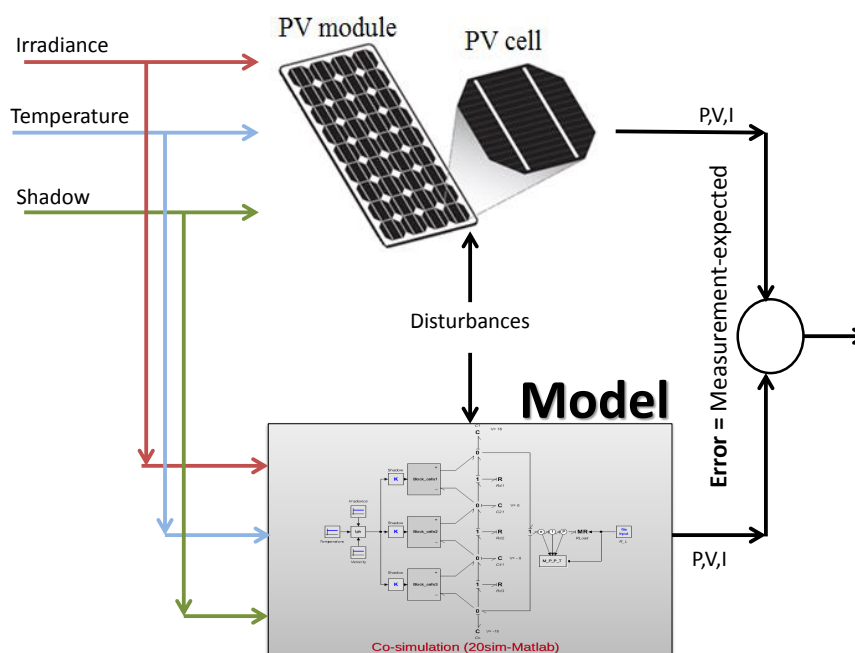


**Figure 19** Stratégie de diagnostic de panne basée sur le modèle

### Détection de défauts dans le module photovoltaïque: ombrage

Les données extraites du système de surveillance et qui sont ensuite comparées aux modèles proposés au chapitre 2 de cette thèse, sont par exemple comme ceux

indiqués en figure (20). Cette comparaison permet de détecter un comportement anormal du système surveillé.

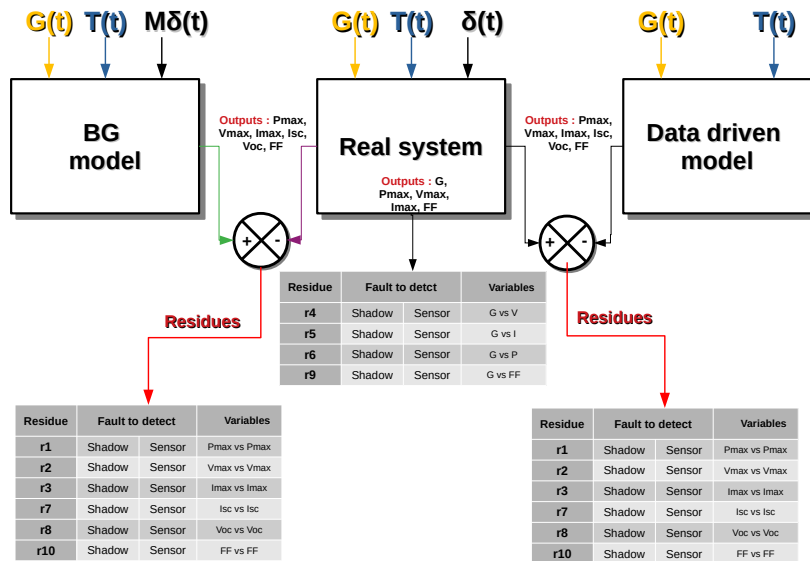


**Figure 20** Détection générale des fautes basée sur un modèle, données réelles du système et data-driven

### Diagnostic de défauts temporaires sur le générateur photovoltaïque: cas de points chauds, de MPPT et de vieillissement

La figure 21 décrit la structure de la FDD concernant les points chauds, le MPPT et le vieillissement. Cette stratégie est détaillée et discutée pour chaque défaut dans le manuscrit.

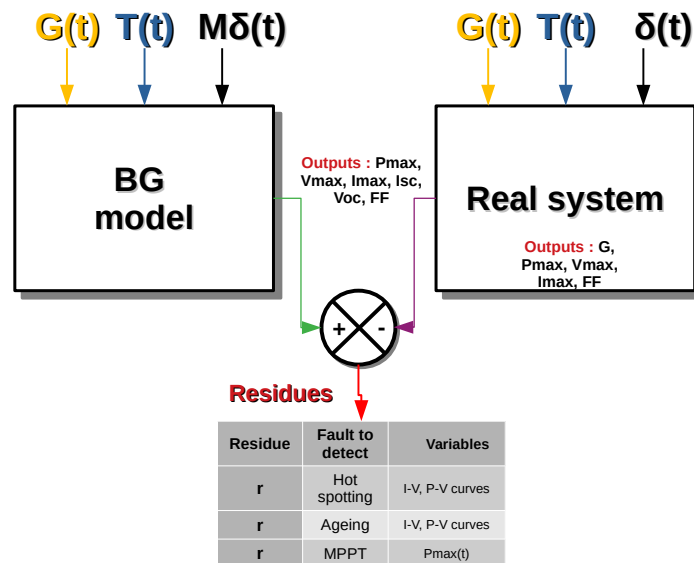


**Figure 21** Structure du diagnostic pour PV

### Diagnostic des défauts sur le convertisseur élévateur DC-DC et l'onduleur

Cette partie consiste à effectuer le diagnostic de panne des équipements de puissance. La stratégie de diagnostic réside dans la comparaison entre le modèle et le système est dans la génération de relations de redondance analytique comme décrit en Figure(22).

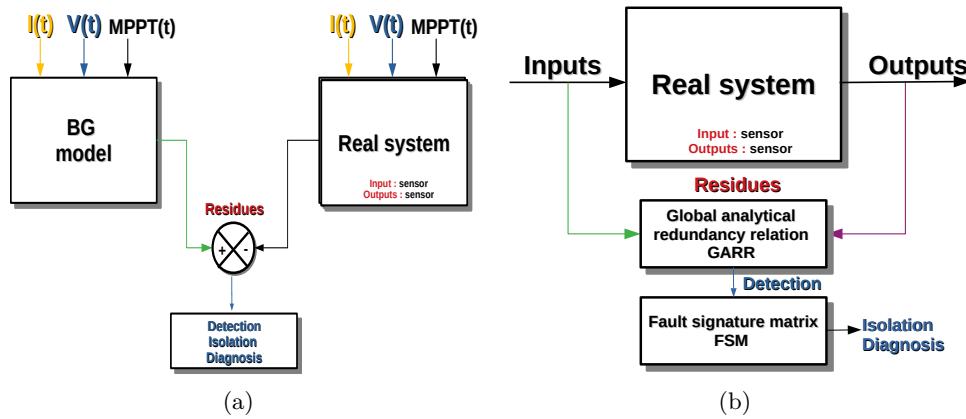


**Figure 22** Structure de diagnostic pour le convertisseur élévateur (a) et le système de comparaison versus système utilisant la redondance des relations analytiques (b)

#### 0.3.1 Contrôle tolérant aux pannes appliqué aux systèmes photovoltaïques

Dans cette section, la stratégie de contrôle à tolérance de pannes est présentée et développée à l'aide du contrôle en mode de glissement appliqué au convertisseur DC-DC et à l'onduleur.

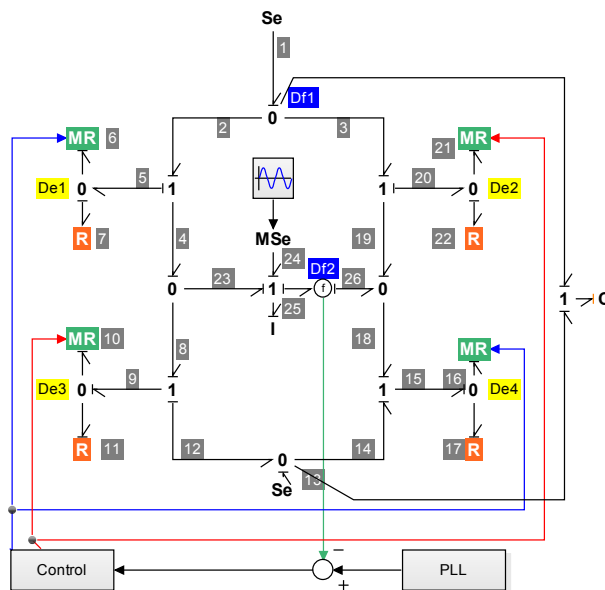


**Figure 23** Modèle HBG d'onduleur CC-CA avec stratégie de contrôle

### 0.3. Diagnostic de défauts et contrôle actif de tolérance de pannes appliqué au PV

La figure 24 présente le modèle complet du système photovoltaïque avec la stratégie de contrôle à tolérance de pannes proposée.

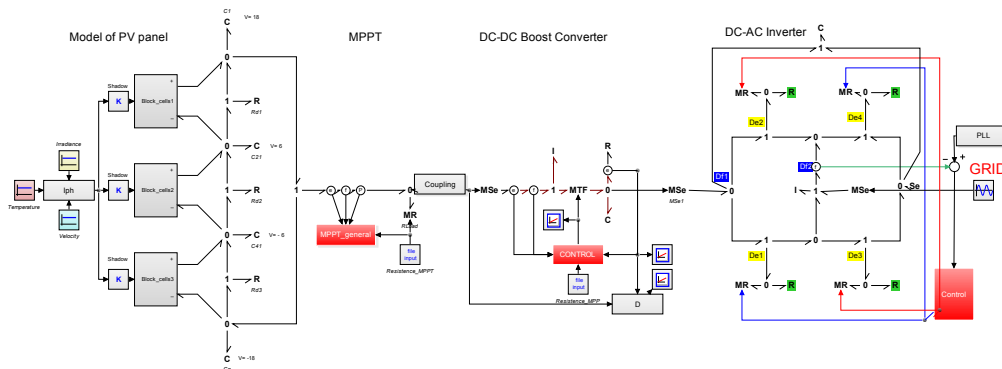


**Figure 24** Modèle photovoltaïque en bongraph avec commande à tolérance de pannes

Le résultat principal de ce chapitre est présenté ci-dessous. La figure (25) présente les signaux de sortie en tension et en courant du système connecté au réseau électrique 220V et 50Hz.

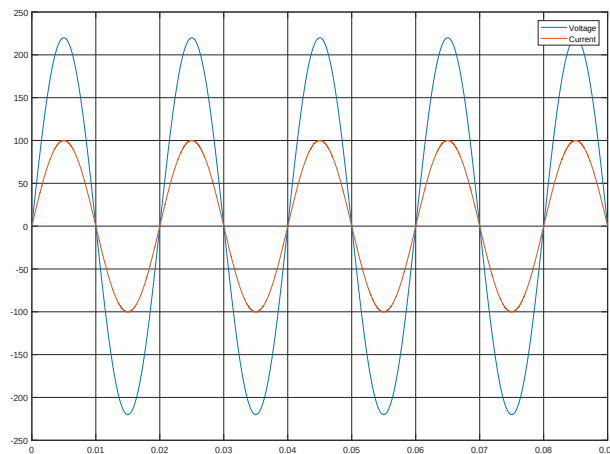


**Figure 25** Représentation de la tension d'entrée, de la tension de sortie, et du courant de sortie

## 0.4 Diagnostic intégré dans un FPGA

Ce chapitre présente l'utilisation du FPGA pour les tâches de dépannage dans les systèmes photovoltaïques.

### 0.4.1 Prévention de hot-spotting

La première partie de ce travail présente une émulation en temps réel des systèmes PV ombragés avec une prévention de hot-spot.

L'émulation de systèmes PV ombrés et la prévention à chaud nécessitent des dispositifs d'implémentation de traitement du signal aptes à effectuer des calculs en grande quantité en temps réel tels que les FPGA. Le modèle proposé et l'algorithme de point chaud ont été implémentés à l'aide du langage de description très haute vitesse (VHDL) et mis en œuvre sur un Xilinx ZedBoard. En utilisant différentes parties de la structure du FPGA, les blocs fonctionnels du FPGA, tels que la mémoire et les ressources logiques, fonctionnant en parallèle à très haute fréquence, offrent une vitesse d'exécution élevée. En premier lieu, réduire la vitesse d'exécution permet de consommer moins de ressources matérielles FPGA. De plus, le nombre de bits utilisés peut affecter l'ensemble du système en termes de réduction de la précision et d'erreurs de calcul. La figure 26 montre la carte FPGA avec l'entrée principale des mesures pour effectuer la prévention de hot-spot.

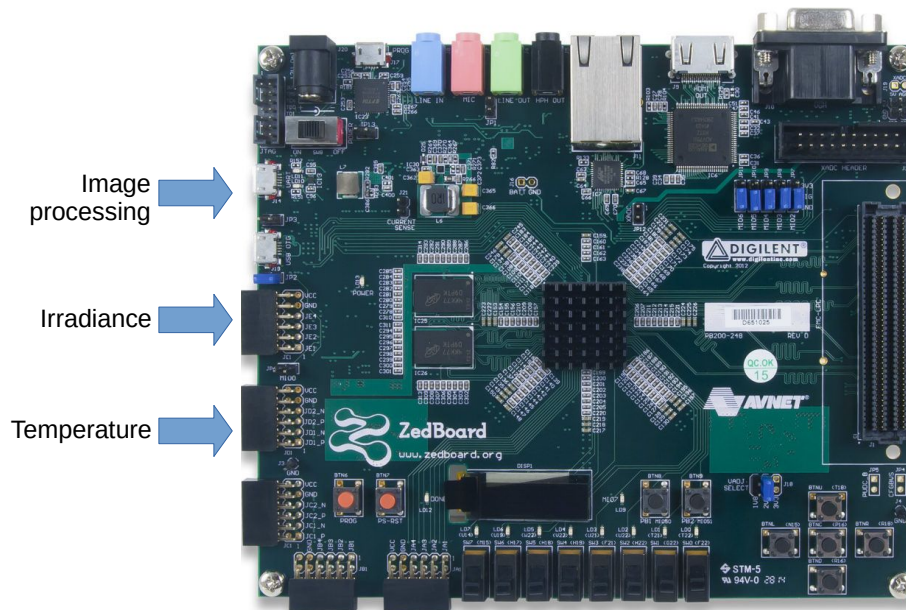
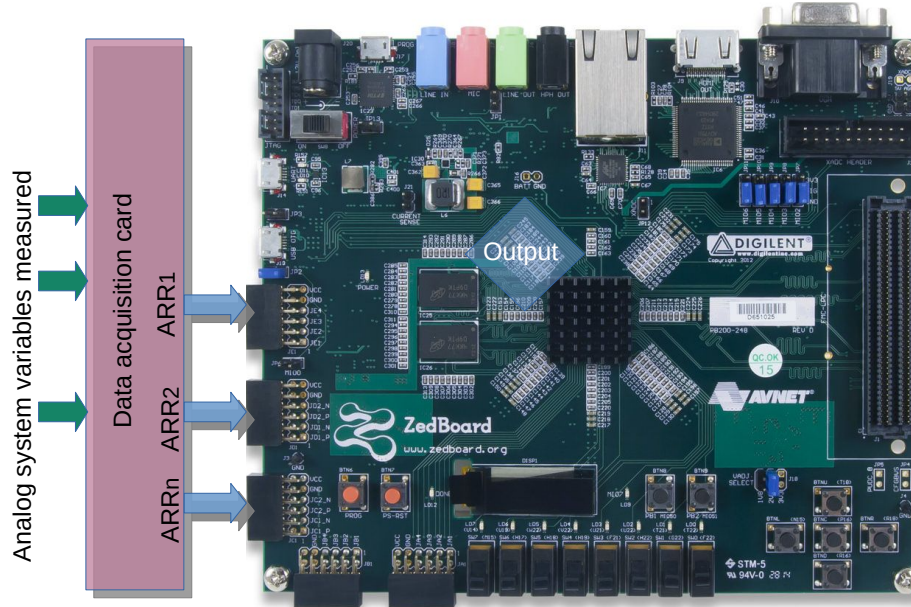


Figure 26 Carte FPGA avec entrées de mesure

### 0.4.2 Mise en œuvre de la matrice de fautes d'un diagnosticien

La deuxième partie de ce chapitre présente la mise en œuvre d'une partie d'un diagnostic de défaut dans un onduleur CC-CA.



**Figure 27** Diagnostic d'un onduleur DC-AC intégré sur FPGA

A ce jour, seulement une partie du système FDD est implémentée dans un FPGA, elle consiste en particulier à mettre en œuvre une matrice de signature de panne d'un onduleur CC-CA. Cette partie présente le processus mis en œuvre dans un FPGA. .

## **Conclusion et perspectives**

Cette thèse apporte des contributions pour prolonger les durées de vie de systèmes comme ceux du domaine des nouvelles sources d'énergie renouvelables intermittentes en terme de connaissances approfondies de leur comportement et leur modélisation associée et dans celui des systèmes de contrôle à tolérance de pannes reposant sur ce type de modèles à description fine des phénomènes physiques.

## Dedications

I dedicate this dissertation to my family: to my wife Monica, my mother Georgina, my father Luis, my brother Javier, my sister Diana Carolina, my sister-in-law Yorlady, my dear nephews Omar Andres, Jorge, Isabella, and Luisa. Without their help I would never have completed this dream; they helped me keep going despite all the obstacles.

I also dedicate this dissertation to:

- the memory of my grandmothers Clementina, Rosita, and Hortencia, my uncles Jorge and Rozo, and my friend Elkin Muskus
- my advisors: Corinne Alonso and Michael Bressan
- my friends: Diego Y, Elvis E, Diego U, P. Alonso, Irlene, and Pili

# Acknowledgements

I would like to acknowledge:

- The Laboratory for Analysis and Architecture of Systems-LAAS-CNRS, University of Toulouse III-Paul Sabatier, and the Universidad de los Andes
- COLCIENCIAS, the Department of Electrical and Electronic Engineering at the Universidad de los Andes, Andres Gomez, Tatiana Galvis, Fernando Jimenez, Angela Cadena, and Alain Gauthier.
- Salvador de-las Heras for his friendship and his enormous help
- all my colleagues and friends at the Universidad de los Andes especially Freddy, Rafael, and Alejandra.
- Jean Pierre, and all the Bressan Family for their fraternal support during my stay in France.
- all my colleagues and friends at the LAAS: Bruno, Margot, Jérémy, Ilias, and Kjolia for everything we shared, and our excellent talks .
- the members of my PhD thesis panel

...and finally, thanks to all those who were part of my life and accompanied me in my work in obtaining a PhD.

to Dantito...



# Contents

<b>Abstract</b>	<b>i</b>
<b>Résumé</b>	<b>iii</b>
0.1 Introduction . . . . .	iii
0.2 Création d'un modèle d'un système photovoltaïque orienté vers le diagnostic de défauts . . . . .	vi
0.3 Diagnostic de défauts et contrôle actif de tolérance de pannes appliqué au PV . . . . .	xiv
0.3.1 Contrôle tolérant aux pannes appliqué aux systèmes photovoltaïques . . . . .	xix
0.4 Diagnostic intégré dans un FPGA . . . . .	xxi
0.4.1 Prévention de hot-spotting . . . . .	xxi
0.4.2 Mise en œuvre de la matrice de fautes d'un diagnosticien . . . . .	xxii
<b>Dedications and acknowledgments</b>	<b>xxiv</b>
<b>Contents</b>	<b>xxvii</b>
<b>List of Figures</b>	<b>xxxii</b>
<b>List of Tables</b>	<b>xxxvii</b>
<b>1 Introduction</b>	<b>1</b>
1.1 Global energy in context . . . . .	3
1.2 Photovoltaic systems and their reliability . . . . .	5
1.2.1 The interest in photovoltaics and the objective of this thesis . . . . .	5
1.2.2 Structure of a photovoltaic system . . . . .	6
1.2.2.1 Solar cells . . . . .	7
1.2.2.2 Structure cell, module, string, and array . . . . .	9
1.2.2.3 Solar tracker . . . . .	9
1.2.2.4 Maximum Power Point Tracking (MPPT) . . . . .	10
1.2.2.5 DC-DC converters . . . . .	11
1.2.2.6 DC-AC inverter . . . . .	12
1.2.2.7 Energy Storage systems . . . . .	12
1.2.2.8 AC - DC BUSs . . . . .	14
1.2.3 Architectures of PV systems . . . . .	15
1.2.3.1 Central inverters . . . . .	15
1.2.3.2 String inverters . . . . .	15
1.2.3.3 Multi-string inverters . . . . .	16
1.2.3.4 Micro-inverters . . . . .	16
1.2.4 Losses, defects, and possible faults in PV systems . . . . .	19

1.2.4.1	PV cells . . . . .	19
1.2.4.2	Diode bypass . . . . .	22
1.2.4.3	DC-DC converters with MPPT and DC-AC in- verters . . . . .	24
1.3	Fault detection and diagnosis in PV systems . . . . .	24
1.3.1	Model-based fault diagnosis . . . . .	25
1.3.1.1	Detection and diagnosis of faults based on a quan- titative analysis of PV arrays . . . . .	25
1.3.1.2	Detection and diagnosis of faults based on a quan- titative analysis of power converters . . . . .	26
1.3.2	Data-driven fault diagnosis . . . . .	26
1.3.3	Fault-tolerant control of PV systems . . . . .	27
1.4	Detecting and diagnosing faults . . . . .	28
1.5	Conclusion . . . . .	30
<b>Bibliography</b>		<b>31</b>
<b>2 PV system modeling for fault diagnosis</b>		<b>37</b>
2.1	Modeling PV array . . . . .	40
2.1.1	Modeling the PV cell . . . . .	40
2.1.2	Modeling the PV module . . . . .	44
2.1.2.1	Model based on the electrical characteristics of a PV module . . . . .	45
2.1.2.2	Model based on the cell's series/parallel intercon- nection . . . . .	48
2.2	The proposed PV module using HBG . . . . .	50
2.2.1	Model of PV module using shadow parameters . . . . .	51
2.2.2	Image processing: shadows . . . . .	54
2.2.3	Validation of the PV Model and processing images . . . . .	57
2.2.3.1	Case 1: Validation of the HBG model when op- erating normally . . . . .	57
2.2.3.2	Case 2: Validation under a uniform shadow . . . . .	58
2.2.3.3	Case 3: Validation under complex shading con- ditions . . . . .	59
2.2.4	Non-uniform shading conditions during the day . . . . .	61
2.2.4.1	Case 1 . . . . .	61
2.2.4.2	Case 2 . . . . .	63
2.3	Global Maximum Power Point Tracking under shading conditions	64
2.3.1	A GMPPT algorithm based on the model . . . . .	65
2.3.2	How the GMPPT algorithm evolves in shadow conditions during one production day . . . . .	66
2.3.2.1	Case 1: Uniform shadow on the PV module . . . . .	67
2.4	DC-DC Converter . . . . .	68
2.4.1	DC-DC converter sizing . . . . .	68
2.4.2	Modeling the boost-converter using HBG . . . . .	69
2.5	DC-AC Inverter . . . . .	71
2.5.1	Modeling the isolated inverter using HBG . . . . .	71
2.5.2	Modeling a single-phase inverter connected to the grid . . . . .	72
2.5.3	Modeling a bidirectional boost-inverter . . . . .	74
2.5.3.1	Connected to the grid . . . . .	75

2.5.4	Modeling the entire network . . . . .	77
2.6	Conclusion . . . . .	78
<b>Bibliography</b>		<b>79</b>
<b>3</b>	<b>Diagnosis and FTC on PV systems</b>	<b>83</b>
3.1	Fault detection strategies for PV systems . . . . .	85
3.1.1	Fault Diagnosis system purposed . . . . .	86
3.1.2	Diagnosis of temporary faults on the PV array: shading on a PV module and sensor-measurement error . . . . .	89
3.1.2.1	Analysis of real system data based on residue . . . . .	89
3.1.2.2	Shading on sensors: error in parameter measure- ments . . . . .	92
3.1.2.3	Shadow on PV module: comparison between the real system and the model . . . . .	93
3.1.2.4	Error of Detection of shadow on PV panel linked to sensor generating error of measurement . . . . .	99
3.1.3	The diagnosis of temporary faults on a PV array: hot spot- ting, MPPT, and aging . . . . .	103
3.1.3.1	Diagnose of temporary faults on the PV: hot spot- ting . . . . .	103
3.1.3.2	Diagnosis of temporary faults on the MPPT . . . . .	106
3.1.4	Diagnosis of permanent faults on PV: aging . . . . .	108
3.1.4.1	Synthesis of the phenomena that our FDD can detect . . . . .	109
3.1.5	Fault diagnosis on the DC-DC boost converter . . . . .	110
3.1.6	Fault Diagnosis on DC-AC inverters . . . . .	114
3.1.6.1	Fault diagnosis on DC-AC that can be connected to the grid . . . . .	114
3.1.7	General diagnosis of the PV system . . . . .	116
3.2	Fault Tolerant Control on the PV system . . . . .	117
3.2.1	FTC: Redesigning strategies . . . . .	119
3.2.1.1	Strategy based on: Boosting the converter and H-bridge inverter . . . . .	119
3.2.1.2	Strategy based on: Boost DC-AC inverter . . . . .	124
3.2.2	FTC: Reconfiguration of the photovoltaic system (proposal)	126
3.2.2.1	Reconfiguration architecture of the PV generator side . . . . .	126
3.2.2.2	Reconfiguration architecture of the converters . . . . .	127
3.3	Conclusion . . . . .	128
<b>Bibliography</b>		<b>129</b>
<b>4</b>	<b>Diagnosis embedded in an FPGA</b>	<b>133</b>
4.1	Diagnosis of hot-spot apparition that is implemented using FPGA	133
4.1.1	Calculation of the derivative error for a PV module . . . . .	134
4.1.2	Hot-spot prevention algorithm, implementation, and re- sults of the emulator . . . . .	135
4.2	Diagnosis of PV converters implemented in FPGA . . . . .	139
4.2.1	Embedded diagnostics of a H-Bridge DC/AC converter . . . . .	139

---

4.3 Conclusion . . . . .	142
<b>Bibliography</b>	<b>143</b>
<b>Conclusions, Perspectives and Future Works</b>	<b>144</b>
<b>A Appendix A</b>	<b>149</b>
A.1 Introduction to Bond Graph Modelling . . . . .	149
A.2 Photovoltaic cell code . . . . .	151
<b>B Appendix B</b>	<b>153</b>
B.1 Co-simulation of the photovoltaic system: 20sim-Matlab . . . . .	153
<b>C Appendix C</b>	<b>157</b>
C.1 ADREAM: Input and Output Variables . . . . .	157
<b>D Appendix D</b>	<b>161</b>
D.1 Introduction to fault diagnosis . . . . .	161
D.2 Detection, isolation, and diagnosis of faults using FDD methods . . . . .	162
D.2.1 Hardware redundancy approach and analytical redundancy approach . . . . .	162
D.3 Residues . . . . .	163
D.3.1 Fault detection . . . . .	164
D.3.1.1 Threshold of the residuals . . . . .	164
D.4 Fault isolation and fault signature . . . . .	165
<b>E Appendix E</b>	<b>167</b>
E.1 Monitoring interface of the PV system . . . . .	167
E.1.1 Monitoring PV system . . . . .	167
E.1.2 Display interface 1: diagnosis based data driven . . . . .	168
E.1.3 Display interface 2: diagnosis based on the model . . . . .	169
<b>Bibliography</b>	<b>170</b>

## List of Figures

1	Exemple de structure d'un système PV connectée réseau [1] . . .	vi
2	Modélisation d'un système photovoltaïque utilisant les bondgraphs	vii
3	Modélisation d'une cellule photovoltaïque en Bond-Graph . . . .	vii
4	Modèle du panneau solaire représenté en Bond-Graph . . . . .	viii
5	(a) Courbes I(V) avec activation des diodes de dérivation (condition d'ombrage) et (b) variation de la résistance de charge $RL$ . .	viii
6	Production d'un Photo-courant d'une cellule PV recevant plusieurs types d'irradiances et effectuant une combinaison d'irradiations directe et indirecte . . . . .	ix
7	Processus d'expérimentation pour obtenir la zone d'ombre sur le module PV . . . . .	x
8	Module PV affecté par une ombre mobile au cours de la journée du 27 février 2018 . . . . .	xi
9	Comparaison du modèle de GMPPT avec les mesures . . . . .	xi
10	Modélisation d'un convertisseur boost DC-DCr . . . . .	xii
11	Modèle onduleur DC-AC avec BG . . . . .	xii
12	Modélisation BG de systèmes photovoltaïques . . . . .	xiii
13	a) Conversion de l'irradiation solaire en courant électrique b) Tension d'entrée du convertisseur élévateur c) Tension de sortie du convertisseur élévateur d) Tension de sortie convertisseur DC-AC	xiii
14	Processus de diagnostic de défaut (surveillance, détection, isolement, estimation de l'importance du défaut) . . . . .	xiv
15	Diagnostic de défaut basé sur le modèle . . . . .	xiv
16	Schéma des défauts pour le diagnostic sur système PV . . . . .	xv
17	Structure générale de l'interface de test et d'acquisition de données	xvi
18	(a) Courbes I-V et P-V sans ombre (b) Courbes I-V et P-V avec ombre . . . . .	xvii
19	Stratégie de diagnostic de panne basée sur le modèle . . . . .	xvii
20	Détection générale des fautes basée sur un modèle, données réelles du système et data-driven . . . . .	xviii
21	Structure du diagnostic pour PV . . . . .	xviii
22	Structure de diagnostic pour le convertisseur élévateur (a) et le système de comparaison versus système utilisant la redondance des relations analytiques (b) . . . . .	xix
23	Modèle HBG d'onduleur CC-CA avec stratégie de contrôle . . . .	xix
24	Modèle photovoltaïque en bongraph avec commande à tolérance de pannes . . . . .	xx
25	Représentation de la tension d'entrée, de la tension de sortie, et du courant de sortie . . . . .	xx
26	Carte FPGA avec entrées de mesure . . . . .	xxi
27	Diagnostic d'un onduleur DC-AC intégré sur FPGA . . . . .	xxii

1.1	Global Energy Consumption Statistics [6] . . . . .	3
1.2	Global energy consumption by energy source (1990-2040) Adapted from: [7] . . . . .	3
1.3	Global energy production statistics [6] . . . . .	4
1.4	Distributed sources, adapted from [8] . . . . .	4
1.5	Complete structure of PV system with energy storage connected to the grid . . . . .	7
1.6	Photovoltaic effect under illumination [9] . . . . .	7
1.7	Electromagnetic spectrum and spectral irradiance [10] . . . . .	8
1.8	Evolution of cell efficiencies for different technologies (1975 to 2018)	9
1.9	PV Cell, PV module or panel, PV string, and PV array . . . . .	10
1.10	Electric behaviour of a PV module with MPPT in normal operation when in shadow . . . . .	11
1.11	Classification of DC-DC converters for PV systems . . . . .	11
1.12	Comparison of types of DC-AC Inverter [11] . . . . .	13
1.13	Classification of energy storage systems [12] . . . . .	13
1.14	Architectures of PV systems with an AC bus connection . . . . .	18
1.15	Complete structure of PV module [13] . . . . .	19
1.16	Example of dust accumulation on a PV module . . . . .	20
1.17	Example of other types of obstacles generating shadow problems on PV modules (bird droppings, cobwebs, and fixed obstacles such as stairs) . . . . .	20
1.18	IR camera test on a PV module that has hot-spot formation . . . . .	21
1.19	Electrical behaviour of the PV module in a hot-spot condition. . . . .	21
1.20	Snail trails on PV module [1] . . . . .	22
1.21	Failure of diodes in PV modules [1] . . . . .	22
1.22	The two types of fault detection and diagnosis for PV systems: Residue versus Inference . . . . .	24
1.23	Schematic of FDI process based on residuals analysis . . . . .	25
1.24	Schematic of the main methodologies to detect and diagnose faults	27
1.25	Causes, types, and classification according to dynamics, methods, and diagnostic steps . . . . .	29
2.1	Simplified structure of a conventional PV system (Adapted from [1])	39
2.2	Modeling of complete PV system using HBG . . . . .	39
2.3	Granularity of PV cell, string, and array (Adapted from [1]) . . . . .	40
2.4	Single diode model of solar cell . . . . .	41
2.5	Double diode model of solar cell . . . . .	42
2.6	Electrical schematic of the cell, including the reverse bias . . . . .	42
2.7	PV cell HBG model . . . . .	43
2.8	Complete I-V curve (a) and variation of the load resistance $RL$ (pos-neg) (b) . . . . .	43
2.9	I-V curves of the PV cell under different irradiation conditions . . . . .	44
2.10	The I-V Curves of the two kinds of PV modules (Tenesol 2200: 240W and 250W) (a) and P-V curves (b) . . . . .	45
2.11	Dependence values for solar radiation (a) and interpolation of irradiation $G$ in function of the voltage, current, and power of the PV module . . . . .	46
2.12	Extrapolation of I-V curves (a) and PV curves (b) . . . . .	47
2.13	HBG model of PV module <i>Tenesol 2200</i> . . . . .	48

2.14 I-V curve of the PV module (a) and variation of the load resistance $RL$ (b) . . . . .	48
2.15 I-V curves under various irradiation conditions . . . . .	49
2.16 I-V curves with the activation of the bypass diodes (shadow condition) (a) and variation of the load resistance $RL$ (b) . . . . .	49
2.17 I-V curves with one activated diode bypass under various irradiation conditions . . . . .	50
2.18 Example of shadow size and shape affecting PV cell production . . . . .	50
2.19 General schematic of the proposed PV module model . . . . .	51
2.20 Complete description of shadows affecting the output current of the cell . . . . .	51
2.21 Photo-current of a cell as a linear combination of direct and indirect irradiation . . . . .	52
2.22 Experimentation process to obtain the shaded area of the PV module . . . . .	54
2.23 Cropped image (a) and superpixel process (b) . . . . .	55
2.24 Image segmentation of the whole panel (a) and analysis of the shadow area (b) . . . . .	56
2.25 Comparison of the I-V curve measurement with the model during normal operation . . . . .	58
2.26 Test for shadow on module Tenesol 2200 with shadows on March, 22nd, 2018 . . . . .	59
2.27 Comparison of the measurement of I-V curves with the model during normal operation and under shading conditions . . . . .	59
2.28 Test for shadow on a module Tenesol 2200 with shadows on February 9th, 2018 . . . . .	60
2.29 Comparison of the measurement of I-V curves with the model in normal operating conditions and under shading conditions . . . . .	61
2.30 PV module affected by a mobile shadow on February, 27th, 2018 . . . . .	61
2.31 Comparison of the I-V curve model with experimental I-V curves on February 27th, 2018, at 2.00pm . . . . .	62
2.32 PV module affected by a mobile shadow on March 8th, 2018 . . . . .	63
2.33 Comparison of the I-V curve model with experimental I-V curves on March 8th, 2018 . . . . .	64
2.34 a) I-V curve, b) P-V curve, c) Evolution of the MPPT algorithm, d) Detection of GMPP . . . . .	66
2.35 Comparison of the GMPPT model with the measurements . . . . .	66
2.36 Validation of GMPPT without calibration of parameters . . . . .	67
2.37 Electrical structure of the boost converter . . . . .	68
2.38 HBG Model of a boost Converter . . . . .	69
2.39 Simplified HBG model of the boost converter . . . . .	70
2.40 Input voltage and output voltage of the boost converter . . . . .	70
2.41 Schematic of a single-phase inverter (a) and its HBG model (b) . . . . .	71
2.42 Simplified model of an isolated single-phase inverter . . . . .	72
2.43 Output Voltage . . . . .	72
2.44 Inverter DC-AC (a) Electrical diagram (b) BG model . . . . .	72
2.45 Output Voltage . . . . .	74
2.46 Explication of Boost inverter . . . . .	74
2.47 Boost inverter bidirectional (a) diagram (b) model . . . . .	75
2.48 Model boost inverter using matlab . . . . .	76

2.49	Simulation of boost inverter $V_{ref}=V_o$ . . . . .	76
2.50	PV system modeling using HBG . . . . .	77
2.51	Outputs . . . . .	77
3.1	Process of fault diagnosis (monitoring, detection, isolation) . . .	85
3.2	Faults for diagnosing a PV system shown in schematic form . . .	87
3.3	General structure of a test and data acquisition interface . . . . .	88
3.4	General fault detection based on the model, real data from the system, and driven data . . . . .	89
3.5	Behavior normally followed by a photovoltaic panel . . . . .	90
3.6	Characterization of the mathematical model using electrical characteristics of the PV module tenesol . . . . .	91
3.7	(a) Fault from irradiation measurement and (b) PV power measurement . . . . .	92
3.8	(a) Temperature measurement fault, and (b) PV power measurement fault . . . . .	93
3.9	(a) I-V and P-V curves with no shadow (b) I-V and P-V curves with shadow (c) P-t curve . . . . .	94
3.10	Fault diagnosis strategy based on the model . . . . .	95
3.11	(a) Photographs of shadow evolution on a PV module during the day (b) and surface I-V-t representation produced by the shadow . . . . .	95
3.12	Zoom of I-V curves zoom in function of time . . . . .	96
3.13	PV output power measurements of both PV modules on March 8th, 2018 . . . . .	96
3.14	(a) Photographs of the evolution of shadows (b) surface I-V-t produced by the shadow . . . . .	98
3.15	PV output power measurements of both PV modules on February 27th, 2018 . . . . .	98
3.16	Representation of two fault-detection zones . . . . .	100
3.17	Normal Behavior parameters under normal and abnormal operation conditions . . . . .	100
3.18	Diagnosis of faults identifying fault sensor problems or shadow on the PV module . . . . .	101
3.19	Results of shadow detection, based on G versus P . . . . .	101
3.20	Results of the shadow detection based on G versus V . . . . .	102
3.21	Structure of diagnosis for the PV . . . . .	103
3.22	Appearance of hot-spots on the PV array and electric behaviour . . . . .	104
3.23	Temperature effect on I-V curves . . . . .	104
3.24	I-V curves under hot-spots (a) and P-V curves (b) . . . . .	105
3.25	Estimation of the hot spotting power dissipation magnitude . . . . .	106
3.26	(a) PV systems under normal and shading conditions and (b) P-V curves from both PV systems . . . . .	107
3.27	(a) Measurement of <i>MPP</i> with no shadow with an EKO system in real working conditions, (b) Corresponding <i>MPP</i> with no shadow obtained with our model (Power measured campaign on a day with no shadow (22/03/2018) . . . . .	107
3.28	(a) V-I Aging (b) P-V Aging . . . . .	108
3.29	Evolution of the P versus G slope under aging conditions . . . . .	109
3.30	Diagnosis structure for boost converter (a) and comparison system versus system using analytic relation redundancy (b) . . . . .	110

3.31	Diagnostic Bondgraph of the Boost converter . . . . .	110
3.32	Model with and without fault . . . . .	111
3.33	(a) Boost converter without fault (b) Boost converter with fault (c) Detection of fault . . . . .	111
3.34	Residues boost converter . . . . .	113
3.35	General structure of diagnosis for the inverter (a), and comparison system versus a system that uses analytic relation redundancy (b)	114
3.36	HBG model of H bridge DC-AC inverter str . . . . .	114
3.37	Model with and without fault . . . . .	115
3.38	(a) Output Voltage (without/with faults), (b) Detection of fault	115
3.39	General Diagnosis . . . . .	116
3.40	Algorithm of the PV Diagnostic . . . . .	116
3.41	FTC Structure for a PV system . . . . .	117
3.42	Layer FTC . . . . .	118
3.43	Fault-Tolerant Control on the PV system . . . . .	119
3.44	Strategy boost and MPPT . . . . .	120
3.45	Boost converter with a control strategy . . . . .	121
3.46	Representation of the input and output voltage of the boost con- verter for the whole day (March 23rd, 2018) . . . . .	121
3.47	Control strategy for the boost and inverter . . . . .	122
3.48	HBG model of DC-AC inverter with control strategy . . . . .	122
3.49	Block diagram representing the current loop control of the in- verter, adapted from ([14]) . . . . .	123
3.50	PVS Model with BG . . . . .	123
3.51	Representation of the input voltage, output voltage, and output current . . . . .	124
3.52	Control strategy with global MPPT . . . . .	124
3.53	Model boost inverter . . . . .	125
3.54	The whole system with the boost inverter . . . . .	125
3.55	(a) $V_o$ in phase of the inverter and the grid (b) $I_o$ injected into the grid . . . . .	126
3.56	FTC: based on reconfiguring panels [15] . . . . .	126
3.57	FTC: based on the reconfiguration of AC Inverters . . . . .	127
4.1	FPGA board with measurement inputs . . . . .	135
4.2	Real-time FPGA-based platform for emulation of complex shaded PV systems . . . . .	135
4.3	Experimental tests for the monocrystalline PV module . . . . .	136
4.4	I-V curves for both cases . . . . .	136
4.5	VHDL flowchart of hot-spot prevention . . . . .	137
4.6	Hot-spot prevention results and response time for Case 1. . . . .	138
4.7	Hot-spot prevention results and response time for Case 2. . . . .	138
4.8	HBG inverter model based on [16] . . . . .	139
4.9	Diagnosis of a DC-AC inverter embedded in FPGA . . . . .	141
4.10	Diagnosis . . . . .	141
A.1	Bond graph Multidomain . . . . .	149
B.1	Co-simulation 20sim-matlab . . . . .	153
B.2	(a) CoSimulation Matlab (b) CoSimulation 20sim . . . . .	154

---

B.3	Simulation every minute I-V and P-V curves . . . . .	154
B.4	(a) Simulation of the curve P versus V (one day) (b) Simulation of the curve I versus V (one day) . . . . .	155
C.1	Terrace of the ADREAM building . . . . .	157
C.2	ADREAM . . . . .	158
C.3	Terrace 1 in the ADREAM . . . . .	158
C.4	(a) Acquisition system (b) Pelican . . . . .	159
C.5	Sun path at LAAS-ADREAM . . . . .	159
D.1	Diagnosis process . . . . .	161
D.2	Hardware redundancy and analytical redundancy for FDI [17] . .	162
D.3	The fault model used for the residual generation based on the model	163
D.4	Residue . . . . .	164
D.5	Control chart . . . . .	165
D.6	Region signature of faults . . . . .	165
D.7	Isolation of faults . . . . .	166
E.1	Monitoring interface . . . . .	167
E.2	Data driven diagnosis . . . . .	168
E.3	Monitoring and comparison system interface vs. model . . . . .	169

## List of Tables

1.1	Advantages and disadvantages of PV systems [18] . . . . .	5
1.2	Classification of catastrophic and non-catastrophic faults . . . . .	19
1.3	Summary of the different type of faults [19] for PV cells, modules, arrays . . . . .	23
2.1	Cell parameters of the PV cell used in the literature . . . . .	43
2.2	Electrical characteristics of PV module <i>Tenesol 2200</i> . . . . .	46
2.3	Quantification of the area of each selected PV Cell . . . . .	56
2.4	Quantification of the shadow of each affected PV cell area . . . . .	56
2.5	Percentage of the shadow area and attenuation factor calculation . . . . .	57
2.6	Parameters of boost inverter . . . . .	76
3.1	Evaluation of the output power losses in function of the shaded area on March 8th, 2018 . . . . .	97
3.2	Comparison of the output power of a PV module under normal operation and a PV module in shade on February 27th, 2018 . . . . .	99
3.3	Fault Matrix under shadow conditions . . . . .	102
3.4	Fault signature matrix of a boost converter . . . . .	112
3.5	Fault signature matrix . . . . .	116
4.1	Signature Matrix fault of DC-AC inverter . . . . .	140
A.1	Power and energy variables in various energy domains . . . . .	150
A.2	Elements, symbol and description BG . . . . .	150
C.1	List of PV equipment of ADREAM plataform . . . . .	158



# 1

## Introduction

A smart grid is a modernized electrical network in which various power components and functional technologies such as dispersed power generators are integrated, and there are dispatched loads associated with communication systems and storage devices that can operate in grid-connected or island modes [1]. A smart grid can be considered to be "smart" when it has fluctuating renewable energy with a bi-directional power flow between (producers and consumers). The consumers are also producing and sending energy to the grid, which differs from the traditional grid in which there is a clear separation between producers and consumers, which results in a uni-directional power flow [2]. The term micro-grid refers to a set of loads, power resources, and energy storage devices [1]. In other words a micro-grid constitutes a single element of a smart-grid (or a power network node). The integration of intermittent renewable energy sources and loads in power grids or smaller versions (micro-grids) have been developed as a solution to energy-access problems [3]. [4] presents a comparative and critical study on the strategies for micro-grid energy management and summarizes various methods for uncertainty quantification to manage the volatility and variability of renewable energy resources and load demand. In terms of possible problems on micro-grids [5], presents a survey on methods to diagnose faults, electrical infrastructure, and a description of component failure modes in smart micro-grids. In [6], prerequisites are discussed for fault-tolerant power management systems in PV systems. The importance of working on diagnostic methods for micro-grids is for these systems to be operated safely and the system to operate despite faults. The diagnostic methods for a photovoltaic micro-grid can also be used by other types of micro-networks. This thesis proposes a new method for intelligent diagnosis that is focused on photo-voltaic power processing segments.

- Chapter 1 presents the general concepts about PV systems, faults, and their integration in microgrids.
- Chapter 2 presents the development of PV systems modeling strategy, the purpose of which is to diagnose faults.

- Chapter 3 presents the development of fault diagnosis algorithms in photovoltaic systems (PV modules, converters, and inverters). Additionally, it presents the control strategies that tolerate the fault on the PV systems.
- Chapter 4 presents the FPGA implementation of a fault diagnostics applied to photovoltaic system.

## 1.1 Global energy in context

The three most basic drivers of energy demand are: economic activity, population, and technology. Longer-term trends in economic growth for a particular economy depend on the underlying demographic and productivity trends, which, in turn, are a reflection of population growth, labor force participation rate, productivity growth, national savings rate, and capital accumulation [7]. Figure 1.1 shows the statistics for global energy consumption. Countries with a large population stand out for their high energy consumption.

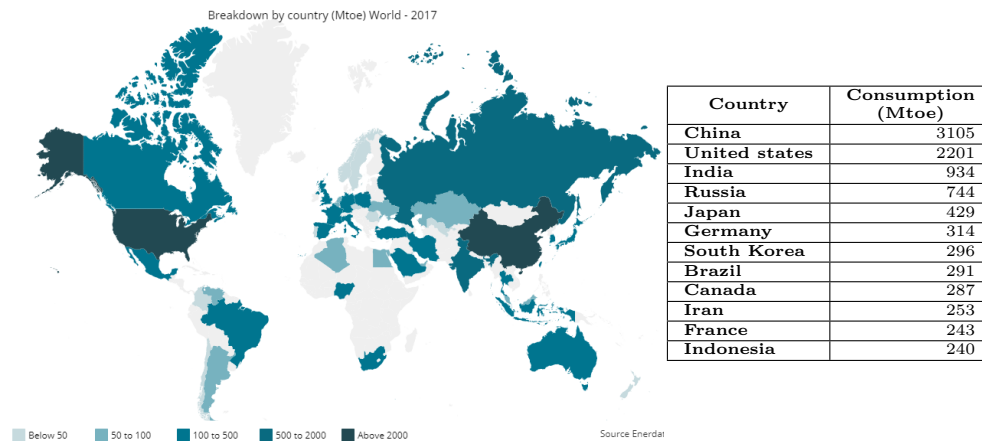


**Figure 1.1** Global Energy Consumption Statistics [8]

Global demand for energy has an upward trend. The U.S. Energy Information Administration states that world energy consumption will grow by 28% between 2015 and 2040, as illustrated in Figure 1.2. The projection for the next 25 years is that renewable energies will grow and fossil fuels will decrease.

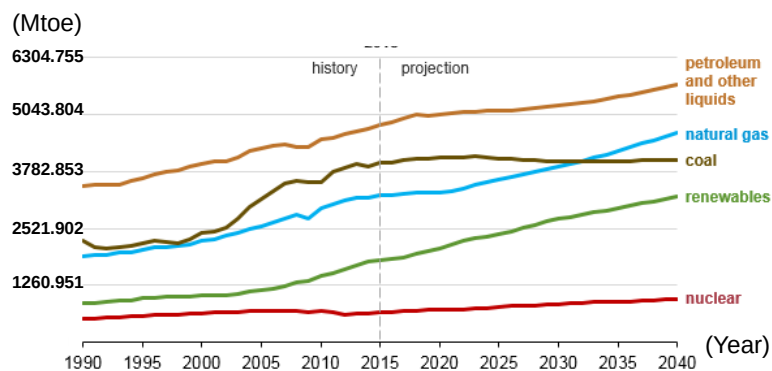


**Figure 1.2** Global energy consumption by energy source (1990-2040) Adapted from: [9]

Figure 1.3 shows the world energy production statistics. Conventional energy resources (e.g, coal, oil, and gas) are exhaustible and have a limited supply. Using these resources causes a series of environmental problems such as climate change, global warming, air pollution, and acid rain [10]. Countries such as China and the United States continue to use fossil fuels regardless of various established climate change protocols.

There is an urgent need to explore alternative energy resources and avoid con-

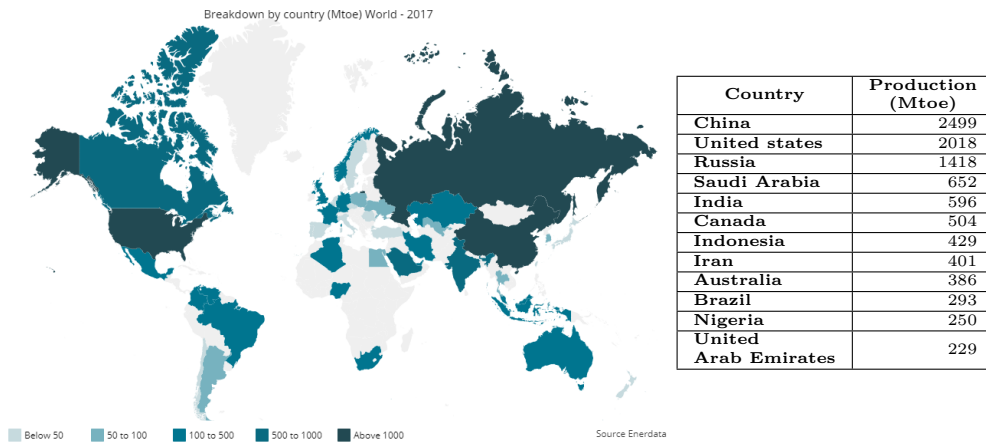


**Figure 1.3** Global energy production statistics [8]

ventional energies. Kannan [11] explains the importance of the solar industry by using fundamental concepts, the global energy scenario, and highlighting research undertaken to improve the solar industry. Moreover, potential applications for and removing barriers to improve future solar industry would help the energy crisis. [1] presents an interesting review of the intersection between renewable energies and politics from an multidisciplinary social sciences perspective. [12] includes a survey of different microgrid control strategies (centralized, decentralized, distributed, and hierarchical frameworks) that would help improve the distribution of electrical energy.

The energy distributed produces electricity from small energy sources. The energy sources are directly connected to medium-voltage or low-voltage distribution systems rather than to the bulk power transmission systems. Different types of the distribution generation resources are shown in Figure 1.4. The photovoltaic element is the principal element studied in this thesis.

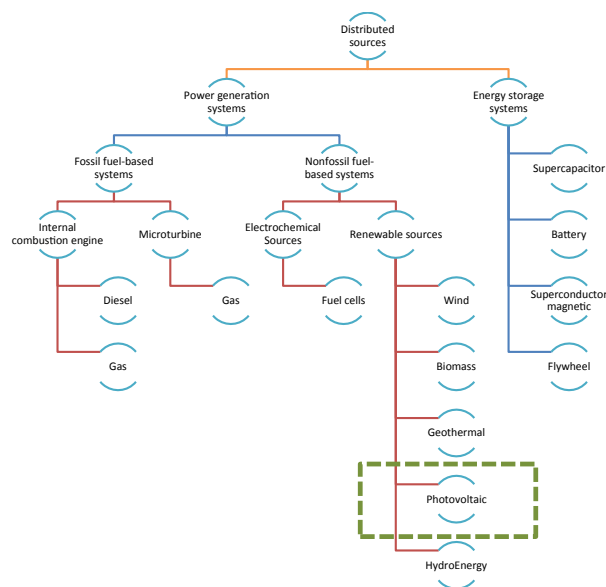


**Figure 1.4** Distributed sources, adapted from [13]

## 1.2 Photovoltaic systems and their reliability

### 1.2.1 The interest in photovoltaics and the objective of this thesis

Solar energy has received special attention because of its easy implementation, environmental benefits, and good return on any economic investment made [14]. As PV systems have no moving parts (compared to wind and hydro systems), they are extremely reliable. The design of any PV system is based on an awareness of the phenomena that might lead to a decrease in plant power production, in real conditions, and over its whole lifetime [15]. The external conditions linked to the weather, pollution, and geographic sites constitute an important environmental factor in PV system operation, which is affected by variables such as solar radiation, temperature, wind speed, dust, and shadow.

It is difficult to find a complete PV conversion system that includes electrical interfaces and has the same lifetime in its interfaces as the PV cells in terrestrial applications. The main advantages and disadvantages of photovoltaic solar energy are described in Table 1.1.

Advantages	Disadvantages
<ul style="list-style-type: none"> <li>- Reliable system</li> <li>- Low operation and maintenance cost</li> <li>- Low maintenance</li> <li>- Free energy source</li> <li>- Clean energy</li> <li>- Highly available</li> <li>- Energy generation closer to the consumer</li> <li>- Low environmental impact</li> <li>- Potential to mitigate greenhouse gases emissions</li> <li>- Noiseless</li> </ul>	<ul style="list-style-type: none"> <li>- Limits of the systems available on the market</li> <li>- High initial cost</li> <li>- A large area required for installation</li> <li>- High dependence on technological development</li> <li>- Dependent on geography and weather conditions</li> </ul>

**Table 1.1** Advantages and disadvantages of PV systems [10]

Furthermore, faults in modules, in connection lines, or in power converters can seriously affect the efficiency of the PV system and the energy yield as well as the security and reliability of the entire PV plant if it is not detected and quickly corrected [16].

Previous approaches in LAAS-CNRS were undertaken with photovoltaic system efficiencies, the ability to be connected to micro-grids was tested, and their behavior in several working conditions was analyzed. Recently, some research projects are moving toward diagnosis. The first PhD in the diagnosis field that looked specifically at PV systems was defended by Michael Bressan [17]. He proposed a method to detect and identify faults around the shading problem, and the analysis was based on his knowledge of current-voltage and power-time

curves. In addition, Y. El-Basri proposed [18] a methodology to identify the causes of failures of PV systems, particularly the ones linked to shading conditions. This approach provided technical solutions and made matching power conversion systems and their associated sources more reliable and efficient. A. Galeano Gutierrez [19] was the first doctoral student to undertake a PhD in collaboration between the LAAS-CNRS and the Universidad de los Andes (cotutelle PhD with the Paul Sabatier University, Toulouse and The University of Andes, Bogota); the work was undertaken in the field of power conversion. His work was focused on partially shaded PV and architectures DC/AC connected to microgrids. Jeremy Dulout [20] analyzed and modeled the production and consumption of the ADREAM building in order to define the operating profile of an energy storage system that ensures the equilibrium of the microgrid. Kolja Neuhaus [21] developed similar LVDC micro-grids that included PV and storage elements. The specific load of this micro-grid was H<sub>2</sub> electrolyzer, which provided hydrogen.

Based on this scientific experience that was associated with a real experimental platform dedicated to PV systems and micro-grids, this thesis started in 2016 thanks to the continued collaboration between the LAAS-CNRS and the Universidad de los Andes. It was jointly undertaken with the Paul Sabatier University, Toulouse and the Universidad de los Andes. This work's primary objective is to investigate photovoltaic systems, in shading conditions, as well as in degraded operating modes. Based on new models that include these phenomena, this thesis proposes new solutions to diagnose faults and to ensure good operation. The objective of this research is to develop a high granularity tool to diagnose PV systems' electrical failures. This PhD is the second PhD on PV systems fault diagnosis at the LAAS-CNRS.

### 1.2.2 Structure of a photovoltaic system

A complete PV system connected to the grid is composed by an arrangement of several components: a) Solar tracking, b) PV module, c) MPPT, d) Power conversion (DC-DC,DC-AC), e) Energy storage system, and f) loads. An example of the structure is presented in Figure 1.5.

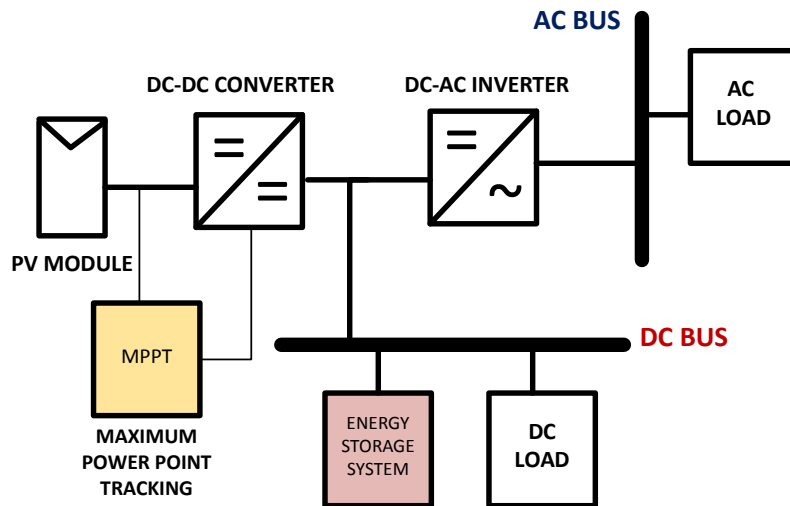


**Figure 1.5** Complete structure of PV system with energy storage connected to the grid

### 1.2.2.1 Solar cells

Photovoltaic energy conversion is the direct production of electrical energy in the form of current and voltage from electromagnetic (i.e., light, including infrared, visible, and ultraviolet) energy. In semiconductor physics, a photon with energy greater than bandgap energy ( $h \cdot \nu > E_{gap}$ ), which is incident on a semiconductor, can excite electrons from the valence band to the conduction band, and this allows current to flow. The energy from a photon ( $E$ ), which appears in the form of packets of energy, is given by:

$$E = h \cdot \nu \quad (1.1)$$

$h$  is Planck constant ( $6.626 \cdot 10^{-34} \text{Ws}^2$ ), and  $\nu$  is frequency in Hertz [22].

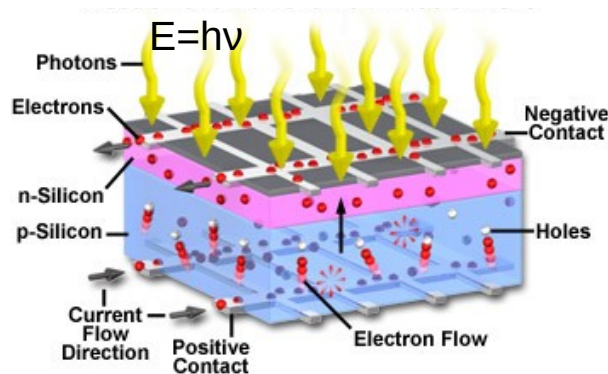


**Figure 1.6** Photovoltaic effect under illumination [23]

Figure 1.6 illustrates the principle of photovoltaic energy conversion. The light absorption process causes a transition in a material (the absorber) from a ground state to an excited state. The excited state is then converted into (at least) a free negative and a free positive-charge carrier pair. The discriminating transport mechanism allows the free negative charge carriers to move in one direction

(i.e., cathode) and the free positive charge carriers to move in another direction (i.e. anode). The energetic photo-generated negative-charge carriers arriving at the cathode result in electrons travelling through an external path (an electric circuit). While traveling on this path, they lose their energy by doing something useful with an electrical "load", and finally they return to the cell's anode. At the anode, every one of the returning electrons is combined with a positive-charge carrier; therefore, the absorber is returned to a ground state.

The energy supply for a photovoltaic solar cell is linked to energy from the sun's photons, and it depends on variables such as latitude, time of day, atmospheric conditions, and over different wavelengths. The input power per area impinging on a cell can be expressed as:

$$P_{IN} = \int_{\lambda} \frac{h \cdot c}{\lambda} \cdot \Phi_0(\lambda) d\lambda \quad (1.2)$$

where  $\Phi_0(\lambda)$  is a photon spectra,  $h$  is a Planck constant, and  $c$  is the speed of the light ( $299792458 \text{ m/s}$ ).

Figure 1.7 illustrates the electromagnetic spectrum and spectral irradiance.

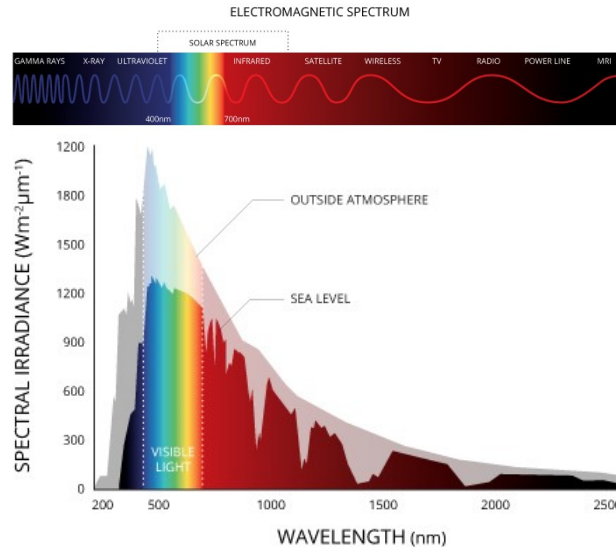


**Figure 1.7** Electromagnetic spectrum and spectral irradiance [24]

According to [10], PV cell technologies can be categorized into three generations, depending on the raw material used and the level of commercial maturity. Goetz et al. [25] showed insights into PV technology and first-and-second-generation materials. Figure 1.8 shows the temporal evolution in graphic form of various cell efficiencies for different technologies used by the National Renewable Energy Laboratory (NREL).

- First generation Photovoltaic systems (fully commercial) use crystalline silicone technology (c-Si) both in its simple crystalline form (sc-Si) as well as in the multicrystalline form (mc-Si).
- Second generation photovoltaic systems are based on thin film photovoltaic technologies and generally include three main families: (1) Amorphous sili-

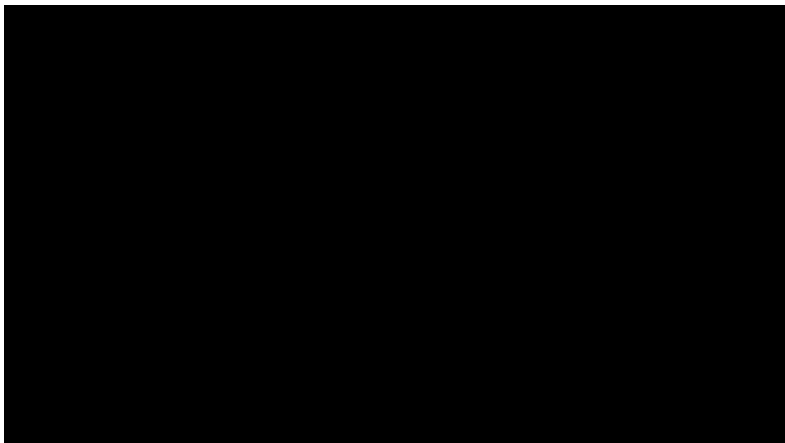


**Figure 1.8** Evolution of cell efficiencies for different technologies (1975 to 2018)

con (a-Si) and micro amorphous silicon (a-Si / $\mu$ c-Si); (2) cadmium telluride (CdTe); and (3) copper indium selenide (CIS) and copper, indium gallium selenide (CIGS).

- Third generation photovoltaic systems include organic photovoltaic technologies that are still in the demonstration phase (or have not been widely marketed) as well as new concepts being developed. [26] summarizes the current progress being made with perovskite photovoltaic materials and addresses future research directions for this topic.

### 1.2.2.2 Structure cell, module, string, and array

Figure 1.9 presents a basic structure cell, a PV string, and a PV array. Classically, to build a solar module, solar cells are connected in series, and solar modules are usually connected in series to form a solar string to increase the DC operating voltage level of the whole system. Usually, these solar strings are connected in parallel to increase the DC current level, which then increases power generation capability. For security reasons, the PV module is equipped with a bypass diode and it is dotted by bypass diodes. These diodes protect and avoid PV cells reverse mode in shadow conditions; they also bypass the current of the other part of the module to be able to produce power even when in this condition. The number of bypass diodes of each module depends on the PV manufacturers. Generally, a PV module has from 3 to 5 diodes for protection.

### 1.2.2.3 Solar tracker

The idea behind designing a solar tracking system is to fix solar photovoltaic modules in a position that can track the motion of the sun across the sky to capture the maximum amount of sunlight. The tracker system should be placed in a position to achieve the best angle of incidence to maximize the electrical energy output. [27] reviews the principles and mechanisms of photovoltaic tracking systems to determine the best panel orientation. The tracking techniques, efficiency, performance, advantages, and disadvantages of simple tracking systems

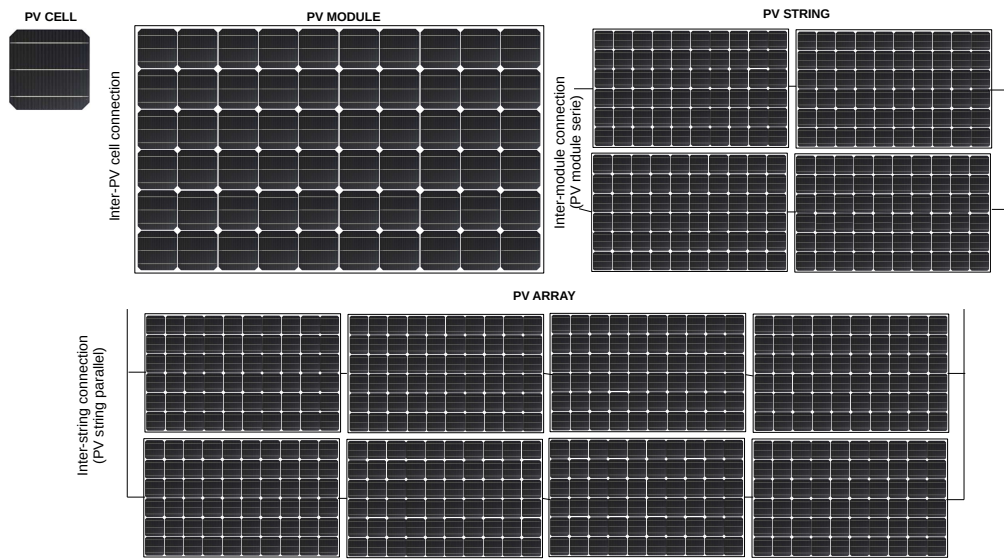


**Figure 1.9** PV Cell, PV module or panel, PV string, and PV array

are compared with those belonging to state-of-the-art tracking systems.

#### 1.2.2.4 Maximum Power Point Tracking (MPPT)

Dedicated Maximum Power Point Tracking (MPPT) algorithms are used in PV systems to maximize the PV array output power depending on irradiance, shadows, and cell temperature. An initial classification of the MPPT can be carried out based on the configuration of PV architectures (i.e., central inverters, string inverters, multi-inverters, and multi-string inverters). A PV module has non-linear I-V (Current-Voltage) characteristics, and its P-V (Power-Voltage) characteristics show only one point (Pmax), named MPP, that has various control methods able to track the maximum power point (MPP). The module delivers maximum power as shown in Figure 1.10. There are various methods reported in the literature to track the maximum power point; some are more reliable than others when finding the true MPP point [28]. As shown in Fig(1.10), when PV strings receive uniform irradiation from the sun, I-V curves and P-V curves only have one peak. But when PV module, array, or string has partial shading, there can be multiple peaks on the curves, depending on temperature and irradiation disparities. The first peak near the open circuit voltage is called global maximum power point (GMPP), and the other peaks are called local maximum power points (LMPP). In this case, the main drawbacks of numerous MPPT algorithms is their inability to distinguish between GMPP and LMPP; therefore, it can work at one of the LMPP but produce drastic losses in PV power productions.

Some new MPPT algorithms, contained in the state-of-the-art, have the ability to find (or not) the global power maximum in non-homogenous shadow conditions: named MPPT with shadow [29].

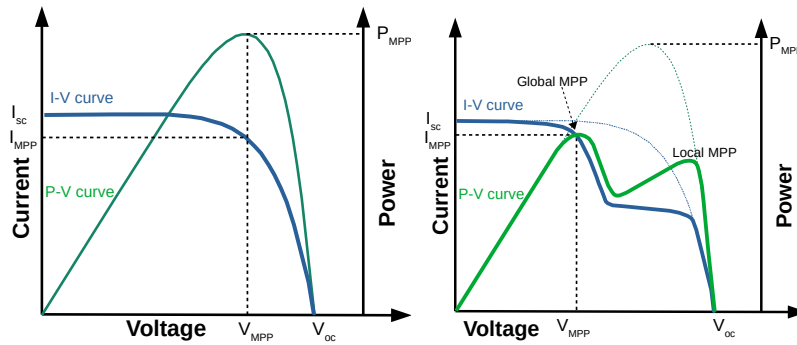


**Figure 1.10** Electric behaviour of a PV module with MPPT in normal operation when in shadow

### 1.2.2.5 DC-DC converters

Static converters can ensure various functions. They can adapt voltage levels between the PV generator and the load. The introduction of a galvanic isolation provides safety. Depending on the choice of DC-DC conversion, static converters can increase or decrease the voltage level.

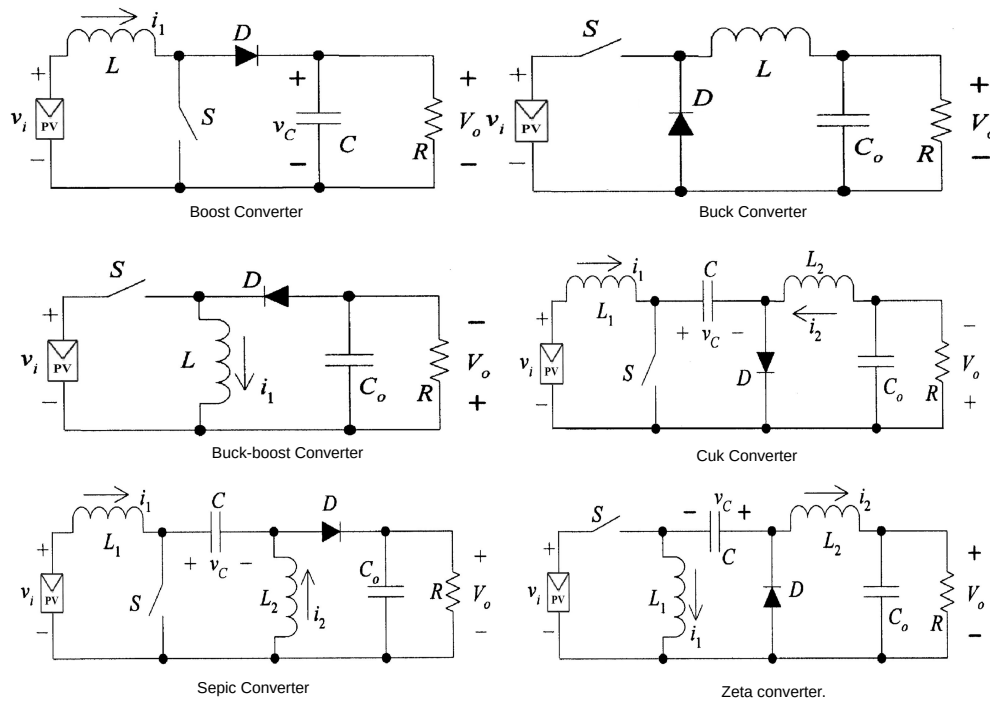


**Figure 1.11** Classification of DC-DC converters for PV systems

Although there is a wide number of different families of DC-DC converters, figure 1.11 shows some of the main converters used in photovoltaic systems:

1. Boost converter: is a DC-DC converter that is able to generate an output voltage greater than the input voltage.
2. Buck converter: is a DC-DC converter with an output voltage that is lower than the input voltage.

3. Buck-boost converter: is a DC-DC converter able to generate an inverted output voltage greater than or less than the input voltage.
4. Cuk converter: is a DC-DC converter that is able to generate an inverted output voltage which is greater than or less than the input voltage (similar to a buck-boost converter).
5. Single ended primary inductor converter-(SEPIC): this converter behaves in a similar way to a buck-boost and to a cuk converter. It provides non-inverted output voltage.
6. Zeta converter: this also provides a non inverted output voltage, which is greater than or less than the input voltage; it is similar to a SEPIC converter [30].

#### 1.2.2.6 DC-AC inverter

DC-AC converters are the most common inverters, and are at the center of every PV plant. They convert direct current (DC) from the PV generator into grid-compliant alternating current. At its output, the inverter imposes a system of electrical curves, that are quite similar to alternative sinusoidal signals, through a pulse width modulation control (PWM). On each of the inverter's outputs, an inductance acts as a filter and allows the inverter to supply almost sinusoidal currents to the grid. The role of this filter, the major disadvantage of which is its size, is to limit electromagnetic compatibility (EMC) problems related to the shape of the current injected into the network. The transformer can also replace the filter coil that acts as a filter. The current harmonics can be eliminated using the control by injecting harmonics out of phase by  $180^\circ$ . The non-linear loads generate these harmonic currents. Harmonic currents are currents the frequency of which is an integer multiple of the fundamental (that of the power supply). The superposition of harmonic currents on the fundamental current causes non-sinusoidal wave-forms that are associated with nonlinear charges.

Hybrid inverters go a step further and work with batteries to also store excess power. This type of system solves issues related to renewable energy variability and unreliable grid structures. At string level, a simple inverter can be used. For several strings, there are multi-string inverters that have a DC/DC stage per string doted by its own MPPT. For example, inverters called single-stage boost inverters (SSBI) have diverse advantages as they have a reduced and robust circuitry and are also reliable and efficient. [32] presented a review of single-stage inverters for a PV system.

#### 1.2.2.7 Energy Storage systems

A storage component is used to optimize power management and to do optimal matching between production and consumption. It can be used to ensure load demand or to reduce the time deficit by intermittence of the renewable source; it uses storage devices such as the flywheel, batteries, and super-capacitors. Fig(1.13) shows a classification of energy storage systems.

Topology	Switch Type	Switch Frequency	Waveform Type	Total Harmonic Distortion	Typical Efficiency	Idle Power Consumption	Surge Ability	Interference	DC-AC Isolation	Reliability
Vibrator	Mechanical	Low	Square	High ( $\approx 50\%$ )	60-80%	High	Poor	Medium	Yes	Poor
Push-Pull	SCR	Low	Square	High ( $\approx 50\%$ )	80%	High	Good	Low	Yes	Good
Push-Pull	MOSFET	Low	Modified Square	Medium ( $\approx 15-35\%$ )	80-90%	Low	Very Good	Low	Yes	Good
H-Bridge Low Freq.	MOSFET	Low	Modified Square	Medium ( $\approx 15-35\%$ )	85-95%	Low	Very Good	Low	Yes	Good
H-Bridge High Freq.	MOSFET	High	Modified Square	Medium ( $\approx 15-35\%$ )	85-90%	Medium	Poor to Good	High	No	Poor
Dual Xfrmr	MOSFET	Low	Modified Square	Medium ( $\approx 15-35\%$ )	80-90%	Medium	Good	Low	Yes	Good
Rotary	Mechanical	Low	Sine wave	Low	50-70%	High	Poor	Low	Yes	Poor
Ferro Resonant	MOSFET	Low	Semi-Sine wave	Medium ( $\approx 15-35\%$ )	50-70%	High	Poor	Low	Yes	Good
High Frequency	MOSFET	High	Sine wave	Very Good (1-5%)	70-90%	High	Poor	High	Yes	Poor
Low Frequency Multi-Step	MOSFET	Medium-low	Sine wave	Very Good (3-5%)	85-95%	Low	Very Good	Low	Yes	Very Good
Hybrid High/Low	MOSFET	High	Sine wave	Very Good (1-5%)	85-95%	Medium	Good	Low	Yes	Very Good

Figure 1.12 Comparison of types of DC-AC Inverter [31]

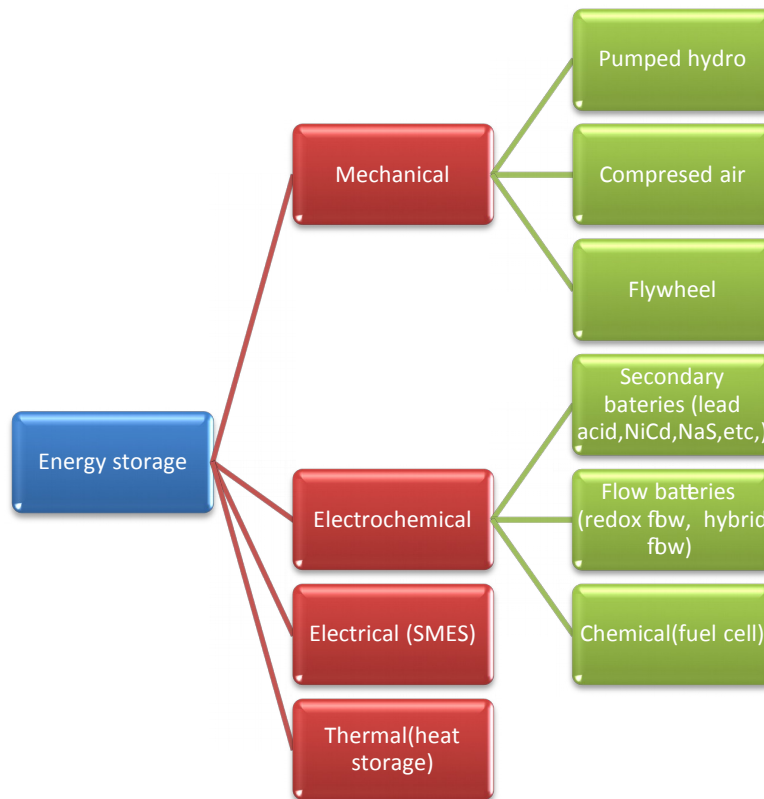


Figure 1.13 Classification of energy storage systems [33]

### 1.2.2.8 AC - DC BUSs

A microgrid can operate in both grid-connected mode and islanded mode. In order to make a smooth transfer from islanded mode to grid-connected mode, a synchronization is necessary.

- AC micro-grids have a common AC bus, which is generally connected to mixed loads (DC and AC loads), distributed generations, energy storage devices. AC micro-grids are easily integrated to conventional AC grids because most loads and grids are AC [34].
- DC micro-grids have a common DC bus connected to the grid through an DC/AC converter. The operation principle of a DC micro-grid is similar to an AC micro-grid. Compared with AC micro-grids, DC micro-grids are a good solution to reduce power conversion losses because they only need one power conversion to connect a DC bus [34].

### 1.2.3 Architectures of PV systems

Figure 1.14 presents an example of various topologies of PV systems that have different configurations in the AC - DC bus connections.

Inevitably, the problem arises when trying to manage the flow of energy between various micro-sources that switch process in a micro-grid connection/isolation operating state. Yoldas et al. [34] and [35] present a detailed technical overview of micro-grids and smart grids.

#### 1.2.3.1 Central inverters

Central inverters are designed for applications such as large arrays installed on buildings, industrial facilities, and field installations. The advantages of this structure are:

- Low capital price per watt
- High efficiency
- Comparative ease of installation (a single unit in some scenarios)

The drawbacks of this structure can be:

- Its reliability
- It does not reach maximum efficiency when in shadow
- Use of high voltage DC cables, high power losses due to common MPPTs, module mismatch, non flexible design, losses in the string diodes, expensive, failure of central inverter leads to whole PV plant shutting down

#### 1.2.3.2 String inverters

A string inverter is most commonly used in home and commercial solar power systems. It is a large box that is often situated some distance away from the solar array. Depending on the size of the installation, there may be more than one string inverter. The advantages of this structure are:

- Great design flexibility
- Highly efficient
- Robust
- 3 phase variations available
- Low cost
- Remote system monitoring capabilities
- No string diode losses, low cost compared to central inverter topology, has a higher overall efficiency, individual MPPTs can be applied for every string

The drawbacks of this structure are:

- No panel level MPPT

- No panel level monitoring
- High voltage levels are a potential safety hazard
- The necessary high voltage-amplification may reduce the overall efficiency and increase the cost per kW of power produced

### 1.2.3.3 Multi-string inverters

This architecture uses a single inverter with one MPPT per string, which uses a chopper that reduces the number of interactions between the grid and the PV system. The main purpose is to reduce the cost compared with the previous architecture as the chopper does not need to integrate functionalities of measurement and monitoring with the grid's electrical data. The advantages of this structure are:

- Reduction in cost compared to the string inverter
- No integration of AC control in the chopper
- No detection of residual direct current in the grid
- Every string can be controlled separately; this allows the integration of strings from different technologies and of various orientations; there are small DC-link capacitors; and there is high energy due to local MPPT and optimum monitoring of the PV system

The drawbacks of this structure are:

- No continuity if the inverter fails
- The use of both DC-DC and DC-AC converters increases the cost per kW of this inverter

### 1.2.3.4 Micro-inverters

A micro-inverter consists of a small box located on the back of or situated very close to a solar panel. Its role is to convert the DC that is electricity produced by a single solar panel. The advantages of this structure are:

- Panel level
- System availability: a single malfunctioning panel will not have such an impact on the entire array
- Panel level monitoring
- Lower DC voltage increases safety
- Increase of design flexibility
- Increase of yield from very shady sites as one shade module does not drag down a whole string
- Panel level monitoring

- Low manufacturing and retail costs, minimum power loss, maximum power extraction from the PV module, easy expansion of the system due to the modular structure

The drawbacks of this structure are:

- Higher costs in terms of dollars per watt: currently double the cost of string inverters
- Complex installation
- Increase of maintenance costs due to there being multiple units in an array
- Reduced overall efficiency, higher amplification, higher installation cost, main challenge for the designers is to develop an inverter that can amplify a very small voltage

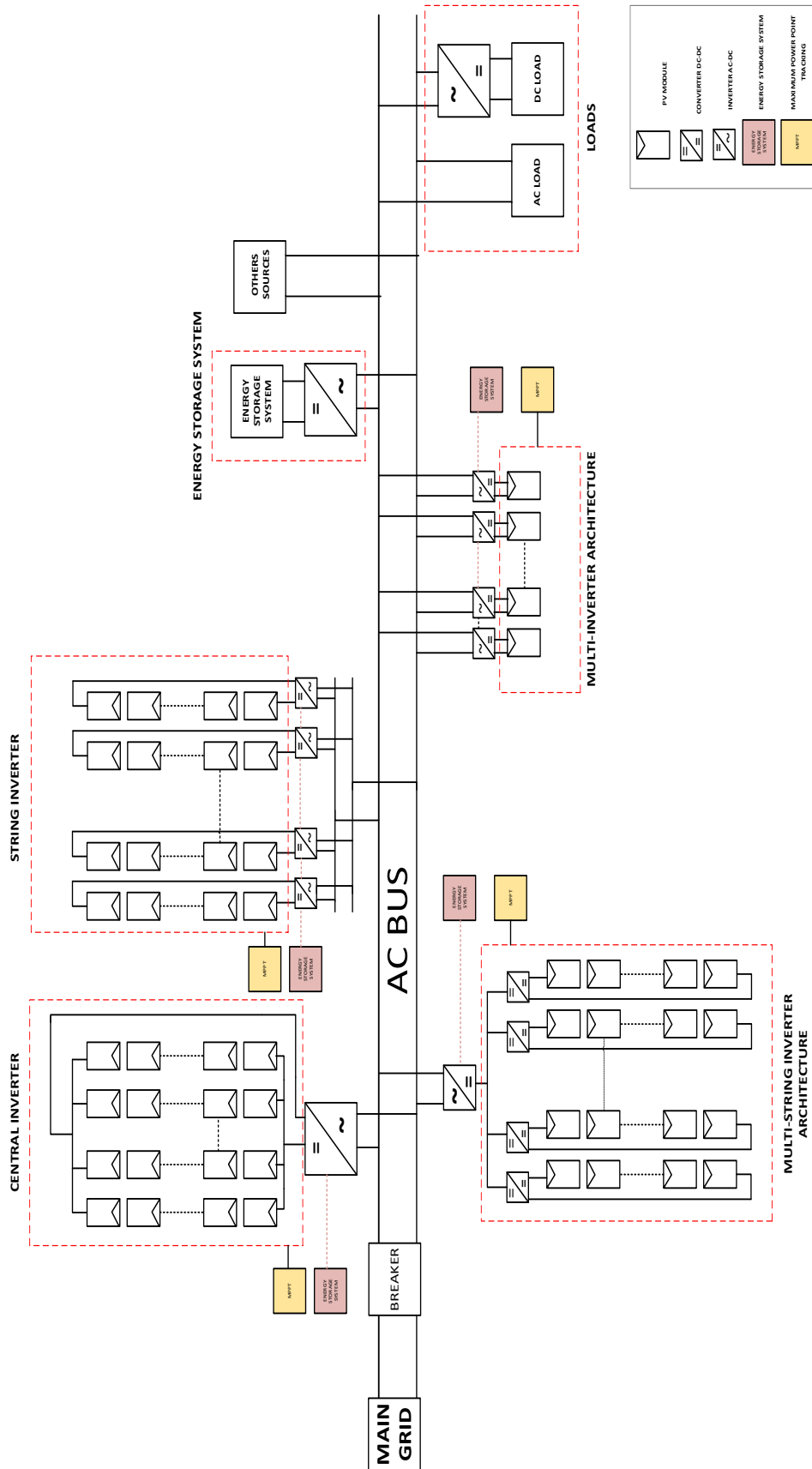


Figure 1.14 Architectures of PV systems with an AC bus connection

### 1.2.4 Losses, defects, and possible faults in PV systems

Photovoltaic systems are subject to different varieties of faults. They can involve all PV system components (modules, wiring, protections, and power converters). It is necessary to identify types of internal and external system faults under operating conditions. Table 1.2 presents two levels of possible faults, which can be catastrophic (or not).

Faults	
No catastrophic faults (Factors responsible for energy losses)	Catastrophic faults
Changing solar radiation	Ground faults [16, 36]
Operating temperature [37–41]	Line-to-Line [16]
Mismatch in PV module parameters	Hotspot
Error in MPPT	Polarity mismatch
Shading effect	Arc fault [16]
Ageing	Bypass diode
Snow or dust accumulation on PV modules	Dust/soil formation PV
DC-DC and DC-AC power devices [37, 41–44]	

**Table 1.2** Classification of catastrophic and non-catastrophic faults

#### 1.2.4.1 PV cells

Faults in PV cells, strings, and arrays are caused by shading effects, module soiling, inverter failure, and mismatch due to manufacturing differences or aging. Fig(1.15) shows a complete structure PV module schematic. This consists of a stack of different kinds of materials: frame, glass, encapsulant, solar cells, blacksheet, and junction box. Guiheneuf et al. [45] characterized the functional properties of glass used in PV applications (i.e. transmittance) and their degradation mechanisms.

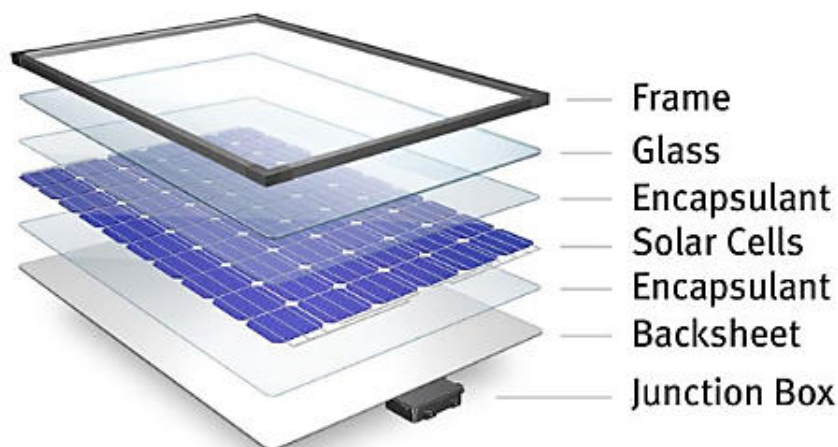


**Figure 1.15** Complete structure of PV module [46]

### A. Shadow

Shading due to soiling can be divided into two categories: soft shading such as air pollution and hard shading which occurs when a solid such as accumulated dust blocks the sunlight. Fig (1.16) shows examples of dust accumulation on an operational PV module that is almost horizontally inclined. Abderrezek et al. [47] investigated the effects of dust and the thermal behavior of PV modules for several types of dusts, which led to different panel behaviors in terms of thermal, optical, and electrical aspects. The authors also show light transmission variation with dust type. Figure 1.17 shows other kinds of obstacles that generate shadow problems.



**Figure 1.16** Example of dust accumulation on a PV module

ow



**Figure 1.17** Example of other types of obstacles generating shadow problems on PV modules (bird droppings, cobwebs, and fixed obstacles such as stairs)

### B. Hotspot

PV arrays in shadow not only decrease the energy produced but also increase the risk of structural failures as they cause localized hot-spots. A hot-spot refers

to the portion of the cell that has a higher temperature increase. The power dissipated in the solar cell is the product of the reverse bias voltage and the current; it can heat the solar cell as shown in Fig(1.18). In the worst case scenario, the solar cell may electrically breakdown due to the reverse bias voltage stress, which can result in a high current density and high-temperature area [37, 48–52].

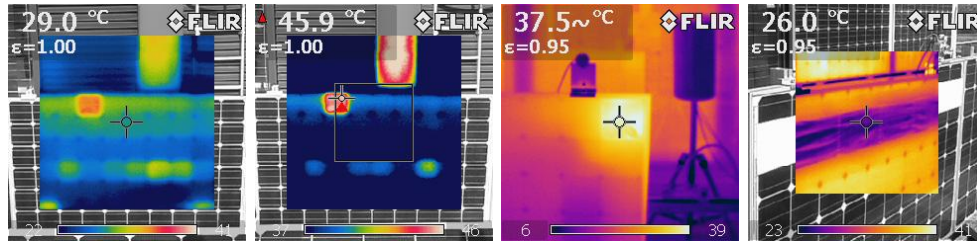


**Figure 1.18** IR camera test on a PV module that has hot-spot formation

Figure 1.19 shows the I-V curves for a group of PV cells that have different radiations under hot-spot conditions. Two areas are represented: the generator area and the receptor area. This explains the electrical behaviour of the PV module in a hot-spot condition [53].

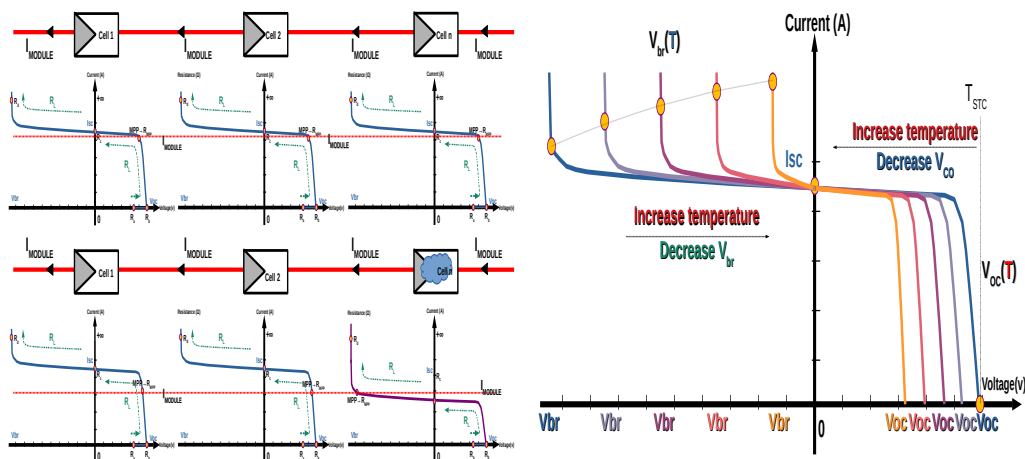


**Figure 1.19** Electrical behaviour of the PV module in a hot-spot condition.

### C. Snail trail

Figure 1.20 shows a PV module with a discoloration effect. It appeared after being operational for several years. Richter et al. show that humidity was a factor in the formation of snail trails. There are no indications that this phenomenon decreases the efficiency of the PV module, and, therefore, has no influence on the PV module's output power .

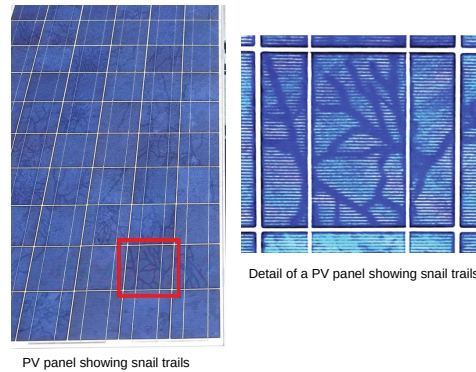


**Figure 1.20** Snail trails on PV module [54]

### D. Aging

PV arrays often operate in harsh environments, and non-uniform aging can occur and adversely impact PV systems' performance, especially in the middle and late-periods of their service lives. Due to the high cost of replacing aged PV modules, it is appealing to improve the energy efficiency of aged PV systems. Ottersbock et al. [55] showed that different climates had a strong influence on the aging behavior of polymeric encapsulant materials.

#### 1.2.4.2 Diode bypass

Bypass and blocking diodes are the primary security protections used to maintain the PV Systems' performance. The bypass diodes are used for reverse voltage protection, and blocking diodes are used for reverse current protection [56–62]. The electrical faults associated with diodes are that diodes short-circuit and open-circuit. These faults may occur when a PV module/array is partially shaded for a long period. Figure 1.21 illustrates the types of faults that can occur on bypass diodes located in a junction box.

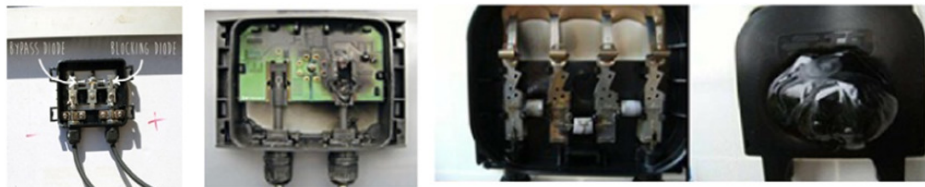


**Figure 1.21** Failure of diodes in PV modules [54]

Table 1.3 summarizes the external and internal faults in PV generators. The causes and effects are presented for each type of fault identified.

Type of fault	Affected components	Causes	Effects
<b>Hot spot</b>	Cells/Module	<p><b>External causes</b></p> <ul style="list-style-type: none"> <li>-Soiling, dust, snow, and shade</li> <li>-PV modules of different classes or technologies</li> </ul> <p><b>Internal causes</b></p> <ul style="list-style-type: none"> <li>-Fragmentation of cells</li> <li>-Current mismatch between cells</li> <li>-High resistance or "cold" solder points</li> <li>-Aging and degradation of cells</li> <li>-Partially shaded cells</li> <li>-Overheating</li> </ul>	<ul style="list-style-type: none"> <li>-Damage to solar cells.</li> <li>-Open circuits~</li> <li>-Reduced efficiency and reliability</li> </ul>
<b>Diode faults</b>	Bypass or blocking diodes	<p><b>External causes</b></p> <ul style="list-style-type: none"> <li>-Loosening and oxidation</li> </ul> <p><b>Internal causes</b></p> <ul style="list-style-type: none"> <li>-Glass breakage of frameless PVMs caused by the clamps</li> <li>-Connector failure (disconnection)</li> <li>-Isolated from ground</li> <li>-Encapsulation</li> </ul>	<ul style="list-style-type: none"> <li>-Damaged diodes</li> <li>-Short circuited diode, open circuited or Shunted diode</li> <li>-Damage and risk of fire</li> <li>-Reduced efficiency and reliability</li> <li>-Shunted module</li> <li>-Short circuit within a module</li> <li>-Short circuit between PV modules</li> <li>-Leaking currents within a PV Module</li> <li>-Damaged PV Module</li> <li>-Reduced efficiency and reliability</li> <li>-Reduced output power</li> </ul>
<b>Junction box fault</b>	Junction box~  PV module	<ul style="list-style-type: none"> <li>-Fretting corrosion,</li> </ul> <p><b>External causes</b></p> <ul style="list-style-type: none"> <li>-Wiring mistake or installation fault</li> </ul> <p><b>Internal causes</b></p> <ul style="list-style-type: none"> <li>-Corrosion of solar cells</li> <li>-Manufacturing defects</li> <li>-Delaminated, bubbles, yellowing, scratches, and burnt cells</li> <li>-Cable insulation failure</li> <li>-Incidental short circuit between normal conductor and ground</li> <li>-Ground Fault within PV Modules cable insulation damage during installation</li> <li>-Ground Fault within the PV Modules (e.g., degraded sealant and water entering)</li> <li>-Insulation damage of cables.</li> <li>-Accidental short circuit inside the PV combiner box.</li> <li>-A short break is created in a conductor</li> <li>-Two conductors of widely different voltages are placed near one another</li> <li>-Degradation in solder joints, wiring, or connections inside the insulation damage</li> <li>-due to mechanical damage, aging, or wildlife at junction box, or loosening of screws.</li> <li>-An unintentional low impedance current path between two points.</li> </ul>	<ul style="list-style-type: none"> <li>-Risk of fire</li> </ul>
<b>Ground fault</b>	PV array or PV string	<ul style="list-style-type: none"> <li>-Ground Fault within PV Modules cable insulation damage during installation</li> <li>-Ground Fault within the PV Modules (e.g., degraded sealant and water entering)</li> <li>-Insulation damage of cables.</li> <li>-Accidental short circuit inside the PV combiner box.</li> <li>-A short break is created in a conductor</li> <li>-Two conductors of widely different voltages are placed near one another</li> <li>-Degradation in solder joints, wiring, or connections inside the insulation damage</li> <li>-due to mechanical damage, aging, or wildlife at junction box, or loosening of screws.</li> <li>-An unintentional low impedance current path between two points.</li> </ul>	<ul style="list-style-type: none"> <li>-Risk of fire</li> <li>-Damage of PV String</li> <li>-Risk of fire</li> </ul>
<b>Arc fault</b>	PV string	<ul style="list-style-type: none"> <li>-Degradation in solder joints, wiring, or connections inside the insulation damage</li> <li>-due to mechanical damage, aging, or wildlife at junction box, or loosening of screws.</li> <li>-An unintentional low impedance current path between two points.</li> </ul>	<ul style="list-style-type: none"> <li>-Damage of PV String</li> <li>-Risk of fire</li> </ul>
<b>Line-to-line fault</b>	PV array	<ul style="list-style-type: none"> <li>-Insulation failure of cables</li> <li>-Incidental short circuit between conductors</li> <li>-Line-to-line fault within the DC junction box.</li> </ul>	<ul style="list-style-type: none"> <li>-Damaged PVMs and conductors.</li> <li>-Risk of fire</li> </ul>

**Table 1.3** Summary of the different type of faults [16] for PV cells, modules, arrays

### 1.2.4.3 DC-DC converters with MPPT and DC-AC inverters

Generally, static converters suffer from failure mechanisms such as wire bond fatigue, wire bond lift, solder fatigue, and loose gate control voltage, which mainly occur in power switches. Switching static converters have the following four basic forms: AC-DC converters, AC-AC converters, DC-AC converters, and DC-DC converters. Converters suffer from three common faults: open-circuit faults, gain deviation faults, and noise abnormality faults. Verma et al. [28] investigated MPPT algorithms under normal operation. When covered by shade, MPPT algorithms have been developed in order to optimize extracting the maximum power from the PV module [63–66].

The requirements for the grid-connected inverter include: a) low total harmonic distortion of the currents injected into the grid, b) maximum power point tracking, c) a high efficiency, and d) controlled power injected into the grid. The performance of the inverters connected to the grid mainly depends on the control scheme applied. [67] presents a classification of grid-connected PV inverter configurations as well as a classification of various inverter types; topologies are also discussed and described.

A survey [2] was conducted on the reliability of power electronic systems, and it found that power switches, electrolytic capacitors, and diodes are the most common components that are prone to failure.

## 1.3 Fault detection and diagnosis in PV systems

The term fault means that there is an unpermitted deviation occurring in a system. The literature distinguishes between two main strategies:

- The model-based strategy is a technique that relies on an accurate dynamic model of the system, which is able to detect unanticipated faults.
- The knowledge and training based strategy is a technique that only addresses anticipated fault conditions, for which a set of inferences can be developed.

Figure 1.22 illustrates two kinds of high-performance diagnoses .

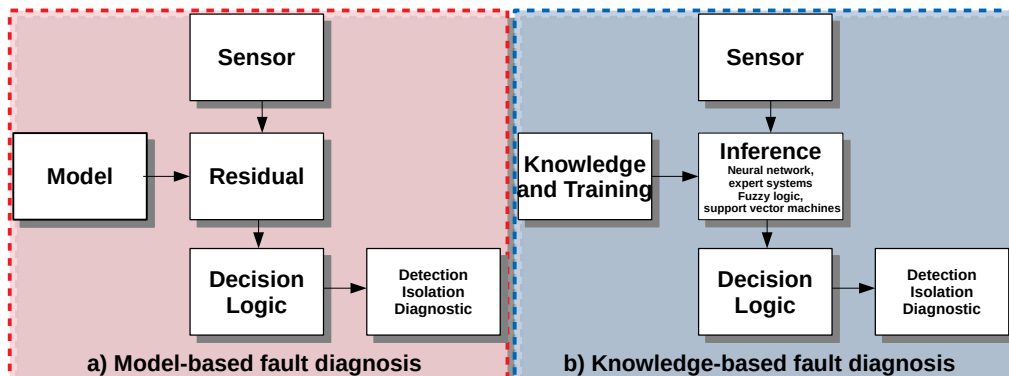


**Figure 1.22** The two types of fault detection and diagnosis for PV systems: Residue versus Inference

### 1.3.1 Model-based fault diagnosis

The feature and advantage of this method is that with a mathematical model that accurately represents the real system, we can decide whether the system works correctly or not.

Degradation and mismatching in PV systems require models that have different levels of detail and granularity [15]. Modeling tools are important to be able to estimate PV performance and to accurately characterize the electrical behavior of real PV systems. Proposed models in the literature differ in accordance with the objective, which depends on PV systems' configuration and several other aspects that the system is composed of. Sumathi et al. [68] presented some major developed models for PV systems. A good model is able to accurately predict the response of the system for a certain future time horizon. Fault Detection and Isolation (FDI) is important in many industries for a process to be operated safely. An explanation of GARRs, residue, fault signatures, detection, and fault isolation is presented in the appendix A.

In figure (1.23) it can be seen that the process and the model work in parallel. When the process variables move away from the value of the model variables, a residue is generated. After analyzing the residue, it can be determined if: a) there is a fault and b) the magnitude of the fault.

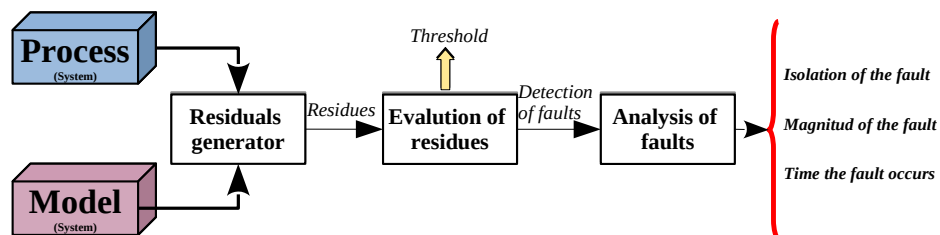


**Figure 1.23** Schematic of FDI process based on residuals analysis

Trave-Massuyes et al. [69] presented an interesting survey about the diagnosability of faults based on a model applied to continuous systems (CS) and discrete event systems (DES).

The methods to diagnose systems can be either a qualitative or quantitative analysis of analytic constraint equation system models, which generate possible candidates for fault diagnostics.

- Qualitative: derived from analytic analysis or equations that provide a level of abstraction
- Quantitative: derived from a numeric analysis of the functions and equations that provide a level of numeric analysis

#### 1.3.1.1 Detection and diagnosis of faults based on a quantitative analysis of PV arrays

This section presents various research projects that have used detection and diagnosis methods with model and threshold evaluation. Garoudja et al. [62] presented the electrical behaviour of PV array using single-diode PV cell modeling.

An exponentially weighted moving average control chart is used to detect incipient changes in a PV system. With this model, the specific differential residue is quantified and it indicates an electrical fault signature. Similar to PV cells modeling, Dhimish et al. [70] compared and analyzed the performance of multiple array configurations under partial shading and faulty PV conditions. Ali et al. [71] presented a two-diode PV cell model that endeavored to detect problems in the interconnection of PV string under shadow conditions. Hosseinzadeh et al. [6] proposed a scheme to detect shadow problems that impacted power converter performances in a PV system. This method allowed the maximum available solar power under shading conditions to be determined.

### 1.3.1.2 Detection and diagnosis of faults based on a quantitative analysis of power converters

Alavi et al. [42] presented a diagnosis algorithm applied to a DC-AC half-bridge inverter in order to isolate switch faults. The circuit is modelled using a hybrid bond graph generating residual data. An electrical fault signature matrix is used to determine the minimum number of detectors to isolate faults. A mode of detection algorithm is proposed to estimate switch states. By tracking the switch modes, and based on the fault signature, we can find out if the switch is in a failure mode.

Benyoussef et al. [44] discussed Fault Detection and Isolation (FDI) and Fault Tolerant Control (FTC) applied to three phase inverter problems for PV system application. The FDI approach is experimentally demonstrated on a nanogrid prototype with a 380V DC bus. Poon et al.'s [43] study, presents the analysis, design, and experimental validation of a model-based fault detection and identification method for switching power converters. They used a model-based state estimator approach to detect any power component switch related anomaly.

### 1.3.2 Data-driven fault diagnosis

The method based on data most commonly known as "model-free" consists in designing an algorithm that can to make connections and correlations between cause and effects based on historical data. The feature and advantage of this method is that parameters of the system under consideration may be unknown. Chen et al. [72] presented a sequential fault detection in the PV array based on a strategy called vector AutoRegressive (AR) model. This method is most common statistical method. It has only been performed by simulation when some parameters have been varied such as the irradiance sensor, the line-line, and ground faults. In Zhao et al.'s [73] study, the machine learning method is applied to detect faults based on measurements, such as PV array voltage, current, irradiance, and temperature. The existing solutions usually use supervised learning models, which are trained by numerous labeled data (known as fault types). There are various drawbacks of this method including the labeled PV data, which are difficult or expensive to obtain. Akram et al. used a health monitoring method for PV systems based on a probabilistic neural network (PNN). This method can, in real-time, detect and classify short-circuit and open-circuit problems.

### 1.3.3 Fault-tolerant control of PV systems

Fault-tolerant control is the way of describing a set of recent techniques that were developed to increase plant availability and reduce the risk of safety hazards. Its aim is to prevent simple faults developing into serious failures. Fault-tolerant control merges several disciplines to achieve this goal, including on-line fault diagnosis, automatic condition assessment, and calculating remedial actions when a fault is detected [74]. The control strategy can be separated into two types: passive (i.e., robust) or active. A classification of the strategies according to the method used is presented in Figure 1.24.

- Passive: The process consists in designing a "robust" control strategy that, despite the system's deviation, continues to function.
- Active: The process allows fault to be detected, isolated, and diagnosed, and then a new control strategy is established according to the fault.

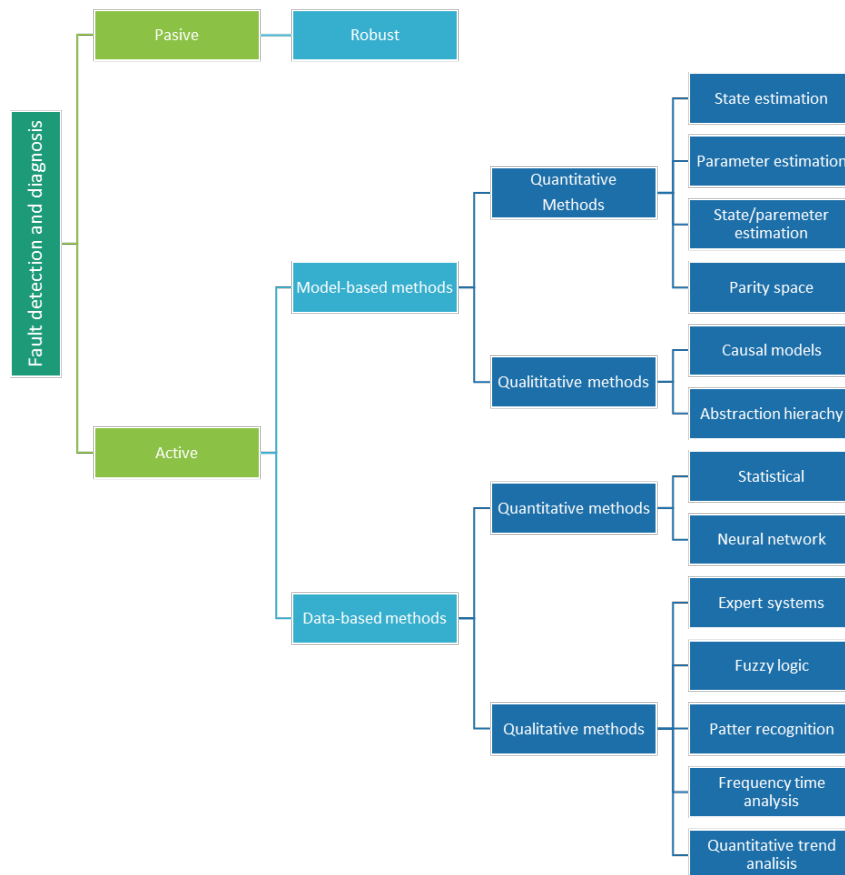


**Figure 1.24** Schematic of the main methodologies to detect and diagnose faults

The expected value and the real obtained value of the power generated by PV systems is significantly different. This difference is due to the variability of solar radiation and / or disturbances and / or faults presented in the PV system.

Three improvements could be made: firstly PV array performances, secondly the reliability of the complete PV system, and, finally, the extraction of the maximum power available from PV panels using major GMPPs. These systems are vulnerable to faults that drastically hinder the efficiency, reliability, and safety of the system [75].

A hybrid system is a dynamic system that exhibits both continuous and discrete dynamic behavior. It is a system that can both flow (described by a differential equation) and jump (described by a state machine). [76] presents a strategy to detect, isolate, and identify fault in hybrid systems using BG.

## 1.4 Detecting and diagnosing faults

Hare et al. [5] reviewed different fault modes that occurred in elements on microgrids. Figure 1.25 presents a general synthesis of faults based on time, the type and location, the dynamic, and the methods of diagnosis. These steps show the work that was undertaken in this thesis to validate the objective, fault detection, and diagnosis in PV systems. Faults can be present on one system by changing the system parameters or structural changes; and there can be faults on the actuator or sensor systems.

- The first step consists of detecting the cause of the fault, which can be considered to be structural, parametric, or just a local problem (sensor and actuator).
- The second step consists of classifying the fault depending on its criticality level. The most efficient fault diagnosis method will be chosen depending on the type of fault and its critical level.
- The third step is classification according to the dynamics of the system in which the failure is presented. Dynamics are described by discrete events or by differential equations. For this reason, we apply a strategy that allows hybrid faults to be detected.
- The fourth step will differ according to the chosen method and will be based on a model.
- The fifth step is recognizing the four stages of fault diagnosis: detection, isolation, identification, and estimation of the magnitude of failure.

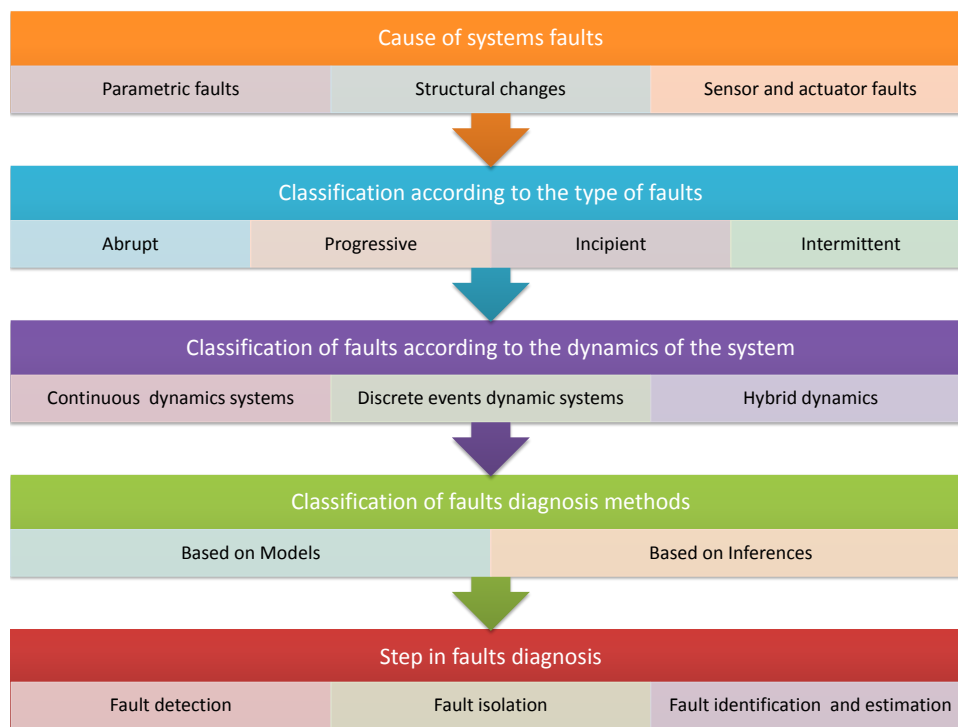


**Figure 1.25** Causes, types, and classification according to dynamics, methods, and diagnostic steps

## Contributions of this thesis

The following are the ways in which this thesis provides a contribution:

- Models the detail of photovoltaic panels, which allows specific characteristics of G, T, and shadows in a panel's particular photovoltaic cells to be analyzed.
- Models the multi-domain energy systems by using a bond graph energy exchange description structure. This is the first work to describe different sources of energy using a unified description structure.
- Analysis of shadows on photovoltaic panels and implementing image processing techniques to detect shadows and estimate the magnitude of shaded areas.
- Simulates photovoltaic systems, which allows input variables to be shared with the G, T model, and shadows to be used to find out energy production.
- Diagnosis of the faults of model-based photovoltaic systems. Diagnosis of faults of photovoltaic systems based on data and signal analysis. Faults such as shadows, hot-spots, and sensor faults diagnosed.
- Uses and applies an FPGA when diagnosing faults.

## 1.5 Conclusion

This chapter has revised the general context of photovoltaics and provides all the information needed to understand the operation of a photovoltaic system. This thesis researches the production of electricity produced by photovoltaic systems to supply energy to micro-grids that are either isolated or connected to others. Previous work that has been undertaken by LAAS or in collaboration with the Universidad de los Andes and LAAS provides a knowledge base in the field of photovoltaics - specifically on the behavior of PV systems in both real conditions and under fault conditions.

To understand the complexity of the fault detection system that is to be implemented, it is important to remember that a photovoltaic system is composed of several functions ranging from production elements (cells, panels, fields) to elements of conversion (DC/DC or DC/AC converters associated with specific algorithms called MPPT). These systems are designed to connect to a specific load. If this is to be injected into the electricity network, it will eventually be necessary to manage intermittency through the use of various types of storage. Although mentioned in this chapter, this is not the subject of this thesis.

Previous work undertaken by the LAAS as well as internationally has shown that the current adaptation stages have yields close to 100%. It could be concluded that, in this regard, the system works well, and it would be difficult to better this. However, more research is necessary if we want to use PV systems in urban areas, or if we want the converters to be more robust and have a longer life, or if we want to make the PV perform better. Also, it is important to know if the PV plant works well. If it does not, it is important to know where the loss of production is located, if these losses are temporary or permanent, and what solutions are possible once the fault is identified.

This chapter has presented the main faults that can occur both in the cells and in the converters. A review of previous work has been undertaken in the area of fault-detection as well as of the methods to make diagnoses in the photovoltaic system. This thesis is situated within this scientific context.

Chapter 2 focuses on modeling each function in the system. Thus, although there are many ways of modeling PV fields, the modeling used in this chapter builds on the work undertaken by Alonso Gutierrez Galeano. The goal is to be precise in terms of the several defects related to shading that have an impact on accelerated aging in certain cells. The modeling protocol chosen makes it possible to perform multi-physic modeling of the BondGraph type.

## Bibliography

- [1] H. Abdi, S. D. Beigvand, and M. L. Scala, “A review of optimal power flow studies applied to smart grids and microgrids,” *Renewable and Sustainable Energy Reviews*, vol. 71, pp. 742 – 766, 2017.
- [2] H. Lund, A. N. Andersen, P. A. Østergaard, B. V. Mathiesen, and D. Connolly, “From electricity smart grids to smart energy systems – a market operation based approach and understanding,” *Energy*, vol. 42, no. 1, pp. 96 – 102, 2012. 8th World Energy System Conference, WESC 2010.
- [3] S. Bacha, D. Picault, B. Burger, I. Etxeberria-Otadui, and J. Martins, “Photovoltaics in microgrids: An overview of grid integration and energy management aspects,” *IEEE Industrial Electronics Magazine*, vol. 9, no. 1, pp. 33–46, 2015.
- [4] M. F. Zia, E. Elbouchikhi, and M. Benbouzid, “Microgrids energy management systems: A critical review on methods, solutions, and prospects,” *Applied Energy*, vol. 222, pp. 1033 – 1055, 2018.
- [5] J. Hare, X. Shi, S. Gupta, and A. Bazzi, “Fault diagnostics in smart micro-grids: A survey,” *Renewable and Sustainable Energy Reviews*, vol. 60, pp. 1114 – 1124, 2016.
- [6] M. Hosseinzadeh and F. R. Salmasi, “Determination of maximum solar power under shading and converter faults—a prerequisite for failure-tolerant power management systems,” *Simulation Modelling Practice and Theory*, vol. 62, pp. 14 – 30, 2016.
- [7] K. Yeager, F. Dayo, B. Fisher, R. Fouquet, A. Gilau, H.-H. Rogner, M. Haug, R. Hosier, A. Miller, S. Schmittger, *et al.*, “Energy and economy,” *Global Energy Assessment (GEA)*, pp. 385–422, 2012.
- [8] “World energetic consumption statistics.” <https://yearbook.enerdata.net>, May 2018.
- [9] “U.s energy information administration.” [www.eia.gov](http://www.eia.gov), May 2018.
- [10] P. G. V. Sampaio and M. O. A. González, “Photovoltaic solar energy: Conceptual framework,” *Renewable and Sustainable Energy Reviews*, vol. 74, pp. 590 – 601, 2017.
- [11] N. Kannan and D. Vakeesan, “Solar energy for future world: - a review,” *Renewable and Sustainable Energy Reviews*, vol. 62, pp. 1092 – 1105, 2016.
- [12] S. Sen and V. Kumar, “Microgrid control: A comprehensive survey,” *Annual Reviews in Control*, vol. 45, pp. 118 – 151, 2018.

- [13] T. Funabashi, *Integration of distributed energy resources in power systems: implementation, operation and control*. Academic Press, 2016.
- [14] S. Lamnini and P. Kadar, "Survey on perspectives of pv technology and their applications," in *2017 IEEE 15th International Symposium on Applied Machine Intelligence and Informatics (SAMII)*, pp. 000503–000510, Jan 2017.
- [15] G. Petrone, C. A. Ramos-Paja, and G. Spagnuolo, *Index*, pp. 185–186. John Wiley & Sons, Ltd, 2017.
- [16] A. Mellit, G. Tina, and S. Kalogirou, "Fault detection and diagnosis methods for photovoltaic systems: A review," *Renewable and Sustainable Energy Reviews*, vol. 91, pp. 1 – 17, 2018.
- [17] M. Bressan, *Development of a tool for supervision and control for a solar photovoltaic system*. Theses, Université de Perpignan, June 2014.
- [18] Y. El Basri, *Reconfigurable distributed power architecture for the optimisation of photovoltaic energy*. Theses, Universite Paul Sabatier - Toulouse III, June 2013.
- [19] A. G. Galeano, *Study of Photovoltaic System Integration in Microgrids through Real-Time Modeling and Emulation of its Components Using HiLeS*. Theses, Université de Toulouse 3 Paul Sabatier, Sept. 2017.
- [20] J. Dulout, *Optimal sizing and energy management of storage systems for renewable sources deployment, design of a LVDC microgrid*. Theses, Université Toulouse 3 Paul Sabatier (UT3 Paul Sabatier), Dec. 2017.
- [21] K. Neuhaus, *Design of an LVDC microgrid based on renewable sources and multiple electrochemical storage elements*. PhD thesis, UNIVERSITE DE TOULOUSE, 2018.
- [22] S. Qazi, *Standalone Photovoltaic (PV) Systems for Disaster Relief and Remote Areas*. Elsevier, 2016.
- [23] "Molecular expressions." <http://micro.magnet.fsu.edu/>, May 2018.
- [24] <https://www.fondriest.com/>, May 2018.
- [25] A. Goetzberger, J. Luther, and G. Willeke, "Solar cells: past, present, future," *Solar Energy Materials and Solar Cells*, vol. 74, no. 1, pp. 1 – 11, 2002. PVSEC 12 Part I.
- [26] X. Zhou, J. Jankowska, H. Dong, and O. V. Prezhdo, "Recent theoretical progress in the development of perovskite photovoltaic materials," *Journal of Energy Chemistry*, vol. 27, no. 3, pp. 637 – 649, 2018.
- [27] N. AL-Rousan, N. A. M. Isa, and M. K. M. Desa, "Advances in solar photovoltaic tracking systems: A review," *Renewable and Sustainable Energy Reviews*, vol. 82, pp. 2548 – 2569, 2018.
- [28] D. Verma, S. Nema, A. Shandilya, and S. K. Dash, "Maximum power point tracking (mppt) techniques: Recapitulation in solar photovoltaic systems," *Renewable and Sustainable Energy Reviews*, vol. 54, pp. 1018 – 1034, 2016.

- [29] J. D. Bastidas-Rodriguez, E. Franco, G. Petrone, C. A. Ramos-Paja, and G. Spagnuolo, "Maximum power point tracking architectures for photovoltaic systems in mismatching conditions: a review," *IET Power Electronics*, vol. 7, pp. 1396–1413, June 2014.
- [30] D. G and S. Singh, "Selection of non-isolated dc-dc converters for solar photovoltaic system," *Renewable and Sustainable Energy Reviews*, vol. 76, pp. 1230 – 1247, 2017.
- [31] Trace engineering, 5916 195th St.NE Arlington, WA, *A review of inverter design and topologies*.
- [32] Ankit, S. K. Sahoo, S. Sukchai, and F. F. Yanine, "Review and comparative study of single-stage inverters for a pv system," *Renewable and Sustainable Energy Reviews*, vol. 91, pp. 962 – 986, 2018.
- [33] D. W. Gao, *Energy storage for sustainable microgrid*. Academic Press, 2015.
- [34] Y. Yoldaş, A. Önen, S. Muyeen, A. V. Vasilakos, and İrfan Alan, "Enhancing smart grid with microgrids: Challenges and opportunities," *Renewable and Sustainable Energy Reviews*, vol. 72, pp. 205 – 214, 2017.
- [35] O. P. Mahela and A. G. Shaik, "Comprehensive overview of grid interfaced solar photovoltaic systems," *Renewable and Sustainable Energy Reviews*, vol. 68, pp. 316 – 332, 2017.
- [36] P. Hacke, S. Lokanath, P. Williams, A. Vasan, P. Sochor, G. TamizhMani, H. Shinohara, and S. Kurtz, "A status review of photovoltaic power conversion equipment reliability, safety, and quality assurance protocols," *Renewable and Sustainable Energy Reviews*, vol. 82, pp. 1097 – 1112, 2018.
- [37] J. Solorzano and M. Egido, "Automatic fault diagnosis in pv systems with distributed mppt," *Energy Conversion and Management*, vol. 76, pp. 925 – 934, 2013.
- [38] S. Spataru, A. Amoiridis, R. N. Beres, C. I. Ciontea, T. Klein, and D. Sera, "Development of an intelligent maximum power point tracker using an advanced pv system test platform," in *2013 IEEE 39th Photovoltaic Specialists Conference (PVSC)*, pp. 2953–2958, June 2013.
- [39] A. Dong, Y. Zhao, X. Liu, L. Shang, Q. Liu, and D. Kang, "Fault diagnosis and classification in photovoltaic systems using scada data," in *2017 International Conference on Sensing, Diagnostics, Prognostics, and Control (SDPC)*, pp. 117–122, Aug 2017.
- [40] R. Platon, J. Martel, N. Woodruff, and T. Y. Chau, "Online fault detection in pv systems," *IEEE Transactions on Sustainable Energy*, vol. 6, pp. 1200–1207, Oct 2015.
- [41] C. Ventura and G. M. Tina, "Utility scale photovoltaic plant indices and models for on-line monitoring and fault detection purposes," *Electric Power Systems Research*, vol. 136, pp. 43 – 56, 2016.
- [42] M. Alavi, M. Luo, D. Wang, and D. Zhang, "Fault diagnosis for power electronic inverters: A model-based approach," in *8th IEEE Symposium on*

- Diagnostics for Electrical Machines, Power Electronics Drives*, pp. 221–228, Sept 2011.
- [43] J. Poon, P. Jain, I. C. Konstantakopoulos, C. Spanos, S. K. Panda, and S. R. Sanders, “Model-based fault detection and identification for switching power converters,” *IEEE Transactions on Power Electronics*, vol. 32, pp. 1419–1430, Feb 2017.
- [44] F. B. Youssef and L. Sbita, “Sensors fault diagnosis and fault tolerant control for grid connected pv system,” *International Journal of Hydrogen Energy*, vol. 42, no. 13, pp. 8962 – 8971, 2017. Hydrogen Fuel Cell & Renewable Energy Techniques: The 8th International Conference on Renewable Energy (CIER-2015), 21-23 December 2015, Sousse, Tunisia.
- [45] V. Guiheneuf, F. Delaleux, O. Riou, P.-O. Logerais, and J. F. Durastanti, “Investigation of damp heat aging on soda-lime glass for photovoltaic applications,” 06 2016.
- [46] “Dupont.” <http://www.dupont.co.in/>, May 2018.
- [47] M. Abderrezek and M. Fathi, “Experimental study of the dust effect on photovoltaic panels’ energy yield,” *Solar Energy*, vol. 142, pp. 308 – 320, 2017.
- [48] J. Bishop, “Computer simulation of the effects of electrical mismatches in photovoltaic cell interconnection circuits,” *Solar Cells*, vol. 25, no. 1, pp. 73 – 89, 1988.
- [49] C. Olalla, M. N. Hasan, C. Deline, and D. Maksimović, “Mitigation of hot-spots in photovoltaic systems using distributed power electronics,” *Energies*, 2018.
- [50] S. Daliento, F. D. Napoli, P. Guerriero, and V. d’Alessandro, “A modified bypass circuit for improved hot spot reliability of solar panels subject to partial shading,” *Solar Energy*, vol. 134, pp. 211 – 218, 2016.
- [51] J. C. Arnett and C. C. Gonzalez, “Photovoltaic module hot spot durability design and test methods,” in *15th Photovoltaic Specialists Conference*, pp. 1099–1105, 1981.
- [52] M. Dhimish, V. Holmes, B. Mehrdadi, M. Dales, and P. Mather, “Pv output power enhancement using two mitigation techniques for hot spots and partially shaded solar cells,” *Electric Power Systems Research*, vol. 158, pp. 15 – 25, 2018.
- [53] K. A. Kim, “Hot Spot Detection and Protection Methods for Photovoltaic Systems,” p. 135, 2014.
- [54] G. Petrone, C. A. Ramos-Paja, and G. Spagnuolo, *Photovoltaic Sources Modeling*. 2017.
- [55] B. Ottersböck, G. Oreski, and G. Pinter, “Comparison of different microclimate effects on the aging behavior of encapsulation materials used in photovoltaic modules,” *Polymer Degradation and Stability*, vol. 138, pp. 182 – 191, 2017.

- [56] M. Bressan, Y. E. Basri, A. Galeano, and C. Alonso, "A shadow fault detection method based on the standard error analysis of i-v curves," *Renewable Energy*, vol. 99, pp. 1181 – 1190, 2016.
- [57] M. G. Villalva, J. R. Gazoli, and E. R. Filho, "Comprehensive approach to modeling and simulation of photovoltaic arrays," *IEEE Transactions on Power Electronics*, vol. 24, pp. 1198–1208, May 2009.
- [58] B. P. Kumar, G. S. Ilango, M. J. B. Reddy, and N. Chilakapati, "Online fault detection and diagnosis in photovoltaic systems using wavelet packets," *IEEE Journal of Photovoltaics*, vol. 8, pp. 257–265, Jan 2018.
- [59] K. A. Kim, G. S. Seo, B. H. Cho, and P. T. Krein, "Photovoltaic hot-spot detection for solar panel substrings using ac parameter characterization," *IEEE Transactions on Power Electronics*, vol. 31, pp. 1121–1130, Feb 2016.
- [60] J. D. Bastidas-Rodriguez, G. Petrone, C. A. Ramos-Paja, and G. Spagnuolo, "Photovoltaic modules diagnostic: An overview," in *IECON 2013 - 39th Annual Conference of the IEEE Industrial Electronics Society*, pp. 96–101, Nov 2013.
- [61] M. Dhimish, V. Holmes, B. Mehrdadi, and M. Dales, "Simultaneous fault detection algorithm for grid-connected photovoltaic plants," *IET Renewable Power Generation*, vol. 11, no. 12, pp. 1565–1575, 2017.
- [62] E. Garoudja, F. Harrou, Y. Sun, K. Kara, A. Chouder, and S. Silvestre, "Statistical fault detection in photovoltaic systems," *Solar Energy*, vol. 150, pp. 485 – 499, 2017.
- [63] A. Mohapatra, B. Nayak, P. Das, and K. B. Mohanty, "A review on mppt techniques of pv system under partial shading condition," *Renewable and Sustainable Energy Reviews*, vol. 80, pp. 854 – 867, 2017.
- [64] H. M. El-Helw, A. Magdy, and M. I. Marei, "A hybrid maximum power point tracking technique for partially shaded photovoltaic arrays," *IEEE Access*, vol. 5, pp. 11900–11908, 2017.
- [65] K. Chen, S. Tian, Y. Cheng, and L. Bai, "An improved mppt controller for photovoltaic system under partial shading condition," *IEEE Transactions on Sustainable Energy*, vol. 5, pp. 978–985, July 2014.
- [66] S. K. Das, D. Verma, S. Nema, and R. Nema, "Shading mitigation techniques: State-of-the-art in photovoltaic applications," *Renewable and Sustainable Energy Reviews*, vol. 78, pp. 369 – 390, 2017.
- [67] K. Zeb, W. Uddin, M. Khan, Z. Ali, M. U. Ali, N. Christofides, and H. Kim, "A comprehensive review on inverter topologies and control strategies for grid connected photovoltaic system," *Renewable and Sustainable Energy Reviews*, vol. 94, pp. 1120 – 1141, 2018.
- [68] S. Sumathi, L. A. Kumar, and P. Surekha, *Solar PV and Wind Energy Conversion Systems: An Introduction to Theory, Modeling with MATLAB/SIMULINK, and the Role of Soft Computing Techniques*. Springer, 2015.

- [69] L. Trave-Massuyès, M.-O. Cordier, and X. Pucel, “Comparing diagnosability in cs and des,” *IFAC Proceedings Volumes*, vol. 39, no. 13, pp. 1163 – 1168, 2006. 6th IFAC Symposium on Fault Detection, Supervision and Safety of Technical Processes.
- [70] M. Dhimish, V. Holmes, B. Mehrdadi, M. Dales, B. Chong, and L. Zhang, “Seven indicators variations for multiple pv array configurations under partial shading and faulty pv conditions,” *Renewable Energy*, vol. 113, pp. 438 – 460, 2017.
- [71] M. H. Ali, A. Rabhi, A. E. Hajjaji, and G. M. Tina, “Real time fault detection in photovoltaic systems,” *Energy Procedia*, vol. 111, pp. 914 – 923, 2017. 8th International Conference on Sustainability in Energy and Buildings, SEB-16, 11-13 September 2016, Turin, Italy.
- [72] L. Chen, S. Li, and X. Wang, “Quickest fault detection in photovoltaic systems,” *IEEE Transactions on Smart Grid*, vol. 9, pp. 1835–1847, May 2018.
- [73] Y. Zhao, R. Ball, J. Mosesian, J. F. de Palma, and B. Lehman, “Graph-based semi-supervised learning for fault detection and classification in solar photovoltaic arrays,” *IEEE Transactions on Power Electronics*, vol. 30, pp. 2848–2858, May 2015.
- [74] M. Blanke, W. C. Frei, F. Kraus, J. R. Patton, and M. Staroswiecki, “What is fault-tolerant control?,” *IFAC Proceedings Volumes*, vol. 33, no. 11, pp. 41 – 52, 2000. 4th IFAC Symposium on Fault Detection, Supervision and Safety for Technical Processes 2000 (SAFEPROCESS 2000), Budapest, Hungary, 14-16 June 2000.
- [75] D. S. Pillai and N. Rajasekar, “A comprehensive review on protection challenges and fault diagnosis in pv systems,” *Renewable and Sustainable Energy Reviews*, vol. 91, pp. 18 – 40, 2018.
- [76] W. Borutzky, *Bond graph model-based fault diagnosis of hybrid systems*. Springer, 2015.

# 2

## PV system modeling for fault diagnosis

### Introduction

This chapter presents a modeling strategy for photovoltaic systems that have PV arrays, MPPT, a dedicated converter, and an inverter that is connected to the grid. It shows several strategies to model photovoltaic systems. These models can be considered to be white, gray, or black boxes depending on the available input information, the system, and the information that the user needs. The PV plant model can be treated as a box that has several inputs (irradiation, temperature, and wind speed, for example) and one output power. There are two major types of modeling to represent this box and to estimate the power output [1]:

- Parametric modeling conceives the PV system as a white box where each subsystem, or component, can be modeled using a collection of parameters and physical equations. Some of these equations are used to model the performance of components and others are used to obtain the operation conditions of the PV generator. The parametric approach is a multi-step model that requires detailed characterization of the performance of the PV plant's significant components. It is necessary to understand the correlation model that fits correctly to the site to be able to obtain the PV generator's operation conditions .
- Non-parametric modeling conceives the PV system to be a black box and presumes no knowledge of the PV system's internal characteristics and processes. It estimates the PV system's behavior using a historical time series of inputs and outputs. The accuracy of a non parametric model depends mainly on the quality of these data. However, this characteristic is also its main disadvantage: the PV plant must have been operational for some time so that relevant input/output information is available.

This chapter uses a white box description and parametric modeling. The conver-

sion of PV energy is a physical process. The model describes the hybrid behavior of the PV system (i.e continuous and discrete states). Each element that composes the conventional PV system is modeled, which allows the emulation of the complete system's electrical behavior, particularly in failure conditions. We modelled a high-granularity level of the PV system to reproduce the influence of a small fault such as shadow effects or other mismatch effects on electrical generation. This precise model helps us to understand and to diagnose a large number of internal and external faults (and/or disturbances) that may occur in the PV system. The model is oriented towards fault detection. Hybrid Bond-Graph Graphical (HBG) representation was used to address the issue in this thesis.

## Modeling PV systems using Hybrid Bond-Graph (HBG) representation

This section presents the PV system model that endeavors to diagnose the fault using HBG. Figure 2.1 represents each electrical component of a conventional PV system connected to the grid. It is composed of a PV array, a DC-DC converter, and a DC-AC inverter. Each converter obtains a specific control system, which allows it to have a good electrical conversion process from a PV array until it reaches the grid connection. The electrical generation depends strongly on parameters such as irradiation, the temperature, and shadow.

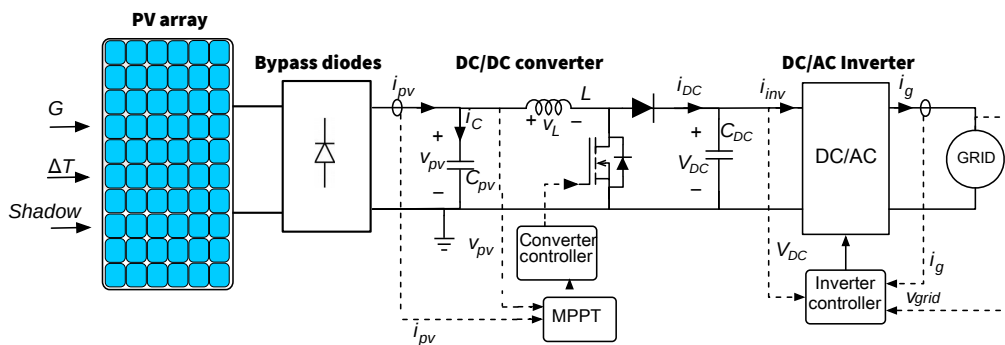


Figure 2.1 Simplified structure of a conventional PV system (Adapted from [2])

Figure 2.2 shows an HBG representation of the complete PV system that this thesis developed. Four blocks were identified to be able to model PV systems depending on input parameters. The first block involves modeling the PV array, which can be affected during any changes in meteorological conditions. The second block is the model of a specific control used to extract the Maximum Power Point (MPP) of the PV array. This control is integrated into the DC-DC converter, which represents the third model's block. Finally, the fourth block represents the model of the single-phase DC-AC inverter that is connected to the grid.

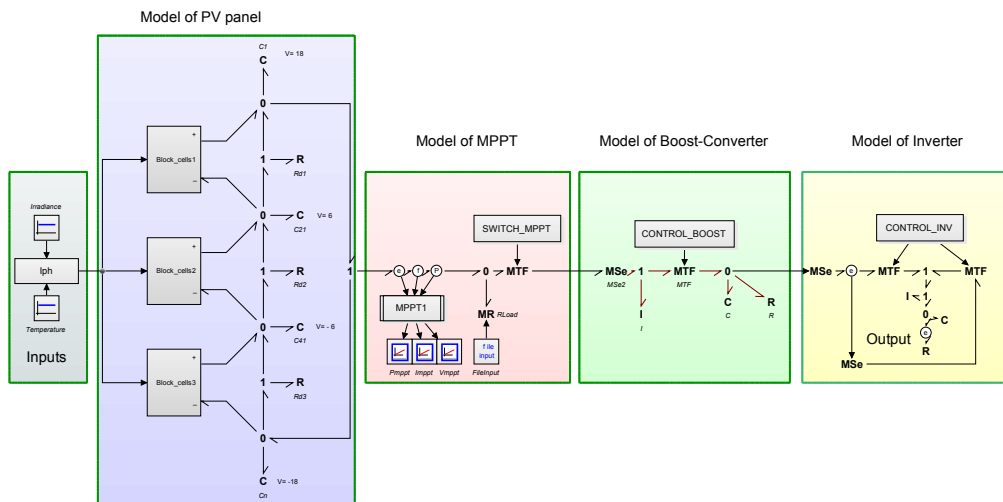


Figure 2.2 Modeling of complete PV system using HBG

## 2.1 Modeling PV array

In recent years, there has been much literature devoted to modelling PV sources. The three main purposes of this are:

- The model is used to reproduce the current-voltage characteristic (I-V curve) at the generator terminals through a suitable electrical model. The model could be a simple PV cell representation, sub-portions of it, or even a large PV field made of series-connected modules forming strings that are in turn connected in parallel. The following are tools used to obtain an I-V curve: Matlab, PSPICE, PSIM, SCILAB [3]
- The model is used for energetic analyses of plant productivity, and models are based on empirical or semi-empirical equations for long-term analysis (over days or months). Tools such as PVSYST and SOLARGIS can be used to estimate PV production. [4]
- The model also endeavors to detect fault. The high- granularity of the PV array model allows its electrical behaviour to be seen when it is shady and when there are other mismatch effects. This allows the fault behavior of each cell to be defined independently, which is the objective of this thesis.

This section introduces the different parts of the development process of the PV model using HBG and is shown in Figure 2.3 .

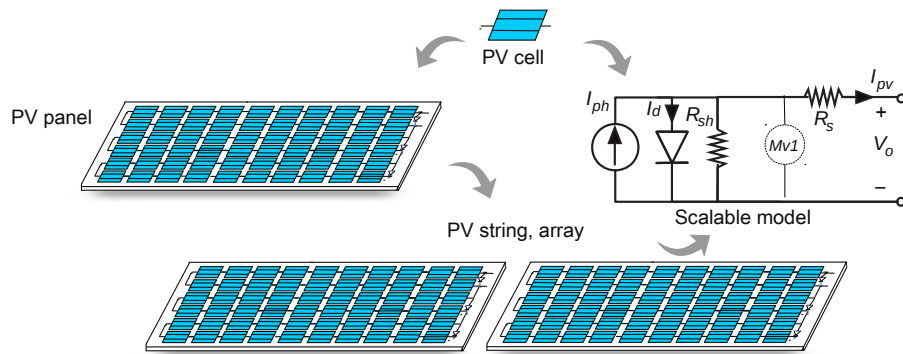


**Figure 2.3** Granularity of PV cell, string, and array (Adapted from [2])

### 2.1.1 Modeling the PV cell

The capability of a PV model to accurately reproduce the I-V curve of a PV source does not depend exclusively on model complexity; it also depends on the model's parameter values, which are adapted to reproduce the behavior of different PV cells, panels, and arrays.

The single-diode model is the one that is most widely used because of the small number of circuit parameters that need to be identified. Figure 2.4 represents the classic electrical structure of a PV cell.

Photo-current generated by a solar cell depends on the technological characteristic of the cell and environmental conditions: a) the technological factors depend

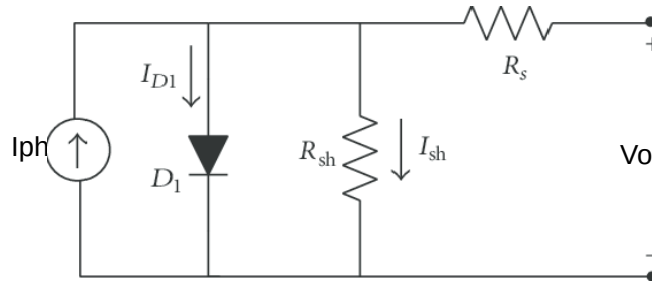


**Figure 2.4** Single diode model of solar cell

on the absorption spectrum and the spectral responsivity of the PV material used and the construction of the cell, b) the environmental factors are associated with solar irradiation, ambient, and panel temperature. The general output current from PV cell is

$$I = I_{ph} - I_o \left[ e^{\frac{V_c + IR_s}{V_t}} - 1 \right] - \frac{V_c + IR_s}{R_{sh}} \quad (2.1)$$

The photo-current  $I_{ph}$  is the electric current that runs through a cell in function of the irradiation that the PV cell receives as well as its temperature; this is shown in Eq.(2.2).

$$I_{ph}(t) = I_{ph_{STC}} \frac{G(t)}{G_{STC}} [1 + \alpha_I (T_c(t) - T_{c_{STC}})] \quad (2.2)$$

where  $I_{ph_{STC}}$  is the photo-current in the short-circuit at the standard test condition (STC),  $G(t)$  is the global radiation that receives the PV array,  $G_{STC}$  is the irradiance at STC ( $1000W/m^2$ ),  $\alpha_I$  is the attenuation coefficient of the current due to the temperature given by the PV module manufacturer ( $\%/^{\circ}C$ ),  $T_c$  is the temperature of the PV cell ( $^{\circ}C$ ), and  $T_{c_{STC}}$  is the temperature on STC ( $25^{\circ}C$ ).

Generally, the ambient temperature is different from the temperature on the surface of the photovoltaic cell. For this reason, in the literature, different equations were used to model the effects of the temperature change in the output current cell. [5] summarized the main temperature models in the literature. There are two kinds of temperature models:

- The implicit model, which is based on knowledge of the thermal properties of the module and their heat transfer mechanism. It considers an energy balance in the cell.
- The explicit model based on the calculation of the operating temperature of the cell using known parameters, as shown in Eq.(2.2).

The double-diode model has more accurate physical phenomena, especially at low irradiance levels, but it requires a more thorough identification of the parameter values (Figure 2.5). The usefulness of the double-diode-based modeling of crystalline cells is that it has an improved accuracy at both high and low irradiance levels.

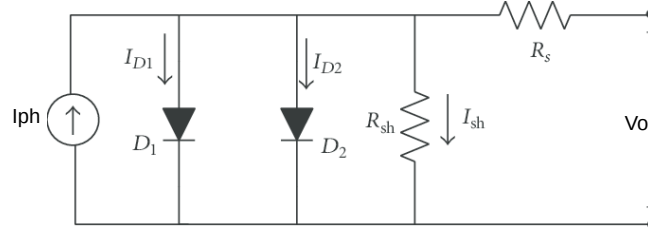


**Figure 2.5** Double diode model of solar cell

Most of the models in the literature do not take into account the effect of the reverse bias [6, 7]. A precise model was proposed by Bishop [8], as shown in Figure 2.6, which incorporates the avalanche effect as a non-linear multiplier factor that affects the shunt resistance current term, as shown in Eq(2.3):

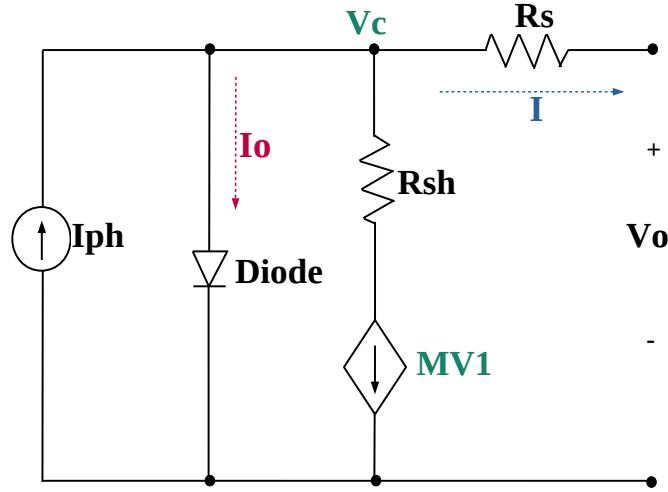


**Figure 2.6** Electrical schematic of the cell, including the reverse bias

$$I = I_{ph} - I_o \left[ e^{\frac{V_c + I \cdot R_s}{V_t}} - 1 \right] - \frac{V_c + I \cdot R_s}{R_{sh}} \left[ 1 + k \left( 1 - \frac{V_c + I \cdot R_s}{V_{br}} \right)^{-n} \right] \quad (2.3)$$

$I_{ph}$  is the generated photo-current (A),  $I_o$  is the reverse saturation current (A),  $R_s$  is the series resistance ( $\Omega$ ),  $R_{sh}$  is the shunt resistances ( $\Omega$ ),  $V_{br}$  is the breakdown voltage (V), and  $k$  and  $n$  are constants. In reverse bias conditions, free electrons inside the p-n material are able to gain enough energy to collide with other atoms and to separate electrons [9]. After of each collision, the new free electron can cause other collisions, which could lead to an avalanche breakdown voltage condition.

Figure 2.7 shows the Hybrid Bondgraph Graphical (HBG) model of a PV cell. It uses nine basic elements or building blocks that represent physical subsystems, components, or phenomena in every energy domain. The elements are classified into three categories: the passive elements, the active elements, and the elements at the junction. In addition to the detectors, these elements represent phenomenon that connect the generalized variables.

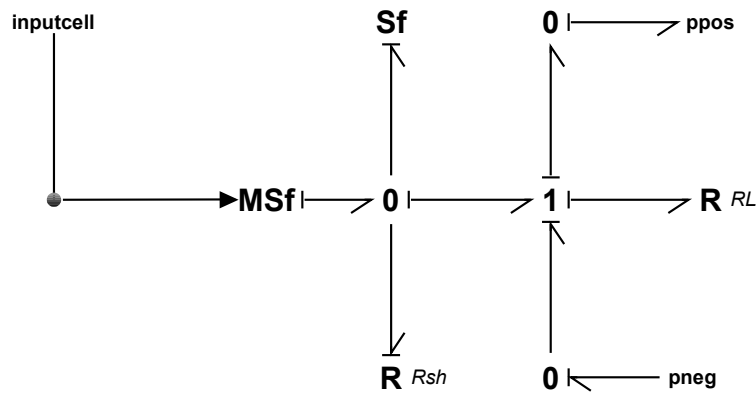


Figure 2.7 PV cell HBG model

where the source  $M_{Sf}$  is the new photo-current  $I_{ph}$  taking into account the attenuation factor  $\delta$ ,  $R_{sh}$  and  $R_s$  are parallel and series resistance, and  $S_f$  is the physical behavior of the P-N junction of the diode. 0 is the parallel junction, and 1 is the serial junction. A brief description of the bond graph models can be seen in the appendix. General research into the estimation of PV module parameters is still being carried out. For example, the parameters of the model used to obtain an I-V curve has been characterized in different studies and is shown in Table 2.1. These parameters can be found thanks to fitting experimental curves [10] and are presented as follows:  $I_{ph}=8.6(A)$ ,  $I_s=1.55e-5(A)$ ,  $a=1e-3(V)$ ,  $R_s=9(m\Omega)$ ,  $R_{sh}=9(\Omega)$ ,  $V_{br}=-15(V)$ ,  $m=3$ .

Parameter model of the PV cell									
Publication	$R_s(\Omega)$	$R_{sh}(\Omega)$	$I_o(A)$	$k$	$m$	$V_{br}(v)$	a	$V_{oc}(v)$	Icc (A)
[11]	0.027	512	-	-	3	-17,69	0.268	0.62	8.6
[12]	0.009	9	0.0000155	0.001	3	-15	1.486	-	8.6
[13]	0.005	35	-	0.001	3.4	-30	-	-	8.6

Table 2.1 Cell parameters of the PV cell used in the literature

The complete I-V curve is obtained thanks to the positive and negative variations of the  $R_L$  resistance that respond to the  $I=[0, \infty]$  and  $V=[V_{OC}, V_{br}]$  conditions. Figure 2.8 represents the variation process of  $R_L$  to construct the complete I-V curve.

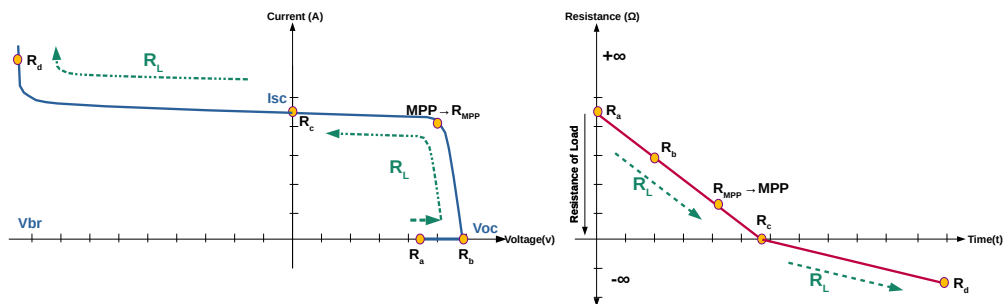


Figure 2.8 Complete I-V curve (a) and variation of the load resistance  $RL$  (pos-neg) (b)

The variation of the output resistance  $RL(\Omega)$  allows the I-V curves to be ob-

tained:

1. The current and voltage are positive in the first quadrant (X and Y axes) and induce a positive resistance.
  - $Ra(\Omega)$  represents infinite resistance.
  - $Rb(\Omega)$  is the resistance for a maximum value of voltage  $Voc(V)$  and a minimum value of current  $I(A)$ .
  - $R_{MPP}(\Omega)$  is the resistance at maximum power point.
  - $Rc(\Omega)$  is the resistance value for a maximum value of current  $I(A)$  and a minimum value of voltage  $Voc(v)$ .
2. The voltage is negative and the current is positive in the second quadrant (X and Y axes), which induces a negative resistance.
  - $Rd(\Omega)$  is the resistance of the avalanche effect.

Figure 2.9 shows the complete I-V curves of the PV cells in which the irradiation and the resistance value vary from infinity to zero between points  $p_{pos}$  and  $p_{neg}$ . Cosimulation was used to simulate different scenarios relating to irradiation, temperature, and shade as well as to obtain the I-V curve. The explication of the Cosimulation process is contained in Appendix(B).

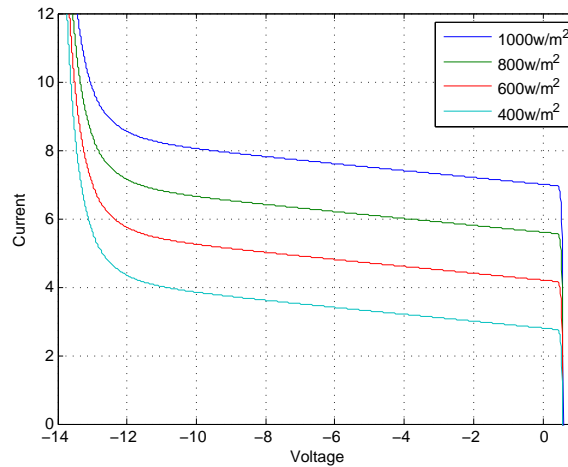


**Figure 2.9** I-V curves of the PV cell under different irradiation conditions

### 2.1.2 Modeling the PV module

Extrapolating the characteristics of a simple photovoltaic cell to a parallel series arrangement of cells is explained below. An approximate model for module level to be obtained allows us to find out the electrical relationship for each cell that is operating in homogeneous conditions. The assumption is that all the cells are equal and subject to the same environmental conditions. They can be scaled up or down by accounting for the number of the cells/panels that are connected in series to form a string and taking into consideration the number of strings connected in parallel. This is done by modeling a cell as a simple diode and

/ or double diode. In these conditions, the voltages are multiplied by  $N_s$  = number of the series-connected cells, and all the currents are multiplied by  $N_p$  = number of parallel-connected strings. Consequently, the series resistance  $R_s$  and the parallel resistance  $R_{sh}$  increase by a factor  $N_s$  and are divided by a factor  $N_p$  [2].

$$\begin{aligned}
 I_{ph} &= N_p \times I_{ph,cell} \\
 I_s &= N_p \times I_{s,cell} \\
 \eta &= \eta_{cell} \\
 V_t &= N_s \times V_{t,cell} \\
 R_s &= \frac{N_s}{N_p} \times R_{s,cell} \\
 R_{sh} &= \frac{N_s}{N_p} \times R_{h,cell}
 \end{aligned} \tag{2.4}$$

Eq. (2.4) does not provide a good approximation to obtain a detailed model that detects failures. The following two possibilities for models can be used to represent the PV module's electrical behavior:

1. The first is the fit of the I-V curves thanks to the manufactures' electrical specifications and the practical data from each module.
2. The second is the series / parallel interconnection of the cell model developed in the subsection 2.1.1, which forms modules, arrays, or strings.

### 2.1.2.1 Model based on the electrical characteristics of a PV module

PV Panel manufacturers provide information about the electrical behavior of the module under standard conditions. Table 2.2 resumes the main electrical characteristics of two types of panel (*Tenesol 2200*).

Figure 2.10 (a) and Figure 2.10 (b) illustrate respectively, I-V curves and P-V curves that were provided by the solar panel manufacturer for both modules.

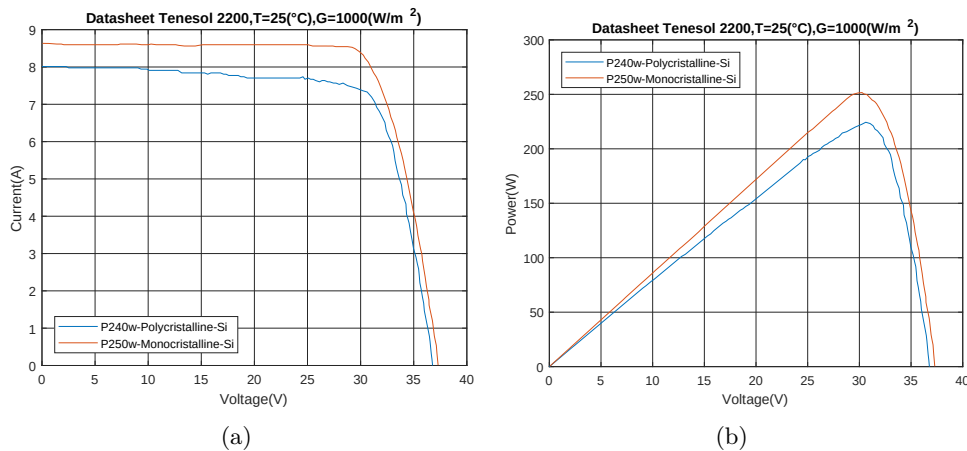


**Figure 2.10** The I-V Curves of the two kinds of PV modules (Tenesol 2200: 240W and 250W) (a) and P-V curves (b)

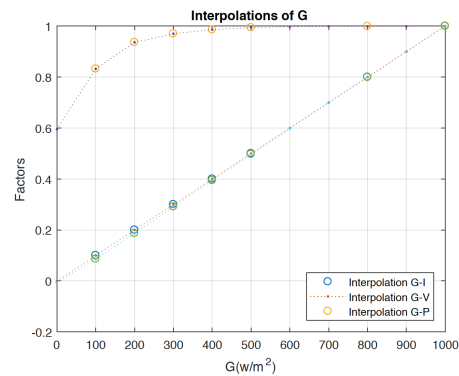
Electrical Characteristics		Tenesol TE2200	
Typical power (STC)	Wc	240	250
Minimum power		235	245
Maximum power		245	255
Power class limit	Wc	-5/5	
Power class limit	%	+2,1	+2
Voltage (MPPT)	(V)	30,1	30,3
Current (MPPT)	(A)	8,0	8,3
Voltage Voc	(V)	37,0	37,3
Current Isc	(A)	8,3	8,6
<b>Influence of temperature</b>			
Temperature coefficient voltage (V)		-129,0 mV/°C	
Temperature coefficient current (A)		+4,4 mA/°C	
Temperature coefficient Power (W)		-0,46%/°C	
NOCT		45°C	
<b>Cellules</b>			
Size		156x156 mm	
Disposition		60 cells / 6x 10	
Type		Monocrystalline	Polycrystalline

**Table 2.2** Electrical characteristics of PV module *Tenesol 2200*

Each point  $(x, y)$  of the graph was extracted using a computational tool that provided great detail about the value of current versus voltage for each panel. The table below shows the values of power  $P$ , current  $I$ , and voltage  $V$  for various radiation values (Figure 2.11).

Dependence on solar irradiation			
$G$ ( $W/m^2$ )	$P_{pm}$	$V_{pm}$	$I_{pm}$
1000	1	1	1
800	0,799	0,999	0,8
500	0,497	0,994	0,5
400	0,394	0,986	0,4
300	0,291	0,97	0,3
200	0,187	0,936	0,2
100	0,086	0,862	0,1

(a)



(b)

**Figure 2.11** Dependence values for solar radiation (a) and interpolation of irradiation  $G$  in function of the voltage, current, and power of the PV module

This allows us to build three functions: a) solar irradiation versus power, b) solar irradiation versus current, and c) solar irradiation versus voltage, which provides information about the power, the current and the voltage. Figure 2.12(a) and Figure 2.12(b) represent I-V curves and P-V curves, respectively, with different solar radiation conditions.

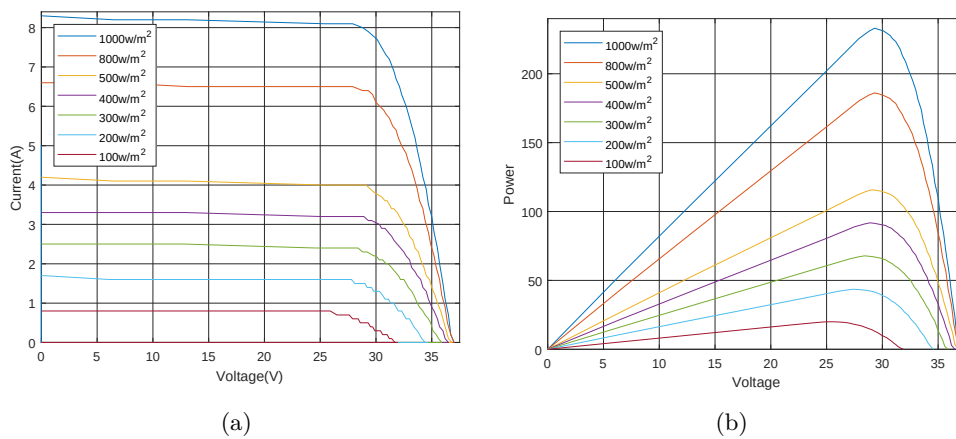


**Figure 2.12** Extrapolation of I-V curves (a) and PV curves (b)

Obviously, I-V curves supplied by the manufacturer do not characterize the individual operation of each cell inside a larger structure such as a PV module, as shown in Figure 2.10. Moreover, they do not allow the system's real behavior to be characterized in dusty conditions, when there is shade, when there are non-uniform temperatures, as well as when there are other operation problems in the PV system. For this reason, a highly-detailed model was developed and used to diagnose system failures.

2.1.2.2 Model based on the cell's series/parallel interconnection

Figure 2.13 represents a HBG model of the PV module *Tenesol 2200*. The input parameters are the panel temperature and the global irradiation receptor. The three blocks represent twenty cells in series connected to a one bypass diode. The panel has three bypass diodes.

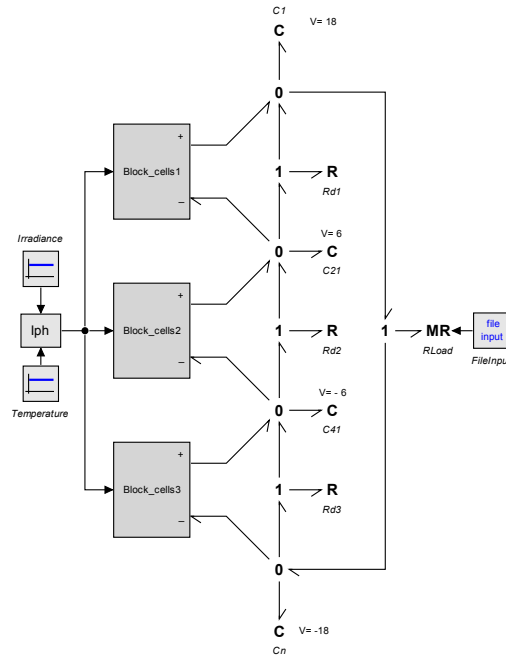


Figure 2.13 HBG model of PV module *Tenesol 2200*

where  $R$  corresponds to the bypass diode,  $C$  is the parasitic capacitance,  $MR$  is the variable resistance ( $R_L$ ) that allows the I-V characteristics varying the resistance value  $R_L$  between  $[0, \infty)$  to be obtained, as shown in Figure 2.14. The variation of  $R_L$  is represented by a green arrow that allows the voltage and current points of the curve to be obtained.

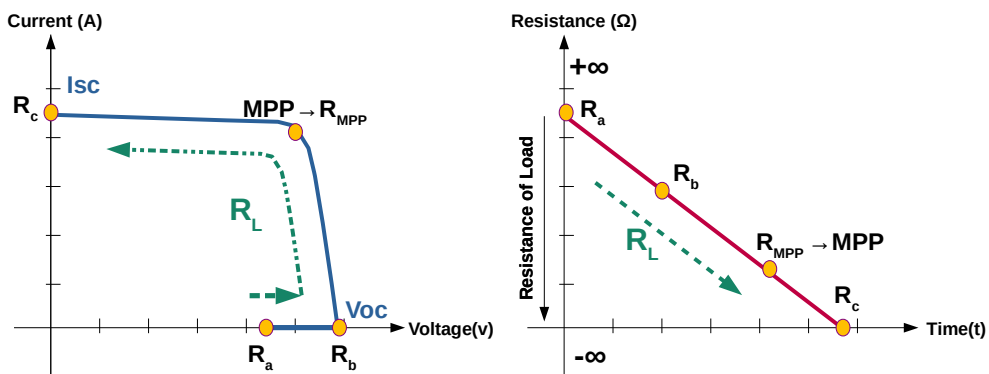


Figure 2.14 I-V curve of the PV module (a) and variation of the load resistance  $RL$  (b)

Figure 2.15 illustrates I-V curves of the HBG model under different homogeneous irradiation during normal operation.

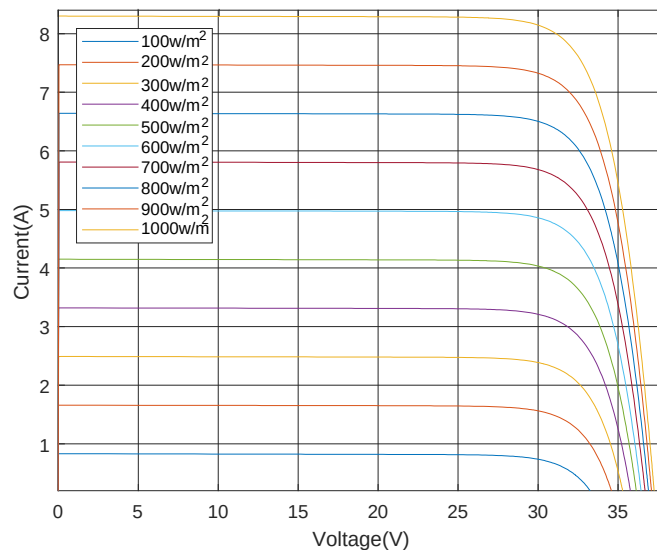


Figure 2.15 I-V curves under various irradiation conditions

Figure 2.16 explains the model so the activation of a bypass diode can be considered. This was undertaken by varying the load resistance.

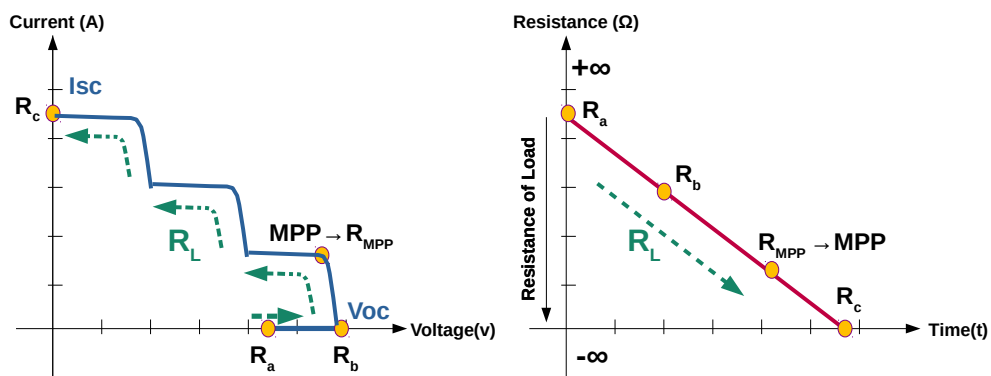
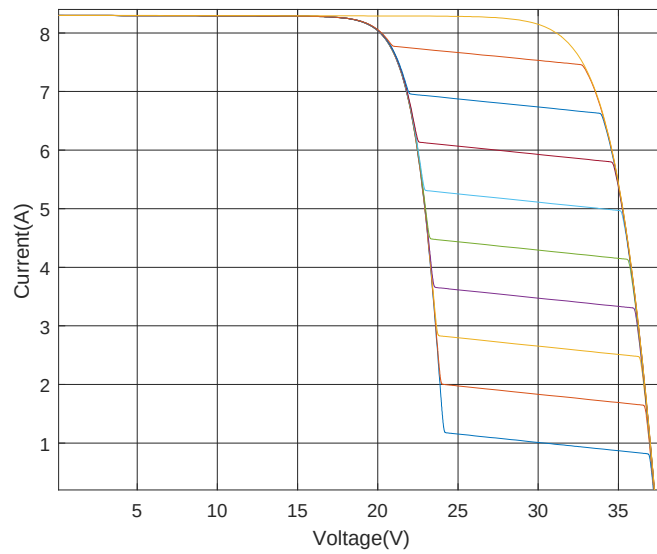


Figure 2.16 I-V curves with the activation of the bypass diodes (shadow condition) (a) and variation of the load resistance  $RL$  (b)

Figure 2.17 shows the simulation of I-V curves in HBG under different irradiation conditions. If the string voltage exceeds the transmission voltage of the bypass diode, it becomes active. Theoretically, the breakdown voltage is not reached. In this simulation, there are one block of cells bypassed by the diode and the two others blocks in normal operating. A point of inflection of the curve  $I(V)$  occurs when one of the bypass diodes is activated.



**Figure 2.17** I-V curves with one activated diode bypass under various irradiation conditions

PV arrays in shading conditions not only decrease the produced energy [14, 15] but also increase the risk of structural failures with the apparition of localized hot-spot despite the activation of bypass diodes [16]. A hot-spot refers to the portion of the cell with a higher temperature increase. In the study of Kim [17, 18], it was shown that the hot-spot phenomena can lead to second breakdown or cell encapsulant damage although the activation of bypass diodes.

Shadows can have different shapes and sizes affecting differently PV production as shown in Figure 2.18.

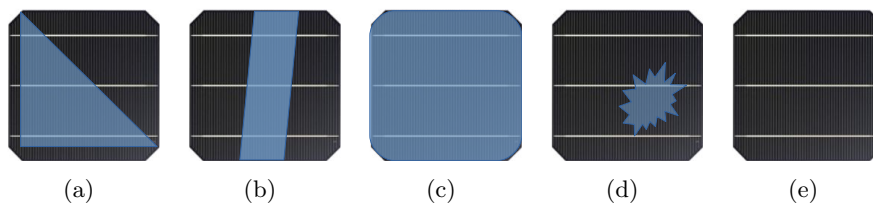


**Figure 2.18** Example of shadow size and shape affecting PV cell production

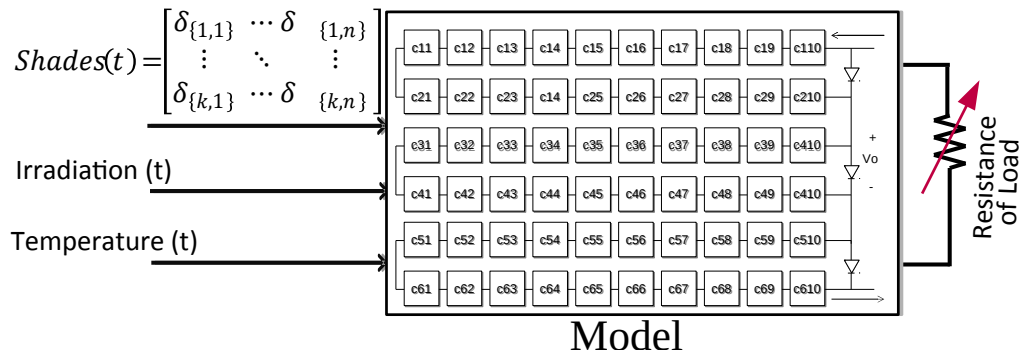
The next part consists in presenting the proposed model using shading parameters able to identify the shape and the size of the shadow thanks to an image processing.

## 2.2 The proposed PV module using HBG

The proposed model in this thesis takes into account the electrical and thermal behaviour of each cell of a PV module. The configuration of a cell interconnection circuit suitable for powering a given application is obtained by calculating the number of cells in series needed to generate a convenient voltage  $V_o(t)$ , and the

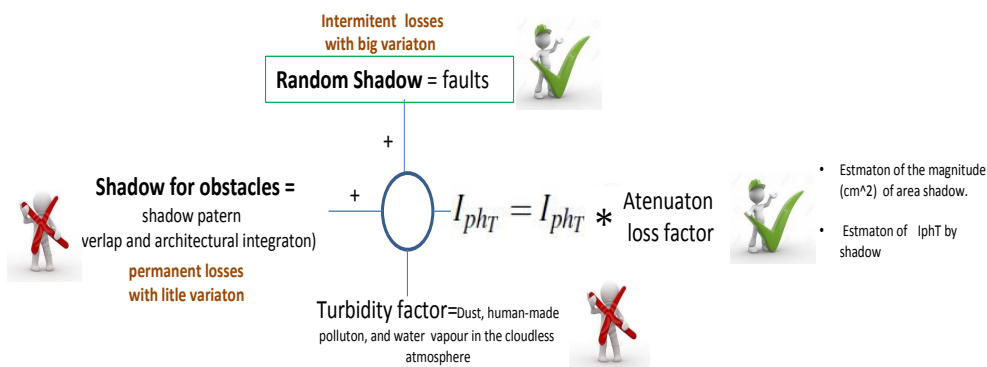
number of strings in parallel needed to produce sufficient current  $I_o(t)$ . Normally, a PV panel is composed on a set of cells (e.g., 36, 60, 72), and a set of bypass-diodes.

Figure 2.19 illustrates the proposed PV model using shadow parameters. The model inputs represents the environmental variables such as solar irradiation, temperature, matrix of shadow and the electrical parameters of PV cells.



**Figure 2.19** General schematic of the proposed PV module model

Due to the complex nature of the shading on PV modules, it is necessary to analyze some parameters in order to obtain an accurate model. PV arrays can be subjected to shading: either homogeneous or non-homogeneous. Homogeneous shading refers to balanced but reduced irradiation over all PV panels while, non-homogeneous shading is the uneven distribution of irradiation across the panels in a PV array [19–37]. Non-homogeneous shading most often occurs due to the following: 1) Shadow from tall buildings or trees, 2) Movement of clouds and 3) Bird droppings. Figure 2.20 shows a general description of the model with the shadow parameters.



**Figure 2.20** Complete description of shadows affecting the output current of the cell

### 2.2.1 Model of PV module using shadow parameters

Direct and indirect irradiation on all cells of a panel is not the same because of buildings or trees shades, atmosphere fluctuation, the existence of clouds and daily sun angle changes. The impact of the non-uniform irradiation in the production of energy depends on several aspects as cell material, the magnitude

of the area of shade, bypass diode placement, string configuration, etc. For this reason, the PV module can have different values of  $I_{ph}$  for each cell. The global irradiance on Earth consists of the direct irradiance, diffuse irradiance, and reflected irradiance (2.5).

$$G_T = G_D + G_d + G_r \quad (2.5)$$

where  $G_T$  is the global irradiance,  $G_D$  the direct radiation,  $G_d$  the diffuse radiation and  $G_r$  the reflected radiation.

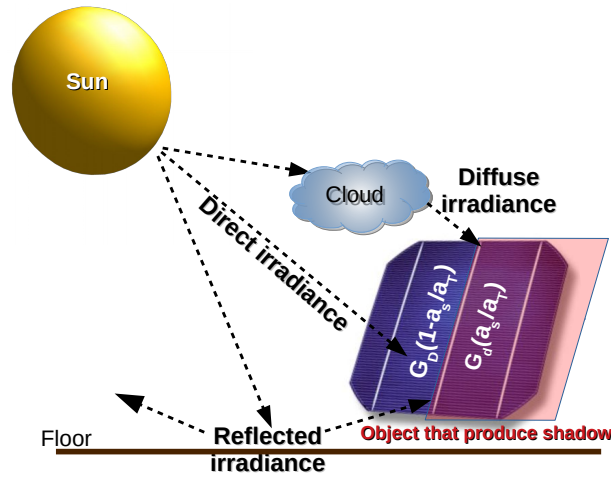


**Figure 2.21** Photo-current of a cell as a linear combination of direct and indirect irradiation

Eq 2.6 describes the behavior of conversion of light on electrical energy:

$$I_{ph} = \frac{G_T \cdot I_{phTi}}{G_{STC}} \quad (2.6)$$

Eq 2.7 is divided in two terms. Term 1 of the equation is the direct solar radiation that arrives to the PV cell. Term 2 of the equation is the non-direct radiation that receives the cell.

$$I_{ph} = \underbrace{\left( G_D \cdot \left( 1 - \frac{a_s}{a_T} \right) \right)}_1 + \underbrace{G_d \cdot \frac{a_s}{a_T}}_2 \cdot \frac{I_{phTi}}{G_{STC}} \quad (2.7)$$

$$I_{ph} = \underbrace{\frac{G_D \cdot I_{phTi}}{G_{STC}} \cdot \left( 1 - \frac{a_s}{a_T} \right)}_1 + \underbrace{\frac{G_d \cdot I_{phTi}}{G_{STC}} \cdot \frac{a_s}{a_T}}_2$$

where  $G_{STC} = 1000 \text{ W/m}^2$ ,  $a_T = \text{area total of the cell}$ , and  $a_s = \text{shadow area of the cell}$ . Eq.(2.8) shows two attenuation factors  $\delta_1$  representing the unshaded part and  $\delta_2$  the shaded part.

$$\begin{aligned}\delta_1 &= \frac{G_D}{G_{STC}} \cdot \left(1 - \frac{a_s}{a_T}\right) \\ \delta_2 &= \frac{G_d}{G_{STC}} \cdot \frac{a_s}{a_T}\end{aligned}\quad (2.8)$$

The effective input current produced by the cell, is showed in Eq.(2.9) in function of these factors. The current produced by the cell, is mainly produced by the irradiation (Eq. 2.6). A mathematical expression to model the partial shading at the level of the PV cell is described in Eq.(2.9):

$$\begin{aligned}I_{ph} &= (\delta_1 + \delta_2) \cdot I_{phTi} \\ I_{ph} &= \delta_T \cdot I_{phTi}\end{aligned}\quad (2.9)$$

i.e.,  $\delta_T$  is an attenuation factor (e.g., one without shadow) ( $0 \leq \delta \leq 1$ ),  $I_{phTi}$  is the input nominal current of each cell, and  $I_{ph}$  is the effective input current. PV cells can have different value of  $\delta$  and these modifications allow to build a shadow matrix  $M\delta(t)$  (Eq. (2.10)). The elements of  $M\delta(t)$  represent the number of cells of module.

$$M\delta(t) = \begin{bmatrix} \delta_{11} & \delta_{12} & \delta_{13} & \delta_{14} & \delta_{15} & \delta_{16} & \delta_{17} & \delta_{18} & \delta_{19} & \delta_{110} \\ \delta_{21} & \delta_{22} & \delta_{23} & \delta_{24} & \delta_{25} & \delta_{26} & \delta_{27} & \delta_{28} & \delta_{29} & \delta_{210} \\ \delta_{31} & \delta_{32} & \delta_{33} & \delta_{34} & \delta_{35} & \delta_{36} & \delta_{37} & \delta_{38} & \delta_{39} & \delta_{310} \\ \delta_{41} & \delta_{42} & \delta_{43} & \delta_{44} & \delta_{45} & \delta_{46} & \delta_{47} & \delta_{48} & \delta_{49} & \delta_{410} \\ \delta_{51} & \delta_{52} & \delta_{53} & \delta_{54} & \delta_{55} & \delta_{56} & \delta_{57} & \delta_{58} & \delta_{59} & \delta_{510} \\ \delta_{61} & \delta_{62} & \delta_{63} & \delta_{64} & \delta_{65} & \delta_{66} & \delta_{67} & \delta_{68} & \delta_{69} & \delta_{610} \end{bmatrix}\quad (2.10)$$

The proposed model uses the energy flows that convert sunlight into electrical energy. PV cell modeling can be done with different levels of accuracy, depending of the purpose of the user. Eq.(2.3) gives no accurate information about the effects of inherent variations on the cell performance (influenced by the uniformity of cell fabrication processes) and on the array performance. In order to describe each electrical behaviour of each PV cell of a PV module, the photo-current term  $I_{ph}$  is replaced by the relation shown in Eq.(2.9)

$$I = \delta \cdot I_{phTi} - I_o \left[ e^{\frac{V_c + I \cdot R_s}{V_t}} - 1 \right] - \frac{V_c + I \cdot R_s}{R_{sh}} \left[ 1 + k \left( 1 - \frac{V_c + I \cdot R_s}{V_{br}} \right)^{-n} \right] \quad (2.11)$$

Eq (2.11) describes the behaviour of the interconnection circuit of each PV cell under abnormal, but common, operating conditions, e.g. partial shadowing of the array by nearby structures at any times of the day. A complete description of the effects of electrical mismatches in real interconnection circuits requires the determination of cell operating currents and voltages. Direct measurements of the operating points of PV cells are not possible because of their encapsulation in the panel.

The normal electrical behaviour of PV modules can be drastically affected by the nature of the shadow. Another factor that can influence the shape of the I-V curve is the activation (or not) of the bypass diodes. Diodes must enter in conduction when even only one cell is in shadow. The conditions of the activation of the bypass diode are presented in the follow equation Eq (2.12) :

$$V_{G_k} = \begin{cases} V_{diode} & \text{if } n < \frac{V_{shadowed} - V_{bypass}}{V_{non-shadowed}} + 1 \\ \sum_{i=1}^n V_{cell_i} & \text{if } n \geq \frac{V_{shadowed} - V_{bypass}}{V_{non-shadowed}} + 1 \end{cases} \quad (2.12)$$

$$I_{G_k} = I_{C_1} = I_{C_2} = I_{C_3} = \dots = I_{C_n} \quad (2.13)$$

where  $V_{G_k}$  is a string of series cells connected to one bypass diode,  $V_{shadowed}$ , the cell voltage in shadow,  $V_{bypass}$  the forward voltage when the bypass diode turns ON and  $V_{nonshadowed}$  the forward voltage for each cell under normal operating.

$$\begin{aligned} V_{module} &= V_{G_1} + V_{G_2} + V_{G_3} + \dots + V_{G_k} \\ I_{module} &= I_{G_1} = I_{G_2} = I_{G_3} = \dots = I_{G_k} \end{aligned} \quad (2.14)$$

The next section explains image processing, which allows the shape and the area of the shadow affecting PV module to be known.

### 2.2.2 Image processing: shadows

The methodology for shadow detection and shadow magnitude estimation is explained in this sub-section. The experimental setup to process images was performed using the ADREAM platform. The I-V characteristics were measured using a) Curve tracer (EKO MP160), b) a PV selector (EKO 510), c) acquisition software, d) a weather station, and e) a thermal camera (FLIR i-60). Two PV modules (TE2200) were used: one as a reference during normal operation and the other to perform shading tests, as shown in Figure 2.22.

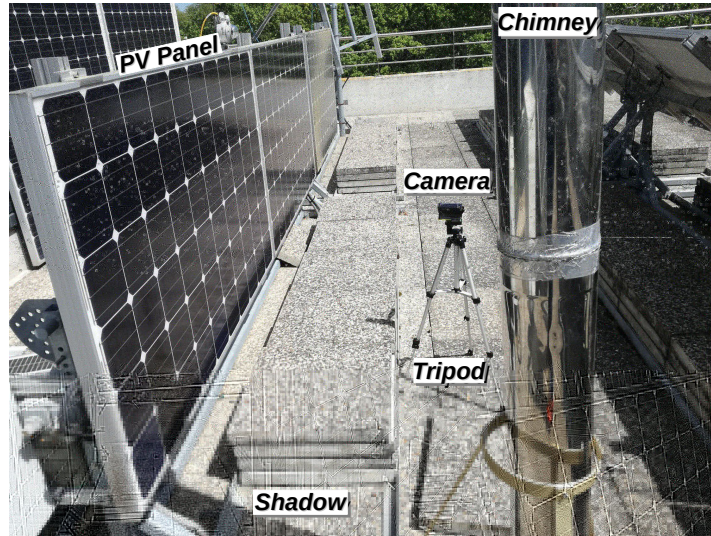


**Figure 2.22** Experimentation process to obtain the shaded area of the PV module

A Huawei VNS-L31 digital camera (primary camera 13 MP (f/2.0, 1/3", 1.12 $\mu$ m) with auto-focus) was used to capture the image of the PV module in shadow. The camera was placed on a tripod to record the shade that affects the panel from a fixed position. The second step was to treat the image using the superpixel method, which allowed the area in shadow  $a_s$  to be calculated. Estimating the magnitude of the shadow was performed using Matlab2017a. The complete image processing depended on various conditions being satisfied:

1. The panel was in vertical position.
2. The image was cropped to the width and height of the panel.
3. The shadow was detected using the superpixel algorithm.
4. The image segmentation toolbox was used to isolate the shadow, food fill, and active contours.
5. The toolbox image region analyzer was used to estimate the magnitude of the shadow.

Figure 2.23 and Figure 2.24 show four shadow processing pictures to obtain the area in shadow and the attenuation factor. The effective area of the cell is smaller since the cell is not a square but an octagon. The octagon is divided into four regions representing cells C5.9, C5.10, C6.9, C6,10. Firstly, it is necessary to quantify the complete area of each selected PV cell. Table 2.3 shows the result of the segmentation of the whole panel so the area of each selected PV cell can be determined. Each result value is represented in pixel numbers. The second step involves isolating and quantifying the shadow of the selected region in the PV module. Table 2.4 presents the result of the segmentation of the shadow for each PV cell. The shadow (as a percentage of the total area) ( $a_s$ ) can be deducted by dividing the quantification of the shadow of each cell by the quantification of the total area of each cell. Finally, the attenuation factor ( $\delta$ ) is calculated using Eq.(2.9) that includes the shading factor. Table 2.5 summarizes the results of each affected shadow zone to determine the attenuation factor.

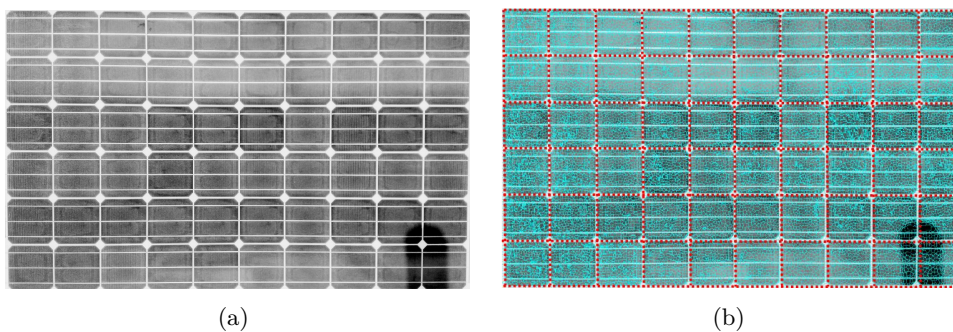


**Figure 2.23** Cropped image (a) and superpixel process (b)

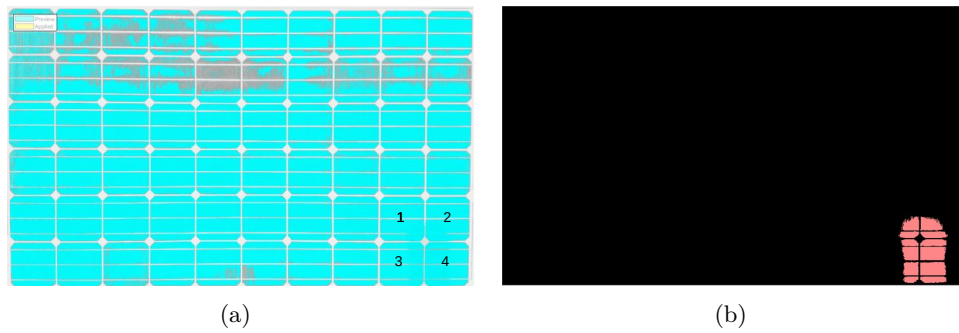


**Figure 2.24** Image segmentation of the whole panel (a) and analysis of the shadow area (b)

Cell	Section cell	Area	Subtotal	Total Area
5,9	a	67362	132189	525963
	b	19261		
	c,d	45566		
5,10	a	66607	129406	
	b	44272		
	c,d	18527		
6,9	a	19454	131160	
	b	45944		
	c	45783		
	d	19979		
6,10	a	22183	133208	
	b	45078		
	c	45226		
	d	20721		

**Table 2.3** Quantification of the area of each selected PV Cell

Cell	Section cell	Area	Subtotal	Total Area
5,9	c	8634	22761	164062
	d	14127		
5,10	c	17727	29724	
	d	11997		
6,9	a	7696	37316	
	b	15387		
	c	14233		
	d	6147		
6,10	a	11576	74261	
	b	25462		
	c	25175		
	d	12048		

**Table 2.4** Quantification of the shadow of each affected PV cell area

Cell	Cell Area	Shadow Area	$a_s$ (%)	$\delta$ (%)
5,9	132189	22761	17.21	82.78
5,10	129406	29724	22.97	77.03
6,9	131160	37316	28.45	71.55
6,10	133208	74261	55.75	44.25

**Table 2.5** Percentage of the shadow area and attenuation factor calculation

Cell 6.10 has a shadow area that is bigger than the other areas and a smaller attenuation factor. The next sub-section involves validating the proposed solar PV model with various cases of complex shading experimentation.

### 2.2.3 Validation of the PV Model and processing images

#### 2.2.3.1 Case 1: Validation of the HBG model when operating normally

For this validation, I-V curve measurements of the reference panel are compared with the model. The test was performed on January 25th, 2018 at 10.40am with a global irradiation of  $624W/m^2$  and a cell temperature of  $25^\circ C$ . In this case,  $\delta_2 = 0$  since no shadows are visible on PV module. The attenuation factor  $\delta$  only corresponds to the global radiation that the PV module receives. Each PV cell has the same shadow area. Eq.(2.15) lists the shadow matrix result of the HBG model when operating normally.

$$\delta(t) = \begin{bmatrix} 1.0 & 1.0 & 1.0 & 1.0 & 1.0 & 1.0 & 1.0 & 1.0 & 1.0 & 1.0 \\ 1.0 & 1.0 & 1.0 & 1.0 & 1.0 & 1.0 & 1.0 & 1.0 & 1.0 & 1.0 \\ 1.0 & 1.0 & 1.0 & 1.0 & 1.0 & 1.0 & 1.0 & 1.0 & 1.0 & 1.0 \\ 1.0 & 1.0 & 1.0 & 1.0 & 1.0 & 1.0 & 1.0 & 1.0 & 1.0 & 1.0 \\ 1.0 & 1.0 & 1.0 & 1.0 & 1.0 & 1.0 & 1.0 & 1.0 & 1.0 & 1.0 \\ 1.0 & 1.0 & 1.0 & 1.0 & 1.0 & 1.0 & 1.0 & 1.0 & 1.0 & 1.0 \end{bmatrix} \quad (2.15)$$

Figure 2.25 shows the comparison between the experimental I-V curve when operating normally and the model's I-V curve.

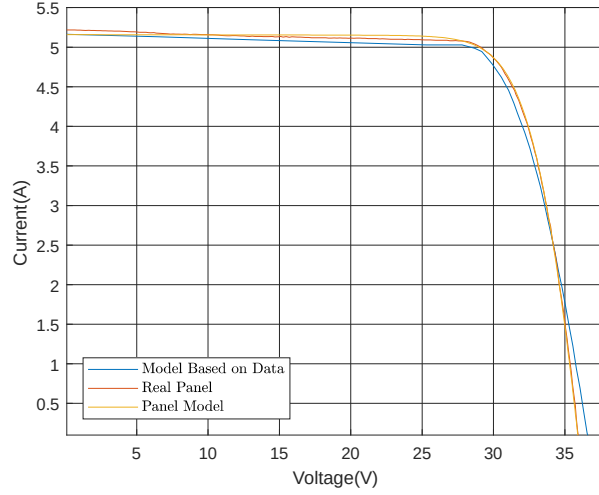


**Figure 2.25** Comparison of the I-V curve measurement with the model during normal operation

The *Mean Square Error* (MSE) result is used to assess modeling accuracy based on the shading ratio. The MSE value shows the model accuracy for the experimental and simulated I-V curves that are depicted in Fig. 2.25.

$$MSE = \frac{1}{N} \sum_{i=1}^N (e_i)^2 \quad (2.16)$$

where  $e_i$  is the  $i$ th error between the modeled value and the measured value, and  $N$  is the amount of analyzed data. For this case,  $N = 872$ .

The *MSE* has a 1.6% accuracy. The next case involves performing a uniform shadow case with various shaded PV cells.

### 2.2.3.2 Case 2: Validation under a uniform shadow

An uniform shading test was performed on a PV module to see the electrical behavior when each PV cell in a string receives the same irradiation. Some sheets of paper were placed in front of the PV module on March 22nd, 2018 at 12.16pm with an irradiation of  $759W/m^2$  and a cell temperature of  $31.2^\circ C$ ; as shown in Figure 2.26. In this case,  $G_d + G_r = 0$  since the paper completely covers the cells. The shaded area  $a_s = 0.5$ : i.e only half the cell is covered by all the string of 20 PV cells. The attenuation factor  $\delta$  is calculated and presented in the shadow matrix in Eq. (2.17).

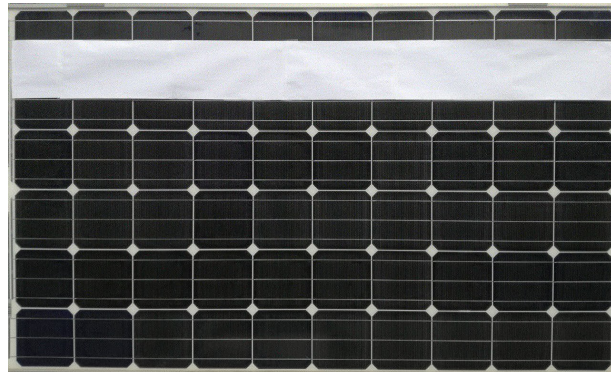


**Figure 2.26** Test for shadow on module Tenesol 2200 with shadows on March, 22nd, 2018

$$\delta(t) = \begin{bmatrix} 0.5 & 0.5 & 0.5 & 0.5 & 0.5 & 0.5 & 0.5 & 0.5 & 0.5 & 0.5 \\ 0.5 & 0.5 & 0.5 & 0.5 & 0.5 & 0.5 & 0.5 & 0.5 & 0.5 & 0.5 \\ 1 & 1 & 1 & 1 & 1 & 1 & 1 & 1 & 1 & 1 \\ 1 & 1 & 1 & 1 & 1 & 1 & 1 & 1 & 1 & 1 \\ 1 & 1 & 1 & 1 & 1 & 1 & 1 & 1 & 1 & 1 \\ 1 & 1 & 1 & 1 & 1 & 1 & 1 & 1 & 1 & 1 \end{bmatrix} \quad (2.17)$$

Figure 2.27 shows the comparison of the I-V curve in normal operating conditions and the I-V curve under complex shading with the I-V curves of the model. The *MSE* of this comparison is of 3%.

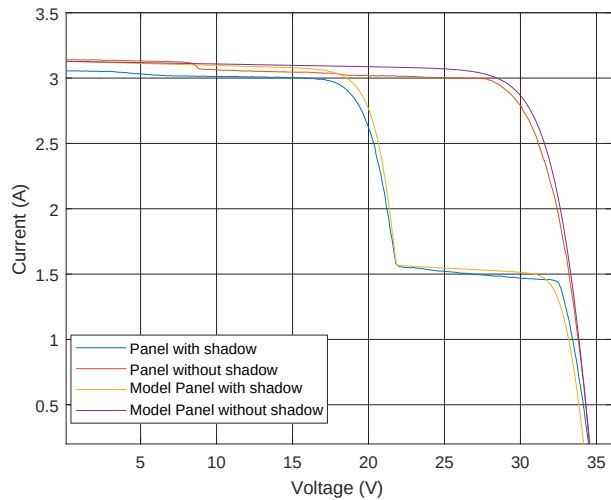


**Figure 2.27** Comparison of the measurement of I-V curves with the model during normal operation and under shading conditions

### 2.2.3.3 Case 3: Validation under complex shading conditions

Partially shading drastically affects PV performance because of the apparition of hot-spot. This phenomena is represented by a portion of the I-V curve that has a more pronounced slope on I-V curves [22]. For this case, two sheets of paper were placed on a PV module with the first having a shadow area of  $a_s = 0.5$  and

the second a shadow area of  $a_s = 0.23$ , as shown in Figure 2.28. The tests were performed on February 9th, 2018 at 12.06pm; there was a  $387.80W/m^2$  solar irradiation and a cell temperature  $19^\circ C$ .



**Figure 2.28** Test for shadow on a module Tenesol 2200 with shadows on February 9th, 2018

In function of the shadow position and its area, the attenuation factor  $\delta$  is calculated and presented in the shadow matrix in Eq. (2.18)

$$\delta(t) = \begin{bmatrix} 0.5 & 1 & 1 & 1 & 1 & 1 & 1 & 1 & 1 & 1 \\ 1 & 1 & 1 & 1.0 & 1.0 & 1.0 & 1.0 & 1.0 & 1.0 & 1.0 \\ 0.77 & 1.0 & 1.0 & 1.0 & 1.0 & 1.0 & 1.0 & 1.0 & 1.0 & 1.0 \\ 1.0 & 1.0 & 1.0 & 1.0 & 1.0 & 1.0 & 1.0 & 1.0 & 1.0 & 1.0 \\ 1.0 & 1.0 & 1.0 & 1.0 & 1.0 & 1.0 & 1.0 & 1.0 & 1.0 & 1.0 \\ 1.0 & 1.0 & 1.0 & 1.0 & 1.0 & 1.0 & 1.0 & 1.0 & 1.0 & 1.0 \end{bmatrix} \quad (2.18)$$

Figure 2.29 shows the I-V curve during normal operation and the comparison between the I-V curves during the experimental test under complex shading and the I-V model. In this case, the *MSE* is equal to 3%. The *MSE* is higher than in the others cases because of the complexity of the shading that is visible on the PV module. However, the value remains acceptable for the rest of the study for DC power losses to be evaluated because of the shadow area and the attenuation factor.

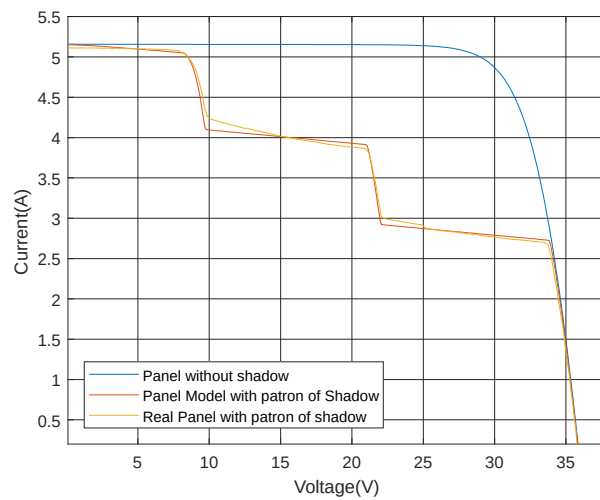


**Figure 2.29** Comparison of the measurement of I-V curves with the model in normal operating conditions and under shading conditions

## 2.2.4 Non-uniform shading conditions during the day

### 2.2.4.1 Case 1

A chimney was placed in front of the PV module on February 27th, 2018, as shown in Figure 2.30. A mobile shadow was visible during the whole measurement day; it was a large shadow that affected the three blocks of twenty cells for the day. The size of the shadow changes progressively: it was narrower in the morning and wider in the afternoon.

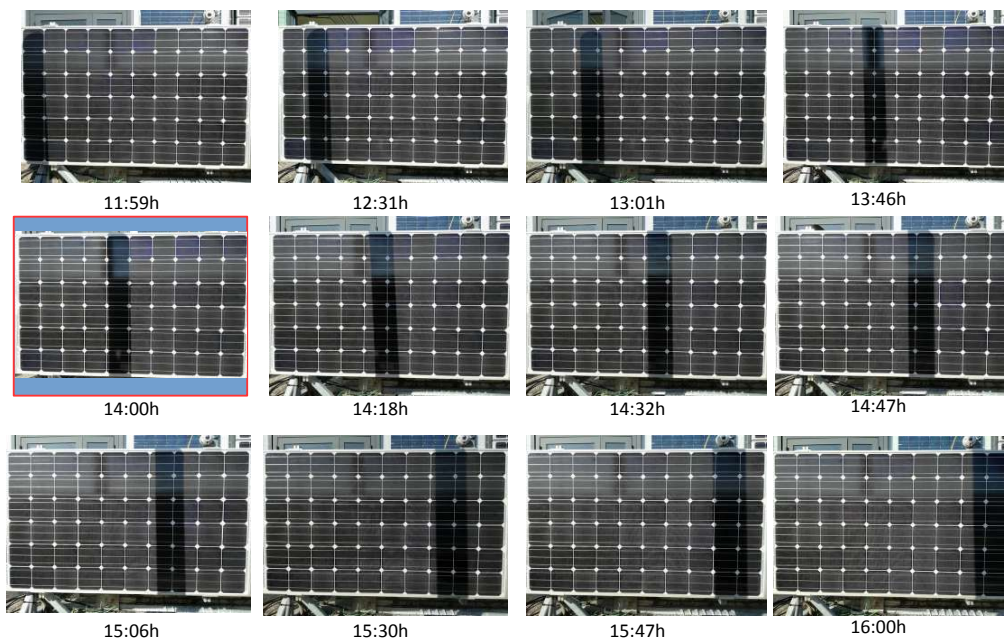


**Figure 2.30** PV module affected by a mobile shadow on February, 27th, 2018

Photography was used during this test to show the matrix of the attenuation

factor. At 2.00pm, the cell temperature was  $T= 30.3^{\circ}\text{C}$  and the irradiation was  $G=832.63\text{W}/\text{m}^2$ . The shadow matrix is shown in Eq. (2.19). The cell C.15 is the most affected by the shadow of the matrix, which affects the electrical generation of the PV module that has an attenuation factor  $\delta$  of 0.01.

$$\delta(t) = \begin{bmatrix} 1 & 1 & 1 & 1 & 0.02 & 1 & 1 & 1 & 1 & 1 \\ 1 & 1 & 1 & 1 & 0.07 & 1 & 1 & 1 & 1 & 1 \\ 1 & 1 & 1 & 1 & 0.01 & 0.93 & 1 & 1 & 1 & 1 \\ 1 & 1 & 1 & 1 & 0.10 & 0.93 & 1 & 1 & 1 & 1 \\ 1 & 1 & 1 & 1 & 0.04 & 0.91 & 1 & 1 & 1 & 1 \\ 1 & 1 & 1 & 1 & 0.10 & 0.90 & 1 & 1 & 1 & 1 \end{bmatrix} \quad (2.19)$$

Figure 2.31 represents two kinds of I-V curve comparison: the first is in shadow and the second is not. This test is a particular case that shows a shadow crossing the whole module. The error between the model and the measured value is 42% for the shadow case. The error between the measurement and the model is more important because of the accuracy of the I-V curve system measurement at low power.

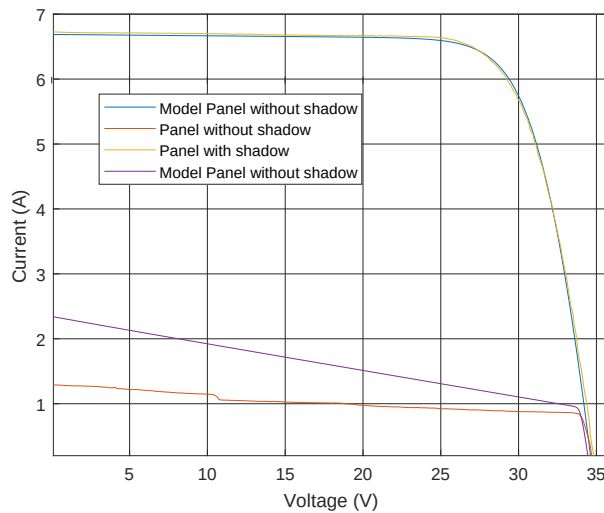


**Figure 2.31** Comparison of the I-V curve model with experimental I-V curves on February 27th, 2018, at 2.00pm

2.2.4.2 Case 2

A chimney was placed in front of the PV module on March 8th, 2018. During the day, the mobile shadow partially affected some small-sized cells, as shown in Figure 2.32.

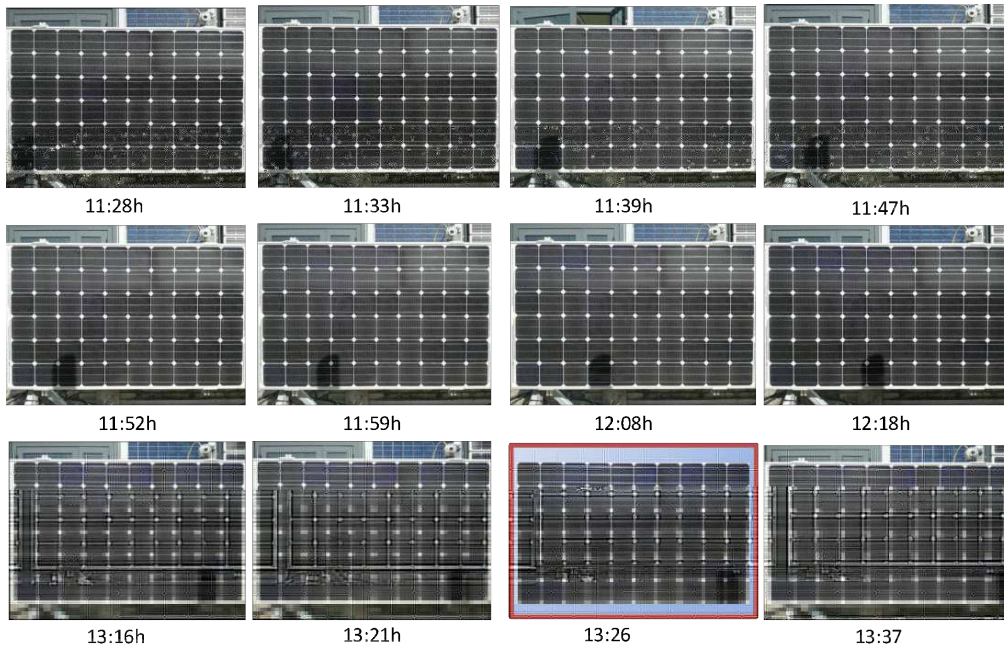
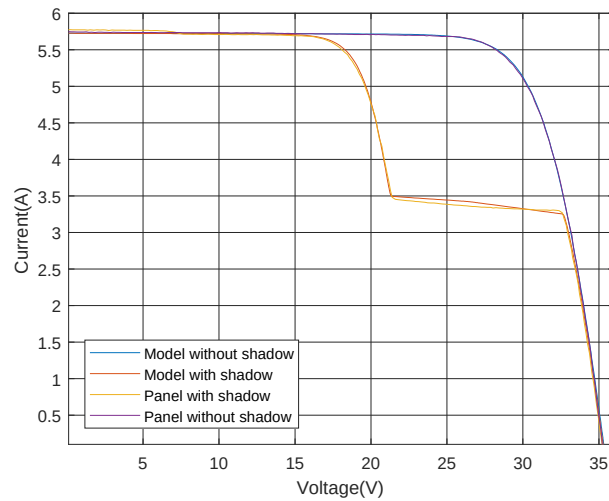


Figure 2.32 PV module affected by a mobile shadow on March 8th, 2018

At 1.26pm, the cell temperature was  $T= 30.2^{\circ}\text{C}$  and the irradiation was  $G=707.89\text{W}/\text{m}^2$ . Eq. (2.20) shows the shadow matrix. Cell C.610 is more affected by the shadow matrix that affects the electrical generation of the PV module and has an attenuation factor  $\delta$  of 0.44.

$$\delta(t) = \begin{bmatrix} 1 & 1 & 1 & 1 & 1 & 1 & 1 & 1 & 1 & 1 \\ 1 & 1 & 1 & 1 & 1 & 1 & 1 & 1 & 1 & 1 \\ 1 & 1 & 1 & 1 & 1 & 1 & 1 & 1 & 1 & 1 \\ 1 & 1 & 1 & 1 & 1 & 1 & 1 & 1 & 1 & 1 \\ 1 & 1 & 1 & 1 & 1 & 1 & 1 & 1 & 0.82 & 0.77 \\ 1 & 1 & 1 & 1 & 1 & 1 & 1 & 1 & 0.77 & 0.44 \end{bmatrix} \quad (2.20)$$

Figure 2.33 shows the comparison of the model with the experimental test. There were two types of comparison: the curves that had shadow and the curves that did not. The *MSE* of the comparison of the curves in shading conditions is 0.27%.



**Figure 2.33** Comparison of the I-V curve model with experimental I-V curves on March 8th, 2018

## 2.3 Global Maximum Power Point Tracking under shading conditions

As described in Chapter 1, the Maximum Power Point Tracking (MPPT) is an algorithm implemented in main DC-DC converters to track PV array maximum power. Under shading conditions, the multiple Maximum Power Point (MPP) is visible on the module's P-V curves. The conventional MPPT algorithm detects a maximum power point, but it does not ensure that it is the photovoltaic array maximum. Therefore, it is necessary to develop a Global Maximum Power Point Tracking (GMPPT) algorithm that can extract the PV array's Global Maximum Power Point (GMPP) under shading conditions and with the bypass diodes being activated.

The relative merits of different MPPT algorithms are discussed in [21]. The author says that it is very difficult to draw conclusions as to which method is better. This comparison depends upon the application, convergence time, the accuracy and reliability required of the algorithm, and finally upon the hardware and money available. For example, in [19, 23], a Global Maximum Power Point Tracking (GMPPT) algorithm was developed to extract the MPP from the PV array under partial shading conditions. In agreement with [21], we also believe that it is necessary to develop a model-based GMPP algorithm as well as an accurate mathematical model under complex shading condition that allows the maximum power of a partially shaded PV array to be tracked. Its properties can easily be used for complex systems such as multi-scale and multi-energy systems (i.e, electrical, mechanical, thermal, etc). A GMPPT algorithm was developed using the PV model proposed in the previous sub-section.

### 2.3.1 A GMPPT algorithm based on the model

The proposed algorithm is based on the precise modeling of the cell, panel, and bypass diodes. A PV model in shadow conditions was presented in the previous section.

The MPPT algorithm developed can be divided in two parts:

- The first part is the PV model with a shadow algorithm, which is based on the evaluation of the equations that describe the system's electrical behavior with current steps. The panel model produces 61 non-linear equations (NLE). It is necessary to carry out a variation of the load resistance ( $RL$ ) from an initial value  $RL=\infty\Omega$  to  $RL=0\Omega$  to obtain the I-V curve. It is impossible to find an analytic response for the set of NLE. Therefore, it was necessary to find a solution using numerical methods. We used a method named backward differentiation formula (BDF) to address the above issue. This method approximates the function derivative using information from computation times. A BDF was used to solve the initial value problem  $y' = f(t, y), y(t_0) = y_0$  and to solve the I-V curve  $\sum_{n=0}^s a_k y_{n+k} = h\beta f(t_{n+s}, y_{n+s})$ , where  $h$  is the step size,  $t_n$  is  $t_0 + nh$ .
- The second part of the GMPPT algorithm compares the  $P(t_n)$  with  $P(t_{n-1})$  values from the  $P(t) = P(0), P(1)...P(n)$ . If  $P(t_n) > P(t_{n-1})$  sequence at instant  $t_n$ , which is a new GMPP point .

Figure 2.34 a) is a system's I-V curve that has three shadows. Figure (2.34 b) is the P-V curve of the system with three power maxima. There are two local maxima (LMPP), but only one is a global maximum (GMPP). Given the exponent behavior of the current with respect to the voltage and the behavior of the system under shadow conditions, the algorithms found in the literature present convergence or calculation time problems, which this algorithm aims to help solve with its proposal. In figure 2.34 c) the pink line is a curve P-t that shows the evolution of the power over time. The blue line shows the evolution of the MPPT algorithm. The algorithm varies the value of  $RL$  and finds a first LMPP point, continues with the variation of  $RL$ , and finds a second point where the power is the highest in the whole system. Figure 2.34 d) shows the evolution of the algorithm, and the Dirac delta function shows the points where the maximum power system is located.

The experimentation and validation tests were performed on February 9th, 2018 with the same shadow pattern as the one shown in 2.28. Figure 2.34 shows an example of the results obtained to detect the GMPPT on I-V curves ( $V_{gmpp} = 21.28V, I_{gmpp} = 5.61A$ ).

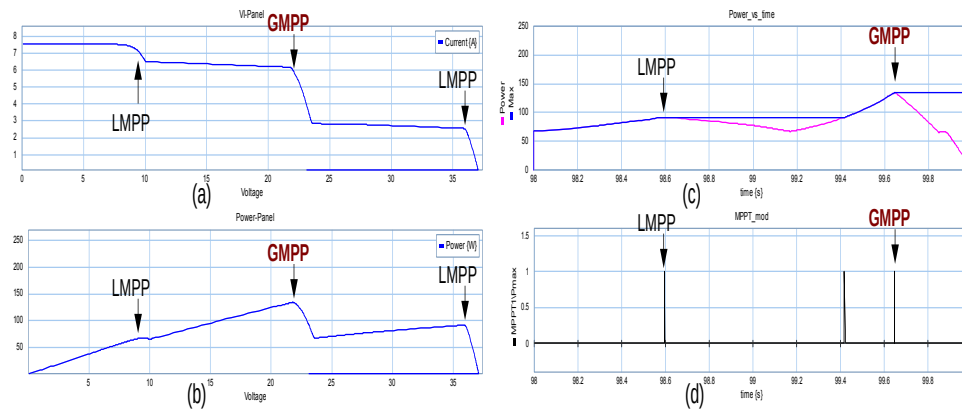


**Figure 2.34** a) I-V curve, b) P-V curve, c) Evolution of the MPPT algorithm, d) Detection of GMPP

The next sub-section presents the evolution of the GMPP during one day of campaign measurements under complex shading conditions.

### 2.3.2 How the GMPPT algorithm evolves in shadow conditions during one production day

This part presents the evolution of the proposed GMPPT algorithm based on time. Figure 2.35 shows the comparison of the model's GMPPT with the GMPPT measurements. This comparison will permit a fault detection method to be constructed for the GMPPT. A PV generator (maximum six panels) is connected to an EKO MP160 curve plotter. This curve plotter provides information on current, voltage, power, and maximum power point every minute.

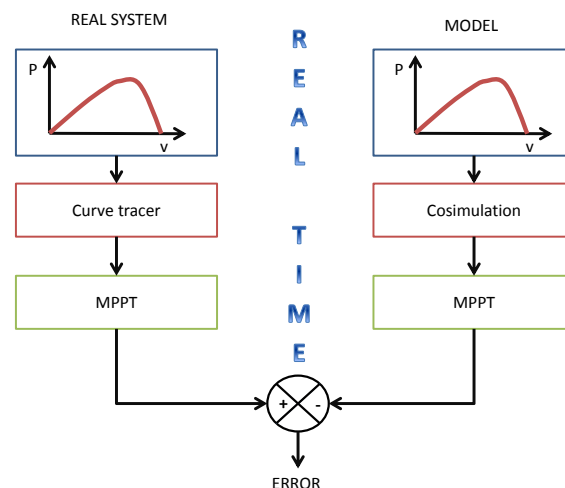


**Figure 2.35** Comparison of the GMPPT model with the measurements

One experiment with the PV module was performed in order to show the evolution of the GMPP throughout the whole day.

### 2.3.2.1 Case 1: Uniform shadow on the PV module

The experimentation was the same as that shown in Figure 2.26. A PV output power campaign measurement was taken on March 23rd, 2018.

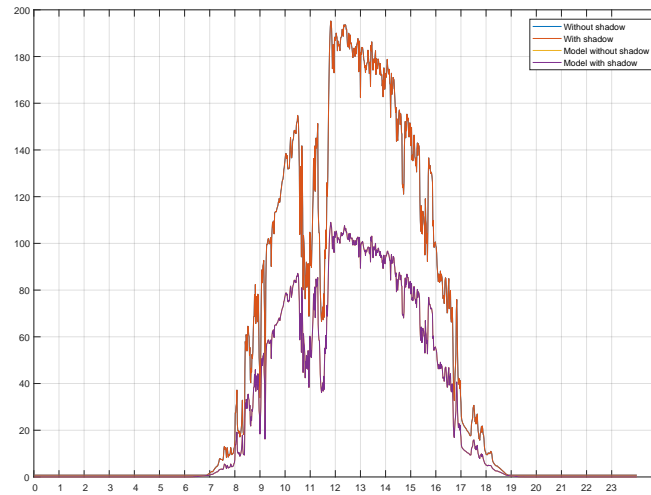


**Figure 2.36** Validation of GMPPT without calibration of parameters

Figure 2.36 shows the comparison of the output PV power model with the measurements based on time. An important difference between both curves exists under shading conditions. It is important to propose a method that detects defects in the GMPPT in order to optimize the PV production.

## 2.4 DC-DC Converter

### 2.4.1 DC-DC converter sizing

A boost converter is a DC-DC power converter that steps up voltage (while stepping down current) from its input (supply) to its output (load). Figure 2.37 shows the general electrical schematic of a boost converter.

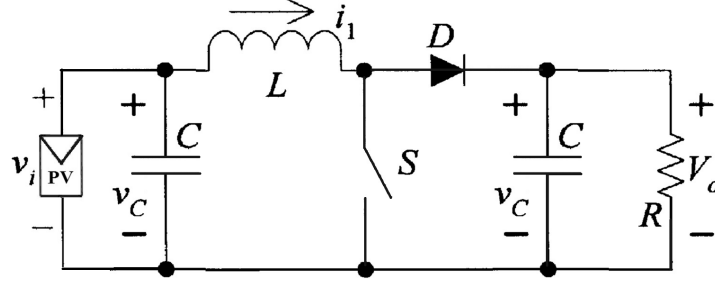


Figure 2.37 Electrical structure of the boost converter

$$\begin{aligned} L \frac{di_L}{dt} &= V_i - u \cdot V_c - R_L \cdot i_L \\ C \frac{dV_c}{dt} &= u \cdot i_L - \frac{V_c}{R} \end{aligned} \quad (2.21)$$

The DC-DC boost converter comprises an inductor ( $L$ ), a diode ( $D$ ), an input capacitor ( $C_i$ ), an output capacitor ( $C$ ), a load resistor ( $R$ ), and the control switch ( $u$ ). These components are connected in such a way that the input voltage source ( $V_{MPP}$ ) was stepped up at the output voltage ( $V_{out}$ ). The relationship between these voltages depends on the duty cycle of control switch  $D$  (i.e. the ON time of the switch), and is shown in the following equation (Eq(2.22)):

$$\frac{V_{out}}{V_{in}} = \frac{1}{1 - D} \quad (2.22)$$

The value for the load resistance  $R$  was selected in such a way that the optimum resistance ( $R_{max} \equiv V_{max}/P_{max}$ ) corresponded to a duty cycle of  $D_{min} = 0.5$  when operating at reference conditions ( $T = 291$  K and  $G = 1000$  W/m<sup>2</sup>). The equation for this calculation is:

$$\frac{V^2_{mpp}}{R_{mpp}} = \frac{\left(\frac{V_{mpp}}{1-D}\right)^2}{R} \quad (2.23)$$

$$R = \frac{R_{mpp}}{(1 - D)^2} \quad (2.24)$$

According to this equation, the connection between the panel and the external load can be optimized by adjusting the duty cycle (between  $D_{min}$  and  $D_{max}$ )

so that the module always operates at maximum power conditions. The input capacitance, the inductance, and the output capacitance were designed based on the following equations [38]:

$$C_{in} \geq \frac{D_{min}}{8 \cdot f^2 \cdot L \cdot 0.01} \tag{2.25}$$

$$L \geq \frac{V_{out} \cdot (1 - D_{min}) \cdot D_{min}}{f \cdot \Delta I_{PSC}} \tag{2.26}$$

$$C_{out} \geq \frac{D_{min} \cdot V_{out}}{f \cdot \Delta V_{out} \cdot R_o} \tag{2.27}$$

Additional design requirements were:

- The commutation frequency:  $f = 100 \text{ kHz}$
- Current Ripple Factor (CRF) [39]:  $\frac{\Delta I_{PSC}}{I_{out}} = 30\%$
- Output Voltage Ripple Factor (OVRF) [39]:  $\frac{\Delta V_o}{V_o} = 5\%$
- Variation of the input voltage:  $V_{mpp} = 28.595V - 31.605V$
- Output voltage:  $V_{out} = 60.2V$

Thus, the chosen values for the boost converter parameters were:  $C_{in} = 1.246\mu\text{F}$ ,  $L = 501.55\mu\text{H}$ ,  $C_{out} = 161.33\text{nF}$ ,  $R_o = 310.95 \Omega$ . The ripple current was  $\Delta I_{mpp} = 4.8\text{A}$  and the ripple voltage  $\Delta V_{out} = 3.010 \text{ V}$ . Finally, the duty cycle ranged from  $D_{min} = 0.5$  to  $D_{max} = 0.89$

The section part involves simulating the boost-converter by using HBG.

### 2.4.2 Modeling the boost-converter using HBG

Figure 2.38 presents the HBG model of the boost converter.

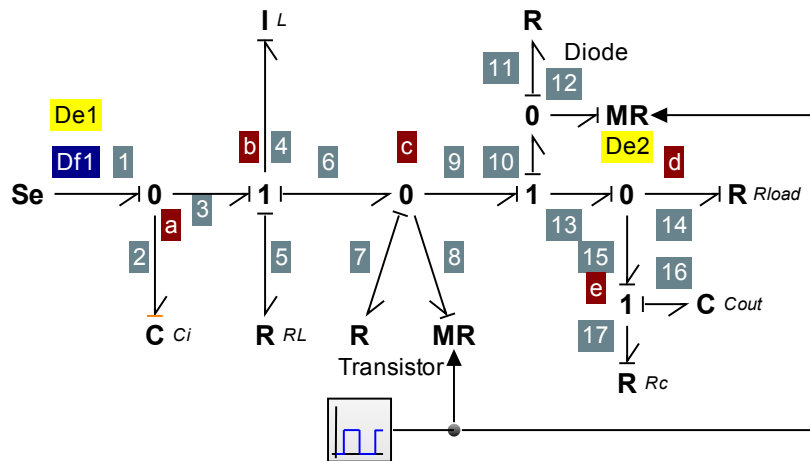
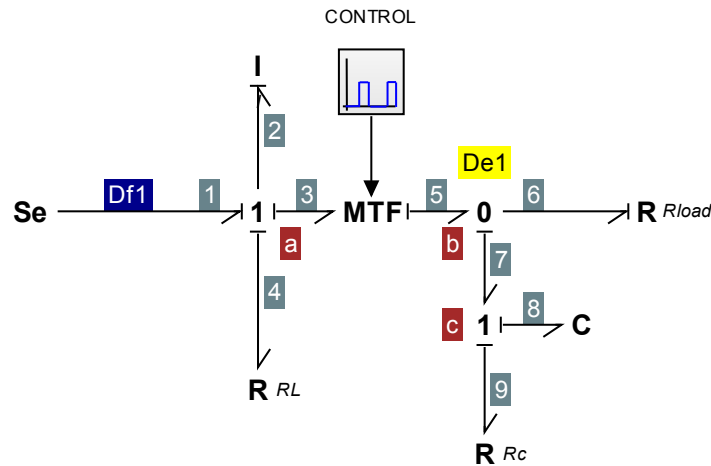


**Figure 2.38** HBG Model of a boost Converter

where  $S_e$  is the voltage source,  $L$  the inductance,  $R_{RL}$  the coil resistance,  $C_i$  the input capacitance,  $MR$  the combination of transistor and diode,  $C$  the output

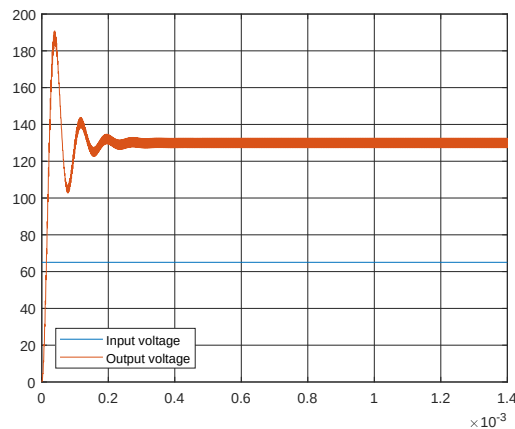
capacitance,  $R_c$  the capacitor resistance, and  $R$  the load resistance.  $D_e$  is a voltage sensor and  $D_f$  a current sensor.

Figure 2.39 shows a simplification of the boost converter model. In which  $MR$  elements were replaced by an ideal Modulated transformer ( $MTF$ ). This model represents a continuous power relation between efforts and flows of ports 3 and 5. The  $MTF$  ratio transform can be set to a certain value, which is given by a control signal: "1" or "0".



**Figure 2.39** Simplified HBG model of the boost converter

Figure 2.40 shows a simulation of the boost converter with the blue line (the input voltage) and the red line (the output voltage).



**Figure 2.40** Input voltage and output voltage of the boost converter

The output voltage information provided by the EKO160 curve plotter is measured in real time using the monitoring system implemented in this thesis, which will be presented in the next chapter. It allows us to control the boost converter by modifying the duty cycle. We propose an MPPT algorithm that works correctly despite shadow conditions.

## 2.5 DC-AC Inverter

An inverter is an electronic device that changes Direct Current (DC) to Alternating Current (AC). This section presents three types of inverter model:

1. The isolated single-phase inverter, which is not synchronized with the grid or any external reference.
2. The connected single-phase inverter, which is synchronized with the grid depending on the grid voltage amplitude and frequency.
3. The bi-directional boost-inverter

### 2.5.1 Modeling the isolated inverter using HBG

Figure 2.41 (a) shows the electrical schematic of a single-phase isolated inverter and Figure 2.41(b) shows its HBG model. Switches  $S_1$ ,  $S_2$ ,  $S_3$ , and  $S_4$  were represented as  $R$  in the HBG model. The ON position of the switch is represented by  $R$  in orange, and the OFF by  $R$  in green.

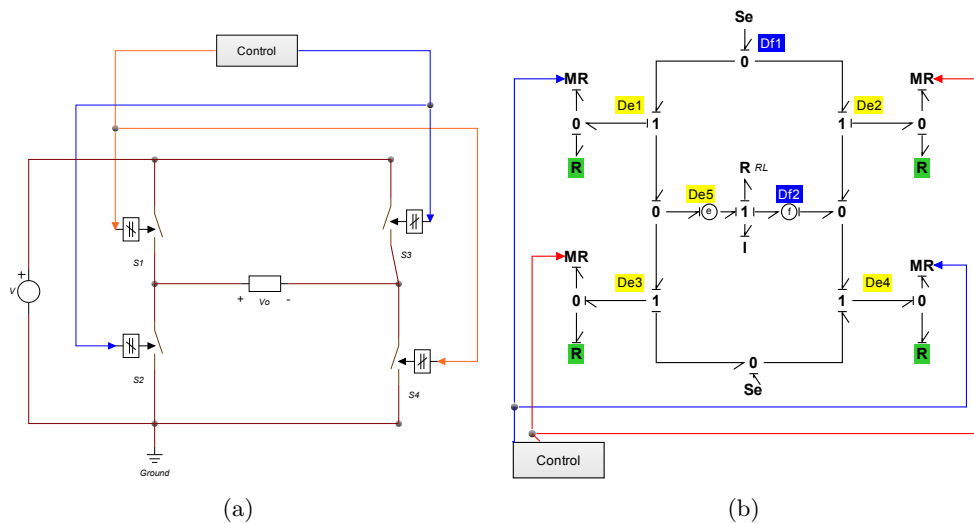
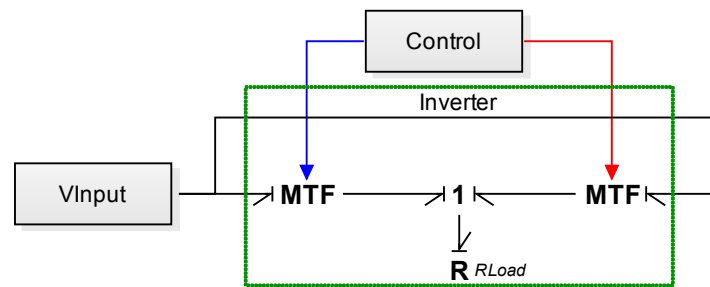


**Figure 2.41** Schematic of a single-phase inverter (a) and its HBG model (b)

The switches of each leg operate complementary. The high-side switch is off when the low-side switch is on, and the high-side switch is on when the low-side switch is off:

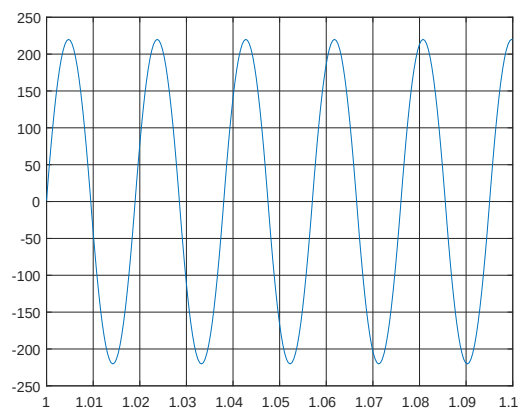
- $S_1$  and  $S_4$  are ON while  $S_2$  and  $S_3$  are OFF,  $v_o = V_s$
- $S_1$  and  $S_4$  are OFF while  $S_2$  and  $S_3$  are ON,  $v_o = -V_s$

Figure 2.42 presents a simplified model replacing the switches  $S_1$  and  $S_4$  with  $MTF$  and switches  $S_2$  and  $S_3$  with  $MTF1$ .



**Figure 2.42** Simplified model of an isolated single-phase inverter

Figure 2.43 presents the output voltage of a single-phase inverter



**Figure 2.43** Output Voltage

### 2.5.2 Modeling a single-phase inverter connected to the grid

Figure (2.44) presents a single-phase inverter with a configuration that is to be connected to the electrical grid. [40]. The DC-AC inverter is connected to an AC grid, with which it works synchronously in both amplitude and frequency.

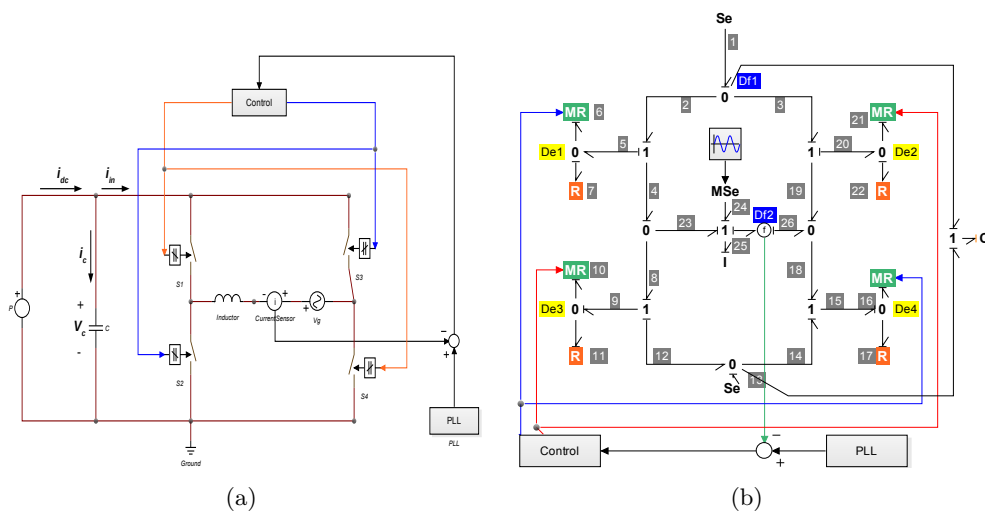
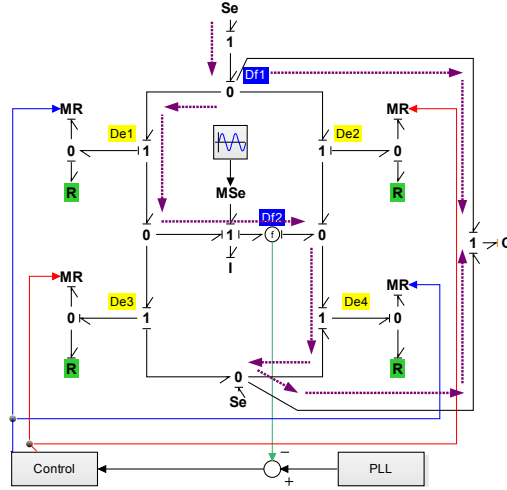


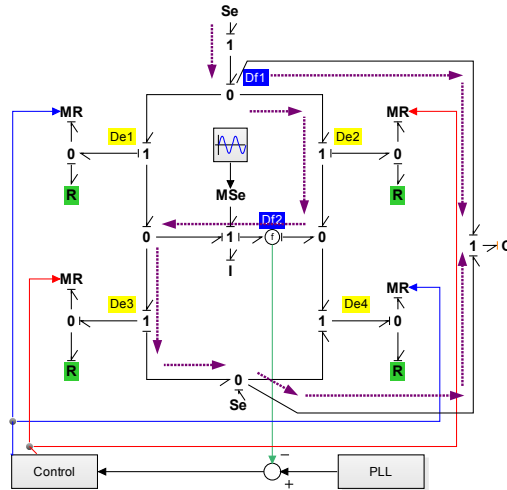
**Figure 2.44** Inverter DC-AC (a) Electrical diagram (b) BG model

Converter circuit structures use bipolar commutation. Similarly to the isolated single-phase inverter, each leg operates in a complementary way:

- $S_1$  and  $S_4$  are ON while  $S_2$  and  $S_3$  are OFF.  $v_L = v_c - v_g$ ,  $i_c = i_{dc} - i_{in}$ ,  $i_{in} = i_L$ .



- $S_1$  and  $S_4$  are OFF while  $S_2$  and  $S_3$  are ON.  $v_L = -v_c - v_g$ ,  $i_c = i_{dc} - i_{in}$ ,  $i_{in} = -i_L$ .



By definition, the control variable  $u$  is  $u = 1$  when  $S_1$  and  $S_4$  are on, and  $u = -1$  when  $S_2$  and  $S_3$  are off, as represented in Eq.(2.28):

$$\begin{aligned} L \frac{di_L}{dt} &= -v_g + v_c u \\ C \frac{dv_c}{dt} &= i_{dc} - i_L u = \frac{P}{v_c} - i_L u \end{aligned} \quad (2.28)$$

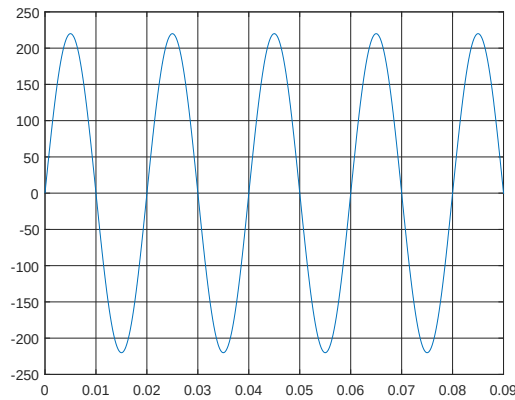


Figure 2.45 Output Voltage

### 2.5.3 Modeling a bidirectional boost-inverter

The Boost inverter is a power electronic converter that is part of a family of inverters formed by two DC/DC converters that have differential output voltages. The Boost inverter is a transformerless power converter which provides a boosting AC output voltage from two individual bidirectional DC-DC Boost converters.

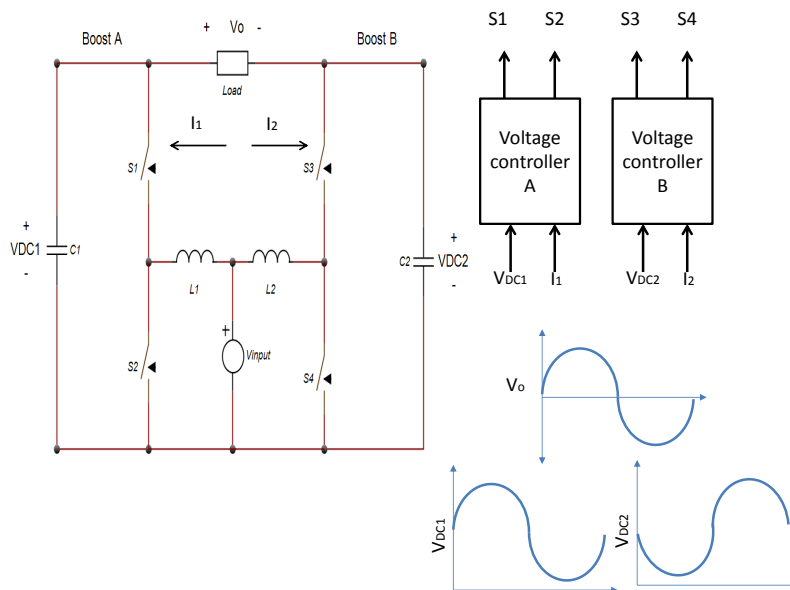


Figure 2.46 Explication of Boost inverter

The inverter output is a floating voltage given by the difference in output between both boosts. The voltage for the boost is shown in Eq(2.29).

$$V_o = V_{DC1} - V_{DC2} = \frac{D_1 - D_2}{(1 - D_1)(1 - D_2)} \quad (2.29)$$

where  $D_1$  and  $D_2$  are the boost duty-cycles.

### Sinusoidal modulation

[41] shows a common technique to achieve a floating sinusoidal output voltage in a step-up inverter, which is to control each converter-leg to generate a sinusoidal waveform with a DC component. However, it uses a  $180^\circ$  degree phase-shift, as depicted in Fig.(2.46).

$$\begin{aligned} V_1(t) &= V_{dc} + \frac{A_m}{2} V_{in} \sin(w \cdot t) \\ V_2(t) &= V_{dc} - \frac{A_m}{2} V_{in} \sin(w \cdot t) \\ V_0 &= V_1 - V_2 \\ V_0 &= A_m V_{in} \sin(w \cdot t) \end{aligned} \quad (2.30)$$

#### 2.5.3.1 Connected to the grid

Fig.(2.47) presents a boost inverter connected to grid. For control purposes, a binary signal  $U(t) = \{0, 1\}$  indicates each topology. Assuming bipolar modulation, switches  $S2$  and  $S3$  are driven by the control signal  $U(t)$ , whereas  $S1$  and  $S4$  are activated by the complementary signal  $1 - U(t)$  [42].

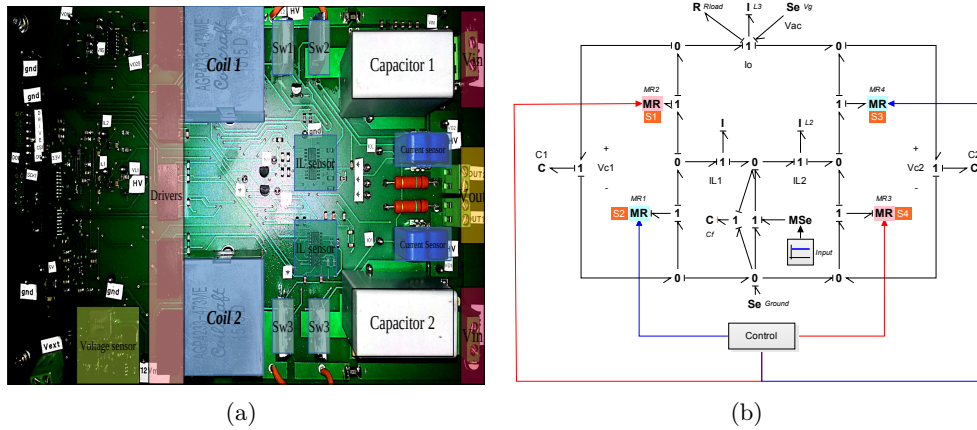


**Figure 2.47** Boost inverter bidirectional (a) diagram (b) model

The state matrix for both topologies and the input vector are shown in Eq.(2.31)

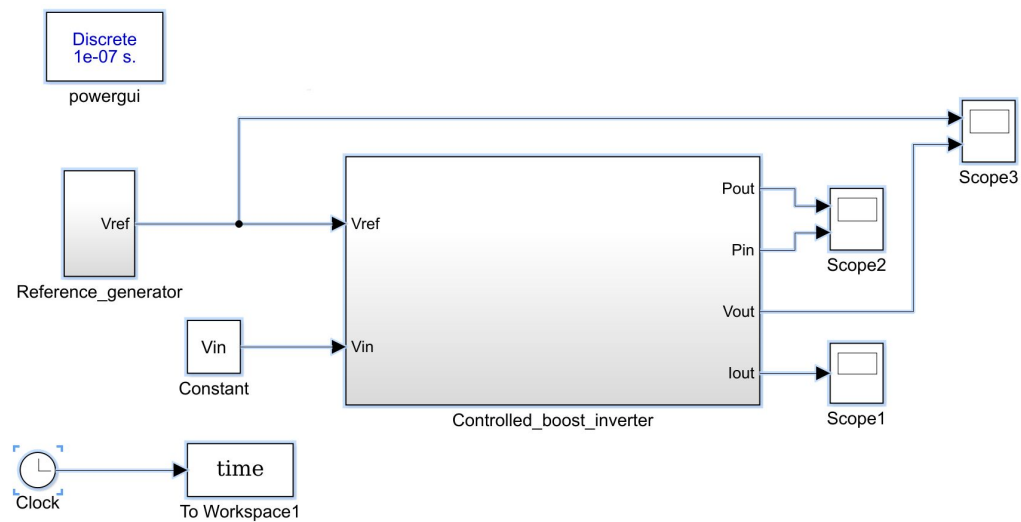
$$\begin{bmatrix} \dot{i}_{L1} \\ \dot{i}_{L2} \\ \dot{v}_{c1} \\ \dot{v}_{c2} \\ \dot{i}_{L3} \end{bmatrix} = \begin{bmatrix} 0 & 0 & \frac{u-1}{L_1} & 0 & 0 \\ 0 & 0 & 0 & \frac{-u}{L_2} & 0 \\ \frac{1-u}{C_1} & 0 & 0 & 0 & \frac{-1}{C_1} \\ \frac{u}{C_2} & 0 & 0 & 0 & \frac{1}{C_2} \\ 0 & 0 & \frac{1}{L_3} & \frac{-1}{L_3} & \frac{-r}{L_3} \end{bmatrix} \cdot \begin{bmatrix} i_{L1} \\ i_{L2} \\ v_{c1} \\ v_{c2} \\ i_{L3} \end{bmatrix} + \begin{bmatrix} \frac{V_m}{L_1} \\ \frac{V_m}{L_2} \\ 0 \\ 0 \\ \frac{-V_{oc}}{L_3} \end{bmatrix} \quad (2.31)$$

where  $u(t) = \{0, 1\}$

Converter Parameter	Value
$L_1, L_2$	47 $\mu\text{H}$
$C_1, C_2$	10 $\mu\text{F}$
$R_{L1}, R_{L2}$	0.003 $\Omega$
$R_{c1}, R_{c2}$	0.05 $\Omega$
$R_{on}$	35m $\Omega$
$R_L$	100 $\Omega$

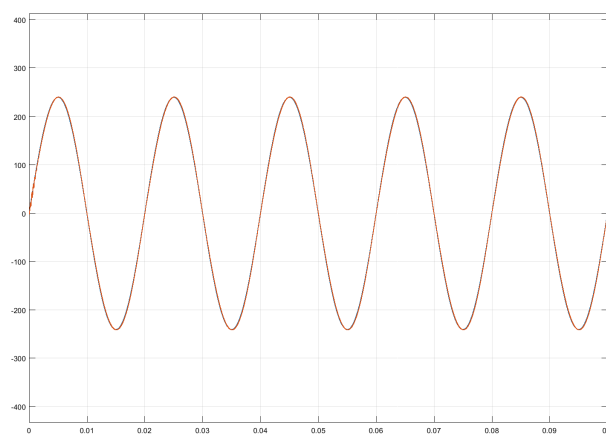
**Table 2.6** Parameters of boost inverter

Figure 2.48 shows the model and the control implemented to the boost inverter using matlab software.



**Figure 2.48** Model boost inverter using matlab

Figure (2.49) shows the output voltage simulation of the inverter boost and grid voltage. This simulation also shows how the output voltage is in phase with the electrical network.



**Figure 2.49** Simulation of boost inverter  $V_{ref}=V_o$

### 2.5.4 Modeling the entire network

The objective of this chapter was to obtain a model that diagnosed faults. The model developed in the previous sections works together as a whole see Fig(2.50), and it will be used in the next chapter.

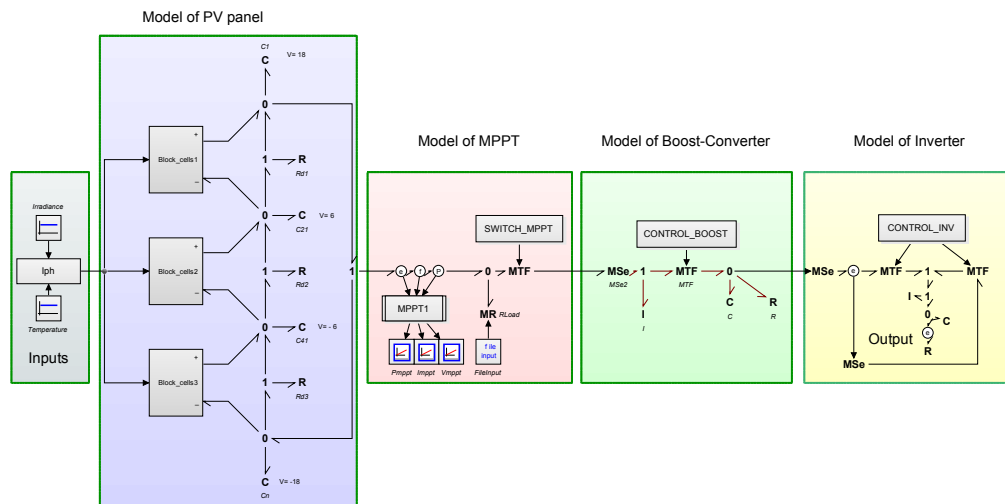


Figure 2.50 PV system modeling using HBG

To provide an example, the voltage outputs for each stage of the photovoltaic conversion system are presented for each moment of time and have a given radiation and temperature of inputs.

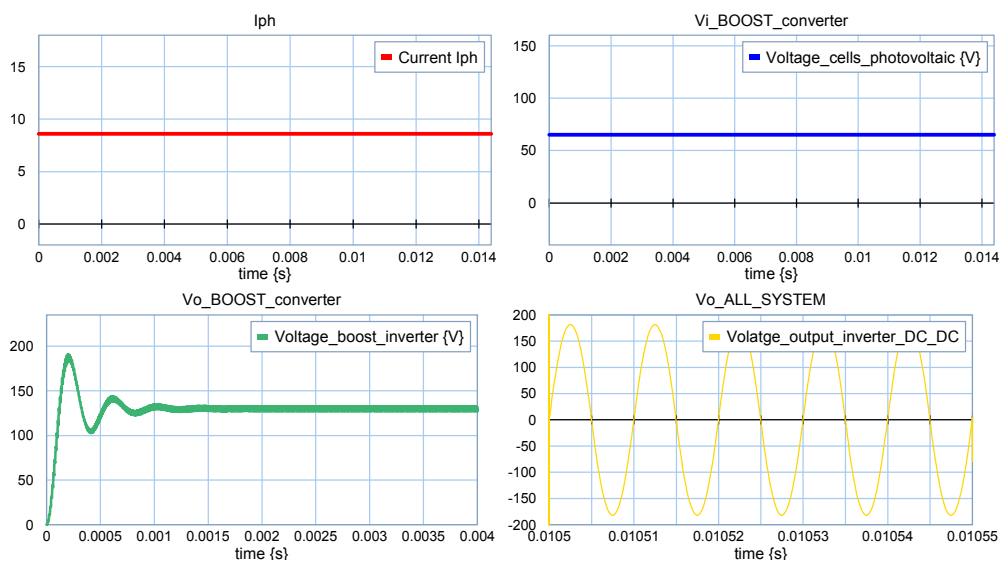


Figure 2.51 Outputs

## 2.6 Conclusion

Detailed modeling of a complete PV system connected to the grid was performed in this chapter. Modeling each element that composes a PV system allowed the electrical behaviour under normal operation and when failing to be characterized. Shading is an external problem that has a serious impact on PV production. The first part of the chapter presented a model able to take into account the effect of complex shading on the I-V curves. The shadow area was deducted thanks to PV module image processing using a superpixel algorithm. Moreover the combination of direct and indirect radiation permitted the attenuation factor to be obtained, which led to a decrease in electrical generation under complex shading conditions. The model was validated using experimental tests that were conducted on specific days. The second part of the chapter developed a strategy to track the global maximum power point under complex shading conditions in order for the system to present better behavior under these conditions. A model was developed and simulated to show the importance of having an new control strategy for DC-DC converters. The last part of the chapter addressed the DC-AC converter. Three kinds of inverter were studied and simulated using HBG. Finally, the modeling of the whole PV system was carried out. This work will allow fault diagnosis methods to be developed based on models and data.

## Bibliography

- [1] M. P. Almeida, M. Munoz, I. de la Parra, and O. Perpignan, “Comparative study of pv power forecast using parametric and nonparametric pv models,” *Solar Energy*, vol. 155, pp. 854 – 866, 2017.
- [2] G. Petrone, C. A. Ramos-Paja, and G. Spagnuolo, *Photovoltaic Sources Modeling*. 2017.
- [3] K. Ding, X. Bian, H. Liu, and T. Peng, “A matlab-simulink-based pv module model and its application under conditions of nonuniform irradiance,” *IEEE Transactions on Energy Conversion*, vol. 27, pp. 864–872, Dec 2012.
- [4] K. J. Sauer, T. Roessler, and C. W. Hansen, “Modeling the irradiance and temperature dependence of photovoltaic modules in pvsyst,” *IEEE Journal of Photovoltaics*, vol. 5, pp. 152–158, Jan 2015.
- [5] E. Skoplaki and J. Palyvos, “Operating temperature of photovoltaic modules: A survey of pertinent correlations,” *Renewable Energy*, vol. 34, no. 1, pp. 23 – 29, 2009.
- [6] S. Liu and R. A. Dougal, “Dynamic multiphysics model for solar array,” *IEEE Transactions on Energy Conversion*, vol. 17, pp. 285–294, Jun 2002.
- [7] M. Dhimish, V. Holmes, B. Mehrdadi, M. Dales, B. Chong, and L. Zhang, “Seven indicators variations for multiple pv array configurations under partial shading and faulty pv conditions,” *Renewable Energy*, vol. 113, pp. 438 – 460, 2017.
- [8] J. Bishop, “Computer simulation of the effects of electrical mismatches in photovoltaic cell interconnection circuits,” *Solar Cells*, vol. 25, no. 1, pp. 73 – 89, 1988.
- [9] W. Herrmann, W. Wiesner, and W. Vaassen, “Hot spot investigations on pv modules-new concepts for a test standard and consequences for module design with respect to bypass diodes,” in *Photovoltaic Specialists Conference, 1997., Conference Record of the Twenty-Sixth IEEE*, pp. 1129–1132, IEEE, 1997.
- [10] M. S. Benghanem and S. N. Alamri, “Modeling of photovoltaic module and experimental determination of serial resistance,” *Journal of Taibah University for Science*, vol. 2, pp. 94 – 105, 2009.
- [11] Y. El Basri, *Reconfigurable distributed power architecture for the optimisation of photovoltaic energy*. Theses, Universite Paul Sabatier - Toulouse III, June 2013.

- [12] Y. E. Basri, M. Bressan, L. Segquier, H. Alawadhi, and C. Alonso, "A proposed graphical electrical signatures supervision method to study {PV} module failures," *Solar Energy*, vol. 116, pp. 247 – 256, 2015.
- [13] A. G. Galeano, *Study of Photovoltaic System Integration in Microgrids through Real-Time Modeling and Emulation of its Components Using HiLeS*. Theses, Université de Toulouse 3 Paul Sabatier, Sept. 2017.
- [14] A. Gutierrez i, M. Bressan, F. Jimenez Vargas, and C. Alonso, "Shading ratio impact on photovoltaic modules and correlation with shading patterns," *MDPI journal energies*, vol. 11, p. 852, 04 2018.
- [15] M. Bressan, A. Gutierrez, L. G. Gutierrez, and C. Alonso, "Development of a real-time hot-spot prevention using an emulator of partially shaded pv systems," *Renewable Energy*, vol. 127, pp. 334 – 343, 2018.
- [16] M. Bressan, Y. El Basri, A. Galeano, and C. Alonso, "A shadow fault detection method based on the standard error analysis of iv curves," *Renewable Energy*, vol. 99, pp. 1181–1190, 2016.
- [17] K. A. Kim, "Hot Spot Detection and Protection Methods for Photovoltaic Systems," p. 135, 2014.
- [18] K. A. Kim, "Hot Spot Detection and Protection Methods for Photovoltaic Systems," p. 135, 2014.
- [19] H. M. El-Helw, A. Magdy, and M. I. Marei, "A hybrid maximum power point tracking technique for partially shaded photovoltaic arrays," *IEEE Access*, vol. 5, pp. 11900–11908, 2017.
- [20] R. Hariharan, M. Chakkarapani, G. S. Ilango, and C. Nagamani, "A method to detect photovoltaic array faults and partial shading in pv systems," *IEEE Journal of Photovoltaics*, vol. 6, pp. 1278–1285, Sept 2016.
- [21] A. Mohapatra, B. Nayak, P. Das, and K. B. Mohanty, "A review on mppt techniques of pv system under partial shading condition," *Renewable and Sustainable Energy Reviews*, vol. 80, pp. 854 – 867, 2017.
- [22] M. Bressan, Y. E. Basri, A. Galeano, and C. Alonso, "A shadow fault detection method based on the standard error analysis of i-v curves," *Renewable Energy*, vol. 99, pp. 1181 – 1190, 2016.
- [23] K. Chen, S. Tian, Y. Cheng, and L. Bai, "An improved mppt controller for photovoltaic system under partial shading condition," *IEEE Transactions on Sustainable Energy*, vol. 5, pp. 978–985, July 2014.
- [24] S. U. Kian Jazayeri, Moein Jazayeri, "Artificial neural network-based all-sky power estimation and fault detection in photovoltaic modules," *Journal of Photonics for Energy*, vol. 7, pp. 7 – 7 – 13, 2017.
- [25] H. Mekki, A. Mellit, and H. Salhi, "Artificial neural network-based modelling and fault detection of partial shaded photovoltaic modules," *Simulation Modelling Practice and Theory*, vol. 67, pp. 1 – 13, 2016.
- [26] M. Hosseinzadeh and F. R. Salmasi, "Determination of maximum solar power under shading and converter faults—a prerequisite for failure-tolerant

- power management systems,” *Simulation Modelling Practice and Theory*, vol. 62, pp. 14 – 30, 2016.
- [27] M. Bressan, *Development of a tool for supervision and control for a solar photovoltaic system*. Theses, Université de Perpignan, June 2014.
- [28] S. Spataru, D. Sera, T. Kerekes, and R. Teodorescu, “Diagnostic method for photovoltaic systems based on light i–v measurements,” *Solar Energy*, vol. 119, pp. 29 – 44, 2015.
- [29] E. I. Batzelis, P. S. Georgilakis, and S. A. Papathanassiou, “Energy models for photovoltaic systems under partial shading conditions: a comprehensive review,” *IET Renewable Power Generation*, vol. 9, no. 4, pp. 340–349, 2015.
- [30] M. Alonso-Garcia, J. Ruiz, and F. Chenlo, “Experimental study of mismatch and shading effects in the i–v characteristic of a photovoltaic module,” *Solar Energy Materials and Solar Cells*, vol. 90, no. 3, pp. 329 – 340, 2006.
- [31] D. Verma, S. Nema, A. Shandilya, and S. K. Dash, “Maximum power point tracking (mppt) techniques: Recapitulation in solar photovoltaic systems,” *Renewable and Sustainable Energy Reviews*, vol. 54, pp. 1018 – 1034, 2016.
- [32] P. Guerriero, F. D. Napoli, G. Vallone, V. d’Alessandro, and S. Daliento, “Monitoring and diagnostics of pv plants by a wireless self-powered sensor for individual panels,” *IEEE Journal of Photovoltaics*, vol. 6, pp. 286–294, Jan 2016.
- [33] B. P. Kumar, G. S. Ilango, M. J. B. Reddy, and N. Chilakapati, “Online fault detection and diagnosis in photovoltaic systems using wavelet packets,” *IEEE Journal of Photovoltaics*, vol. 8, pp. 257–265, Jan 2018.
- [34] K. A. Kim, G. S. Seo, B. H. Cho, and P. T. Krein, “Photovoltaic hot-spot detection for solar panel substrings using ac parameter characterization,” *IEEE Transactions on Power Electronics*, vol. 31, pp. 1121–1130, Feb 2016.
- [35] M. H. Ali, A. Rabhi, A. E. Hajjaji, and G. M. Tina, “Real time fault detection in photovoltaic systems,” *Energy Procedia*, vol. 111, pp. 914 – 923, 2017. 8th International Conference on Sustainability in Energy and Buildings, SEB-16, 11-13 September 2016, Turin, Italy.
- [36] S. K. Das, D. Verma, S. Nema, and R. Nema, “Shading mitigation techniques: State-of-the-art in photovoltaic applications,” *Renewable and Sustainable Energy Reviews*, vol. 78, pp. 369 – 390, 2017.
- [37] E. Garoudja, F. Harrou, Y. Sun, K. Kara, A. Chouder, and S. Silvestre, “Statistical fault detection in photovoltaic systems,” *Solar Energy*, vol. 150, pp. 485 – 499, 2017.
- [38] N. Mohan and T. M. Undeland, *Power electronics: converters, applications, and design*. John Wiley & Sons, 2007.
- [39] S. S. Mohammed and D. Devaraj, “Simulation and analysis of stand-alone photovoltaic system with boost converter using matlab/simulink,” in *2014 International Conference on Circuits, Power and Computing Technologies [ICCPCT-2014]*, pp. 814–821, March 2014.

- 
- [40] O. Lopez Santos, *Contribution to the DC-AC conversion in photovoltaic systems : Module oriented converters*. Theses, INSA de Toulouse, Feb. 2015.
- [41] F. Flores-Bahamonde, H. Valderrama-Blavi, J. M. Bosque, A. Leon-Masich, and L. Martínez-Salamero, “Grid-connected boost inverter for small-wind urban integration: Analysis and design,” in *IECON 2012-38th Annual Conference on IEEE Industrial Electronics Society*, pp. 433–439, IEEE, 2012.
- [42] F. Flores-Bahamonde, H. Valderrama-Blavi, J. M. Bosque, A. Leon-Masich, and L. Martinez-Salamero, “Grid-connected boost inverter for small-wind urban integration: Analysis and design,” in *IECON 2012 - 38th Annual Conference on IEEE Industrial Electronics Society*, pp. 433–439, Oct 2012.

# 3

## Diagnosis and FTC on PV systems

### Introduction

This chapter presents the work undertaken as part of this PhD to develop a real-time tool able to detect defaults, classify them, and choose solutions to remove photovoltaic systems in quasi-normal and optimal working points. The FDD strategies or methods proposed in the literature can be classified into data-driven based model methods, qualitative, or quantitative model-based methods [1]. In all the studies presented in this chapter, we use the real-time dynamic behavior of a system that can be described using a precise model.

- A data-driven based model is a methodology that extracts fault characteristics from historical data. It needs large amounts of data in order to diagnose the state of the process. The feature extraction of a process (in either a fault or normal state) can be either qualitative or quantitative.
- Model-based fault detection methods make use of a precise-system model to compare the behavior of the model with the measurements of the real system.
  - Qualitative methods based on models analyze the cause and effect relationships in a system and their relations with the system's malfunctions. This relation is qualitative and links them with deviations in the measurements.
  - Quantitative methods based on models describe the system's dynamic behavior, which is generally due to physical principles; also, it establishes mathematical relations between the system's inputs and outputs

This chapter presents the strategies used to detect fault in PV systems and the application of one strategy that tolerates shadows over PV Panels.

The first part of this chapter presents a set of fault diagnosis strategies to detect any anomaly that may occur inside or around the complete structure of a PV system connected into the grid. This paper proposes two diagnostic strategies:

- Diagnosis of PV panel that is able to detect the main faults on the DC side linked to a) shadows, b) hot-spotting, c) MPPT, and d) aging.
- Diagnosis of converters that is able to detect the faults on the AC side, which may occur on elements of the converter devices such as switches, inductors, capacitors, and resistances. Direct comparisons between converters and inverters, as well as their respective model, are needed.

The second part of the chapter includes a set of control strategies for the converter and inverter, when a fault has been diagnosed in the photovoltaic panel. The aim of this section is to be able to make a decision after a detected default; for example, isolating the part of the system with the failure so that it can continue to have a new operating mode, even if there is a component or function fault and it is simultaneously necessary to ensure safety (i.e., FTC). The fault tolerant control applied to photovoltaic systems is composed of three layers (measurement of variables; detection, isolation, and fault diagnosis; and the strengths of fault tolerant control), which will be discussed in section 3.2.

### 3.1 Fault detection strategies for PV systems

Fault Detection and Diagnosis (FDD) corresponds to a type of control able to identify anomalies in the performance of the pieces of equipment or sources. More recent advancements in FDD use, as part of complex algorithms, tools that translate the anomalies into real-world faults. They also deliver detailed notifications on the probable origin of the default and solutions of how to resolve the problem and to return to normality [2, 3]. FDD means different successive functions, such as to Detect, Locate, and Identify the type of fault when a fault occurs in the system, as described in figure (3.1). It is also interesting to add other functions to quantify the magnitude of the fault. A monitoring tool with its own FDD dedicated to PV systems is important for several reasons: 1) to relay the state of the PV system's operation to the supervisor; 2) to manage alarms to help them safely operate the system; 3) to identify the causes of faults whilst avoiding PV systems' good behavior ; 4) to quantify the lost production.

In general, the FDD identifies the possible cause of faults using a set of functions with a specific chronology based on the analysis of information such as reference models and/or the analysis of data and signals. Figure (3.1) sums up the process of fault diagnosis to obtain an accurate estimation of the magnitude of the problem in the PV system with its different functions.

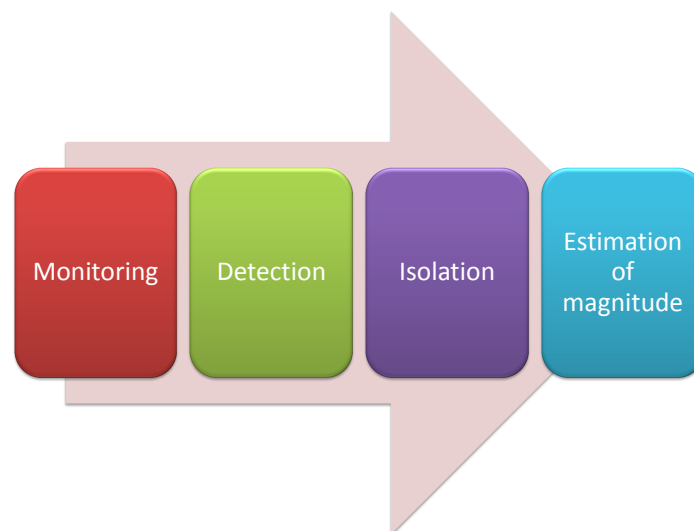


**Figure 3.1** Process of fault diagnosis (monitoring, detection, isolation)

Before designing a complete FDD that is dedicated to PV systems, it is essential to construct a list of possible faults that frequently occur in this type of electrical power production.

### 3.1.1 Fault Diagnosis system purposed

#### Classification of PV system faults proposed

The most common faults essentially occur on a PV array-level. There are two classes of faults: internal and external faults [4,5]. Internal faults in the PV module can be considered to be manufacturing faults; such as delamination, which can occur when the adhesion between the glass, encapsulating, active layers, and back layers becomes weak, and there is back sheet adhesion loss and junction box failure that takes place when there are no reliable soldering contacts between the string interconnects. This could cause high resistance, consequent heating, and frame breakage [6,7]. The faults that occur in the converter can be linked to the active components' switching problems and/or their aging. These faults can be divided into two categories: a) short-circuit fault, which is characterized by the increase in the current by up to four or five times, b) open-circuit fault with a very low current change [8]. Any other failure can be linked to each power passive component such as a capacitor that has its own lifetime or micro-controllers. Even if damages can be definitive, the thesis does not address this issue. For PV systems, the most common faults are due to external environmental causes such as partial shading, dust accumulation, and transport and installation faults. Some faults in a PV module are commonly known as hot spots. These physical phenomena are the result of accelerated aging of a PV cell part and induce a definitive lack of power production. Other phenomena are: degradation, under-performance, or heat loss, which change during the panels' lifetimes. These can be the result of external electrical problems linked to connectors, protection diodes, or intern degradation that are considered to be series and shunt resistors [9].

Figure (3.2) presents a suggested organization of main faults that may occur in a PV system. This thesis only takes certain types of faults into account, which are addressed in the following sections. The faults are classified according to the location of the fault. Faults can then be localized on the DC side [10,11] or the AC side [12].

In another possible classification, as faults and failures that occur on PV array may be either temporary or permanent, it is important to distinguish the evens after which it is possible to resume normal working and others for which performances are definitively degraded [13]. It is important to know this to be able to establish optimal strategies to make the system work normally again. Temporary anomalies are mainly due to weather conditions and, in particular, shadows. The shading impact on PV arrays can be considered to cause major changes in electrical measurements, which have a high impact on  $I(V)$  and  $P(V)$  static characteristics. Definitive damages can be caused by the apparition of hot spots [14–17]. These failures, which, in some cases, are linked to repetitive shading conditions for several years, can be the consequences of previous faults linked to infrastructure or trees situated around the PV arrays. This permanent failure of PV arrays can be detected on other sides because one of its consequences is: cracks on the part of the PV cell during a hot-spot condition, which produces energy dissipation in the panel. Thermal measurements can detect these phenomena [18,19]. If they become dangerous for the rest of the system;

for instance, inducing high localized heating in one cell, this information must be addressed in real-time, and the decision must be made to stop the system, for example.

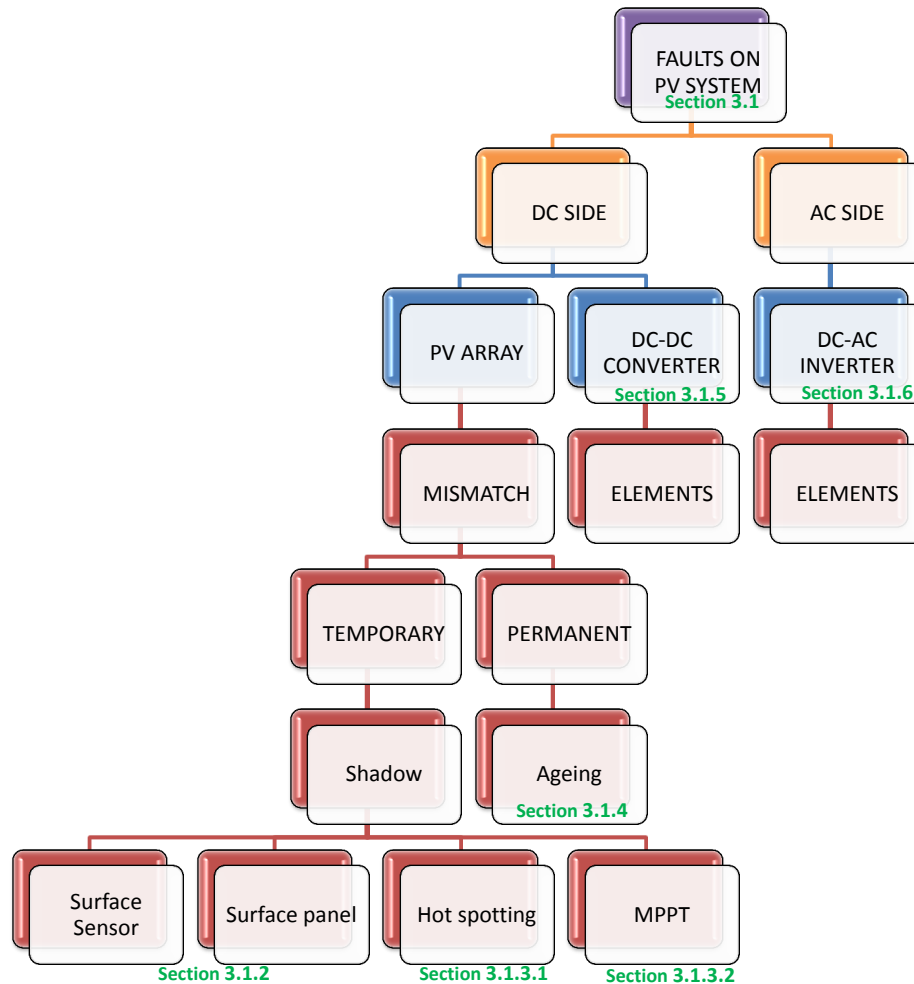


**Figure 3.2** Faults for diagnosing a PV system shown in schematic form

## Monitoring System

As shown in Figure (3.2), the FDD system's first process is to collect measurements. In our case, electrical and meteorological data were processed by our monitoring system. With a good monitoring system, an FDD can be particularly useful to detect faults [20, 21]. Figure (3.3) shows an example of a PV system dotted with its specific monitoring, which integrates an interface with FDD. In our case, the monitoring system was initially designed for four different PV arrays and their converters. This part is further explained in Appendix C.

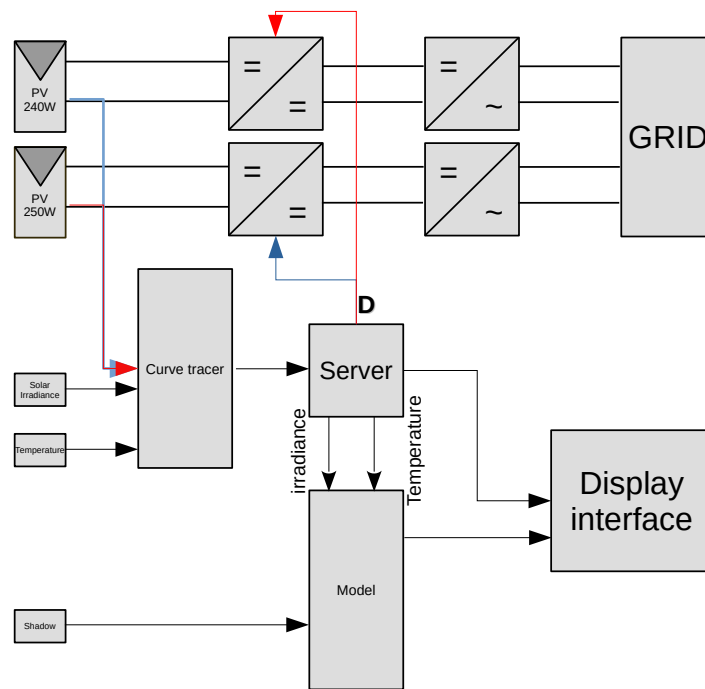


**Figure 3.3** General structure of a test and data acquisition interface

The monitoring system presented in Fig(3.3) was tested on a PV characterization platform at the LAAS-CNRS. Specifically, it used a PV panels arrangement that was located on terrace 2 of the G. Giralt building. The sensors used in this monitoring are described the following:

1. Pyranometer: KIPP ZONEN CMP 3,
2. Thermocouple: T-Type
3. Photographic Camera FLIR i60
4. I-V Curve Tracer: EKO INSTRUMENTS MP160
5. PV selector: EKO INSTRUMENTS MI-510

In order to be able to make comparisons between models and measurements, a special server and specific models are required such as the ones presented in previous chapters; and particular software is also required.

The main work undertaken in this PhD focuses on the diagnosis of temporary faults called partial shading. Figure (3.4) describes our fault-detection strategy that is based on the implemented model as well as the residuals obtained from the comparison.

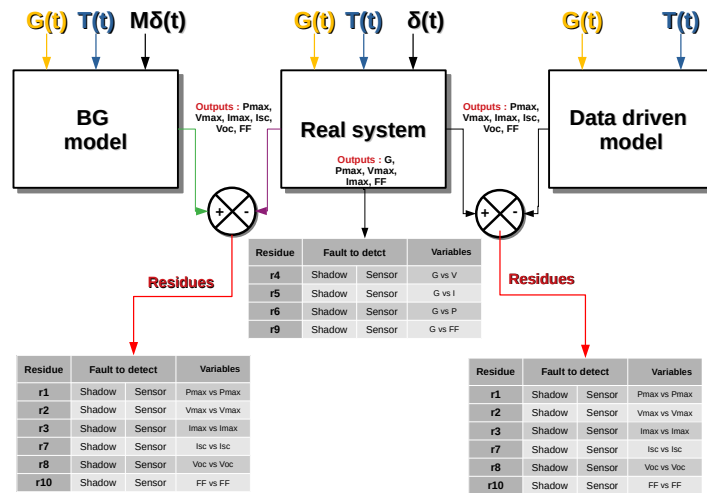


**Figure 3.4** General fault detection based on the model, real data from the system, and driven data

### Proposed FDD based on HBG models

As explained in the introductory part of this chapter, only the comparison between the real system with the HBG model was performed to validate the proposed FDD. The developed model presented in chapter 2 was allowed to describe precise physical phenomena. The comparison was then undertaken of its behavior with the system’s real electrical responses that were measured with the system’s real outputs during the whole day.

Figure (3.5) represents the comparison between the main parameters given by models and the values obtained by measurements in normal conditions. An average taken from them represents a specific function  $y = f(x)$ . Thus, our FDD was dotted with this specific function that represents the system behaving without fault. Each residue is obtained by finding the difference between real measurements in normal working conditions and the corresponding values given by models. If the comparison generates a residue with a low value, the system can be considered to not have faults. In the case that there are faults, each  $f(x)$  was specifically treated.

The following section explains each fault detection step based on residue.

#### 3.1.2 Diagnosis of temporary faults on the PV array: shading on a PV module and sensor-measurement error

##### 3.1.2.1 Analysis of real system data based on residue

The evaluation of each measurement  $(x,y)$ , with respect to the dependent function of the system  $f(x)$ , induces a new parameter for comparison (i.e.  $(x,f(x))$ ) named residue. The health of the PV module can be evaluated by analyzing each residue produced between the irradiation function and electrical measurements (e.g. V, I, P), as shown in Eq. (3.1).

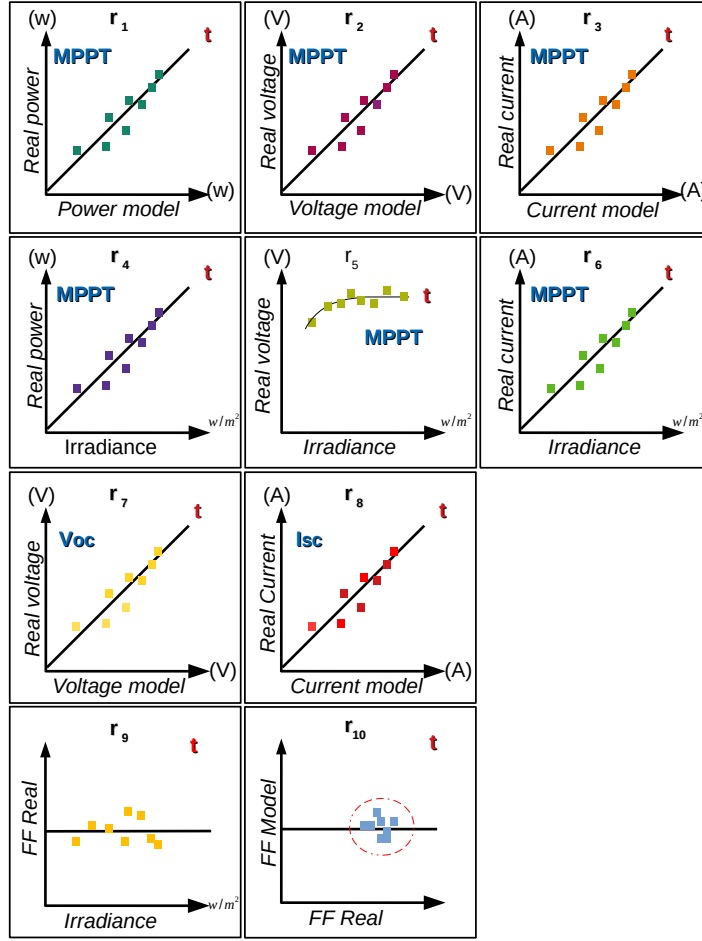


**Figure 3.5** Behavior normally followed by a photovoltaic panel

$$(x, f(x)) - (x, y) = r \quad (3.1)$$

where  $r$  is the residue. The difference or residue can be considered to be an error with a low level value (around noise and/or disturbances that are usual for real systems).  $r$  can be positive or negative within certain threshold limits. Appendix D.3 briefly explains the application of residues. The residuals generated here are sensitive to different kinds of faults, and they allow us to distinguish between them.

Different physical parameters can be studied by the function of  $G$ , which represents the irradiation level, as shown in Figure 3.6. A residue appears if the two parts of Eq. (3.1) are subtracted. A indicator of fault is when the values of these residues are more than the estimated normal values.

The normal Voltage, Current, and Power functions are, respectively, noted  $r_4 = V(G)$ ,  $r_5 = I(G)$ ,  $r_6 = P(G)$ ,  $r_9 = FF(G)$ . Figure 3.6 presents the characterization of the  $V$ ,  $I$ ,  $P$  behavior with respect to  $G$  on a PV panel, as presented in subsection( 2.1.2.1). It can be noticed that the current and the power are proportional with respect to solar irradiation.

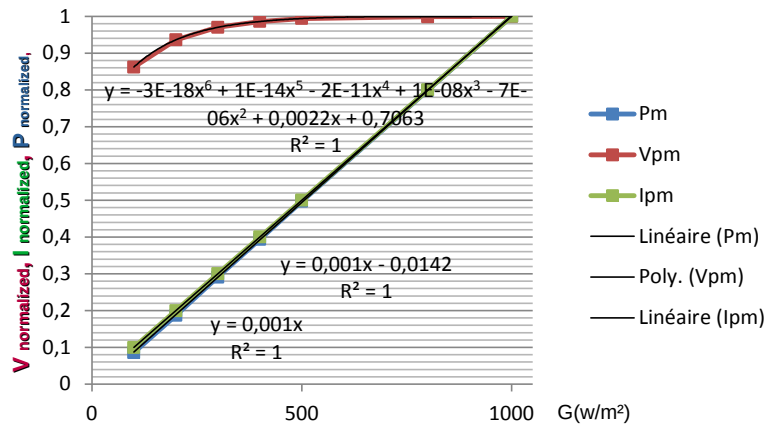


**Figure 3.6** Characterization of the mathematical model using electrical characteristics of the PV module tenesol

$r_4 = V(G)$  represents Eq. (3.2): PV voltage versus the irradiation. The PV Tenesol panel example can be described by:

$$f(x) = -3e-18x^6 + 1e^{-14}x^5 - 2e^{11}x^4 + 1e^{-8}x^3 - 7e^6x^2 + 0.0022x + 0.7063 \quad (3.2)$$

$r_5 = G$  vs.  $I$ , Eq. (3.3) represents the PV current versus  $G$  (irradiation). The PV Tenesol panel corresponds to:

$$f(x) = 0.001x \quad (3.3)$$

$r_6 = G$  vs.  $P$ , Eq. (3.4) presents the PV power versus  $G$  (irradiation), and its corresponding equation is:

$$f(x) = 0.001x - 0.0142 \quad (3.4)$$

$r_9 = G$  vs.  $FF$ , Eq (3.5) shows the Fill Factor equation, which depends on  $G$ . Fill Factor  $FF$  is a proportion factor between the maximum obtainable power (i.e., GMPP) and the product of the open-circuit voltage and short-circuit current. The behavior of  $FF$  with respect to  $G$  should be a straight line of a slope at 0.

$$FF = \frac{P_{MPP}}{V_{OC} \cdot I_{SC}} \quad (3.5)$$

It can be assumed that a  $FF$  value without faults is greater than 75% .

$$\frac{P_{MPP}}{V_{oc} \cdot I_{sc}} = 0.75 \quad (3.6)$$

Therefore,  $r_{10}$  can be written as Eq(3.7):

$$P_{MPP} - 0.7 \cdot V_{oc} \cdot I_{sc} = r_{10} = 0 \quad (3.7)$$

### 3.1.2.2 Shading on sensors: error in parameter measurements

Sensor faults can appear because of malfunctions in the components or in the sensor unit, but there can also be accuracy loss due to wear and tear, and mounting and location problems for the sensor. [22]. Some of these problems were considered:

- Bias corresponds to a constant offset/error between the actual and measured signals.
- Sensor drift: a condition whereby the measurement errors increase over time (and might be due to loss of sensor sensitivity).
- Loss of accuracy occurs when the measurements never reflect the true values of the quantities being measured.
- Freezing of the sensor signals results in the sensor providing a constant value instead of the true value.

It is possible to take into account error measurement from pyranometer, thermocouple, and MPPT in the PV generator part. The pyranometer, which is generally located on the structure of the solar panels to measure the solar incident radiation, can present measurement errors from bad calibration, dirt, or obstacles creating shadows on the sensor. Figure 3.7 (a) shows a photo of a pyranometer affected by shadow and Figure 3.7 (b) presents the solar irradiation curve with the measurement “error”.

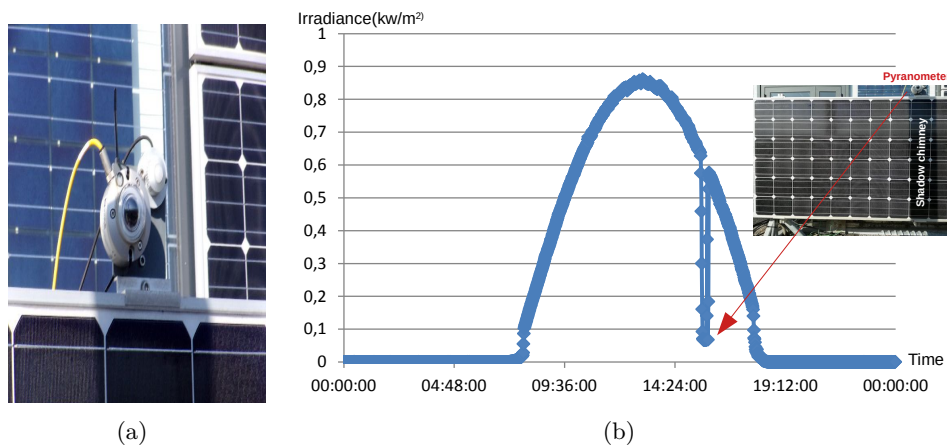


**Figure 3.7** (a) Fault from irradiation measurement and (b) PV power measurement

Thermocouples placed on the surface of the panel to discover the actual temperature of the panel can also create measurement "error". Figure (a) shows a photo of the system affected by shadow from a chimney. The I-V curve tracer uses, among other parameters, information from the temperature and irradiance sensors to adjust the curve I-V. Figure (b) shows the back of the panel with the thermocouple and the temperature measurement.

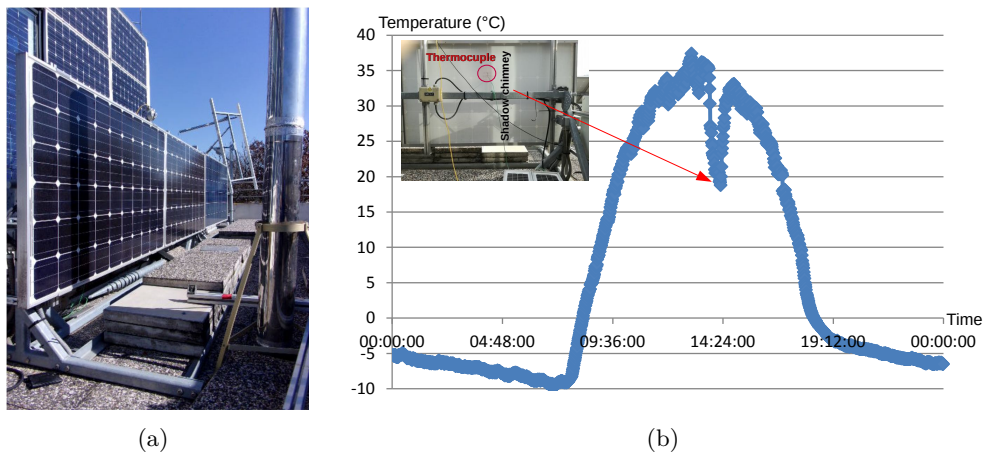


**Figure 3.8** (a) Temperature measurement fault, and (b) PV power measurement fault

### 3.1.2.3 Shadow on PV module: comparison between the real system and the model

The high granularity of the model proposed in Chapter 2 shows a lot of physical phenomena. An efficient model is the first condition to be able to obtain an efficient FDD for PV cells, modules, strings, or PV arrays. In the case of this research, the I-V and P-V curves from the model have enough information to take into account electrical problems that can occur either inside or outside the PV modules: particularly problems linked to non-homogeneous shadows because they modify the shape of these curves.

The HBG PV model can describe the system's electrical responses during the whole day in usual conditions, even if there are shadows. Even though it is complex, comparing the model with the system's real electrical outputs can easily be done. Figure (3.9) shows an example of I-V and P-V curves that are between normal operation and the fault condition under shading conditions. These curves, compared with real ones, allow us to obtain a value called residue (with positive or negative sign). If this is between normal thresholds, the system can be considered to be behaving well. This direct difference between all functions described below generates a set of residues. If treated accurately in real-time, they allow the presence of faults from the shadows to be identified.

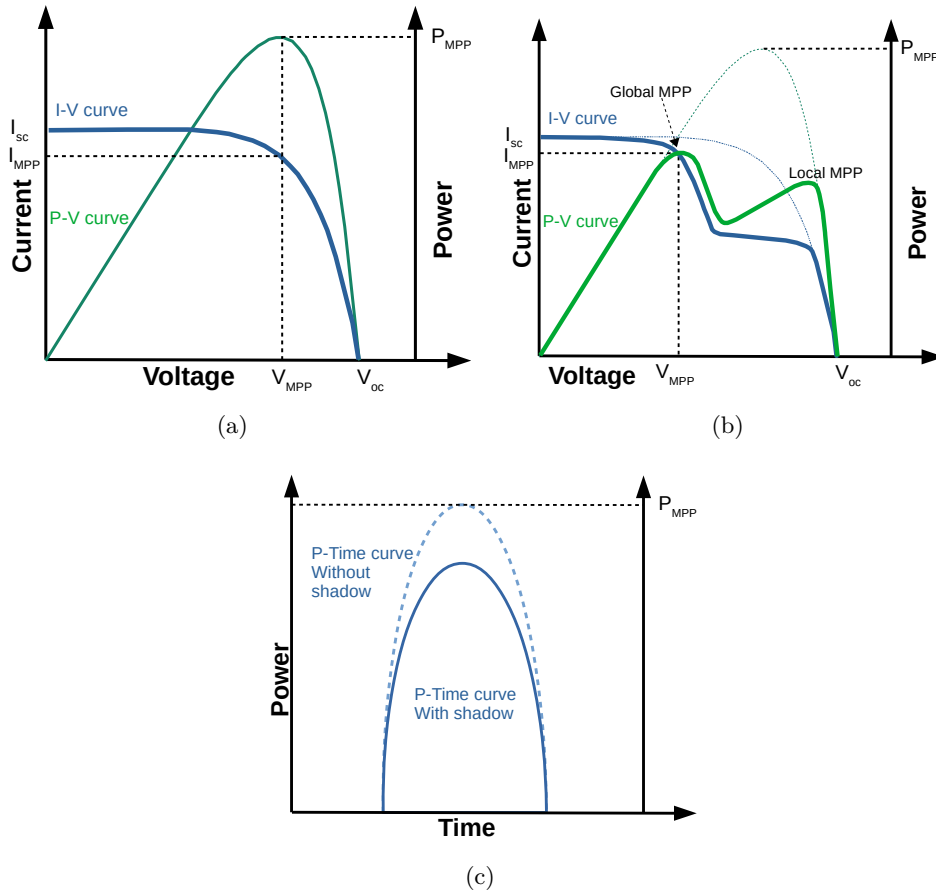


**Figure 3.9** (a) I-V and P-V curves with no shadow (b) I-V and P-V curves with shadow (c) P-t curve

The outputs model is compared to the system outputs, as shown in Figure 3.10. In this configuration, residues are made by:  $r_1 = \Delta P_{MPPT}$ ,  $r_2 = \Delta V_{MPPT}$ ,  $r_3 = \Delta I_{MPPT}$ ,  $r_7 = \Delta V_{oc}$ ,  $r_8 = \Delta I_{sc}$ . To validate our approach, different cases have been verified in the LAAS-CNRS to emulate real infrastructures shadows. These preliminary steps are important to validate our modeling and its capacity to take into account shadows as well as the real impact it has on electrical power production.

**Case 1:** A chimney was placed in front of the PV module on March 8th, 2018. During the day, the mobile shadow only partially affected some cells, as shown in Figure 3.11 (a). At 1.26pm, the average cell temperature was estimated to be  $T = 30.2^\circ\text{C}$ , and the irradiation was estimated to be  $G = 707.89\text{W}/\text{m}^2$ . Estimating the shadow magnitude was obtained by directly purchasing the values of the model's I-V and P-V curves with the real system values. With our FDD system, several pieces of information can be provided to recover faults: safe operation of the process to determine the type of anomaly, its size, its location when the fault occurred, and its duration. Three-dimensional curves can be obtained with our modelling: i.e., current-voltage-time or power-voltage-time graphs (Figure 3.11 (b)).

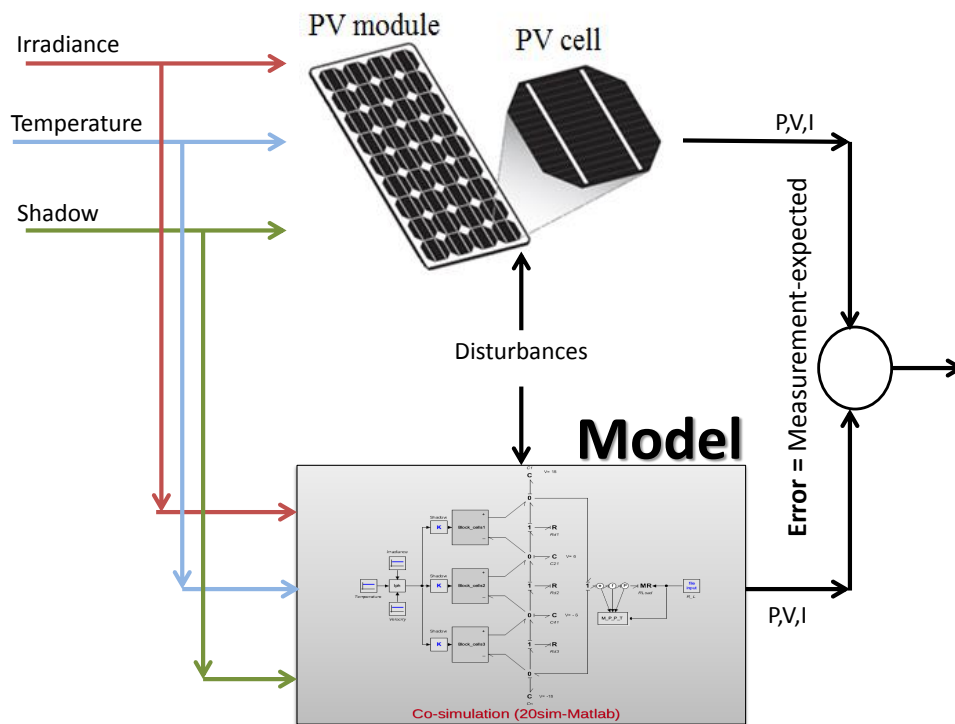


Figure 3.10 Fault diagnosis strategy based on the model

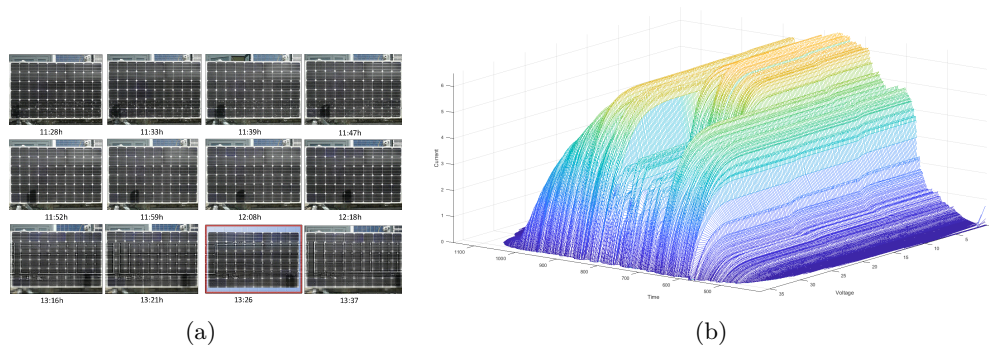
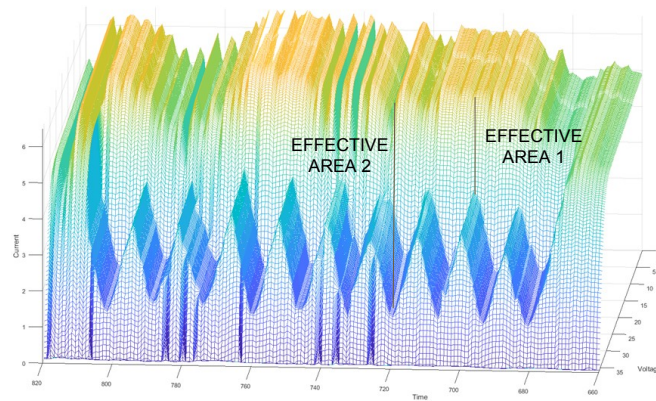


Figure 3.11 (a) Photographs of shadow evolution on a PV module during the day (b) and surface I-V-t representation produced by the shadow

Figure 3.11 (b) shows various I-V real curves obtained during a campaign measurement during the day. When the shadow is present on PV generator, an attenuation of the area is visible, which is characterized by the activation of the bypass diode. The shadow "moves" along the module during the day, and this affects PV production. Figure 3.12 represents a zoom of the Figure 3.11 (b). With FDD, it is important for the process to operate safely; the output power versus time curve and the 3D surface of power (voltage versus time) need to be analyzed.

The power residue  $r_1$  that is generated by the system can be obtained by com-

paring the expected value of the MPP ( $t$ ) with the real value obtained from the MPP ( $t$ ). A flag of value failure "1" indicates a fault detection by the diagnostician. However, in addition to the fault detection, an additional operation is needed to indicate the change of the residue state to the system.



**Figure 3.12** Zoom of I-V curves zoom in function of time

If we analyze the curves from Figure 3.11 (b) more precisely, we can deduce that the impact of the shadow drastically affects the I-V curves through the apparition of an inflection point because of the activation of the bypass diode. Two effective areas appear in function of time. It is possible to determine the moment the fault occurred from the 3D surfaces as well as the duration of the fault and its magnitude. The magnitude of the power is deduced by comparing the measurement with the model, depending on the shadow's characteristics (opacity and area).

Figure 3.13 represents the electrical generation of both PV modules on March 8th, 2018. The shadow started to affect the output power of the PV module at 11.28am. It lasted until approximately 1.37pm. This case only lasted a relatively short time because of the small size of the obstacle and the sun's position.

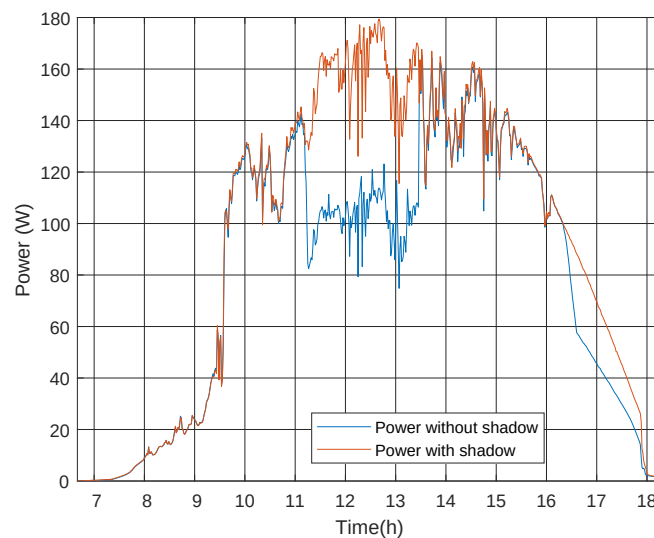


**Figure 3.13** PV output power measurements of both PV modules on March 8th, 2018

Table 3.1 shows the various results of  $\Delta P_{MPPT}$ . This shadow is smaller than in case 1 and only has one diode bypass activation. There is not a big difference in terms of output power losses in function of the shadow area during the day. Only a small shadow affects a portion of the cells in series. When the shadow covers a few cells,  $\Delta P_{MPPT}$  is higher. At 1.26pm, four cells are affected by the small shadow, one of which is the most affected 91.13% and  $\Delta P_{MPPT}$  to 48.7W. At 1.37pm, only two cells are covered: one by an area of 59.76% with  $\Delta P_{MPPT}$  to 61.94W.

Time	Temperature	Irradiance	$\Delta P_{MPPT}(W)$	$a_s(\%)$
11.28am	26.2	604.29	48.60	95.16
11.33am	25.7	641.92	51.01	82.73
11.39am	26.8	735.434	59.92	92.07
11.47am	31.8	742.04	59.36	41.65
11.52am	30.0	739.72	60.48	77.21
11.59am	29.1	745.29	60.17	70.55
12.08pm	28.8	714.05	57.86	99.88
12.18pm	30.4	739.72	57.92	86.28
13.16pm	27.8	667.94	53.78	82.34
13.21pm	29.5	653.42	52.08	67.30
13.26pm	30.2	707.89	48.77	91.13
13.37pm	30.5	705.34	61.94	59.76

**Table 3.1** Evaluation of the output power losses in function of the shaded area on March 8th, 2018

**Case 2:** A chimney was placed in front of the PV module on February 27th, 2018, as shown in Figure 3.14 (a). A mobile shadow is visible during the whole day. In this new case, a large shadow affects the three blocks of twenty cells throughout the day. The size of the shadow changes progressively during the day: it is narrower in the morning and wider in the afternoon. We chose a photograph to show the attenuation factor matrix during this test. At 2.00pm, the average cell temperature is  $T=30.3^\circ\text{C}$  and the irradiation is  $G=832.63\text{W}/\text{m}^2$ .

In the 3D curve of  $I(V)$ , the drastic attenuation of the current can be seen (see figure 3.14b), which coincides with the shadow shown in photographs taken from the panel, figure 3.14(a).

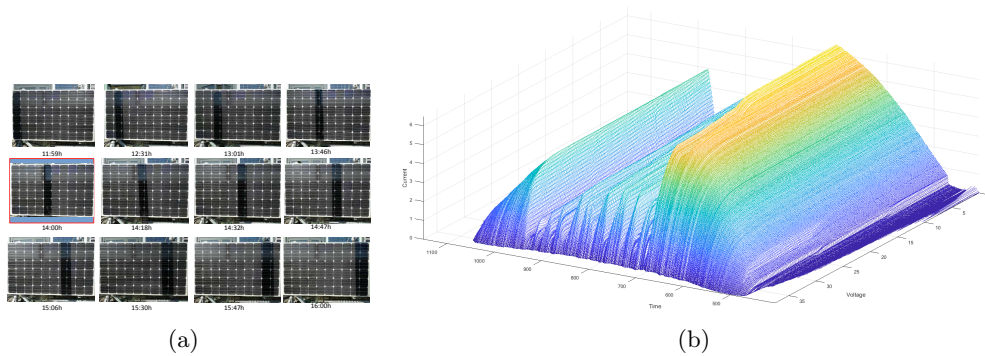


**Figure 3.14** (a) Photographs of the evolution of shadows (b) surface I-V-t produced by the shadow

Figure 3.15 shows the output power of both PV modules during the experimental test. The shadow started to affect the PV module at 12.00am until 2.00pm, and there was a drop in the power generation.

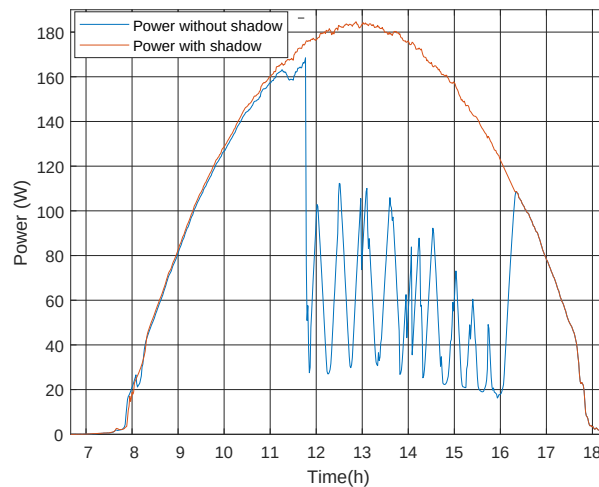


**Figure 3.15** PV output power measurements of both PV modules on February 27th, 2018

Table 3.2 shows the results from the experimental test on this day. In this case, the shadow is more significant than in the first test. Moreover, it affects the whole PV module that activates the two-diodes bypass. At 1.46pm, the shadow partially covers 12 cells. The  $\delta P_{MPPT}$  power difference is low because the larger shadow of the affected cell only covers 59.12%. At 2.00pm, the shadow completely covers six cells, which drastically affects the electrical power generation: a loss of 148.53W. The shadow distribution on the PV module affects electrical power generation when several cells are more affected by a shadow.

Time	Temperature	Irradiance	$\Delta P_{MPPT}(W)$	$a_s(\%)$
11.59am	32.4	807.54	137.47	96.98
12.31pm	33.0	833.68	129.54	79.98
13.01pm	34.2	856.91	116.70	79.87
13.46pm	34.5	832.40	77.10	59.12
14.00pm	30.3	832.63	148.53	99.56
14.18pm	20.4	802.55	113.47	88.58
14.32pm	24.0	783.04	128.93	96.49
14.47pm	31.2	759.69	105.81	82.20
15.06pm	32.1	720.90	108.43	80.29
15.30pm	29.3	637.86	119.19	87.54
15.47pm	30.0	710.80	116.74	100
16.00pm	29.2	678.28	107.59	100

**Table 3.2** Comparison of the output power of a PV module under normal operation and a PV module in shade on February 27th, 2018

The shadow distribution on the PV module affects electrical power generation when several cells are affected by a larger area of shadow. In contrast to case 1, a smaller shadow exists on the PV module and there is not big difference in  $\Delta P_{MPPT}$  between each measurement. It can be noticed that the shadow has the same electric behavior when it is small or when a homogeneous shadow only activates one diode bypass. It can also be said that temperature has a large impact on power generation losses.

#### 3.1.2.4 Error of Detection of shadow on PV panel linked to sensor generating error of measurement

Figure 3.16 represents a plane (x, y) where the P function of the irradiation is traced. The  $G$  variable is located on the X-axis and the power variable  $P_{MPPT}$  on the Y-axis. The solar irradiation goes from a minimum value (midnight) to a maximum value (midday). Therefore, the plane (x,y) allows the solar panel's abnormal behaviors to be detected.

In the plane (x, y) the system's normal and abnormal behavior zones can be clearly differentiated, as shown in Figure 3.16. The normal area of  $P$  vs  $G$  can be modeled by an area between two thresholds, which follows the same trend from midnight to mid-day and vice-versa. This characteristic allows us to determine if the behavior is "normal" or "abnormal" by using data from  $G$  and ( $I$ ,  $V$ ,  $P$ ), as shown Figure 3.17.

Concepts of residue and positive and negative thresholds of residue are developed in Appendix C. Figure 3.17 presents three areas that are delimited by lines or thresholds, which describes the values of the parameters for which the system seems to behave normally without faults for a) voltage, b) current, and c) power in a PV module.

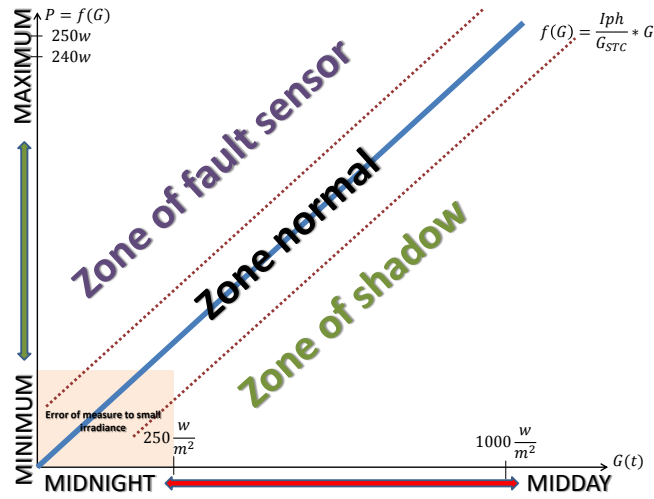


Figure 3.16 Representation of two fault-detection zones

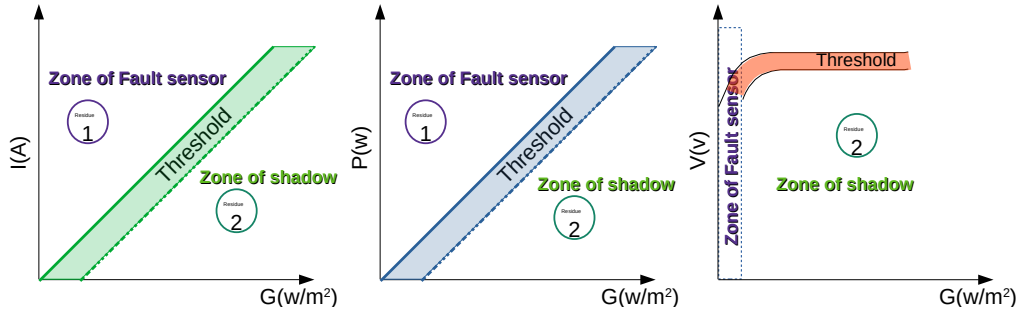


Figure 3.17 Normal Behavior parameters under normal and abnormal operation conditions

Eq. (3.8) defines the shadow detection criteria on the surface of the PV panel.

$$f(x) - y_{data} > 0 \quad (\text{residue2}) \quad (3.8)$$

where  $f(x)$  is an evaluated function of the irradiation  $G$ , and  $y_{data}$  is the value of the measurement of  $G$ .

Eq. (3.9) defines the shadow detection criteria for a pyranometer.

$$f(x) - y_{data} < 0 \quad (\text{residue1}) \quad (3.9)$$

Figure(3.18) shows the behavior of the power in function of the irradiation when a shadow only obstructs one panel, or the associated pyranometer, or both.

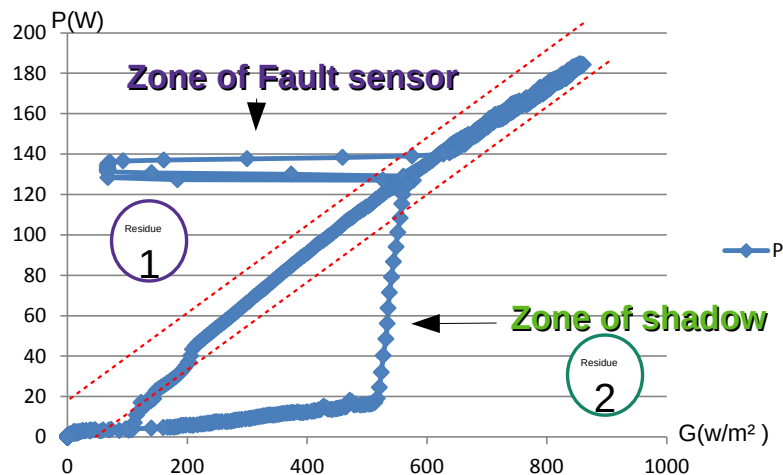


**Figure 3.18** Diagnosis of faults identifying fault sensor problems or shadow on the PV module

Residue  $r_4$  defines the normal behavior of the  $P_{MPPT}(G)$  curves, and Figure 3.19 illustrates PPM of electrical power versus solar radiation  $G$  for different months of the year during a campaign measurement.

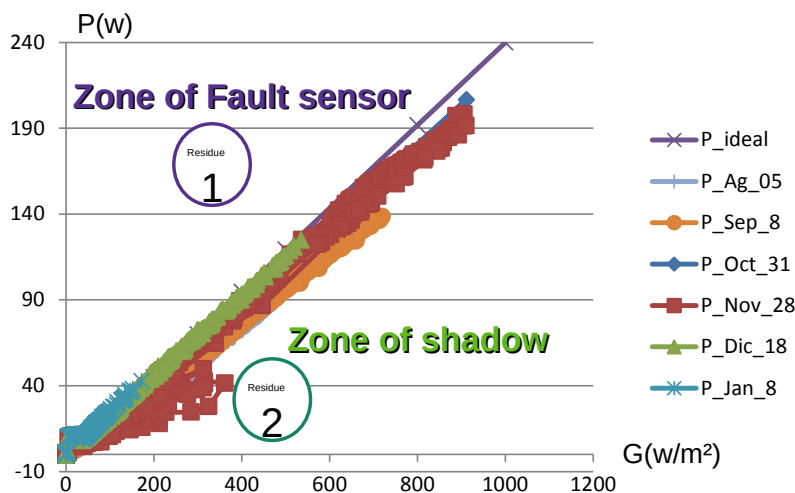


**Figure 3.19** Results of shadow detection, based on  $G$  versus  $P$

This figure shows the  $P_{MPPT}$  versus  $G$  data (during the day) for six very different days in 2018 and 2019. It can be noticed that the relationship between  $P_{MPPT}$  and  $G$  was quite linear, regardless of the weather or if days were sunny or not. The thermal effect on the panel induces a deviation in the highest part of the curves that is more important in the hottest months. The experiment was undertaken in real conditions outside the laboratory on terrace R+1 of the ADREAM platform in uncontrolled conditions. The system was able to detect shadows appearing in the morning and afternoon of November 28th.

For residue  $r_5$  that is linked to the  $V(G)$  curves, Figure 3.20 shows the PV voltage points (VPPM) measured vs solar radiation for different months.

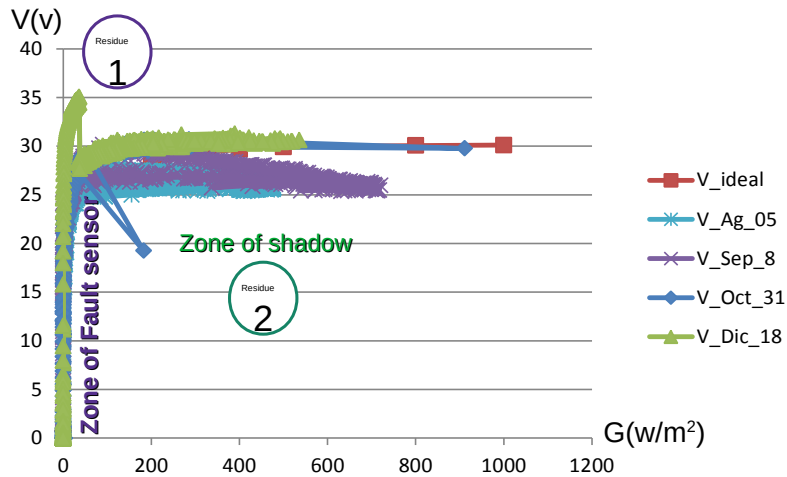


**Figure 3.20** Results of the shadow detection based on G versus V

Figure (3.20) shows the data from  $V_{MPPT}$  versus G (during the day) for six very different days in 2018 and 2019. With these measurements, it is possible to analyze three relevant faults:

- 1) it is possible to see faults in the I-V tracer of curves since, at small irradiance values, this indicates voltage values of zero, which is impossible in reality. This also indicates an accuracy error accuracy in the measurement system.
- 2) Shadow on PV panel, and
- 3) Shadow on the Pyranometer.

Table(3.3) shows the structured residuals. The residue is sensitive to two faults and insensitive to the rest. This table represents a fault signature matrix based on the residue analysis that can be detected with Eq. (3.1). If the evaluation of the residue equation is positive, there is a presence of shadow, which has an influence on the PV panel power production ( Eq.(3.8)). This is marked with the number "2". If the evaluation of the residue equation is negative, shadow is causing a measurement error in the pyranometer Eq.( 3.9).

	Residue											
Faults	$r_1$	$r_2$	$r_3$	$r_4$	$r_5$	$r_6$	$r_7$	$r_8$	$r_9$	$r_{10}$	$D_b$	$I_b$
Sensor	1	1	1	1	1	1	1	1	1	1	1	1
Shadows	2	2	2	2	2	2	2	2	2	2	1	1

**Table 3.3** Fault Matrix under shadow conditions

Table 3.3 represents residues from equations 3.8 and 3.9. When the residue is “1”, this indicates a fault in the sensor; and when the residue is “2”, this indicates the presence of shadows.  $D_b$  indicates whether the diagnostician has detected either of the two faults, and  $I_b$  is "1" if the diagnostician is able to distinguish the type of failure, see Fig(3.18) .

### 3.1.3 The diagnosis of temporary faults on a PV array: hot spotting, MPPT, and aging

Figure 3.21 describes the structure of the FDD concerning hot-spotting, MPPT, and aging. This strategy is detailed and discussed for each fault in the next subsections.

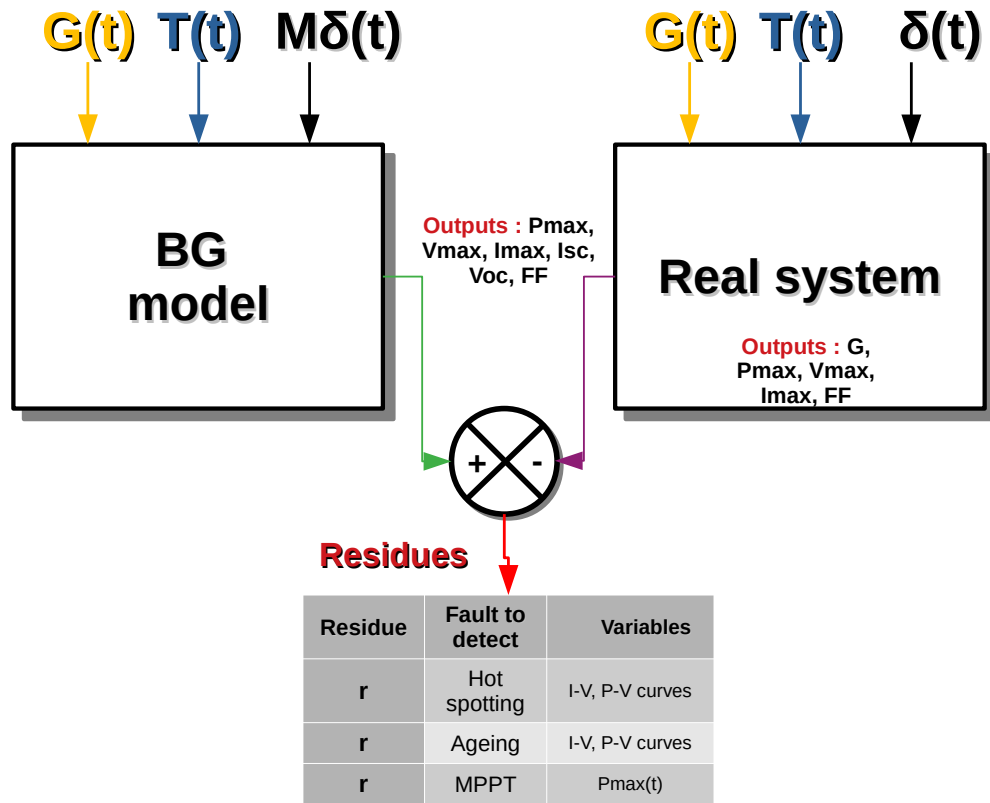
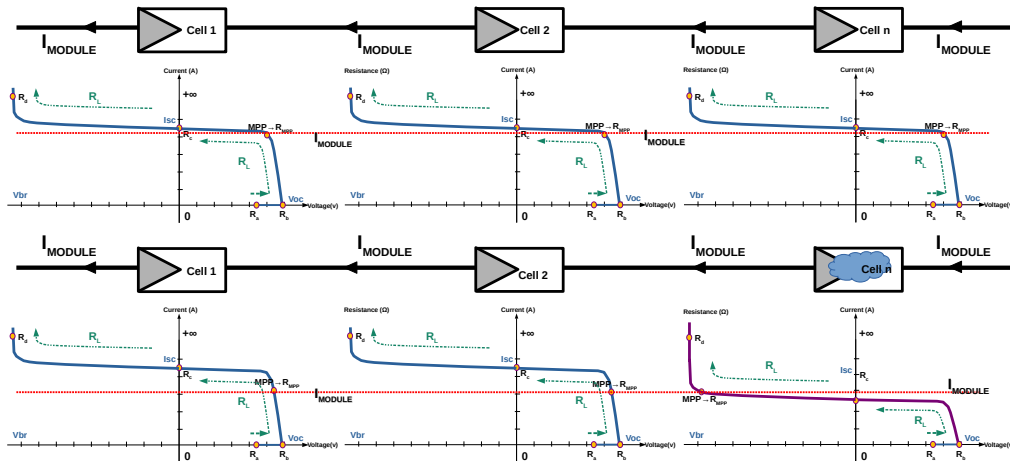


Figure 3.21 Structure of diagnosis for the PV

#### 3.1.3.1 Diagnose of temporary faults on the PV: hot spotting

Hot spotting is identified as a condition that could permanently damage the PV cells and reduce its power generation capability [23]. The term hot-spot means permanent damage or degradation to a PV cell that is a direct result of hot spotting [24]. Hot spotting in a PV cell can be defined as a temperature rise above the average temperature of the cells in the PV module. The difference of temperature is due to the dissipation of power in the cell that works in reverse-biased conditions. The dissipation of power occurs in the portion of the cell that is in shadow [25]. Figure (3.22) shows three PV cells and their respective I-V curves. In this figure, two aspects can be seen: i) the shadow on one cell affects the current of the module, and ii) the current of the photovoltaic module defines the output voltage of each cell.



**Figure 3.22** Appearance of hot-spots on the PV array and electric behaviour

In order to describe the electrical behaviour of each cell of a PV module, the photo-current term  $I_{ph}$  is replaced by the relation shown in Eq.(2.9). The following equation describes the individual behaviour of each cell, and this allows us to simulate hot spotting conditions. Eq.(3.10) describes the relationship between the cell’s voltage and current for different shading and temperature conditions.

$$I = \delta \cdot I_{ph} T_i - I_o \left[ e^{\frac{V_c + I \cdot R_s}{n \cdot k \cdot T/q}} - 1 \right] - \frac{V_c + I \cdot R_s}{R_{sh}} \left[ 1 + k \left( 1 - \frac{V_c + I \cdot R_s}{V_{br}(T)} \right)^{-n} \right] \quad (3.10)$$

Figure (3.23) shows the I(V) curves for one cell and how the temperature affects them. The main effect of the temperature is on the voltages  $V_{br}$  and  $V_{oc}$ . The temperature  $T$  affects the  $V_{oc}$  value, and  $T$  affects the  $V_{br}$  value. In Bressan [26], an IR camera used for tests proved the typical rise of temperature located on shaded PV cells and that they worked during hot-spotting.

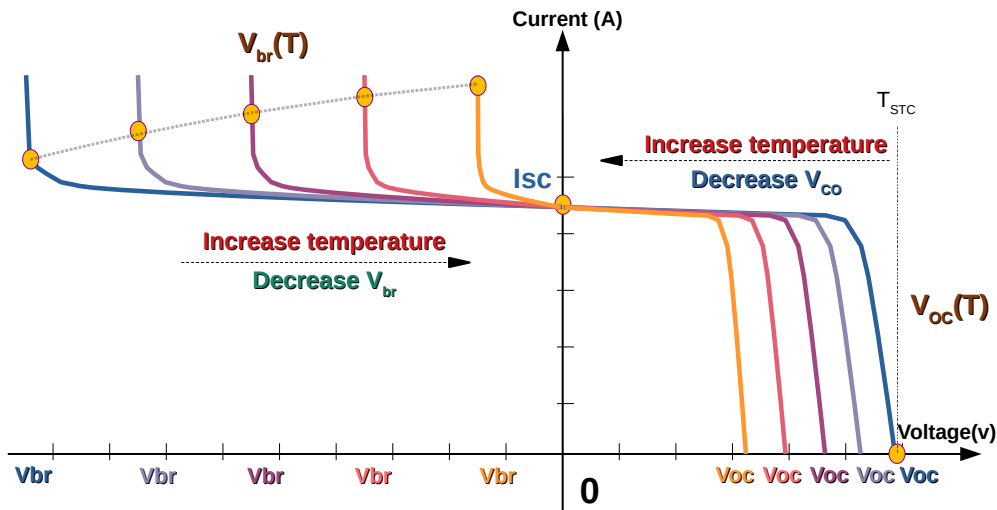


**Figure 3.23** Temperature effect on I-V curves

The main prevention method for hot spotting is bypass diodes placed in anti-parallel of several cells (two to five per panel) for a string. The purpose of the bypass diode is to prevent hot spot damage that can occur in PV cells connected in series. Bypass diodes turn on to provide a negative current in a PV cell and attempt to prevent an extreme reverse voltage bias for PV strings. However, the general misconception is that bypassing a string “protects” cells against hot spotting. In Kim’s PhD thesis [25], she proved that the hot-spotting phenomena could appear despite the activation of the bypass diodes. Eq(3.11) describes how the system’s shadow matrix is able to represent the hot spotting phenomena  $G = 632.23W/m^2, T = 30^{\circ}C$ .

$$M\delta(t) = \begin{bmatrix} 1 & 1 & 1 & 1 & 1 & 1 & 1 & 1 & 1 & 1 \\ 1 & 1 & 1 & 1 & 1 & 1 & 1 & 1 & 1 & 1 \\ 1 & 1 & 1 & 1 & 1 & 1 & 1 & 1 & 1 & 1 \\ 1 & 1 & 1 & 1 & 1 & 1 & 1 & 1 & 1 & 0.82 \\ 1 & 1 & 1 & 1 & 1 & 1 & 1 & 1 & 0.75 & 0.34 \\ 1 & 1 & 1 & 1 & 1 & 1 & 1 & 0.72 & 0.37 & 0.89 \end{bmatrix} \quad (3.11)$$

Nevertheless, this type of modeling using shadows parameters presented in Eq. (3.11) is not sufficient to describe and then detect the hot-spotting phenomena. To more precisely study the hot-spot phenomena in real cases and then have real data to identify model parameters, we have made an experimental test bench in our laboratory to artificially increase temperature and then emulate the increased value of the temperature over the most shaded cell. To do this, we used a hot air gun to heat the back surface of cell C5.10, which is the cell that was tested in reverse bias. We reproduced cases to show the limit of the bypass diode when protecting PV cells in a reverse state from hot spotting at a certain temperature. Experimental results, in particular for I(V) and P(V) curves, are shown in Figure (3.24).

These results helps us to identify the decreasing value of  $V_{br}$  in Eq.(3.10), which is linked to the increase of the PV cell intern temperature. Using this equation, the FDD that are dedicated to detecting hot-spots in the PV array are efficient.

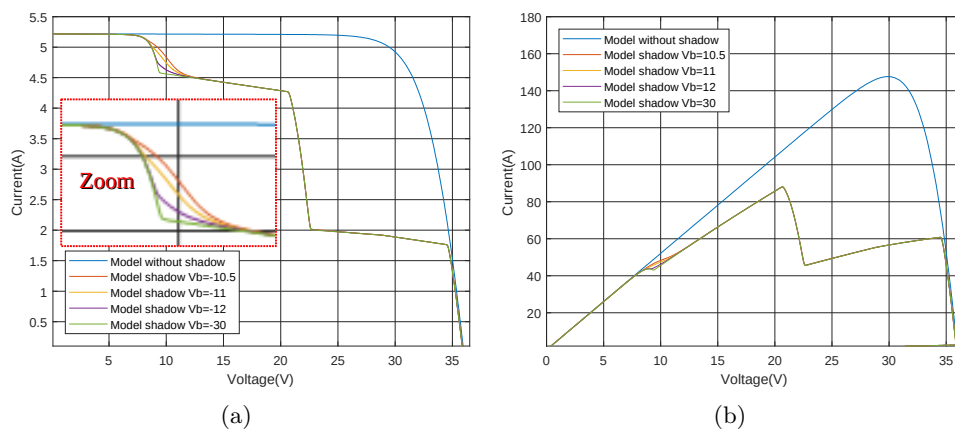


**Figure 3.24** I-V curves under hot-spots (a) and P-V curves (b)

Figure (3.24) presents I(V) and P(V) curves for the PV module under hot-spot

working conditions for one PV cell. The value of  $V_{br} = -30V$  corresponds to the limit between hot spotting either appearing or not appearing. The typical green curve  $I(V)$  can be identified as the limit of working conditions. When the temperature increases,  $I(V)$  changes, and the decrease of the  $V_{br}$  value can be identified.

Figure 3.25 shows the estimation for the hot spotting phenomenon's power dissipation magnitude. This estimation was made by calculating the difference between the model with shadow and without hot spotting and the real PV system with hot spotting. For the Tenesol 250Wc and its modeling, the estimation of power dissipation from by one cell under hot spot conditions was made using two curves, with  $V_{br} = -30V$  and  $V_{br} = -10.5V$ , respectively.

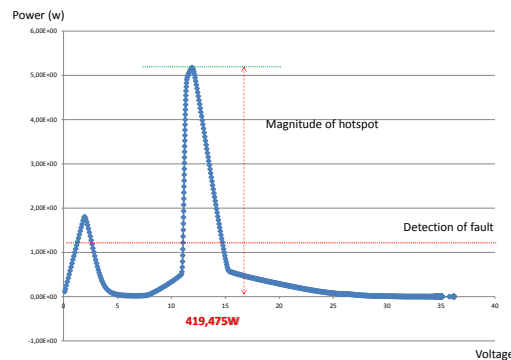


**Figure 3.25** Estimation of the hot spotting power dissipation magnitude

### 3.1.3.2 Diagnosis of temporary faults on the MPPT

Figure(3.26) a) represents the bench test used in the LAAS-CNRS PV platform used to study conditions of possible MPPT faults. It needs two distinguish between PV strings to qualify these types of defaults that are linked to trackers or implemented controllers. The two PV strings can work in different irradiation conditions. For example, the first can work with irradiation without shading and the other with two different partial shadings. An example of experimental data obtained in these conditions relates to the  $P(V)$  curves such as those presented in Figure(3.26) b) by both PV strings. Different optimal points can be established if non-homogeneous shadows are present in the same PV string, if maximum power points appear called Local Maximum Power Points (LMPP), and if there is one maximum global called Global Maximum Power Point (GMPP). Firstly, the control works on the local level (LMPP) instead of a global level (GMPP). The other case deals with the difficulty of finding the maximum power point at a low irradiation [27]. In this PhD thesis, we do not study non-compliance with MPPT algorithms, which induce a lower energy production than expected; these failures are considered to be performance failures as some MPPTs take up a lot of time finding the new MPPT and, therefore, do not adapt to certain intermittencies.

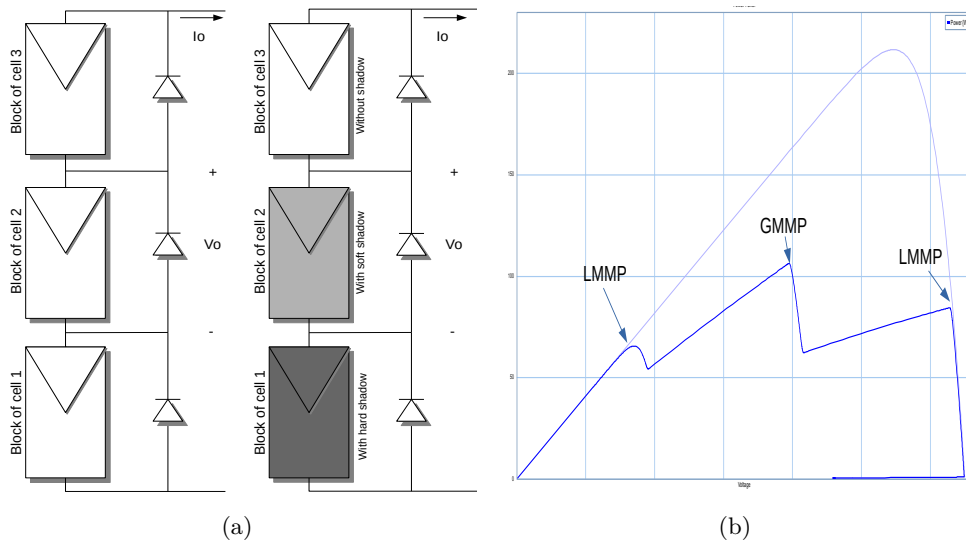


**Figure 3.26** (a) PV systems under normal and shading conditions and (b) P-V curves from both PV systems

It can be easy to represent  $P(V)$  curves with out model depending on the type of shadows and their surface impact, as detailed in the previous chapters. These models help us to design a specific algorithm that is able to find, in real-time, the GMPP under complex shadow conditions such as the work presented in Chapter 2. The first results of this study were presented in [27]. We used these high granular precision levels to built a new FDD that was able to detect fault linked to Trackers based on the model.

The following graphs show the the  $P_{MPPT}$  curves functions (time of a day); they were obtained from real cases, and the EKO 160 system can be compared with those obtained with our model. In this particular case, using a measurement collection undertaken on 22/03/2018, a low solar radiation can be seen at the beginning and the end of the day as well as certain errors linked to the EKO160 precisions inducing wrong voltage and current values and wrong real  $P_{MPPT}$ .

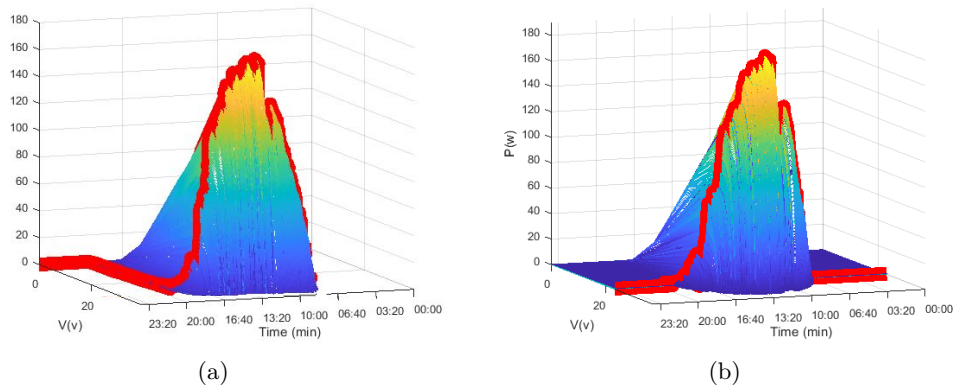


**Figure 3.27** (a) Measurement of  $MPP$  with no shadow with an EKO system in real working conditions, (b) Corresponding  $MPP$  with no shadow obtained with our model (Power measured campaign on a day with no shadow (22/03/2018))

These data are used to build the FDD based on the model that is able to detect these types of errors.

### 3.1.4 Diagnosis of permanent faults on PV: aging

Aging in PV cells can be linked to different phenomena. In our first approach, we only considered two types that could be included in our model's parameters : a) optical: degradation of the glass and losses through encapsulation (transmissivity=  $\tau$ ), and b) electrical: deterioration of electrical parts (resistance series  $R_s$ ). The aging or degradation of  $R_s(t)$  can be calculated, as shown in Eq. (3.12) [28], where  $\delta_E$  is a factor relating to electrical aging.

$$R_s(t) = R_s(t_0) \cdot (1 + \delta_E(t)) \quad (3.12)$$

Optical aging  $\tau(t)$  can be calculated as shown Eq. (3.13) [28], where  $\delta_O$  is a factor of optical aging.

$$\tau(t) = \tau(t_0) \cdot (1 + \delta_O(t)) \quad (3.13)$$

The PV array model presented in Chapter 2 takes into account these phenomena for the photovoltaic cells to modules. In our case, the effect of the electric aging factor on the resistor  $R_s$  can be parameterized differently for each PV cell inside one panel, as seen  $R_s$  in the Eq(3.14).

$$I = \delta \cdot I_{phT_i} - I_o \left[ e^{\frac{V_c + I \cdot R_s}{n \cdot k \cdot T/q}} - 1 \right] - \frac{V_c + I \cdot R_s}{R_{sh}} \left[ 1 + k \left( 1 - \frac{V_c + I \cdot R_s}{V_{br}} \right)^{-n} \right] \quad (3.14)$$

Azizi [28] proposed degradation coefficients for PV cells:  $S_i$  as  $\delta_O = 0.6\%$   $\delta_E = 0.23\%$ , for  $G=518.072 \text{ w}^2/m$ ,  $T=30^\circ\text{C}$ . Figure 3.28) presents I(V) and P(V) curves under various variations of  $R_s(t)$ . The blue curves represent the behavior of the PV array before aging. The others represent the effect of degraded  $R_s$ .

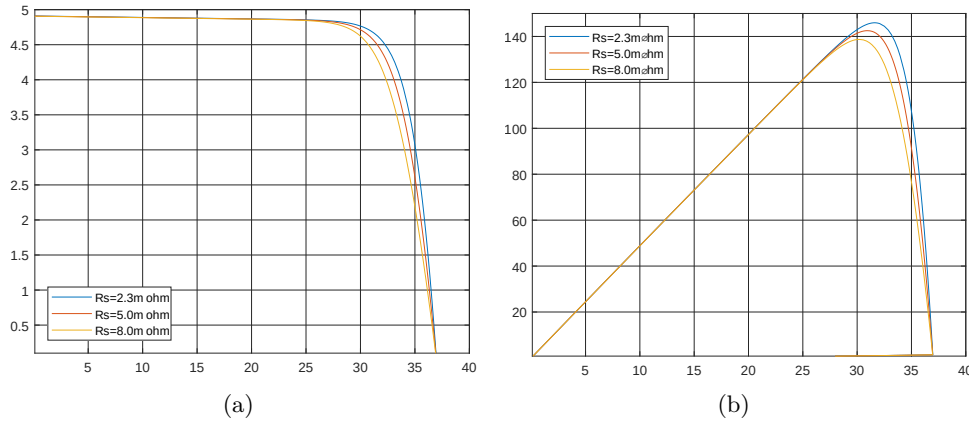


**Figure 3.28** (a) V-I Aging (b) P-V Aging

The changes in the slope of the P(G) line are associated with the increase in the value of resistance  $R_s$ . Taking into account aging linked to the  $R_s$ , this can be

modeled and included in our FDD, as shown in the figure below for the residue  $r_4$ .

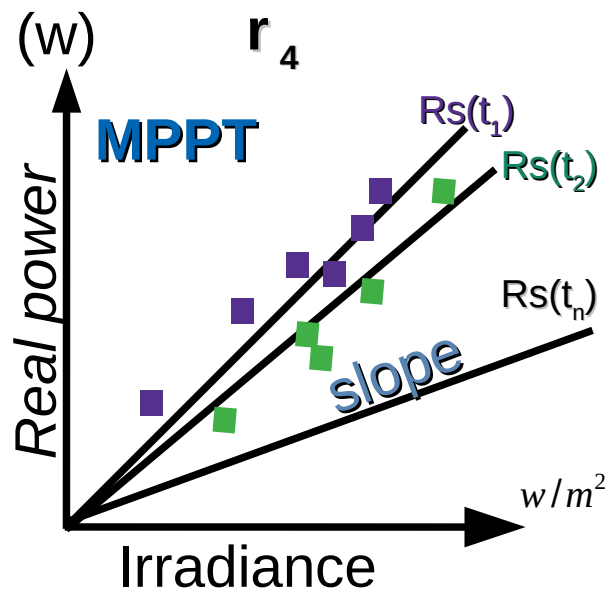


**Figure 3.29** Evolution of the P versus G slope under aging conditions

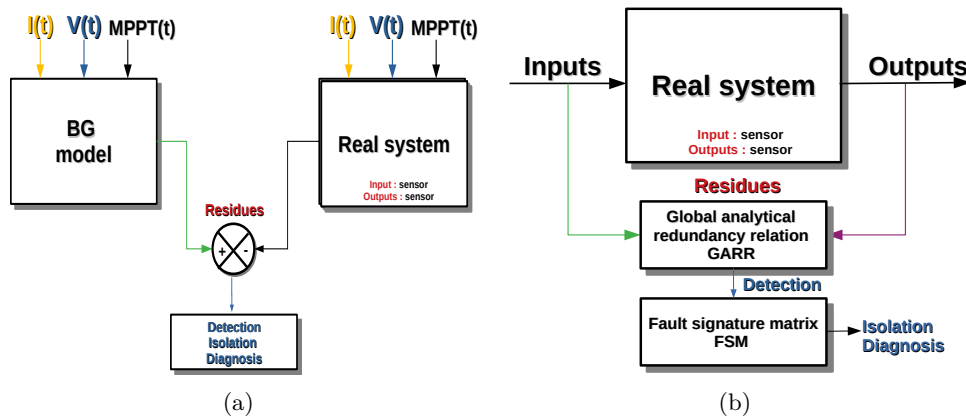
#### 3.1.4.1 Synthesis of the phenomena that our FDD can detect

In synthesis, the strategies to diagnose temporary faults that affect the PV panels proposed in this section are based on the comparison of a system that has developed models. The phenomena we can detect are failures such as shadows, hot spotting, MPPT, and aging.

### 3.1.5 Fault diagnosis on the DC-DC boost converter

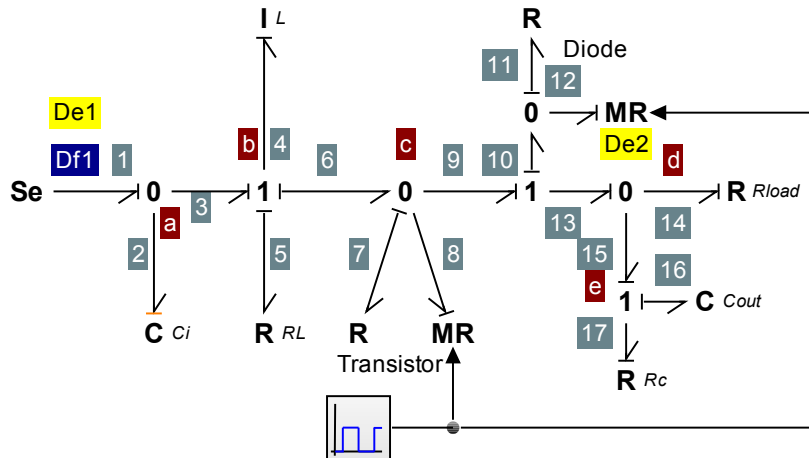
In this second section, fault diagnosis is performed the using Analytical Redundancy Ratios, which is applied to converters that require electrical interfaces between PV arrays and loads. Our approach to create a specific FDD is described in this section.

Figure (3.30) represents two strategies for fault diagnosis. The first is based on the approach we used for PV panels, as shown in Figure (3.30) a). The second uses Analytical Redundancy Analysis (GARRs), as shown in Figure 3.30 (b).



**Figure 3.30** Diagnosis structure for boost converter (a) and comparison system versus system using analytic relation redundancy (b)

Borutzky reported that semiconductors and electrolytic capacitors in power electronic converter systems had a higher failure rate than other components [29]. Figure 3.31 shows a general HBG diagram of a boost converter such as the one described in Chapter two. To validate this model and simply identify its parameters, we controlled the boost model with a simple PWM command that was able to generate a duty cycle. With this approach, we can validate our model and the values of its components.



**Figure 3.31** Diagnostic Bondgraph of the Boost converter

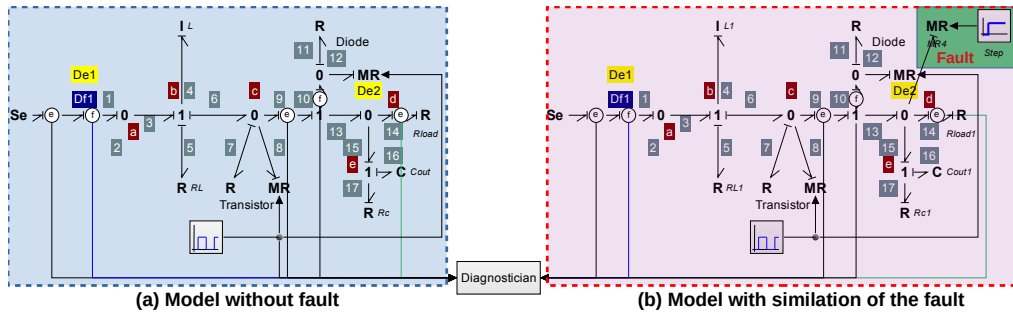


Figure 3.32 Model with and without fault

The parameter  $D_{e1}$  in our model represents the input voltage,  $D_{e2}$  the output voltage, and  $D_{f1}$  the input current. Figure 3.33 (a) illustrates the output response of the boost converter without fault. When a fault occurs on the load resistance, a voltage drop is visible in Figure 3.33 (b). The derivative calculation is performed to detect the fault.

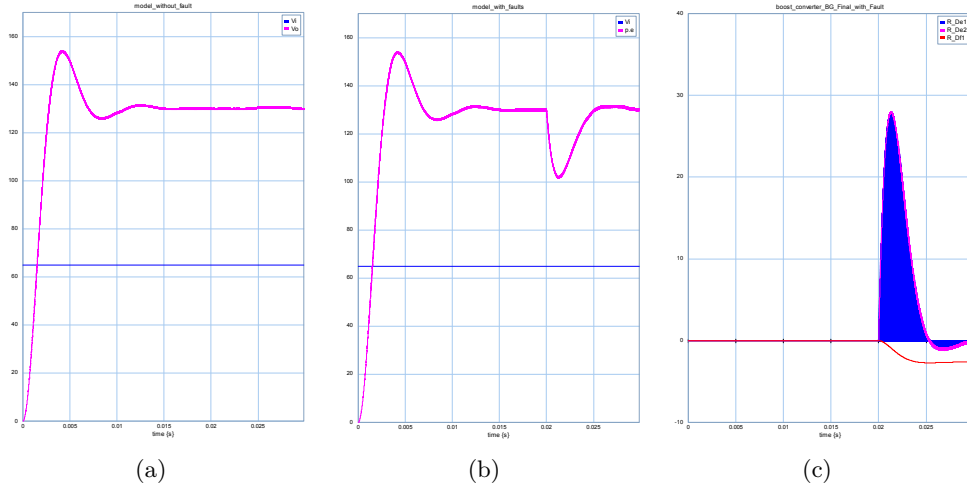


Figure 3.33 (a) Boost converter without fault (b) Boost converter with fault (c) Detection of fault

The first step of parameter identification involves finding the energy equilibrium equations based on the HBG DC DC model described in Eq. (3.15). These equations are written when the transmitter is in both the “ON” and ”OFF” state.

$$\begin{aligned}
 S_e &= L \frac{d(D_{f1})}{dt} - D_{e1} \\
 \frac{D_{e1} - D_{e2}}{R_D \parallel MR_D} &= \frac{D_{e2}}{R} + C \frac{d(D_{e2})}{dt} \\
 D_{f1} &= \frac{D_{e1}}{R_T \parallel MR_T} + \frac{D_{e1} - D_{e2}}{R_D \parallel MR_D} \\
 V_{D_{e2}} &= V
 \end{aligned} \tag{3.15}$$

where  $i_T$  represents the transistor current and  $i_D$ , the diode current. The second step is to calculate the analytic redundancy relationship with the system of

equations as shown in Eq. (3.16). These equations allow the fault signature matrix for the boost converter [29] to be constructed.  $m_1$  is the control action of the transistor, and  $m_2$  is the control action of the diode. In a healthy system operating in a continuous conduction mode, the switch and the diode open and close in opposite directions ( $m_1 + m_2 = 1$ ).

$$\begin{aligned} ARR_1 : 0 &= E - L \frac{d(D_{f1})}{dt} - D_{e1} \\ ARR_2 : 0 &= m \cdot \frac{D_{e1} - D_{e2}}{R_D \parallel MR_D} - \frac{D_{e2}}{R} - C \frac{d(D_{e2})}{dt} \end{aligned} \quad (3.16)$$

Table 3.4 summarizes the fault signature matrix regarding the boost converter's components. Five components are studied for the ARR analysis: transistor, diode, inductor, capacitor, and load resistance. When the result of the ARR is zero, noted as "0", this is an indicator that the ARR does not detect variations or fault in that component. However, when the result of the ARR is one its "1", this is an indicator that the ARR detects variations or fault in that component.  $D_b$  represents the fault detection indicator if one ARR has a value of "1". This is an indicator that there is abnormal behavior in the ARRs and that an anomaly has been detected.  $I_b$  indicates the possible fault isolation of a fault. If this indicator has a value of "1", this signifies that the faults can be isolated thanks to a unique sequence being obtained in the ARR values.

It is worthwhile emphasizing that, if it is possible to obtain a good number of ARRs from the system, they will mostly be independent. This will make it more likely that the diagnosis is able to isolate the component producing the faults in the system.

Component	Residue			
	$ARR_1$	$ARR_2$	$D_b$	$I_b$
<b>Transistor</b>	1	1	1	1
<b>Inductor</b>	1	0	1	1
<b>Capacitor</b>	0	1	1	0
<b>Resistance Load</b>	0	1	1	0

**Table 3.4** Fault signature matrix of a boost converter

Table 3.4 shows that only the faults occurring on the transistor or on the inductor can be detected and isolated. We intend to simulate the fault on transistor and to obtain the ARRs,  $D_b$ , and  $I_b$  for this case. We will carry out a similar procedure for the load resistance and obtain the ARRs,  $D_b$ , and  $I_b$ .

Fig(3.34) simulates an abrupt fault in the inductance and in the residues, respectively.

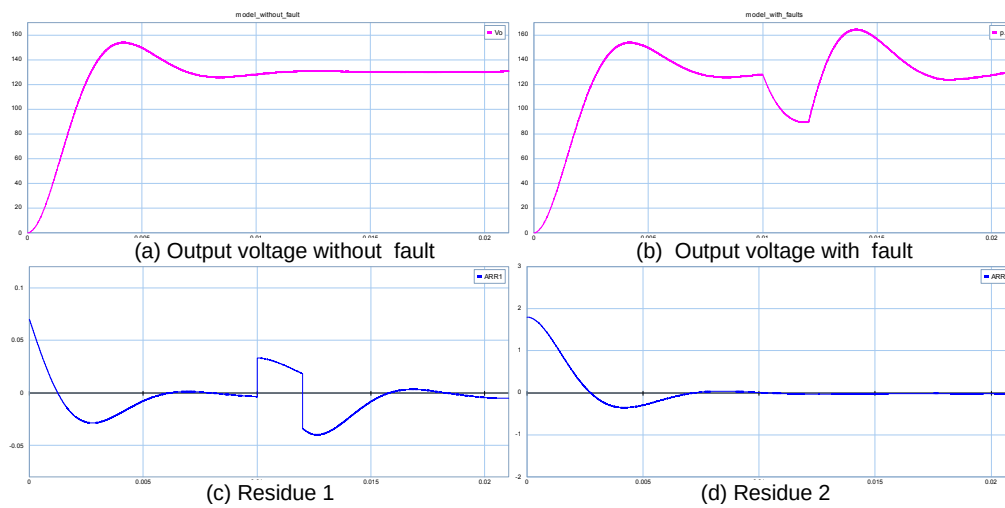


**Figure 3.34** Residues boost converter

### 3.1.6 Fault Diagnosis on DC-AC inverters

Figure (3.35) shows two strategies to diagnose faults: a) based on a model, and b) using an HBG model for a DC-AC inverter. Analytical redundancy analysis GARRs tells us about the component's electric behaviour, and explains this for the boost converter.

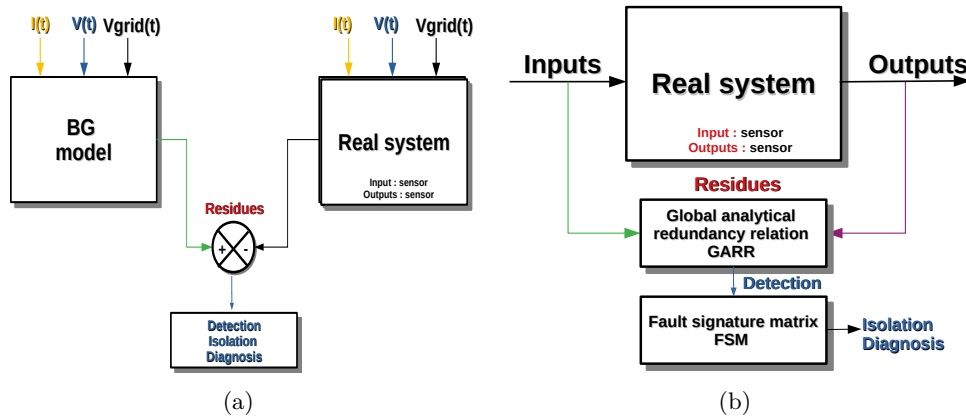


**Figure 3.35** General structure of diagnosis for the inverter (a), and comparison system versus a system that uses analytic relation redundancy (b)

#### 3.1.6.1 Fault diagnosis on DC-AC that can be connected to the grid

Figure (3.36) shows the HBG model for a H bridge DC-AC inverter developed to diagnose fault methods. The sensors that allow this inverter to be controlled are:  $Se$ ,  $PLL$ ,  $Df2$ . When we add the sensors  $Df1$ ,  $De1$ ,  $De2$ ,  $De3$ ,  $De4$ , the fault matrices and their respective ability to detect and isolate the faults will be compared.

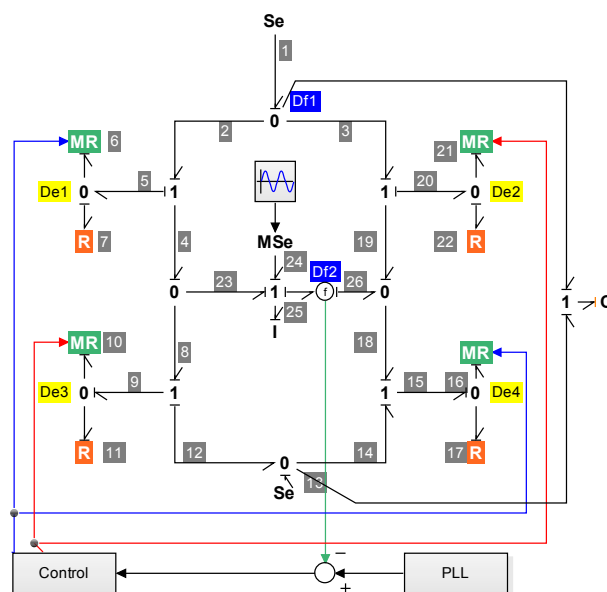


**Figure 3.36** HBG model of H bridge DC-AC inverter str

The diagnostic strategies presented in Figure (3.35) will be tested on this DC-AC inverter. Thanks to the granularity of the developed model, we can compare a model without faults and a model with faults, see Figure (3.37). The conduction state of the switch 2 transistor is modeled by the MR element, and the non-conduction state is modeled by the R element. The modeling of the fault when the switch is in a conduction state is simulated by the fault block.

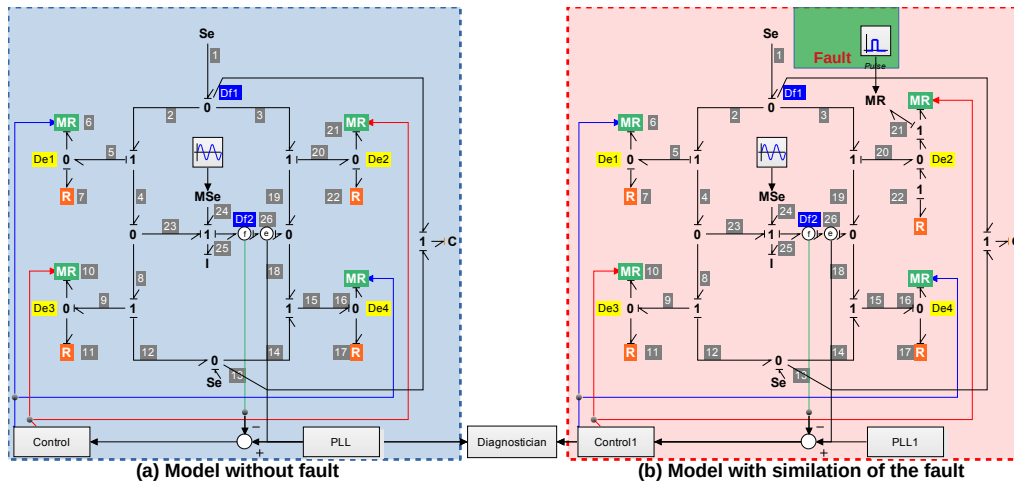


Figure 3.37 Model with and without fault

Figure (3.38(a)) presents the results from the simulation of the system with and without failure in switch 2. The occurrence of an abrupt conduction fault in switch 2 is simulated between 1.6 and 1.75 seconds.

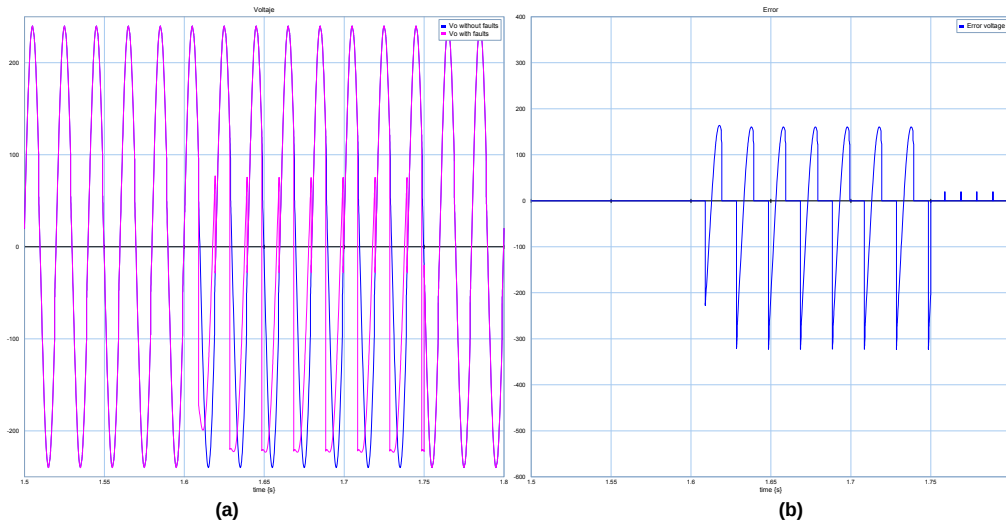


Figure 3.38 (a) Output Voltage (without/with faults), (b) Detection of fault

Figure (3.38(b)) shows the error between both signals that allows the fault to be detected.

### 3.1.7 General diagnosis of the PV system

A general diagnosis can be considered to be made up of the three independent diagnoses, as seen in figure (3.39): one diagnosis for the PV generator, one for the DC-DC converter, and one for the DC-AC inverter, see Table (3.5).

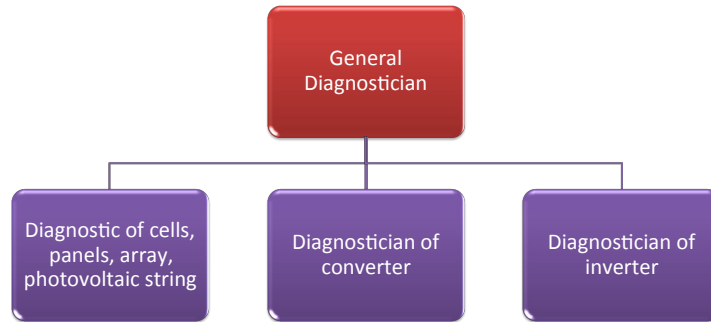
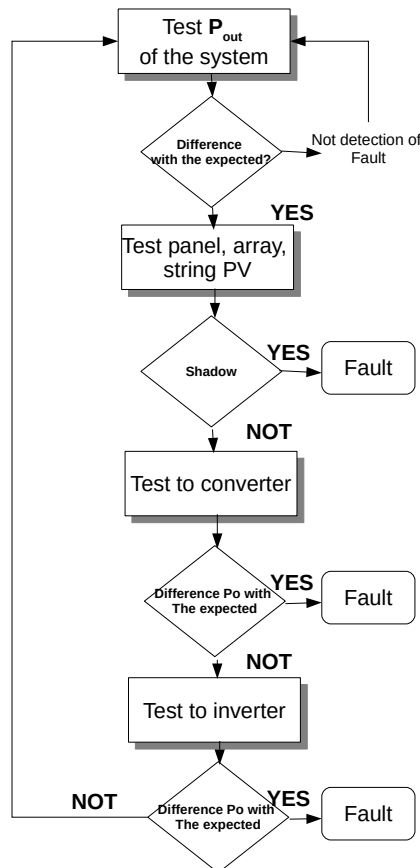


Figure 3.39 General Diagnosis

In addition, assuming there is a single fault in the system, a specific algorithm can be associated with a general diagnosis of the system such as the one presented in figure (3.40)



	Flag		
PV	1	0	0
Converter	0	1	0
Inverter	0	0	1

Table 3.5 Fault signature matrix

Figure 3.40 Algorithm of the PV Diagnostic

### 3.2 Fault Tolerant Control on the PV system

The aim of this section is to react to a fault when it is detected and isolated so that the system can continue or recover its normal or quasi-normal operation, even in the presence of a component fault. It also ensures safety. Fault tolerant strategies are categorized into two classes using either a passive or active approach. [30].

- Passive FTC relies on a robust controller of fixed structure that enables a set of faults to be taken into account at the system design stage.
- Active FTC is a challenging task because the parameters of a control algorithm must be changed online by a supervision system.

Blanke [31] presented the integration of a Fault Detection and Isolation system (FDI) which is a re-configurable control and Fault-tolerant control systems. Once the diagnostician fulfilled its task of locating the fault, the fault-tolerant control stage must generate a strategy that allows it to continue working safely. This can concern a redesigned or reconfigured part of the hard structure, the soft structure, or both depending on the nature of the fault. A Fault Tolerant Control (FTC) applied specifically to the PV system must be dotted by a specific FTC dedicated to the DC side able to redesign of the control strategy while an FTC for the AC side may be able to reconfigure the system and its connection to a grid or a load. Figure 3.41 represents the structure of an FTC with feedback system [30].

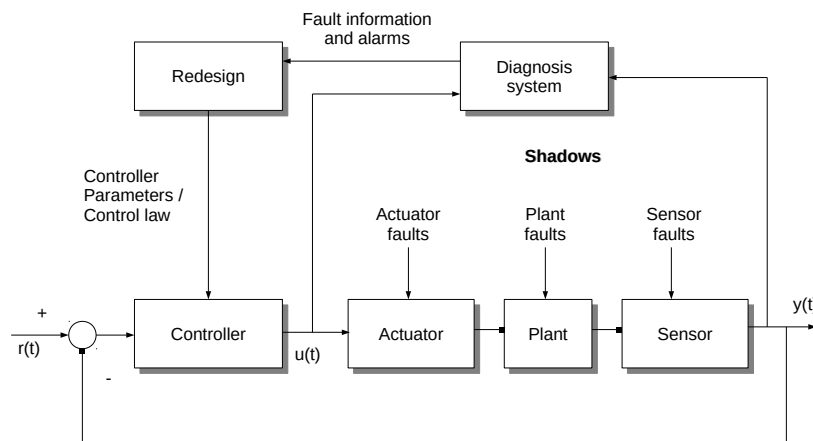


**Figure 3.41** FTC Structure for a PV system

An important criterion to judge the suitability of a control method for the active fault-tolerant cooperative control AFTCC is its ability to be implemented and to maintain an acceptable (nominal or degraded) performance in the impaired system in an on-line real-time setting. In this regard, the following requirements should be satisfied [30]:

- controller must be re-configured in real-time constraints;
- re-configured controller should be designed automatically with little trail-and-error and human interactions;

- the selected strategy must provide a solution even if the solution is not optimal.

The FTC applied to PV systems is composed of three layers:

- measuring variables (addressed in Chapter 2),
- the Detection, Isolation, and Fault Diagnosis functions (discussed in Chapter 3),
- the strengths of fault tolerant control (discussed in this section (AFTCC) that are associated in some cases with hard re-configurable power interfaces),

as seen in Fig(3.42)

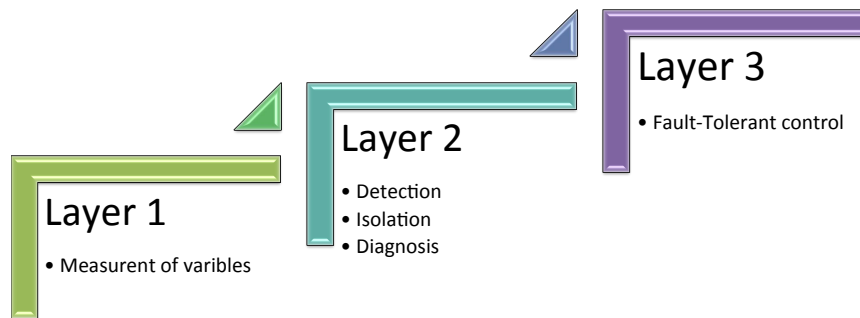


**Figure 3.42** Layer FTC

We assume in this section that there is only a single fault in the PV system. We suppose that its magnitude can be detected, isolated, and estimated by the general diagnosis, as shown in Figure 3.40

- Faults in PV panels:
  - Re-design: implementation of a control strategy that tolerates shadows and makes changes to the converter control strategies. The strategy consists in adapting control surfaces of the DC-DC and DC-AC converters.
  - Re-configuration: implementation of a re-configurable photovoltaic architecture strategy based on the fault diagnosis. This depends on the redundancy in the architecture.
- Faults in converters:
  - Reconfiguration: Dependent on the architectures of PV systems, as shown in Figure 1.14. It is possible to construct strategies based on re-configuring the converter connections; however, it depends on the redundancy in the architecture.

### 3.2.1 FTC: Redesigning strategies

#### 3.2.1.1 Strategy based on: Boosting the converter and H-bridge inverter

The task of designing fault-tolerant control (FTC) strategies is based on the change of the control surface when there are faults, even when there is shadow, and it starts in the lab. The complete FTC control strategy (tolerating temporary faults) can be separated into two cases. The first function involves getting the maximum power out of the DC-DC converter output. The second function treats the output of a DC-AC inverter and its ability to be synchronized with the AC grid in either amplitude and frequency or its ability to create and control the voltage of an isolated micro-grid. Figure 3.43 shows the proposed FTC structure with the PV panel, DC-DC, and DC-AC converters to be able get the maximum output power when there is shade.

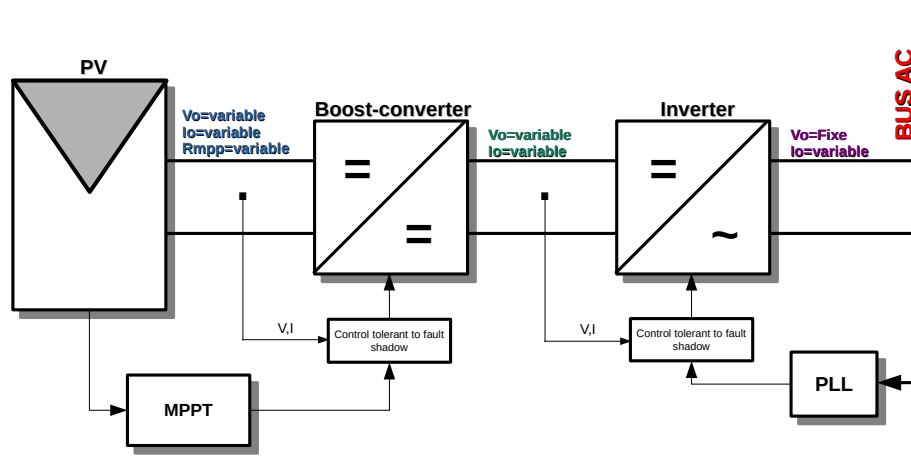


Figure 3.43 Fault-Tolerant Control on the PV system

#### DC-DC boost converter

In previous research undertaken at LAAS in cooperation with the University of Rovira i Virgili in Tarragona on MPPT and non-linear controls, the theoretical models were based on new concepts such as gyrators (MGY modulated gyrator), DC transformers ( MTF modulated transformers), and Loss Free Resistors, which are considered as three canonical elements that can be used to model the DC energy conversion of DC-DC converters [32–35]. The strategy to boost control chosen in this work is based on the sliding mode control. The previous concepts modeled by BondGraph requires a reference resistance value to be controlled such as a Loss Free Resistor, as shown in [36]. Theoretically, it corresponds to an optimal resistor value that is linked to the point of global maximum power. A GMPPT algorithm developed in this thesis is coupled with this FTC control strategy of the DC-DC converter. The main MPPT output variable is the resistance to establish the duty cycle. This is undertaken to obtain the maximum power output.

The Maximum Power Transfer (MPT) from the source to the load in a DC-DC

converter is obtained when the load resistance is equal to the optimal internal resistance of the converter.

Figure (3.44) presents a PV structure with an elementary boost converter and a strategy control using MPPT. The extraction of the MPP is performed to supply the inverter at its optimal efficiency and to generate the maximum energy for injection into the grid. Therefore, the DC-DC converter must be resistive at the input port, whereas it seems to be a power source (an LFR) at the output port. The DC-DC boost converter can be made to be an MTP if there is a proportional relationship between the input voltage and the input current. The control of the input port can then be designed using either the input resistance ( $R$ ) or the input conductance ( $G$ ) as a control variable. A sliding surface which involves these two variables and a proportional constant ( $R$  or  $G$ ), can be proposed to obtain a Sliding Mode Control-MTP property, as Lopez demonstrates in ([36]). Sliding Mode Control (SMC) is a nonlinear control strategy that modifies the dynamics of a nonlinear system by applying a discontinuous control signal that forces the system to "slide" along a cross-section of the normal behavior system.

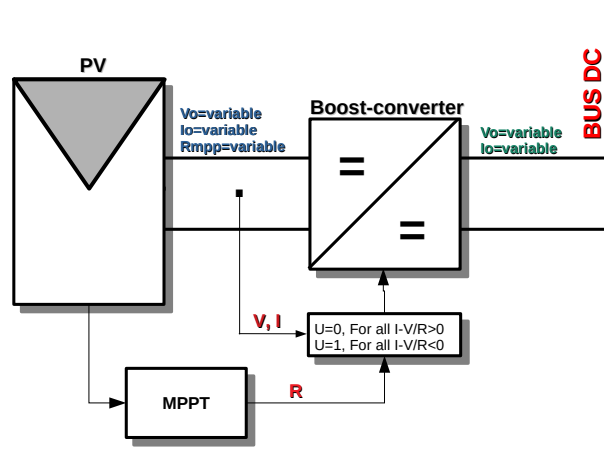
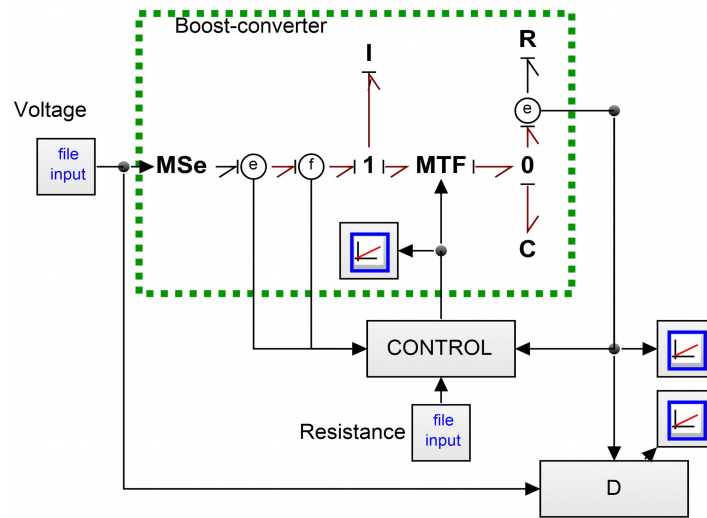


Figure 3.44 Strategy boost and MPPT

Sliding Mode Control (SMC) is a nonlinear control strategy that modifies the dynamics of a nonlinear system through applying a discontinuous control signal that forces the system to "slide" along a cross-section of the normal behavior system [37]. Figure (3.45) presents the HBG model of a conventional boost-converter with the sliding mode control strategy.



**Figure 3.45** Boost converter with a control strategy

The control strategy expressed in terms of sliding surface is shown in Eq. (3.17)

$$S(x) = I_{L1} - \frac{Vi(t)}{R(t)} \tag{3.17}$$

where  $R(t)$  is the resistance given by the MPPT algorithm, ensuring that the maximum power point is tracked,  $Vi(t)$  the input voltage, and  $I_{L1}$  the input current. In sliding mode, if  $S(x) < 0$ , then  $U = 0$ , if  $S(x) > 0$  then  $U = 1$ .

Figure 3.46 shows the output (red line) and voltage input (blue line) for the boost converter during a campaign measurement (March 23rd, 2018). The output voltage is variable and depends on MPP.

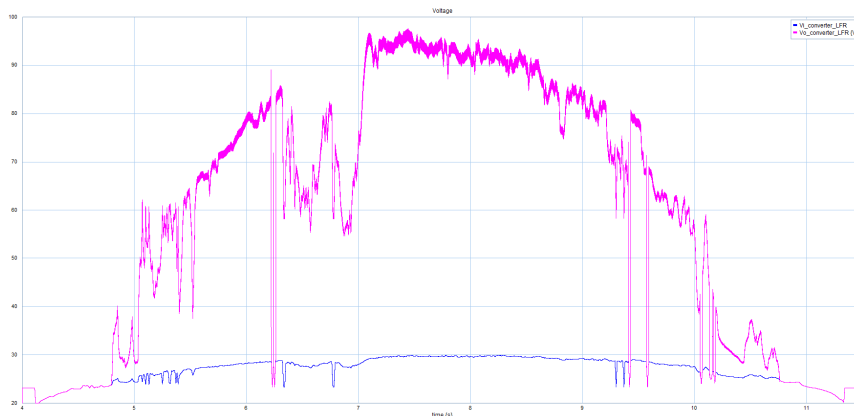


**Figure 3.46** Representation of the input and output voltage of the boost converter for the whole day (March 23rd, 2018)

### DC-AC converter

This section studies the connection of a full bridge converter to the grid through a series inductors. Figure 3.47 presents the global control strategy scheme and

links the MPPT block with power blocks to boost converters and inverters.

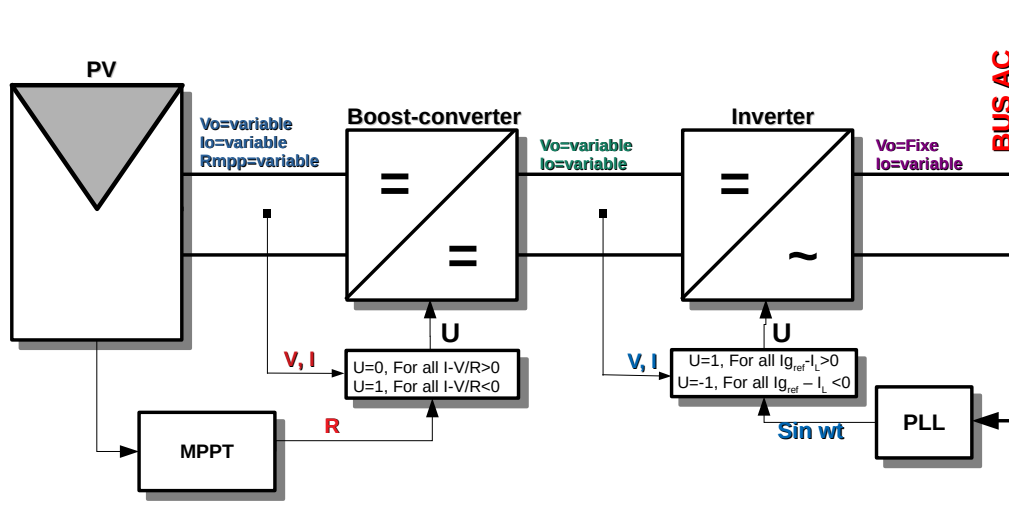


Figure 3.47 Control strategy for the boost and inverter

Lopez Santos [36] presented criteria to select the value of the inductor and the capacitor of the full bridge converter, as shown in Figure 3.48

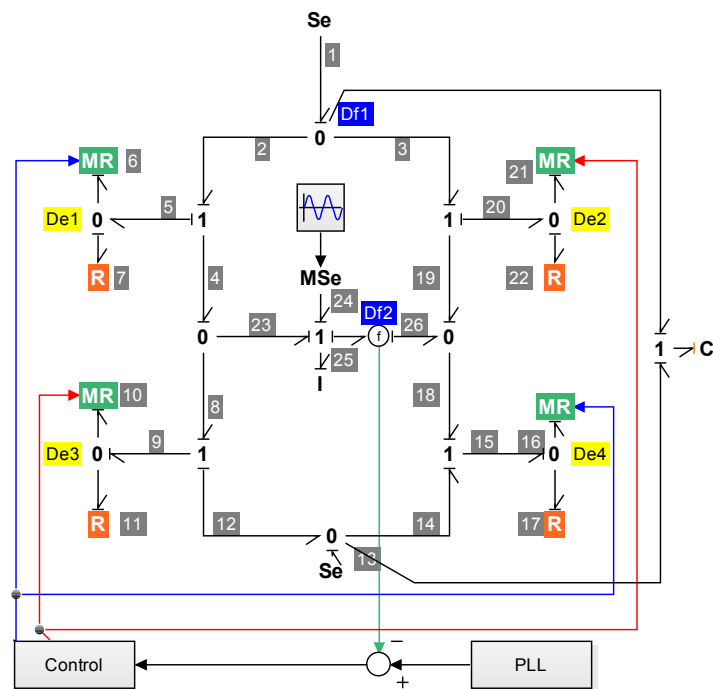
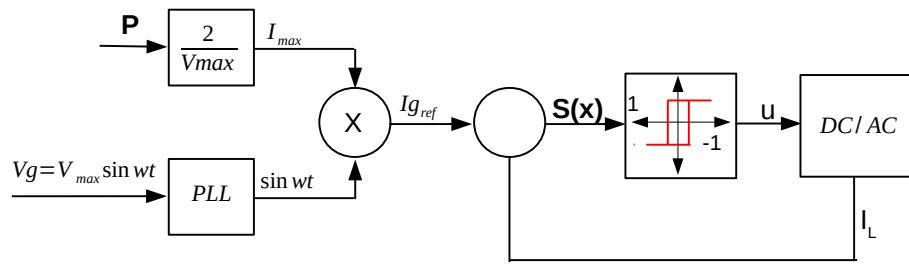


Figure 3.48 HBG model of DC-AC inverter with control strategy

Figure (3.49) presents the sliding mode current control of the inverter where  $V_g$  is the AC voltage source (AC grid) that is considered to be a pure sine-wave signal i.e.,  $V_g = V_{max} \sin(\omega t)$ .  $P$  is a real power source i.e., converter output .



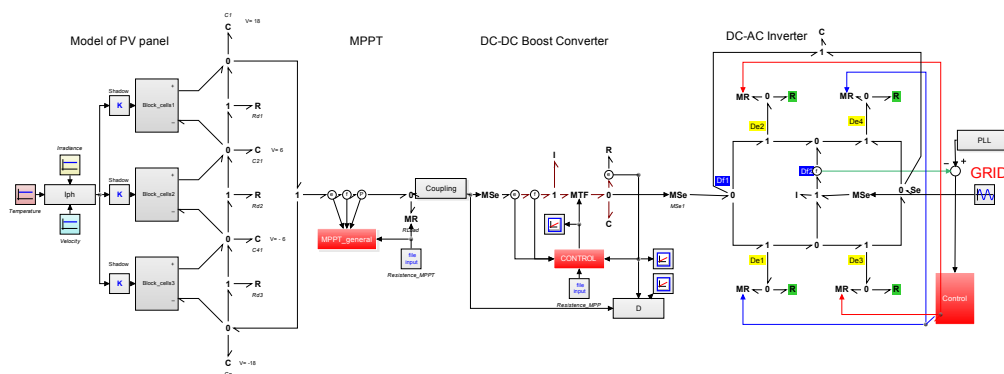
**Figure 3.49** Block diagram representing the current loop control of the inverter, adapted from ( [36])

The DC-AC converter must convert the DC power available at the output ports of the DC-DC converter on AC and inject it into the electrical grid while respecting norms of frequency and amplitude. This can be done by ensuring a power factor ( $PF$ ) equal to one. The sliding surface of the DC-AC inverter is shown in Eq. (3.18).

$$S(x) = i_{g_{ref}} - i_L = i_{max} \cdot \text{Sin}(wt) - i_L \tag{3.18}$$

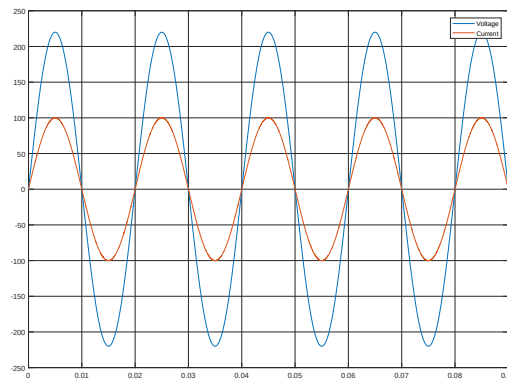
the current loop makes sure that  $i_L = i_{g_{ref}}$ , and hence  $i_g = i_{max} \cdot \text{Sin}(wt)$ . The sliding motion is obtained using the control strategy, when  $S(x) > 0$   $u = 1$ , when  $S(x) < 0$   $u = -1$ .

Figure 3.50 presents the complete model of the PV system with the proposed fault-tolerant control strategy.



**Figure 3.50** PVS Model with BG

Figure (3.51) presents the system's voltage and current output signal that is connected to the 220V, 50Hz electrical network.



**Figure 3.51** Representation of the input voltage, output voltage, and output current

### 3.2.1.2 Strategy based on: Boost DC-AC inverter

This control strategy requires a reference voltage value and the proposed MPPT algorithm that has been developed in this thesis. The Boost inverter is a transformer-less power converter that boosts an AC output voltage from two individual bidirectional DC-DC Boost converters developed by Alonso Gutierrez in his PhD thesis [38].

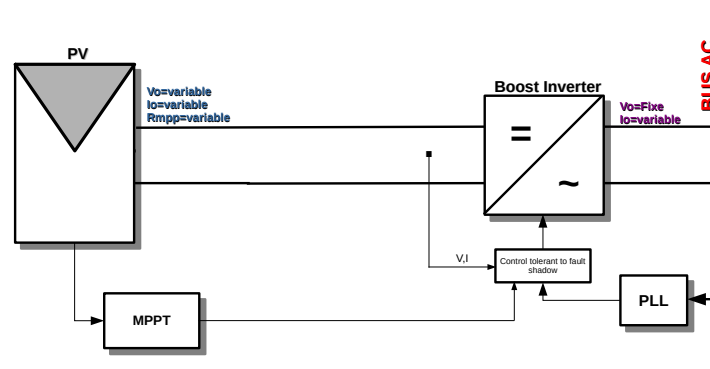


**Figure 3.52** Control strategy with global MPPT

The inverter output is a floating voltage given by the difference in outputs between both boosts, as shown in Eq. (3.19), where  $D_1$  and  $D_2$  are the respective boost duty-cycles.

$$V_o = \frac{D_1 - D_2}{(1 - D_1)(1 - D_2)} \quad (3.19)$$

The main design criteria to select the value of the inductors and the capacitors of the boost inverter in Fig.(3.53) are presented in [38]

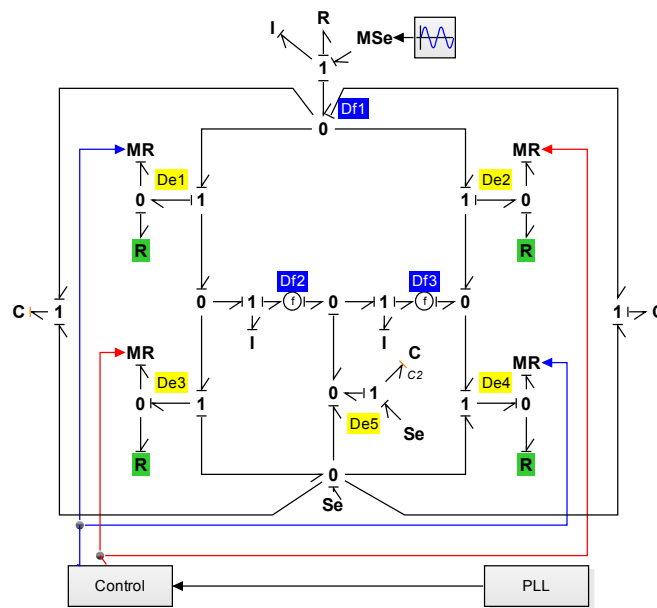


Figure 3.53 Model boost inverter

Figure (3.54) presents the complete model of the photovoltaic system with the fault-tolerant control strategy.

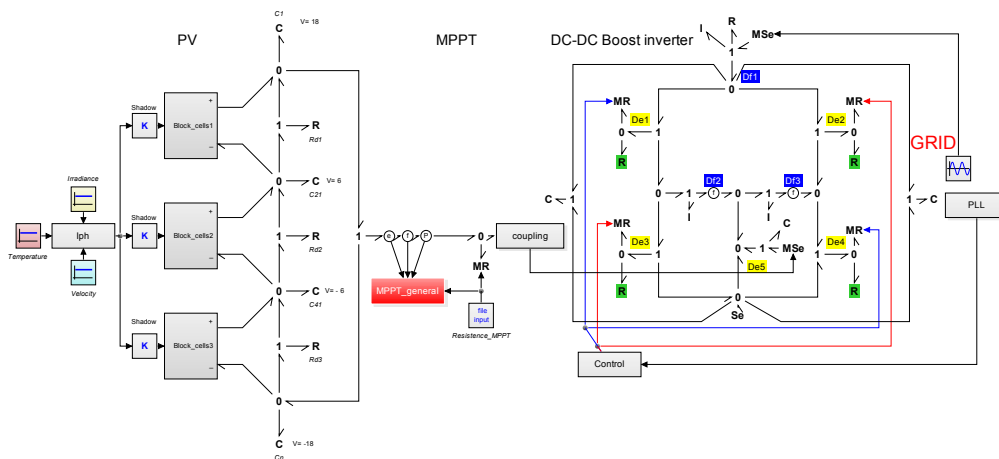
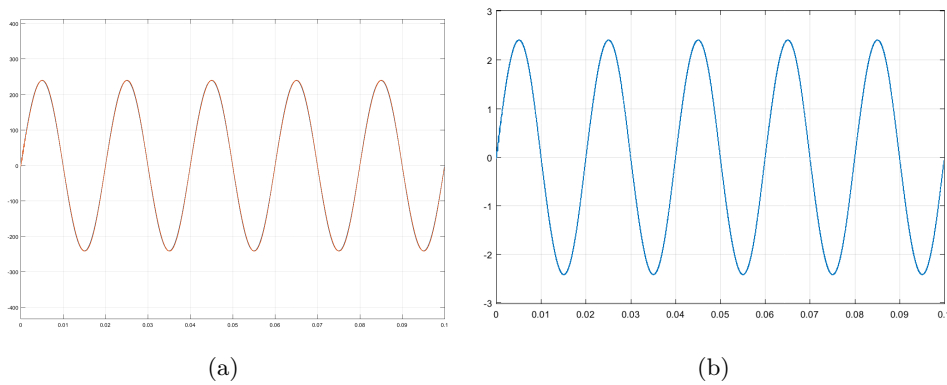


Figure 3.54 The whole system with the boost inverter

Figure (3.55) presents the voltage and system's current output signal that is connected to the electrical network 220v @ 50Hz.



**Figure 3.55** (a)  $V_o$  in phase of the inverter and the grid (b)  $I_o$  injected into the grid

### 3.2.2 FTC: Reconfiguration of the photovoltaic system (proposal)

Fault-tolerant control is a set of techniques that helps to increase plant availability and reduce the risk of safety hazards. Its aim is to prevent simple faults turning in into serious failures. Fault-tolerant control merges several disciplines to achieve this goal. These include on-line fault diagnosis, automatic condition assessment, and calculation of remedial actions when a fault is detected [39]. This could lead to future work that could capitalize on the models and diagnoses developed in previous sections and chapters.

- Reconfiguration architecture of the PV generator
- Reconfiguration architecture of the converters

#### 3.2.2.1 Reconfiguration architecture of the PV generator side

It is possible to reconfigure a PV generator, when the fault is diagnosed by the diagnostician, by connecting panels operating with the same current in a photovoltaic string. Thus, the maximum efficiency of energy generation is achieved. This strategy was developed in El-basri's [40] thesis, and can be seen in Figure 3.56.

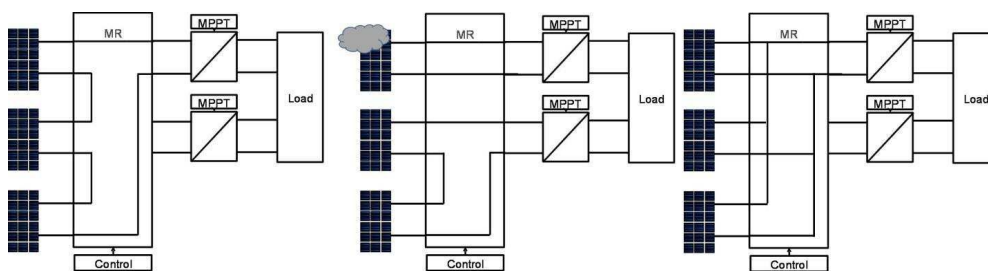


**Figure 3.56** FTC: based on reconfiguring panels [40]

### 3.2.2.2 Reconfiguration architecture of the converters

It is possible to reconfigure the converter-inverter when the fault is diagnosed by the diagnostician by disconnecting them from the system and connecting other converters without faults, as shown in Figure 3.57.

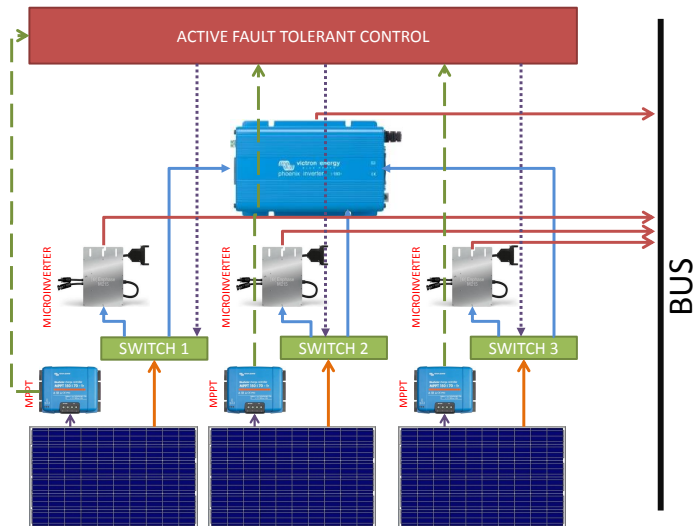


**Figure 3.57** FTC: based on the reconfiguration of AC Inverters

### 3.3 Conclusion

In this chapter, strategies to diagnose faults on PV systems and fault tolerant controls applied to PV systems were presented. The proposed diagnosis strategies depend on the localization of the fault e.g., the PV generator or power elements. A monitoring system was implemented for the PV, which allowed the real system to be compared with developed models.

We developed a diagnosis strategy based on the modeling of each element that composes a PV system. The faults by shadow are detected, isolated, and estimated to obtain the type and magnitude of the faults. The faults diagnosed on PV generator were: shadows, hot-spotting, aging, and MPPT. These diagnosis strategies were simulated using HBG and Matlab. The diagnosed faults on power devices are faults on commutation elements relating to transistors, diodes, inductors, and capacitances. The general diagnosis of the system indicates in which part of the system the fault is present (PV, Boost converter, or Boost inverter).

A fault-tolerant control strategy was proposed to maintain good behaviour in the PV system despite the presence of fault. Once the system identifies the fault on the system, the DC-DC converter and inverter modify their duty cycle to address the fault.

# Bibliography

- [1] W. Borutzky, *Bond graph model-based fault diagnosis of hybrid systems*. Springer, 2015.
- [2] B. Jiang, M. Staroswiecki, and V. Cocquempot, “Fault accommodation for nonlinear dynamic systems,” *IEEE Transactions on Automatic Control*, vol. 51, no. 9, pp. 1578–1583, 2006.
- [3] H. Noura, D. Theilliol, J.-C. Ponsart, and A. Chamseddine, *Fault-tolerant control systems: Design and practical applications*. Springer Science & Business Media, 2009.
- [4] G. Petrone, C. A. Ramos-Paja, and G. Spagnuolo, *Photovoltaic sources modeling*. John Wiley & Sons, 2017.
- [5] A. Livera, M. Theristis, G. Makrides, and G. E. Georghiou, “Recent advances in failure diagnosis techniques based on performance data analysis for grid-connected photovoltaic systems,” *Renewable Energy*, vol. 133, pp. 126 – 143, 2019.
- [6] A. Omazic, G. Oreski, M. Halwachs, G. Eder, C. Hirschl, L. Neumaier, G. Pinter, and M. Erceg, “Relation between degradation of polymeric components in crystalline silicon pv module and climatic conditions: A literature review,” *Solar Energy Materials and Solar Cells*, vol. 192, pp. 123 – 133, 2019.
- [7] C. Ferrara and D. Philipp, “Why do pv modules fail?,” *Energy Procedia*, vol. 15, pp. 379 – 387, 2012. International Conference on Materials for Advanced Technologies 2011, Symposium O.
- [8] S. Moosavi, A. Kazemi, and H. Akbari, “A comparison of various open-circuit fault detection methods in the igbt-based dc/ac inverter used in electric vehicle,” *Engineering Failure Analysis*, vol. 96, pp. 223 – 235, 2019.
- [9] P. Cova, N. Delmonte, and M. Lazzaroni, “Photovoltaic plant maintainability optimization and degradation detection: Modelling and characterization,” *Microelectronics Reliability*, vol. 88-90, pp. 1077 – 1082, 2018. 29th European Symposium on Reliability of Electron Devices, Failure Physics and Analysis ( ESREF 2018 ).
- [10] S. Lu, B. Phung, and D. Zhang, “A comprehensive review on dc arc faults and their diagnosis methods in photovoltaic systems,” *Renewable and Sustainable Energy Reviews*, vol. 89, pp. 88 – 98, 2018.

- 
- [11] E. Garoudja, F. Harrou, Y. Sun, K. Kara, A. Chouder, and S. Silvestre, "Statistical fault detection in photovoltaic systems," *Solar Energy*, vol. 150, pp. 485 – 499, 2017.
- [12] M. Dhimish, V. Holmes, and M. Dales, "Parallel fault detection algorithm for grid-connected photovoltaic plants," *Renewable Energy*, vol. 113, pp. 94 – 111, 2017.
- [13] M. Kumar and A. Kumar, "Performance assessment and degradation analysis of solar photovoltaic technologies: A review," *Renewable and Sustainable Energy Reviews*, vol. 78, pp. 554 – 587, 2017.
- [14] M. A. Garcia, W. Herrmann, W. Böhmer, and B. Proisy, "Thermal and electrical effects caused by outdoor hot-spot testing in associations of photovoltaic cells," *Progress in photovoltaics: research and applications*, vol. 11, no. 5, pp. 293–307, 2003.
- [15] M. Simon and E. L. Meyer, "Detection and analysis of hot-spot formation in solar cells," *Solar Energy Materials and Solar Cells*, vol. 94, no. 2, pp. 106–113, 2010.
- [16] K. A. Kim, G.-S. Seo, B.-H. Cho, and P. T. Krein, "Photovoltaic hot-spot detection for solar panel substrings using ac parameter characterization," *IEEE Transactions on Power Electronics*, vol. 31, no. 2, pp. 1121–1130, 2016.
- [17] W. Herrmann, W. Wiesner, and W. Vaassen, "Hot spot investigations on pv modules-new concepts for a test standard and consequences for module design with respect to bypass diodes," in *Photovoltaic Specialists Conference, 1997., Conference Record of the Twenty-Sixth IEEE*, pp. 1129–1132, IEEE, 1997.
- [18] Y. Hu, W. Cao, J. Ma, S. J. Finney, and D. Li, "Identifying pv module mismatch faults by a thermography-based temperature distribution analysis," *IEEE Transactions on Device and Materials Reliability*, vol. 14, no. 4, pp. 951–960, 2014.
- [19] Y. Hu, W. Cao, J. Wu, B. Ji, and D. Holliday, "Thermography-based virtual mppt scheme for improving pv energy efficiency under partial shading conditions," *IEEE transactions on power electronics*, vol. 29, no. 11, pp. 5667–5672, 2014.
- [20] G. M. Tina, F. Cosentino, and C. Ventura, "Monitoring and diagnostics of photovoltaic power plants," in *Renewable Energy in the Service of Mankind Vol II*, pp. 505–516, Springer, 2016.
- [21] S. R. Madeti and S. Singh, "Monitoring system for photovoltaic plants: A review," *Renewable and Sustainable Energy Reviews*, vol. 67, pp. 1180 – 1207, 2017.
- [22] H. Alwi, C. Edwards, and C. P. Tan, "Fault tolerant control and fault detection and isolation," in *Fault Detection and Fault-Tolerant Control Using Sliding Modes*, pp. 7–27, Springer, 2011.

- [23] E. Molenbroek, D. Waddington, and K. Emery, “Hot spot susceptibility and testing of pv modules,” in *Photovoltaic Specialists Conference, 1991., Conference Record of the Twenty Second IEEE*, pp. 547–552, IEEE, 1991.
- [24] K. Kim, *Hot spot detection and protection methods for photovoltaic systems*. PhD thesis, University of Illinois at Urbana-Champaign, 2014.
- [25] K. A. Kim and P. T. Krein, “Reexamination of photovoltaic hot spotting to show inadequacy of the bypass diode,” *IEEE Journal of Photovoltaics*, vol. 5, no. 5, pp. 1435–1441, 2015.
- [26] M. Bressan, Y. El Basri, A. Galeano, and C. Alonso, “A shadow fault detection method based on the standard error analysis of iv curves,” *Renewable Energy*, vol. 99, pp. 1181–1190, 2016.
- [27] L. Garcia-Gutierrez, M. Bressan, F. Jimenez, S. d. Heras, and C. Alonso, “Design of a global maximum power point tracking (gmppt) for pv array based on precise pv shadow model,” in *2018 7th International Conference on Renewable Energy Research and Applications (ICRERA)*, pp. 275–280, Oct 2018.
- [28] A. Azizi, P.-O. Logerais, A. Omeiri, A. Amiar, A. Charki, O. Riou, F. Delaleux, and J.-F. Durastanti, “Impact of the aging of a photovoltaic module on the performance of a grid-connected system,” *Solar Energy*, vol. 174, pp. 445–454, 2018.
- [29] W. Borutzky, *Bond graph model-based fault diagnosis of hybrid systems*. Springer, 2015.
- [30] Y. Zhang and J. Jiang, “Bibliographical review on reconfigurable fault-tolerant control systems,” *Annual Reviews in Control*, vol. 32, no. 2, pp. 229 – 252, 2008.
- [31] M. Blanke, M. Kinnaert, J. Lunze, M. Staroswiecki, and J. Schröder, *Diagnosis and fault-tolerant control*, vol. 2. Springer, 2006.
- [32] F. Flores-Bahamonde, H. Valderrama-Blavi, L. Martínez-Salamero, J. Maixé-Altés, and G. García, “Control of a three-phase ac/dc vienna converter based on the sliding mode loss-free resistor approach,” *IET Power Electronics*, vol. 7, no. 5, pp. 1073–1082, 2014.
- [33] A. Cid-Pastor, L. Martinez-Salamero, N. Parody, and A. El Aroudi, “Analysis and design of a loss-free resistor based on a boost converter in pwm operation,” in *Proceedings of 2010 IEEE International Symposium on Circuits and Systems*, pp. 2742–2745, IEEE, 2010.
- [34] O. Lopez-Santos, G. Garcia, L. Martinez-Salamero, R. Giral, E. Vidal-Idiarte, M. C. Merchan-Riveros, and Y. Moreno-Guzmán, “Analysis, design, and implementation of a static conductance-based mppt method,” *IEEE Transactions on Power Electronics*, vol. 34, no. 2, pp. 1960–1979, 2019.
- [35] A. León Masich *et al.*, *High voltage efficient lighting based on the loss-free resistor concept*. PhD thesis, Universitat Rovira i Virgili.

- 
- [36] O. Lopez Santos, *Contribution to the DC-AC conversion in photovoltaic systems : Module oriented converters*. Theses, INSA de Toulouse, Feb. 2015.
- [37] W. Perruquetti and J. P. Barbot, *Sliding mode control in engineering*, vol. 11. M. Dekker, 2002.
- [38] A. Gutierrez Galeano, *Study of Photovoltaic System Integration in Micro-grids through Real-Time Modeling and Emulation of its Components Using HiLeS*. Theses, Université Paul Sabatier - Toulouse III, Sept. 2017.
- [39] M. Blanke, W. C. Frei, F. Kraus, J. R. Patton, and M. Staroswiecki, “What is fault-tolerant control?,” *IFAC Proceedings Volumes*, vol. 33, no. 11, pp. 41 – 52, 2000. 4th IFAC Symposium on Fault Detection, Supervision and Safety for Technical Processes 2000 (SAFEPROCESS 2000), Budapest, Hungary, 14-16 June 2000.
- [40] Y. El Basri, *Reconfigurable distributed power architecture for the optimisation of photovoltaic energy*. Theses, Université Paul Sabatier - Toulouse III, June 2013.

# 4

## Diagnosis embedded in an FPGA

This chapter presents the implementation of fault diagnosis based on a particular model. The whole PV system was modeled to develop methods that are able to detect and isolate the fault with high-granularity. Hardware-in-the-loop (HIL) simulation is a type of real-time simulation allowing these methods to be probed by the PV system and the control strategies. This section presents an application of HIL in FPGA.

HIL uses a real-time device as a virtual representation of a PV plant model, and this is a small part of the diagnosis. Processing devices can be required to undertake high performance constraints in real-time emulation. This chapter addresses the application of FPGA when there are shadows and the implementation of PV system diagnostics.

### **4.1 Diagnosis of hot-spot apparition that is implemented using FPGA**

This work presents an emulation in real-time of the shaded PV systems with hot-spot prevention [1]. The PV model presented in Chapter 2 takes into account the photo-induced current contributions from shaded and unshaded sides thanks to parameters such as the shadow transmittance and the percentage area of the shadows. The use of shadow fault detection in real-time is employed, which avoids all forms of hot-spot formation and PV cell power dissipation. The calculation uses a simple derivative equation able to give the detection area as a function of the PV module voltage. Implementing the emulator in FPGA has its advantages because of the adaptability and parallel processing features that are suitable for the emulation of the complex shading visible on PV systems. The emulation of the proposed PV model and the hot-spot prevention are validated through two experimental tests on PV modules.

### 4.1.1 Calculation of the derivative error for a PV module

The developed PV emulators should be able to emulate more complicated test cases with appropriate transient responses. We suggest the development of partial shading PV emulators with fault detection for power electronic converters for decentralized PV systems and the use of higher switching frequency of transistors. The real-time emulation of complex shaded PV models with fault detection application can achieve the performance and accuracy requirements. Bypass diodes are used to mitigate the presence of hot-spots, but this does not prevent hot spotting or the damage it causes. Kim proposed a string-level hot-spot detection concept that measures changes in the string's small-signal impedance to identify hot spotting [2]. Itako's paper [3] presented a development of a real time hot-spot detection system using the scan-method of I-V characteristics to distinguish between normal cells and hot-spot cells depending on the changes of the panel output current.

The proposed method revisits the idea of using a first derivative calculation to prevent the presence of hot-spots that are validated in simulation [1]. The complete implementation process is performed in FPGA, which decreases the computation time and responds to the complexity of shaded PV models and its application in terms of hot-spot prevention. The study of transients and fast responses is essentially used with data mining techniques to compare real-time measurements [4]. The I-V curve acquired during shading conditions is compared to a reference I-V curve issue to a validated solar model. The comparison is made by estimating the standard error using the current from the shaded and reference I-V curves, as defined in Eq. 4.1.

$$E(i)_{standar} = \frac{I(i)_{reference} - I(i)_{shaded}}{\max(I(i)_{reference} - I(i)_{shaded})} \quad (4.1)$$

where  $E(i)_{standar}$  is the standard error of the  $i$ th I-V curve point,  $I(i)_{reference}$  is the current of the I-V curve under reference conditions, and  $I(i)_{shaded}$  is the current of the I-V curve acquired under shaded conditions. The standard error is calculated for all points of the I-V curve, and its variation in relation to the PV voltage is used to monitor any changes in the shaded I-V curve as a whole. This derivative is calculated in Eq. 4.2.

$$\frac{dE(i)_{standar}}{dV_{module}} = \frac{E(i+1)_{standar} - E(i)_{standar}}{V(i+1)_{module} - V(i)_{module}} \quad (4.2)$$

The results of the proposed model were validated using positive and negatives peaks which correspond to presence of uniform shadow and non-uniform shadow, respectively. The positive peak shifts to lower voltage values as the shadow area becomes wider. The negative peak shifts to voltage values close to the open-circuit voltage for severe cases of non-uniform shading. When the positive peak is closed to the short-circuit current, the bypass diode failed.

### 4.1.2 Hot-spot prevention algorithm, implementation, and results of the emulator

Emulation of shaded PV systems and hot-prevention requires powerful processing devices such as FPGAs. The proposed model and the hot-spot algorithm was designed using very high-speed description language (VHDL) and implemented on Xilinx ZedBoard. Using different parts of the FPGA structure, the functional blocks of FPGA such as memory and logic resources work in parallel at a very high frequency with a high execution speed. On one hand, it is necessary to reduce the execution speed so that less FPGA hardware resources are consumed. However, the insufficient speed can affect the whole system in terms of precision reduction and error calculation. Figure 4.1 shows the FPGA board with the main input of measurements to perform the hot-spot prevention.

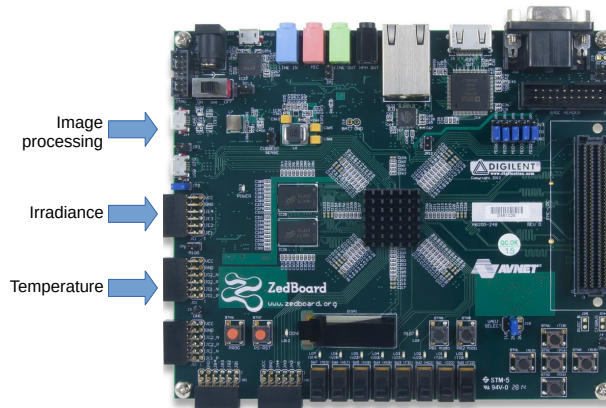


Figure 4.1 FPGA board with measurement inputs

Figure 4.2 shows the real-time FPGA-based platform to emulate complex shaded PV systems. The processing time to evaluate a point in the I-V curve is  $10.5\mu\text{s}$ , and, according to fast computing methods reported in literature, it takes approximately 4ms to generate an I-V curve suitable for real-time applications. Similar work on fast computing methods for PV modeling such as [5] detail a 23ms response time to compute an un-shaded I-V curve. [6] argue that a computing time of around  $10\mu\text{s}$  is needed to evaluate a complex thermal and electrical PV model.

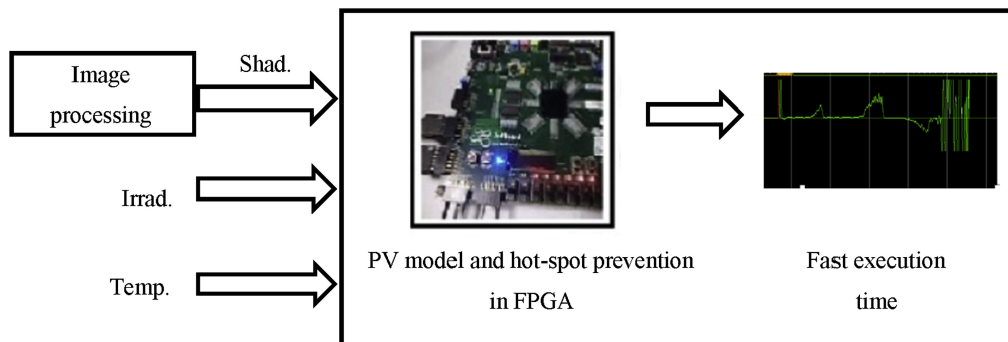


Figure 4.2 Real-time FPGA-based platform for emulation of complex shaded PV systems

Figure 4.3 presents two cases of shadows over a PV module Tenesol.

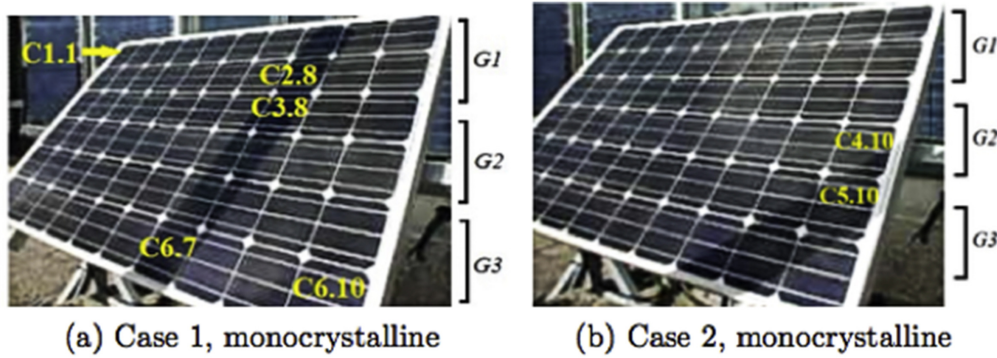


Figure 4.3 Experimental tests for the monocrystalline PV module

Figure 4.4 presents the I-V curves for both cases of complex shading conditions. For each case, the evolution of the standard error will be analyzed to extract a general set of interpretation rules, which will allow hot-spot problems to be identified. This method shows the fault detection area that characterizes the presence of a non-uniform shadow on a PV array, which drastically affects PV performance. The method and the implementation process of the proposed model will be explained to show the importance of having faster hot-spot prevention.

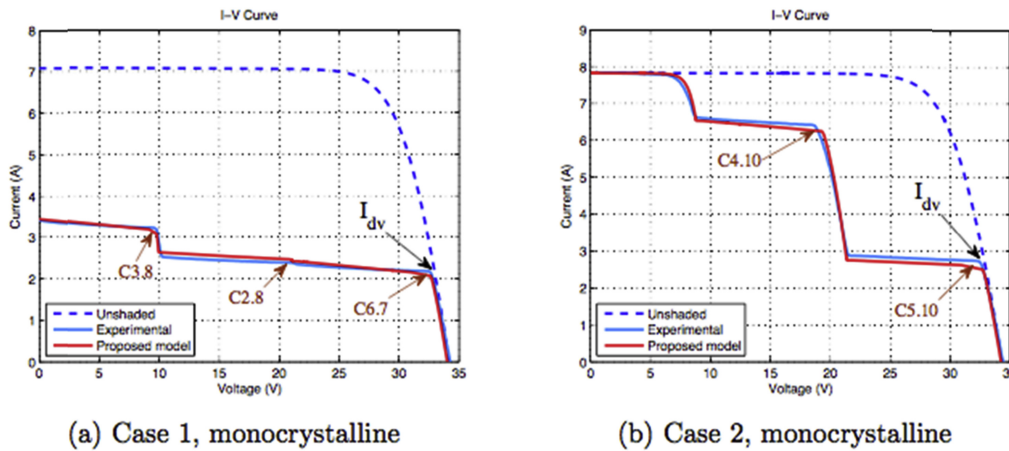


Figure 4.4 I-V curves for both cases

The next step consists in implementing the hot-spot prevention method in the zedboard. Figure 4.5 shows the VHDL flowchart of the presented hot-spot prevention method. Step 1 includes calculating the maximum value of the difference between the reference current and the shaded current. The emulator provides 256 points for the I-V curve measurements, which is the I-V tracer Mp-160. The execution time is  $2.77 \cdot \mu s$ , which depends on the execution time of the used FPGA board: in this case,  $10 \cdot ns$ . Step 2 uses Eq. (4.1) in order to discover the normalized error of both currents. The execution time of this part is  $2.53 \mu s$ . The different value is stored in the ROM memory in order to perform Eq. (4.2). Step 3 allows the hot-spot prevention calculation to commence. The response time of the hot-spot prevention is approximately  $7.54 \cdot \mu s$  as shown in Fig. 4.6,

Fig. 4.7. As a result, the total response time to obtain the I- V curves and to perform the hot-spot prevention is  $18 \cdot \mu\text{s}$

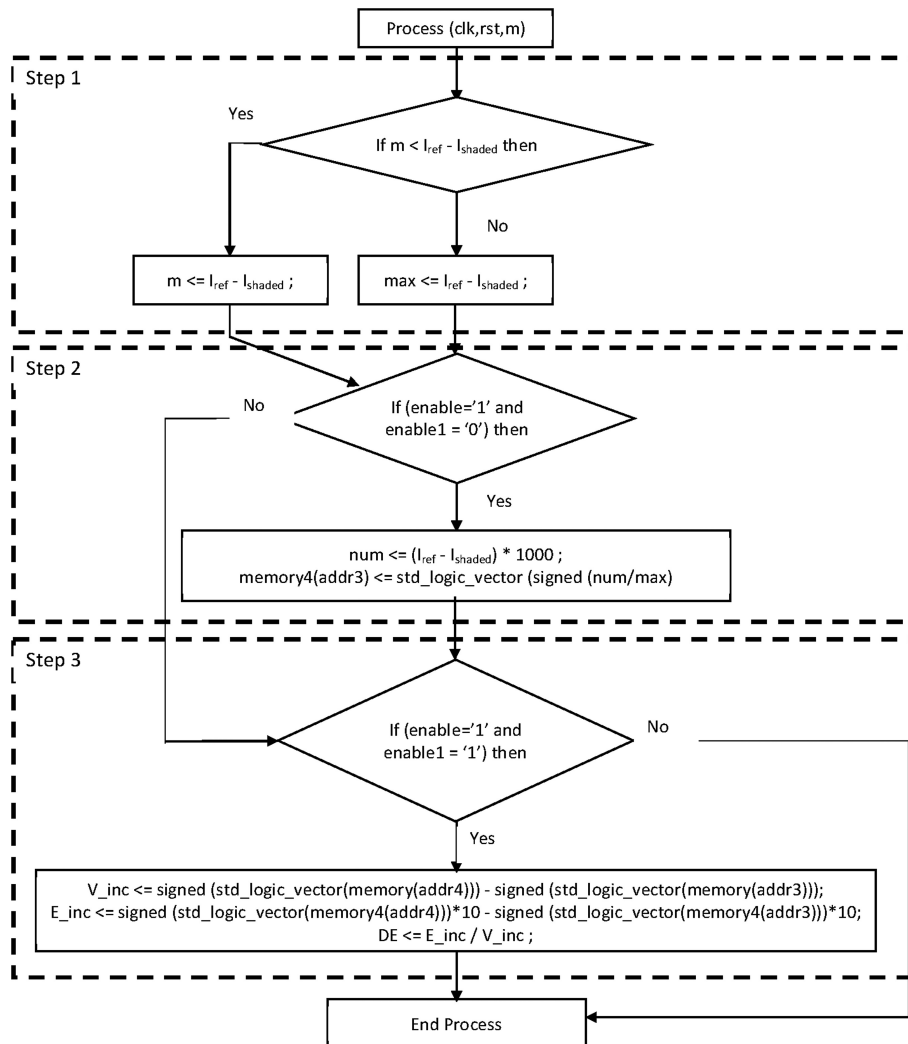


Figure 4.5 VHDL flowchart of hot-spot prevention

Figure 4.6 and Figure 4.7 show the process simulation of the hot-spot prevention in VHDL with the response times for both cases that were presented in part 2. For case 1, there is a positive peak, which activates the only bypass diodes. The negative peak shifts to voltage values close to the open-circuit voltage for severe cases of non-uniform shading. For case 2, two positive peaks characterize the presence of the activation of two bypass diodes. The amplitude of the positive peak depends on the area in shadow, which can be more important and can accelerate the hot-spot apparition in non-uniform shading cases.



## 4.2 Diagnosis of PV converters implemented in FPGA

### 4.2.1 Embedded diagnostics of a H-Bridge DC/AC converter

Based on [7–9], fault diagnosis strategies are presented on a DC-AC inverter. The faults diagnosed on the DC-AC inverter are blocking the switch either in the closed or open position. These faults are modeled by  $\theta = \{ R_{on1}, R_{on2}, R_{on3}, R_{on4}, R_{off1}, R_{off2}, R_{off3}, R_{off4} \}$ . Switch1 has two positions ( $R_{on1}, R_{off1}$ ), switch2 ( $R_{on2}, R_{off2}$ ), switch3 ( $R_{on3}, R_{off3}$ ), and switch4 ( $R_{on4}, R_{off4}$ ). The voltage sensors on the systems are  $D_{e1}, D_{e2}, D_{e3}$ , and  $D_{e4}$ , and the current sensors are  $D_{f1}$  and  $D_{f2}$ .

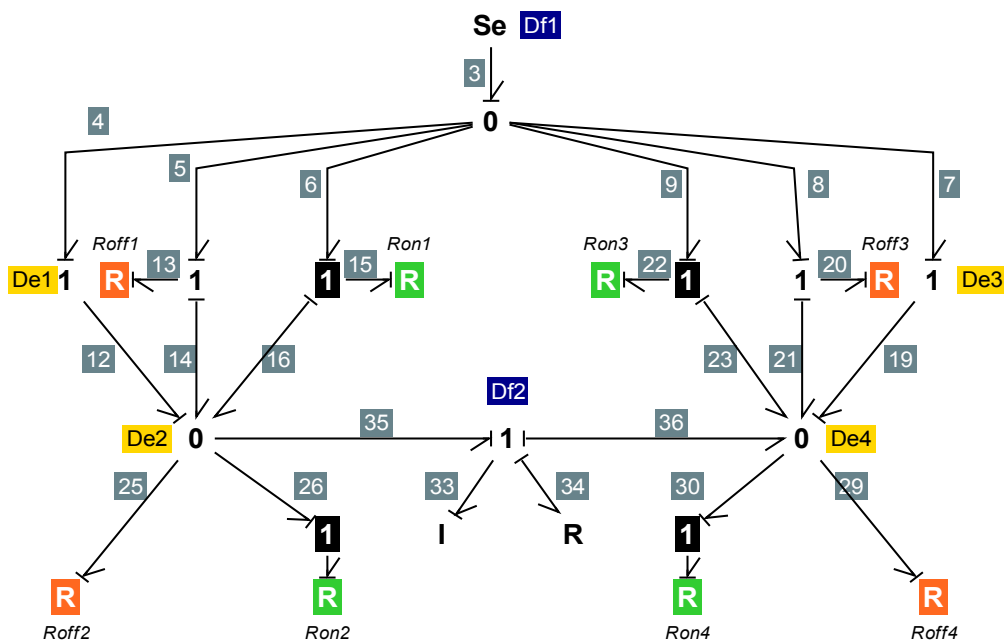


Figure 4.8 HBG inverter model based on [8]

Equations (4.3) represent the model's energy equilibrium in Fig (4.8). They are obtained by analyzing the flows in junctions "1" and the efforts in junctions "0".

$$\begin{aligned}
 0 &= e_{13} + e_{14} - e_5 \\
 0 &= R_{off1} \cdot f_{13} + e_{24} - e_3 \\
 0 &= R_{off1} \cdot f_{14} + D_{e2} - e_1 \\
 0 &= R_{off1} [f_{25} + f_{26} + f_{35} - f_{16} - f_{12} + f_{24}] + D_{e2} - V_s \\
 0 &= R_{off1} [f_{25} + a_2 \cdot f_{26} + f_{35} - a_1 \cdot f_{16}] + D_{e2} - V_s \\
 0 &= R_{off1} \left[ \frac{e_{25}}{R_{off2}} + a_2 \cdot f_{27} + f_{32} - a_1 \cdot f_{15} \right] + D_{e2} - V_s \\
 0 &= R_{off1} \left[ \frac{e_{24}}{R_{off2}} + a_2 \frac{e_{27}}{R_{on2}} + D_{f2} - a_1 \frac{e_{15}}{R_{on1}} \right] + D_{e2} - V_s \\
 0 &= R_{off1} \left[ \frac{D_{e2}}{R_{off2}} + a_2 \frac{e_{26}}{R_{on2}} + D_{f2} - a_1 \frac{e_6 - e_{16}}{R_{on1}} \right] + D_{e2} - V_s
 \end{aligned} \tag{4.3}$$

A brief description of the equations 4.4 allows us to obtain global analytical redundancy relations (GARRs) for the DC-AC inverter.

$$\begin{aligned}
GARR_1 &= D_{f1} - \frac{V_s - D_{e2}}{R_{off1}} - a_1 \frac{V_s - D_{e2}}{R_{on1}} - \frac{V_s - D_{e4}}{R_{off3}} - a_3 \frac{V_s - D_{e4}}{R_{on3}} \\
GARR_2 &= R_{off1} \left[ \frac{D_{e2}}{R_{off2}} + a_2 \frac{D_{e2}}{R_{on2}} + D_{f2} - \frac{V_s - D_{e2}}{R_{on1}} \right] + D_{e2} - V_s \\
GARR_3 &= V_s - a_1 \cdot R_{on1} \left[ \frac{D_{e2}}{R_{off2}} + a_2 \frac{D_{e2}}{R_{on2}} + D_{f2} - \frac{V_s - D_{e2}}{R_{off1}} \right] - D_{e2} \\
GARR_4 &= V_s - R_{off3} \left[ \frac{D_{e4}}{R_{off4}} + a_4 \frac{D_{e4}}{R_{on4}} - D_{f2} - a_3 \frac{V_s - D_{e4}}{R_{on3}} \right] - D_{e4} \\
GARR_5 &= V_s - a_3 \cdot R_{on3} \left[ \frac{D_{e4}}{R_{off4}} + a_4 \frac{D_{e4}}{R_{on4}} - D_{f2} - \frac{V_s - D_{e4}}{R_{off3}} \right] - D_{e4} \\
GARR_6 &= \frac{V_s - D_{e2}}{R_{off1}} + a_1 \frac{V_s - D_{e2}}{R_{on1}} - D_{f2} - a_2 \frac{D_{e2}}{R_{on2}} - \frac{D_{e4}}{R_{off2}} \\
GARR_7 &= \frac{V_s - D_{e4}}{R_{off3}} + a_3 \frac{V_s - D_{e4}}{R_{on3}} + D_{f2} - a_4 \frac{D_{e4}}{R_{on4}} - \frac{D_{e4}}{R_{off4}} \\
GARR_8 &= D_{e2} - D_{e4} - L \frac{dD_{f2}}{dt} - R \cdot D_{f2}
\end{aligned} \tag{4.4}$$

The fault signature matrix is constructed for the DC-AC inverter, as seen in Eq.(4.1).

	Residue								$D_b$	$I_b$
	$r_1$	$r_2$	$r_3$	$r_4$	$r_5$	$r_6$	$r_7$	$r_8$		
$R_{on1}$	1	1	1	0	0	1	0	0	1	1
$R_{on2}$	0	1	0	0	0	1	0	0	1	1
$R_{on3}$	1	0	0	1	1	0	1	0	1	1
$R_{on4}$	0	0	0	1	0	0	1	0	1	1
$R_{off1}$	1	1	0	0	0	1	0	0	1	1
$R_{off2}$	0	1	1	0	0	1	0	0	1	1
$R_{off3}$	1	0	0	1	0	0	1	0	1	1
$R_{off4}$	0	0	0	1	1	0	1	0	1	1

**Table 4.1** Signature Matrix fault of DC-AC inverter

The FPGA program is processed using the failure signature matrix. The inputs of the FPGA are the "1" and "0" flags, as shown in Table (4.1), that can be simulated with the FPGA switches, and the outputs were the FPGA's LEDs.

In this case, the FPGA digital inputs are used as ports of entry and there are eight GARRs. The outputs of the system are the FPGA's LEDs.

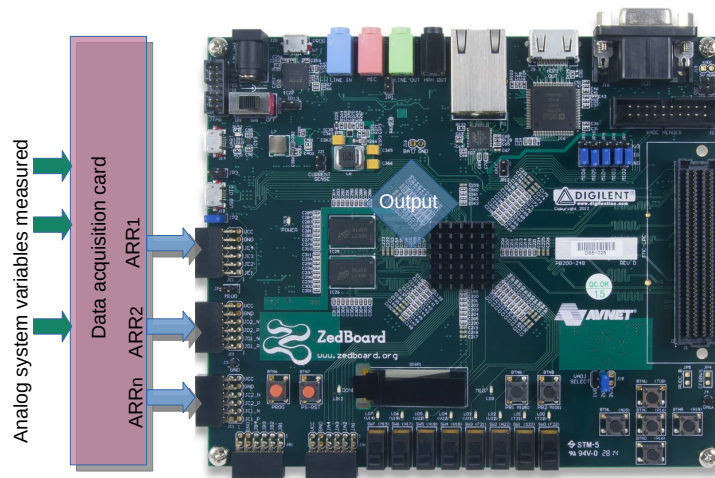


**Figure 4.9** Diagnosis of a DC-AC inverter embedded in FPGA

Figure 4.10 shows the final implementation of the inverter diagnosis.

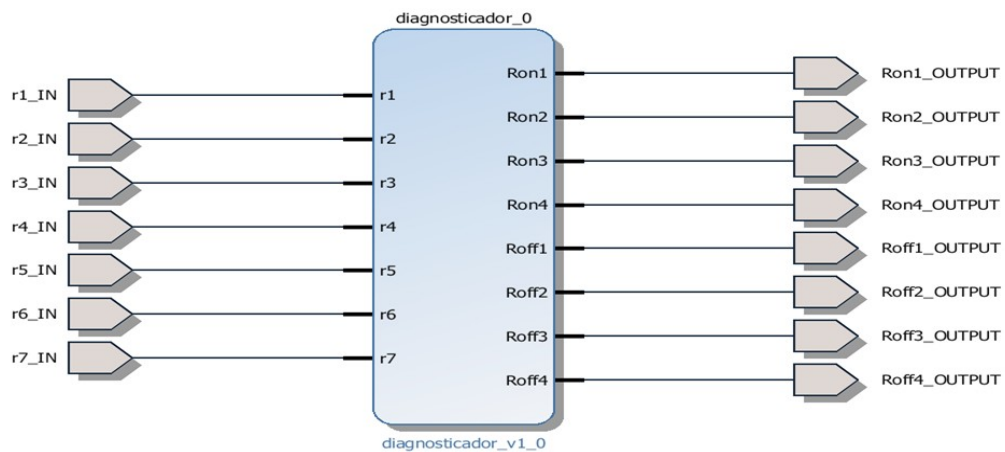


**Figure 4.10** Diagnosis

The FPGA's input switches are used to simulate the change of the ARR states. The FPGA LEDs allow the state of the damaged switch and its position to be verified.

### 4.3 Conclusion

In this chapter, two FPGA applications used to solve problems in the PV system have been developed.

First, a FPGA was used to simulate and prevent hot-spotting on PV systems. A partially shaded PV cell enters the hot spotting condition faster than a fully shaded PV cell. It is important to develop accurate and faster tools such as an emulator to avoid all form of hot-spot apparition. This chapter presented a methodology to model complex partially shaded PV modules and a hot-spot prevention method. Secondly, FPGA was used to implement a diagnosis with a fault signature matrix for a DC-AC inverter.

## Bibliography

- [1] M. Bressan, A. Gutierrez, L. G. Gutierrez, and C. Alonso, “Development of a real-time hot-spot prevention using an emulator of partially shaded pv systems,” *Renewable Energy*, vol. 127, pp. 334 – 343, 2018.
- [2] K. A. Kim, G. S. Seo, B. H. Cho, and P. T. Krein, “Photovoltaic hot-spot detection for solar panel substrings using ac parameter characterization,” *IEEE Transactions on Power Electronics*, vol. 31, pp. 1121–1130, Feb 2016.
- [3] K. Itako, B. Hossam, T. Kudoh, and Q. Huang, “Development of real time hotspot detection system using scan-method for pv generation system,” in *IECON 2015 - 41st Annual Conference of the IEEE Industrial Electronics Society*, pp. 001032–001036, Nov 2015.
- [4] L. Serrano-Luján, J. M. Cadenas, J. Faxas-Guzmán, and A. Urbina, “Case of study: Photovoltaic faults recognition method based on data mining techniques,” *Journal of Renewable and Sustainable Energy*, vol. 8, no. 4, p. 043506, 2016.
- [5] A. C. Atoche, J. V. Castillo, J. Ortégón-Aguilar, R. Carrasco-Alvarez, J. S. Gío, and A. Colli-Menchi, “A high-accuracy photovoltaic emulator system using arm processors,” *Solar Energy*, vol. 120, pp. 389–398, 2015.
- [6] J.-H. Jung and S. Ahmed, “Real-time simulation model development of single crystalline photovoltaic panels using fast computation methods,” *Solar Energy*, vol. 86, no. 6, pp. 1826–1837, 2012.
- [7] W. Borutzky, *Bond graph model-based fault diagnosis of hybrid systems*. Springer, 2015.
- [8] M. Aguilar-Justo and C. de Luna-Ortega, “Fdi with hybrid bond graphs in the full bridge inverter,” in *Electrical Engineering Computing Science and Automatic Control (CCE), 2011 8th International Conference on*, pp. 1–6, IEEE, 2011.
- [9] D. Wang, M. Yu, C. B. Low, and S. Arogeti, *Model-based health monitoring of hybrid systems*. Springer, 2013.

# Contributions, Conclusions, Perspectives, and Future Projects

## Contributions made by this thesis

The following are the contributions made by this thesis:

- Contributes by modeling in detail a photovoltaic panel that allows specific characteristics of G, T, and shade in certain photovoltaic cells that affect the production of electrical energy to be analyzed.
- Contributes by modeling multidomain energy systems through the use of the bondgraph energy exchange description structure. This is the first work that describes different sources of energy through a single description structure.
- Contributes by analyzing shadows on photovoltaic panels and implementing image processing techniques to detect shadows and estimate the magnitude of shaded areas.
- Contributes by simulating photovoltaic systems, which allows input variables to be shared to the G, T model, and shadows to be used to find out about energy production .
- Contributes by diagnosing failures in model-based photovoltaic systems.
- Contributes by diagnosing faults in photovoltaic systems based on data and signal analysis. Allows faults to be diagnosed such as shadows, hot-spots, and sensor faults.
- Contributes by using an FPGA for fault diagnostics.

## General conclusions

Chapter 1 detailed important aspects relating to photovoltaic generation, the faults, and integration into micro-grids.

- The importance of the photovoltaic generation system in producing clean global energy.
- The structure of the photovoltaic conversion chain.
- The main failures that occur in photovoltaic systems.
- The strategies and methodologies for fault diagnosis applied to photovoltaics.

Chapter 2 showed important aspects relating to fault diagnosis on one photovoltaic micro-grid and FTC strategies.

- The first part of this chapter included a detailed modeling of a complete PV system connected into the grid. Modeling each element that composes a PV system allowed the electrical behaviour under normal and failure operations to be characterized. The first part of the work presented a model that was able to take into account the effect that complex shading had on the I-V curves. The area of shadow was deducted thanks to processing images of shadows in the PV module. Moreover the combination of direct and indirect radiation allowed an attenuation factor for under complex shading conditions to be proposed. The model was validated through experimental tests undertaken on several days.
- The second part of the chapter consisted in developing a strategy to track the global maximum power point under complex shading conditions in order for the system to behave better under these conditions. A model was developed and simulated to show the importance of having a new control strategy for DC-DC converters. The last part of the chapter was about the DC-AC converter. Three kinds of inverter were studied and simulated using HBG. Finally, the whole PV system was modelled.

### Chapter 3

This chapter presented the fault diagnosis strategies for PV systems and fault tolerant control applied to PV systems.

- The first section proposed diagnosis strategies that depended on the localization of the fault e.g., the PV generator or power elements. A monitoring system was implemented over the PV, which allowed the real system to be compared with developed models. A diagnosis strategy was developed based on the modeling of each element that composes a PV system. Faults due to shadow were detected, isolated, and estimated to obtain the fault type and magnitude. The diagnosed faults on the PV were shadows, hot-spotting, aging, and MPPT. These diagnosis strategies were simulated using HBG and Matlab. The diagnosed faults on power devices were elements of commutation faults such as transistors, diodes, inductors, and capacitances. The general diagnosis of the system indicates in which part of the system the fault is present (PV, Boost converter, or Boost inverter).

- The first part proposed a fault tolerant control strategy to keep the PV system behaving well despite the presence of fault. Once the system identifies a fault on the system, the DC-DC converter and inverter modify their duty cycle to suit the fault.

Chapter 4 In this chapter, two applications of the FPGA were developed to solve problems in a photovoltaic system.

- First, the FPGA was used to simulate and prevent of hot-spotting on PV systems because a partially shaded PV cell enters the hot-spotting condition faster than a fully shaded PV cell. It is important to develop accurate and faster tools such as an emulator to avoid all form of hot-spot apparition. This chapter presented a methodology to model complex partially shaded PV modules and a hot-spot prevention method.
- Second, FPGA was used to make a diagnosis. We also presented the implementation of the fault signature matrix of a DC-AC inverter.

## **Applications and Future Work**

- The applications of this thesis are linked to modeling renewable and non-renewable energy generation systems. It models a photovoltaic conversion system, using a multi-domain energy representation strategy called a Bond graph. This description of an energy conversion system is the beginning of a project that will allow a smart grid to be described in the future as a single BG representation.
- Modeling of complex Photovoltaic architectures based on the extrapolation of this methodology need to be developed.
- The methodology needs to be extrapolated to model and diagnose faults from other sources of power generation.
- More PV systems fault diagnosis strategies need to be developed and implemented.
- Implementation of the FPGA diagnosis strategies

## Publications

### Journal:

- M.Bressan, A.Gutierrez, L.Garcia-Gutierrez, C.Alonso 2018. Development of a real-time hot-spot prevention using an emulator of partially shaded PV systems *Renewable Energy*, Volume 127, November 2018, Pages 334-343,

### Conferences:

- L.García-Gutiérrez, M.Bressan, Á.Cadena, C.Alonso, F.Jimenez 2017. Development and integration of a PV smart home in Colombia, 33rd European Photovoltaic Solar Energy Conference.
- L.Garcia-Gutierrez, M.Bressan, F.Jimenez, S.de-las Heras, C.Alonso 2018. Design of a Global Maximum Power Point Tracking (GMPPT) for PV array based on precise PV shadow model, ICRERA2018 conference.

### Submitted to journal:

- L.Garcia-Gutierrez, M.Bressan, A.Lebechec, F.Jimenez, C.Alonso, Development of a very-high granularity tool to determine photovoltaic output power losses in complex shading conditions, Submitted *Renewable energy*

### Conferences/congress 2019 (accepted):

- L.Garcia-Gutierrez, M.Bressan, F.Jimenez, S.de-las Heras, C.Alonso. High granularity model of a photovoltaic array considering complex shadow condition. *ELECTRIMACS 2019*. Salerno, Italy, 21st-23rd May 2019.
- L.Garcia-Gutierrez, M.Bressan, Fernando Jimenez, C.Alonso. Fault Tolerant Control applied to photovoltaic systems, *JNRDM2019*. France, Montpellier, 3-5 Jun 2019.
- L.Garcia-Gutierrez, M.Bressan, F.Jimenez, C.Alonso. Development of an active fault tolerant control of photovoltaic systems, *Congress GEET*, Toulouse, 4 April 2019.



# A

## Appendix A

### A.1 Introduction to Bond Graph Modelling

Bond graphs were devised by Professor Henry Paynter at the Massachusetts Institute of Technology (MIT), Cambridge, Massachusetts, USA as early as 1959. The concept was elaborated into a formal physical modelling methodology for multidisciplinary systems by his former PhD students Professor Dean Karnopp and Professor Donald Margolis (University of California at Davis, California) and Professor Ronald Rosenberg (Michigan State University, East Lansing, Michigan). The energy domains in which the bond graph modeling is used are shown in Fig (A.1).

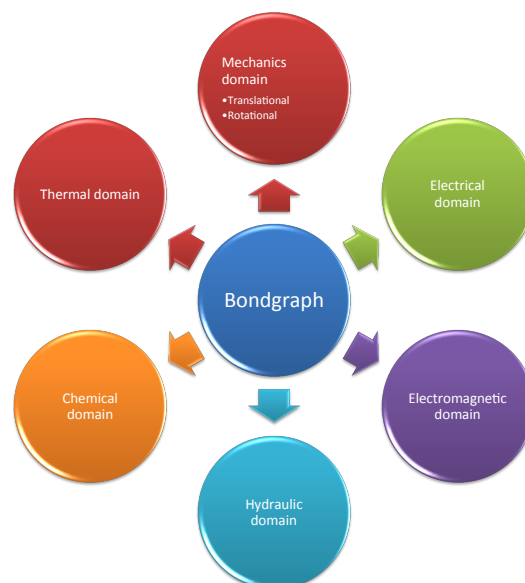


**Figure A.1** Bond graph Multidomain

The equivalences of the efforts and flows for the different energy domains are shown in table (A.1).

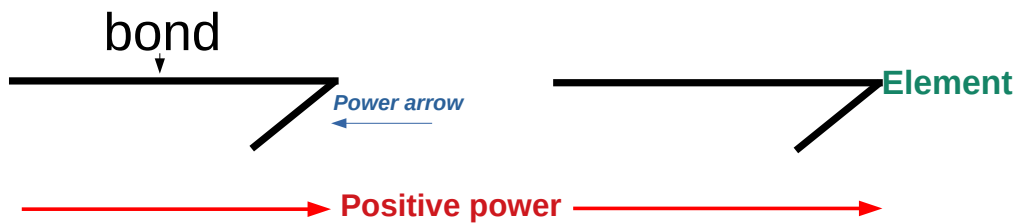
Energy domain	Effort $e$	Flow $f$	Generalized momentum $p$	Generalized displacement $q$
<b>Translational Mechanics</b>	Force $F(N)$	Velocity $v(m/s)$	Momentum $p(Ns)$	Displacement $x(m)$
<b>Rotational Mechanics</b>	Angular moment $M(N.m)$	Angular velocity $\omega(rad/s)$	Angular momentum $P_\omega(Kgm/s)$	Angle $\theta(rad)$
<b>Electrical domain</b>	Voltage $u(V)$	Current $i(A)$	Linkage flux $\lambda(Vs)$	Charge $q(As)$
<b>Hydraulic domain</b>	Total pressure $p(N/m^2)$	Volume flow rate $Q(m^3/s)$	Pressure momentum $P_p(N/m^2s)$	Volume $V_c(m^3)$
<b>Thermodynamic domain</b>	Temperature $T(K)$	Entropy flow rate $S(J/K/s)$	-	Entropy $S(J/K)$
<b>Chemical domain</b>	Chemical potential $\mu(J/mole)$	Molar flow $N(mole/s)$	-	Molar mass $N$ (mole)

**Table A.1** Power and energy variables in various energy domains

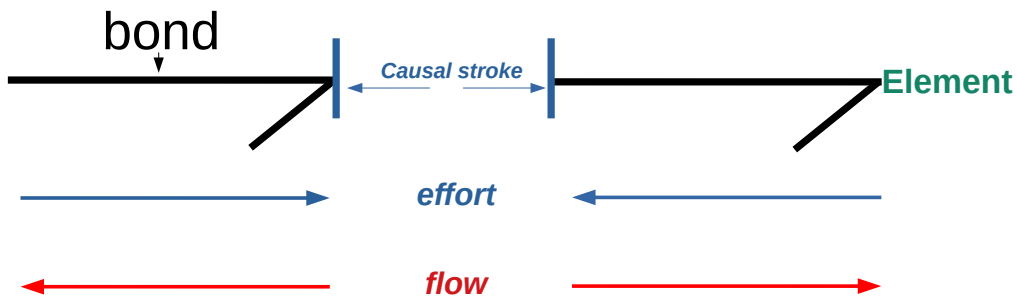
A description of the elements that make up a bond graph diagram are presented in table (A.2).

Element	Symbol	Description
Capacitance	<b>C</b>	This model represents a power continuous storage element. The element has a preferred effort out causality. The corresponding constitutive equations then contain an integration. The element can also have the non-preferred flow out causality.
Inductance	<b>I</b>	This model represents a power continuous storage element. The element has a preferred flow out causality. The corresponding constitutive equations then contain an integration. The element can also have the non-preferred effort out causality.
Resistance	<b>R</b>	elements that dissipate energy. This model represents a linear friction/resistor equation. It can have an effort out as well as a flow out causality.
Junction 0	<b>0</b>	This junction represents a power continuous (no energy storage, dissipation or generation) connection of elements. The sum of the flows on all ports is zero and the efforts on all ports are equal. The constitutive equations are for example: $p1.f + p2.f + p3.f + p4.f = 0$ $p1.e = p2.e = p3.e = p4.e$
Junction 1	<b>1</b>	This junction represents a power continuous (no energy storage, dissipation or generation) connection of elements. The sum of the efforts on all ports is zero and the flows on all ports are equal. The constitutive equations are for example: $p1.e + p2.e + p3.e + p4.e = 0$ $p1.f = p2.f = p3.f = p4.f$
Effort source	<b>Se</b>	This model represents an ideal effort source. The effort can be set to a certain constant value, the flow is indifferent.
Flow source	<b>Sf</b>	This model represents an ideal flow source. The flow can be set to a certain constant value, the effort is indifferent.
Modulated source effort	<b>MSe</b>	This model represents an ideal modulated effort source. The effort can be set to a (fluctuating) value given by an input signal. The flow is indifferent.
Modulated source flow	<b>MSf</b>	This model represents an ideal modulated flow source. The flow can be set to a (fluctuating) value given by an input signal. The effort is indifferent.
Modulated resistance	<b>MR</b>	This model represents a linear friction/resistor equation. It can have an effort as well as a flow causality. The friction/resistor parameter can be set to a (fluctuating) value, given by an input signal.
Modulated Transformers	<b>MTF</b>	This model represents an ideal modulated transformer. The model represents a power continuous relation between the efforts and flows of both its ports.
Modulated Gytrators	<b>MGY</b>	This model represents an ideal modulated gyrator, a power continuous relation between the effort of one port and the flow of the other port and vice-versa.

**Table A.2** Elements, symbol and description BG



(a) A bond as a power connection



(b) A bond as a bilateral signal flow

To indicate the individual direction of the effort and flow, we use a small stroke (causal stroke) that is perpendicular to the bond. This stroke indicates the direction of the effort. The direction of the flow is opposite to the stroke. The choice of the direction of signals, also known as causality, depends on the element that is connected to the bond [20].

## A.2 Photovoltaic cell code

The code developed to solve the non-linear equation for the photovoltaic cell is shown as:

```

parameters
real global rsh;
real global ab;
real global Vb;
real global m;

variables
real rhA; // Equivalent resistance avalanche effect
real Ae; // ()^m
real ush;

equations
ush = dly(p.e,0.0);
Ae = (1 - ush/Vb)^m;
rhA = rsh * Ae/(Ae + ab);
p.e = p.f * rhA;

```



# B

## Appendix B

### B.1 Co-simulation of the photovoltaic system: 20sim-Matlab

Using co-simulation, the different subsystems that form a coupled problem are modeled and simulated in a distributed manner. Hence, the modeling is undertaken on a subsystem level without having the coupled problem in mind. Furthermore, the coupled simulation is carried out by running the subsystems in a black-box manner. During the simulation, the subsystems will exchange data. Co-simulation can be considered to be the joint simulation of the already well-established tools and semantics when they are simulated with their suitable solvers. Co-simulation has an advantage when validating multi-domain and cyber physical systems by offering a flexible solution that allows multiple domains with different time steps to be considered at the same time. As the calculation load is shared among simulators, co-simulation also enables the possibility of large scale system assessment.

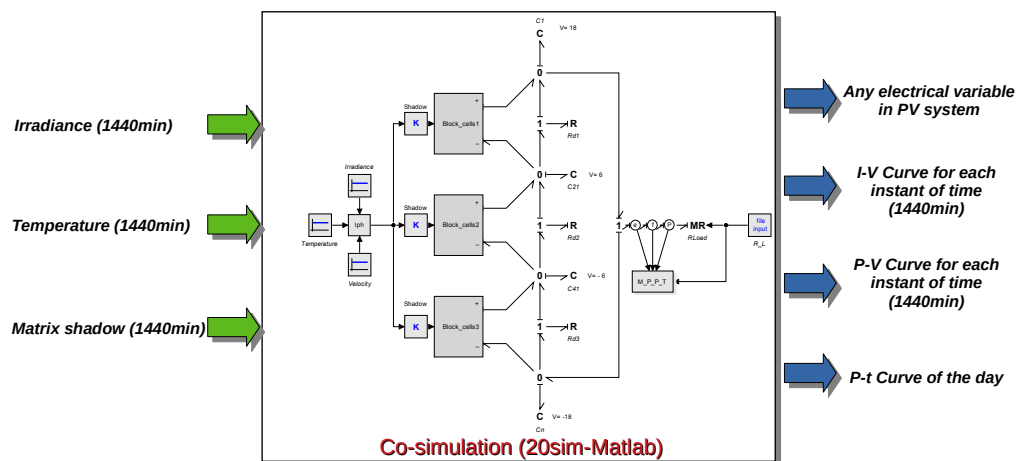


Figure B.1 Co-simulation 20sim-matlab

The problem of obtaining a continuous simulation (24/7) of the photovoltaic production from the bishop model is solved using cosimulation, see Fig(B.2).

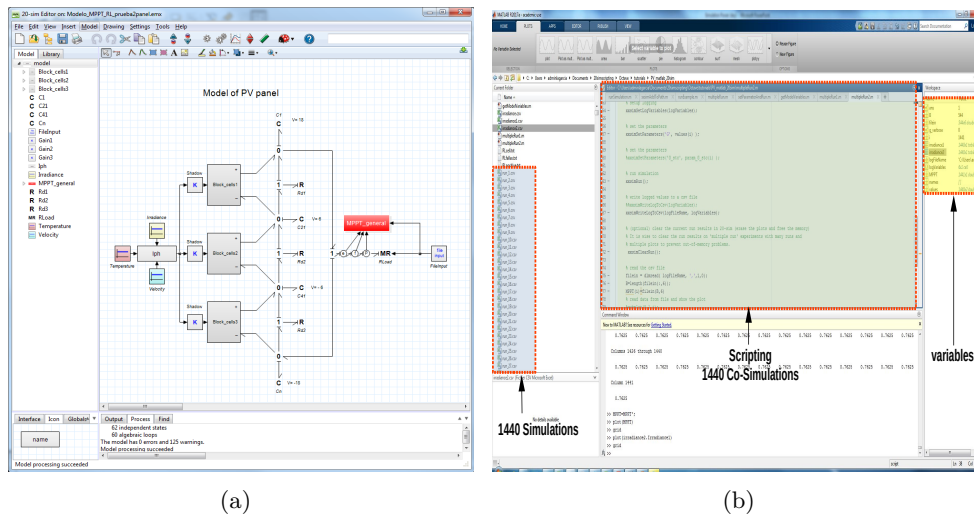


Figure B.2 (a) CoSimulation Matlab (b) CoSimulation 20sim

The model is able to emulate the behavior of panel, string, or array from the environmental information, the panel's characteristics, and the connections it makes every minute see Fig(B.3)

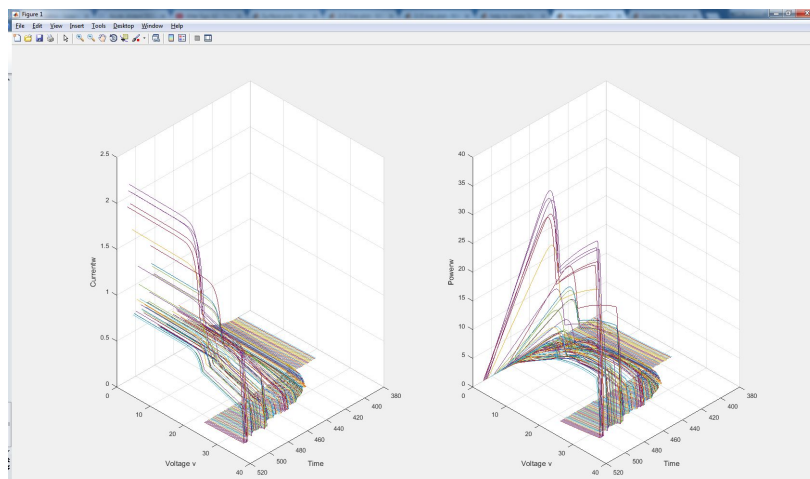
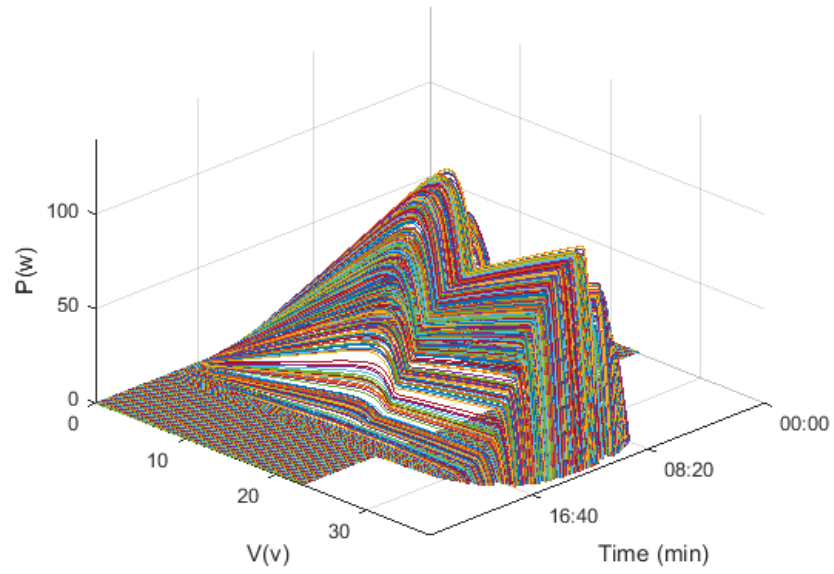
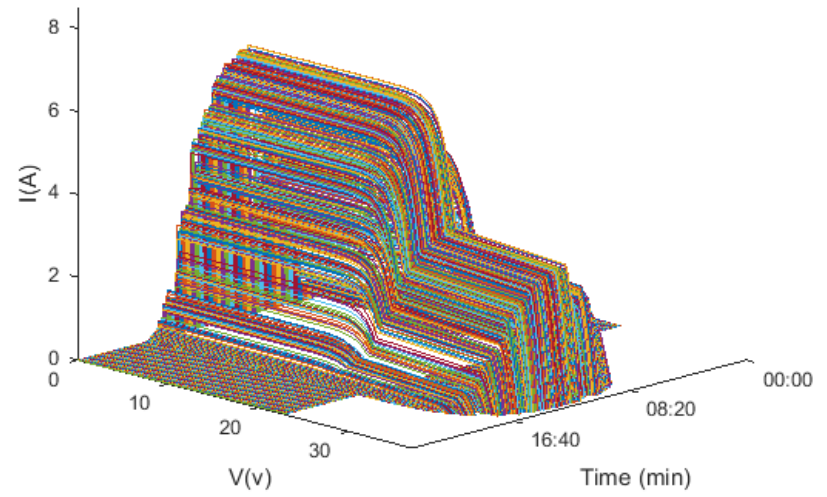


Figure B.3 Simulation every minute I-V and P-V curves

- Interchange of energy (bondgraph) model that described the behaviour of PV system was made using the 20sim software
- Matlab is used to make changes in the value of the input variables (temperature, irradiation, and shadow factor) that allows us to have 1440 simulations (24hx60min).



(a)



(b)

**Figure B.4** (a) Simulation of the curve P versus V (one day) (b) Simulation of the curve I versus V (one day)



# C

## Appendix C

### C.1 ADREAM: Input and Output Variables

A description of the platform that this doctoral thesis used is shown below. The LAAS-CNRS laboratory is in Toulouse, France, located at: (43°33'43.812" N, 1°28'39.294"E), altitude 145 *m*. The ADREAM building (Architectures for Dynamic Resilient Embedded Autonomous and Mobile systems) was inaugurated in July 2012, and it is an experimental platform. It is dedicated to energy optimization and ambient intelligence. This building includes a 720 *m*<sup>2</sup> photovoltaic surface that has a total installed power of 100*kWc*. Most of the solar panels installed are Tenesol 2200s.



**Figure C.1** Terrace of the ADREAM building

The ADREAM platform at the LAAS - CNRS is shown in the figure (C.2)

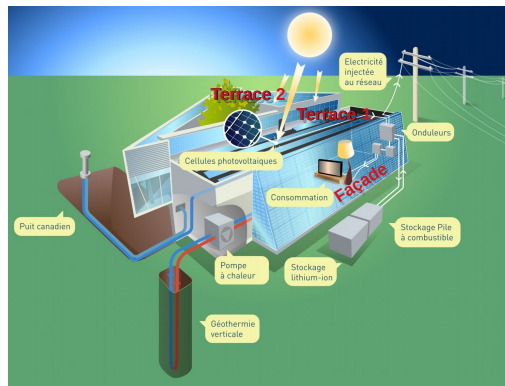


Figure C.2 ADREAM

Field	Power	PV modules	inclination
Facade	38kWp	Bi-glass 529Wp	65°south
Experimental roof+walls "R+1"	35kWp	TE 2200 250p 240p	0°to90° South
Roof "R+2"	24kWp	TE 2200 250p	10°south

Table C.1 List of PV equipment of ADREAM platform

Terrace 1 in the ADREAM building houses eighty TENESOL 2200 solar panels. 26 solar panels are 250W monocrystalline and 54 solar panels are 240W multicrystallines that have sixty photovoltaic cells for each solar panel. Each solar cell has an area of  $0.156\text{ m} \times 0.156\text{ m}$ . The photovoltaic surface of Terrace 1 is  $116.82\text{ m}^2$  [21].

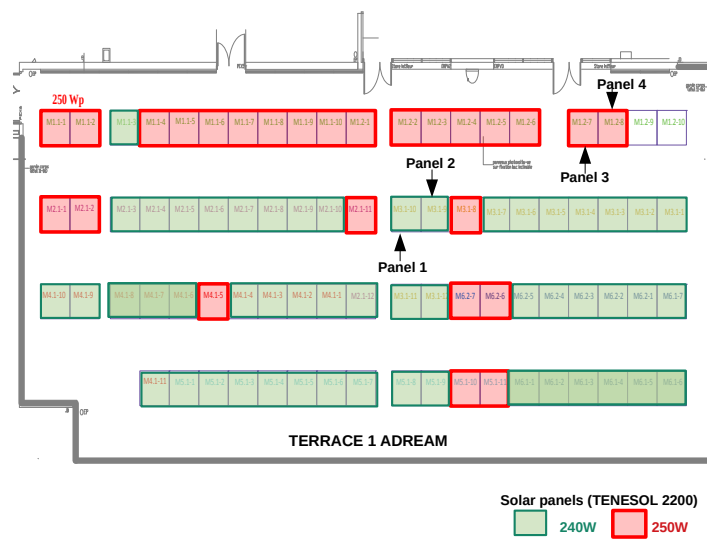
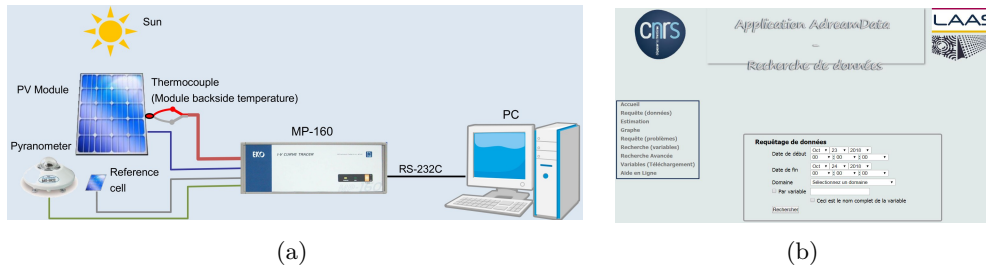


Figure C.3 Terrace 1 in the ADREAM

Information on all sensors and measurements relating to energy production is stored in a database called Pelican, see figure (C.4). The acquisition system with the curve tracer is also shown in Fig(C.4).



**Figure C.4** (a) Acquisition system (b) Pelican

The ADREAM's sun path is shown in Fig C.5

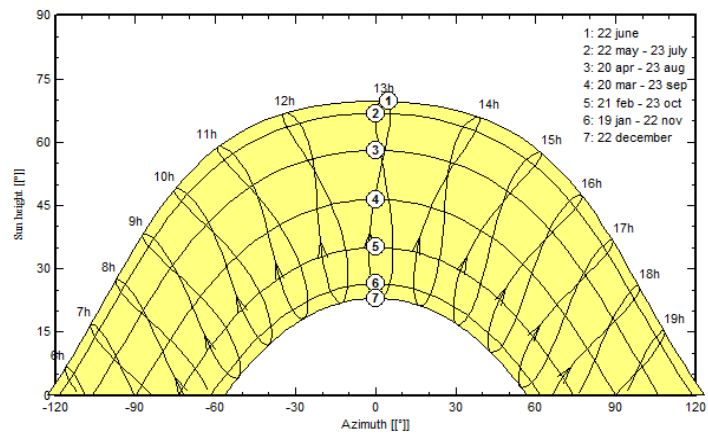


**Figure C.5** Sun path at LAAS-ADREAM



# D

## Appendix D

### D.1 Introduction to fault diagnosis

The fault diagnosis process followed by a system is shown in figure (D.1).

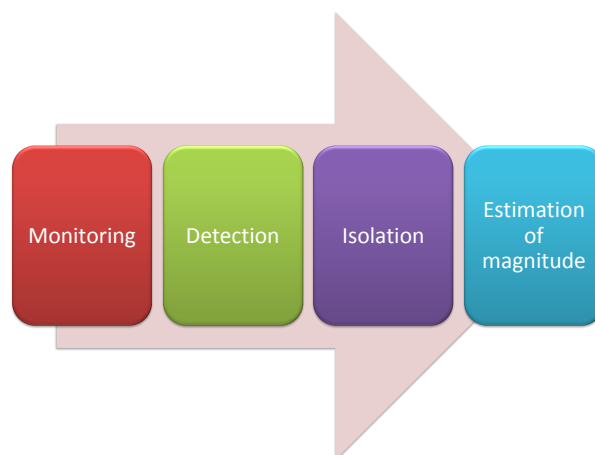


**Figure D.1** Diagnosis process

Fault types are usually classified into: [22]:

- sensor and actuator faults
- parametric faults
- structural changes

In terms of their occurrence, faults are usually classified into:

- abrupt faults,
- progressive faults,

- incipient faults, and
- intermittent faults

## D.2 Detection, isolation, and diagnosis of faults using FDD methods

FDD methods utilize the concept of redundancy, which can be either a hardware redundancy or an analytical redundancy, as shown in Figure D.2.

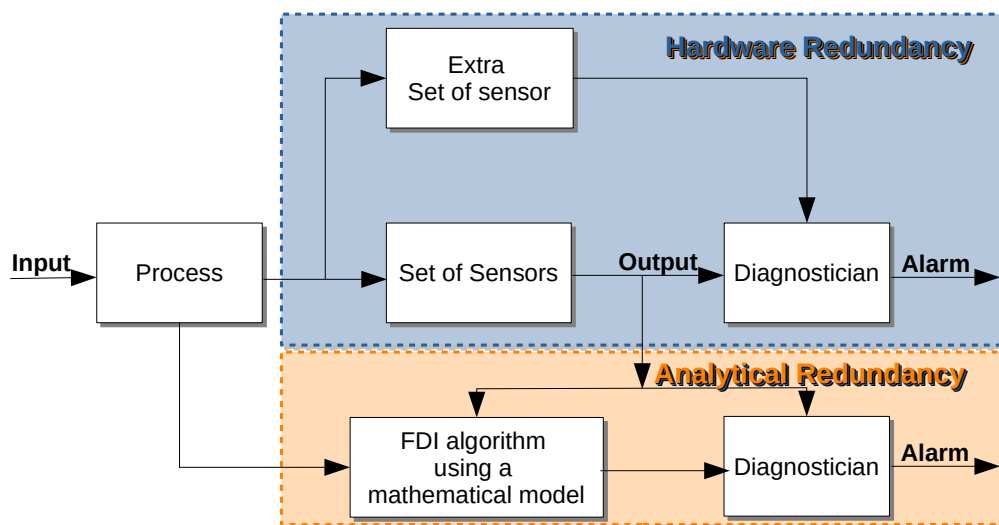


Figure D.2 Hardware redundancy and analytical redundancy for FDI [17]

### D.2.1 Hardware redundancy approach and analytical redundancy approach

- Hardware redundancy compares duplicate signals that are generated by various hardware parameters such as measurements from the same signal given by two or more sensors. Common techniques used in the hardware redundancy approach include: the cross channel monitoring (CCM) method, residual generation using parity generation (based on sensor geometry or signal patterns, for example), and signal processing methods such as wavelet transformation, etc.
- Analytical redundancy uses a mathematical model of the system with some estimation techniques for FDI. Additional hardware is not required as it is with the analytical redundancy approach. It is usually a more cost-effective approach. However, the analytical redundancy approach is more challenging due to the need to ensure its robustness in the presence of model uncertainties, noise, and unknown disturbances. Generally, the analytical redundancy approach can be divided into quantitative model-based methods and qualitative model-based methods [17].

1. The quantitative model-based methods, such as the observer-based methods, use explicit mathematical models and control theories to generate residuals for FDI.
2. The qualitative model-based methods use artificial intelligence (AI) techniques, such as pattern recognition, to capture discrepancies between observed behavior and that predicted by a model.

As illustrated in Fig.(D.3), the residual is a signal generated based on the input vector  $u(t)$  and the output vector  $y(t)$ , or

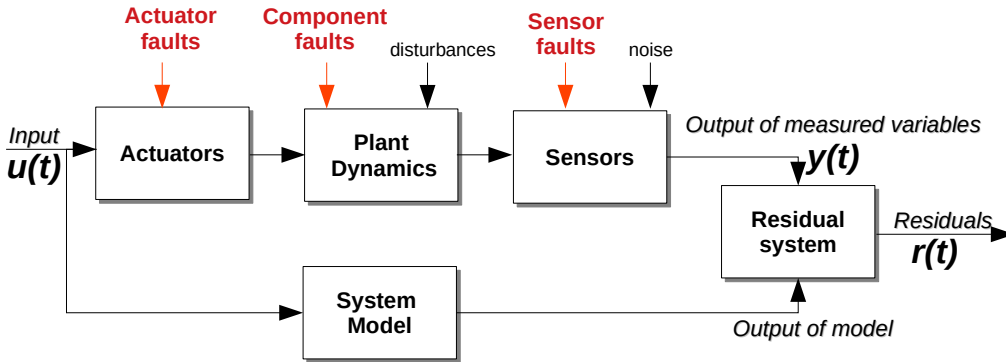


**Figure D.3** The fault model used for the residual generation based on the model

$$r(t) = g(u(t), y(t)) \quad (D.1)$$

Commonly, the residual  $r(t)$  is the difference between the measured output  $y(t)$  and the output on the plant's model  $\hat{y}(t)$ , i.e.,

$$r(t) = y(t) - \hat{y}(t) \quad (D.2)$$

For fault detection Eq.(D.2), the residual should satisfy the following properties:

- Invariance Relation: When no fault occurs, the mean of the residual should be zero.
- Fault Detectability: When there are faults in the system occurs, it should deviate from zero.

### D.3 Residues

For fault isolation, the residuals generated should not only be sensitive to faults, they also need to be able to distinguish between different types of faults. There are two approaches to generate such residuals that facilitate fault isolation:

- Directional residual: generates residual vectors that lie in a specified direction in the residual subspace and correspond to each type of fault. The fault isolation problem is then transformed into one that determines the direction of the residual vector.

- Structured residual: each residual vector is designed to be sensitive to a single or selective set of faults and insensitive to the rest. These residuals are usually characterized by a fault matrix signature in which the rows correspond to residuals and columns correspond to faults. A “1” in the FSM represents coupling between a residual and a fault, and a “0” represents no coupling. For isolation, all columns must be different. A special case in which each residual is designed to respond to a single fault is known as a diagonal structure, see Table (3.5).

### D.3.1 Fault detection

The residue is the difference between the expected value and the actual value. There is a threshold defined by an upper limit and lower limit. Values outside this threshold generate a residue flag "1", see Fig(D.4). If the error  $r_1$  or  $r_2$  is within the threshold, a flag that has a value of value "0" is generated, but if it exceeds the upper or lower limit values of the threshold, a flag that has a value of "1" is generated. If there is a deviation from the expected behavior due to causes other than disturbances or noise, a fault has been detected.

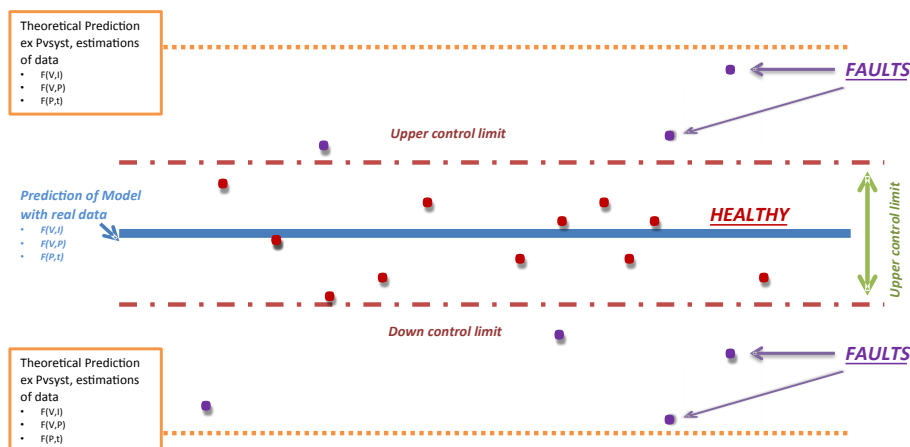
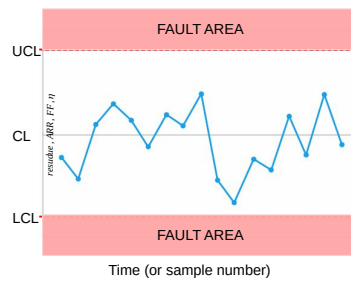


Figure D.4 Residue

#### D.3.1.1 Threshold of the residuals

To avoid fault false alarms, it is necessary to carry out an in-depth analysis of the types of waste as this uses statistical measures of the system.

**Statistical Analysis of residuals** : The chart plots measurements relating to PV quality characteristics of the residues in samples taken from the process versus time, see Fig(D.5). The chart has a center line (CL) and upper and lower control limits (UCL and LCL) [23]. The center line represents where this process characteristic should fall if there are no faults or no disturbances. The control limits are determined from some simple statistical considerations.



**Figure D.5** Control chart

- Shewhart:  $x_i$  are individual observations collected from a monitored process.  $\sigma$  is the standard deviation  $\mu$ . CL is the process mean.  $UCL=CL+3\sigma$  and  $LCL=CL-3\sigma$  is the standard deviation.
- Two very effective alternatives to the Shewhart control chart may be used when small process shifts are of interest.
  - Cumulative sum (CUSUM) control chart:
  - Exponentially weighted moving average (EWMA) control chart:

### D.4 Fault isolation and fault signature

A fault signature is a sequence of flags that allow a fault to be identified. If the fault signature is unique, it can be affirmed that the fault could be isolated and the type of fault is identified, see Fig(D.6).

- Blue region: Flags  $r1 = 0$  and  $r2 = 0$ , system without faults.
- Green region: Flags  $r1 = 0$  and  $r2 = 1$ , existence of a residue, possible presence of failure.
- Pink region: Flags  $r1 = 1$  and  $r2 = 0$ , existence of a residue, possible presence of failure.
- Orange region: Flags  $r1 = 1$  and  $r2 = 1$ , existence of two residues, possible presence of failure.

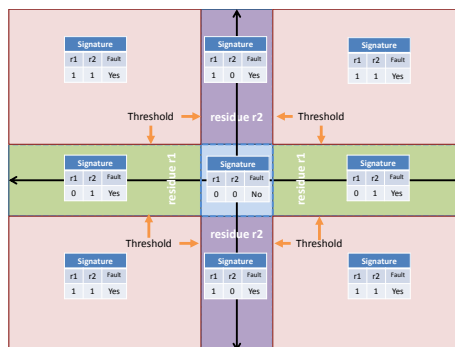


**Figure D.6** Region signature of faults

The problem of fault isolation can be seen in Figure (D.7) which shows how a

fault signature can simultaneously belong to two different types of faults (f1 and f2).

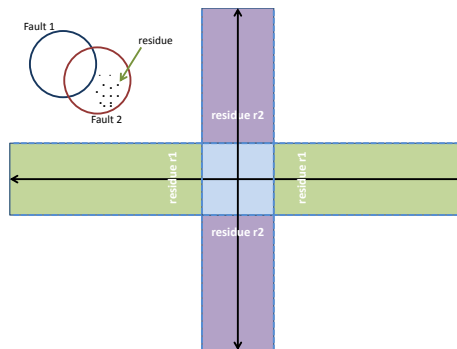


**Figure D.7** Isolation of faults

Once the residuals are generated, the next step is to determine whether any fault has occurred as well as the location and type of each fault based on statistical tests of the residuals. The simplest approach is to decide that a fault has occurred when the instantaneous value of a residual vector exceeds a constant threshold.

# E

## Appendix E

### E.1 Monitoring interface of the PV system

#### E.1.1 Monitoring PV system

Figure(E.1) presents a monitoring interface of four PV panels.

1. irradiation versus time curve.
2. temperature versus time curve.
3. I-V curve
4. P-t curve

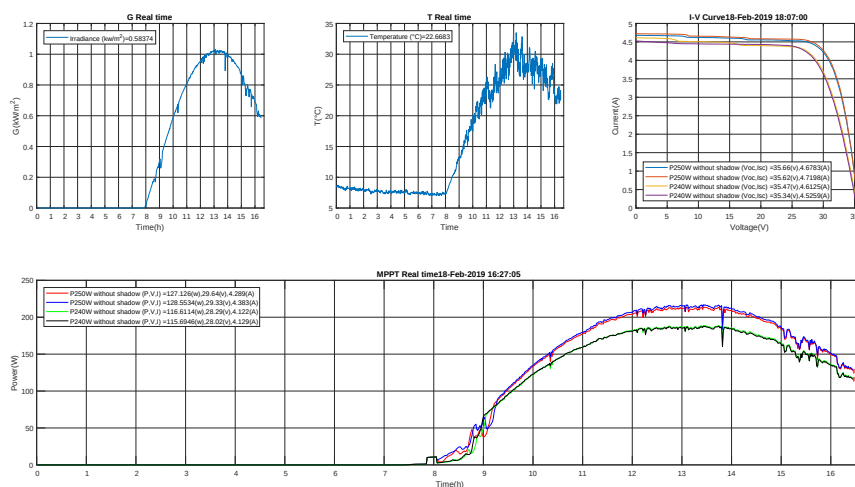


Figure E.1 Monitoring interface

### E.1.2 Display interface 1: diagnosis based data driven

This thesis has developed an interface for fault diagnosis based on data. To develop this interface, we used the monitoring system that was previously shown in the chapter. The interface comprises eight windows:

1. Solar irradiation versus time that shows the current value and values from midnight to the present.
2. Temperature versus time showing the current value and the values from midnight to the present.
3. Voltage versus current of the photovoltaic module that is compared with the models.
4. GMPP versus time
5. Data-based diagnosis G-P
6. Data-based diagnosis G-I
7. Data-based diagnosis G-V
8. Data-based diagnosis FF

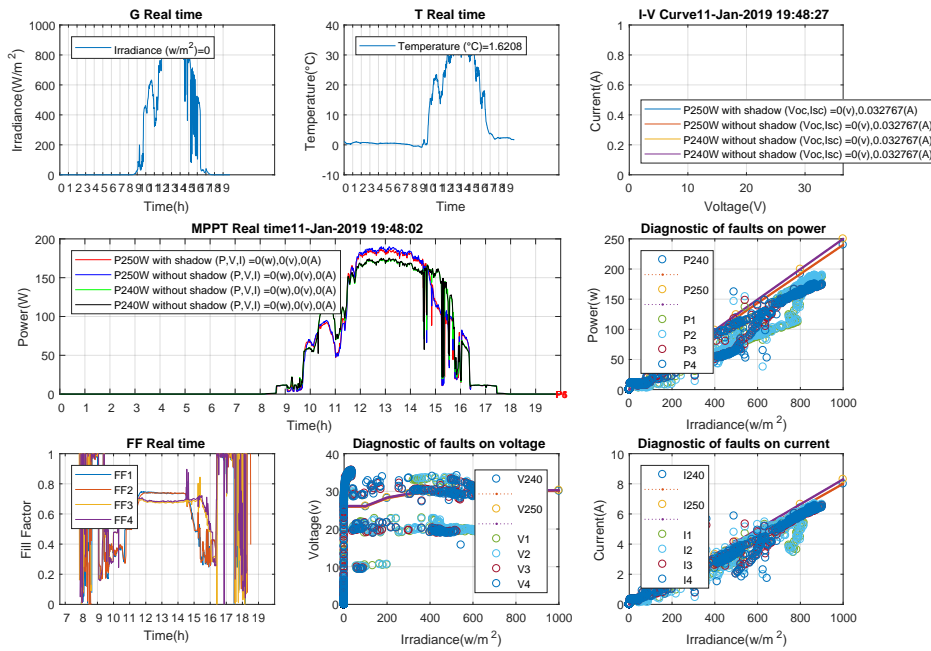


Figure E.2 Data driven diagnosis

### E.1.3 Display interface 2: diagnosis based on the model

We developed an interface for fault diagnosis based on models. To develop this interface, we used the monitoring system previously shown in the chapter. The developed interface consists of four windows:

1. The irradiance curve versus time, it shows the present value and values from midnight to the next midnight
2. Temperature curves (both in time)
3. Curve I-V can be seen through moments in time and the models
4. Maximum system power curve

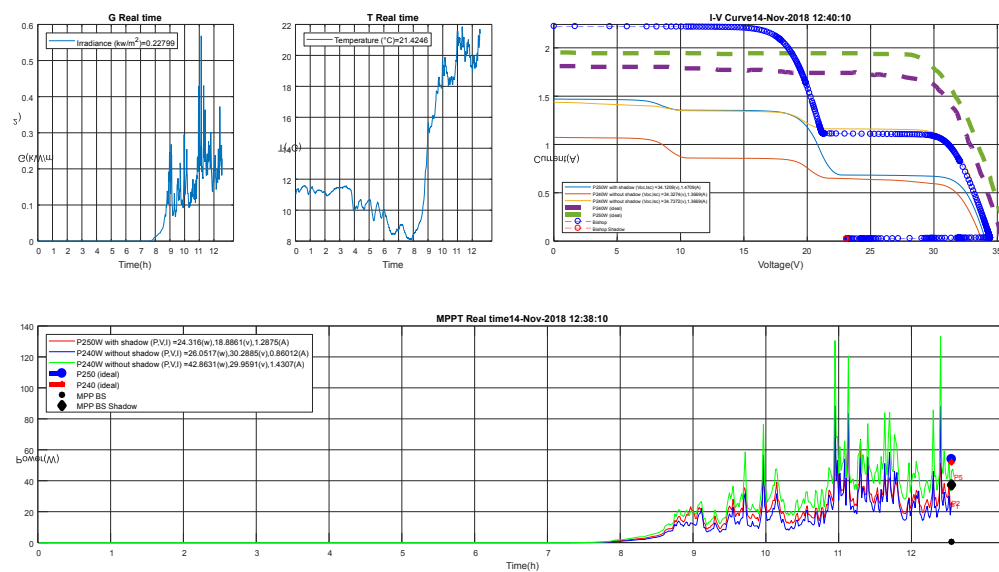


Figure E.3 Monitoring and comparison system interface vs. model

# Bibliography

- [1] G. Petrone, C. A. Ramos-Paja, and G. Spagnuolo, *Photovoltaic Sources Modeling*. 2017.
- [2] A. Gutierrez Galeano, *Study of Photovoltaic System Integration in Microgrids through Real-Time Modeling and Emulation of its Components Using HiLeS*. Theses, Université Paul Sabatier - Toulouse III, Sept. 2017.
- [3] S. Lu, B. Phung, and D. Zhang, “A comprehensive review on dc arc faults and their diagnosis methods in photovoltaic systems,” *Renewable and Sustainable Energy Reviews*, vol. 89, pp. 88 – 98, 2018.
- [4] E. Garoudja, F. Harrou, Y. Sun, K. Kara, A. Chouder, and S. Silvestre, “Statistical fault detection in photovoltaic systems,” *Solar Energy*, vol. 150, pp. 485 – 499, 2017.
- [5] M. Dhimish, V. Holmes, and M. Dales, “Parallel fault detection algorithm for grid-connected photovoltaic plants,” *Renewable Energy*, vol. 113, pp. 94 – 111, 2017.
- [6] “World energetic consumption statistics.” <https://yearbook.enerdata.net>, May 2018.
- [7] “U.s energy information administration.” [www.eia.gov](http://www.eia.gov), May 2018.
- [8] T. Funabashi, *Integration of distributed energy resources in power systems: implementation, operation and control*. Academic Press, 2016.
- [9] “Molecular expressions.” <http://micro.magnet.fsu.edu/>, May 2018.
- [10] <https://www.fondriest.com/>, May 2018.
- [11] Trace engineering, 5916 195th St.NE Arlington, WA, *A review of inverter design and topologies*.
- [12] D. W. Gao, *Energy storage for sustainable microgrid*. Academic Press, 2015.
- [13] “Dupont.” <http://www.dupont.co.in/>, May 2018.
- [14] O. Lopez Santos, *Contribution to the DC-AC conversion in photovoltaic systems : Module oriented converters*. Theses, INSA de Toulouse, Feb. 2015.
- [15] Y. El Basri, *Reconfigurable distributed power architecture for the optimisation of photovoltaic energy*. Theses, Université Paul Sabatier - Toulouse III, June 2013.
- [16] M. Aguilar-Justo and C. de Luna-Ortega, “Fdi with hybrid bond graphs in the full bridge inverter,” in *Electrical Engineering Computing Science and*

- 
- Automatic Control (CCE), 2011 8th International Conference on*, pp. 1–6, IEEE, 2011.
- [17] I. Hwang, S. Kim, Y. Kim, and C. E. Seah, “A survey of fault detection, isolation, and reconfiguration methods,” *IEEE Transactions on Control Systems Technology*, vol. 18, pp. 636–653, May 2010.
- [18] P. G. V. Sampaio and M. O. A. González, “Photovoltaic solar energy: Conceptual framework,” *Renewable and Sustainable Energy Reviews*, vol. 74, pp. 590 – 601, 2017.
- [19] A. Mellit, G. Tina, and S. Kalogirou, “Fault detection and diagnosis methods for photovoltaic systems: A review,” *Renewable and Sustainable Energy Reviews*, vol. 91, pp. 1 – 17, 2018.
- [20] C. Kleijn, *20-sim 4.1 Reference Manual*. Getting Started with 20-sim, 2009.
- [21] B. Jammes, “Analyse et bilan de la production pv adream,” tech. rep., LAAS-CNRS, 2018.
- [22] W. Borutzky, *Bond graph model-based fault diagnosis of hybrid systems*. Springer, 2015.
- [23] D. C. Montgomery, *Introduction to statistical quality control*. John Wiley & Sons (New York), 2009.